Title
Addressing Challenges on the Dark Energy Spectroscopic Instrument (DESI)

Author
Fagrelius, Parker

Publication Date
2018

Peer reviewed|Thesis/dissertation

Addressing Challenges on the Dark Energy Spectroscopic Instrument (DESI)

by

Parker Fagrelius

A dissertation submitted in partial satisfaction of the

requirements for the degree of

Doctor of Philosophy

in

Physics

in the

Graduate Division

of the

University of California, Berkeley

Committee in charge:

Dr. David Schlegel, Co-chair
Professor Saul Perlmutter, Co-chair
Associate Professor Jessica Lu
Professor Martin White

Fall 2018

Addressing Challenges on the Dark Energy Spectroscopic Instrument (DESI)

Abstract

Addressing Challenges on the Dark Energy Spectroscopic Instrument (DESI)

by

Parker Fagrelius

Doctor of Philosophy in Physics

University of California, Berkeley

Dr. David Schlegel, Co-chair

Professor Saul Perlmutter, Co-chair

The Dark Energy Spectroscopic Instrument (DESI) is under construction to measure the expansion history of the universe using the baryon acoustic oscillations technique. The spectra of 35 million galaxies and quasars over 14,000 square degrees will be measured during a 5-year survey. A new prime focus corrector for the Mayall telescope at Kitt Peak National Observatory will deliver light to 5,000 individually targeted fiber-fed robotic positioners. The fibers in turn feed ten broadband multi-object spectrographs. This thesis details original work done in support of the DESI experiment, both for the instrument and survey design and optimization. First, I describe a novel approach for connecting optical fibers using fusion splicing, a method that will be implemented on DESI. Then, I will describe the ProtoDESI experiment, an on-sky technology demonstration with the goal to reduce technical risks associated with aligning optical fibers with targets using robotic fiber positioners and maintaining the stability required to operate DESI. The ProtoDESI prime focus instrument, which was installed and commissioned on the 4-m Mayall telescope from 2016 August 14 to September 30, consisted of three fiber positioners, illuminated fiducials, and a guide camera. ProtoDESI was successful in acquiring targets with the robotically positioned fibers and demonstrated that the DESI guiding requirements can be met. Finally, I will describe a predictive sky background model for DESI, which is built on the spectra from the 5-year Baryon Oscillation Spectroscopic Survey (BOSS). This dataset consists of ∼1 million unique sky spectra covering 360 - 1040 nm collected in a variety of observational conditions. We measure an inter-airglow line continuum value of $\sim 0.81 \times 10^{-17} erg/cm^2/s/\mathring{A}/arcsec^2$ in dark time across the full wavelength range, with a variance of $\sim 0.175 \times 10^{-17} erg/cm^2/s/\mathring{A}/arcsec^2$. The detailed model, which accounts for 50% of the variance, shows that the dark sky continuum consists of ∼ 30% zodiacal light and is significantly impacted by solar activity. The improved spectroscopic sky background model can be used in simulations and forecasting for DESI and other surveys.

To my Parents, Eric and Phylis Fagrelius

I wouldn't be here without you.

Acknowledgments

My career in physics started while I was an undergraduate at Dartmouth College. It would have ended there without the mentorship and guidance from Kristina Lynch. When I started my work at JPL I expected that my career would develop in aerospace engineering. Thanks to my supportive and patient supervisor, Jeff Booth, I was introduced to exciting work in cosmology which inspired me to go to graduate school While at JPL, I also received excellent mentoring from Margaret Frerking who showed me how to be an inquisitive project manager. The skills I learned at JPL enabled me to be successful in research at graduate school. When I arrived at UC Berkeley, and before working on DESI, I worked in two other research groups at Berkeley. I am very grateful to Adrian Lee and Saul Perlmutter for inviting me into their groups and giving me interesting projects to work on, and I am very fortunate that they continued to serve as advisors during my thesis work.

I started my involvement on DESI with Claire Poppet and her work with the optical fibers. At the time I was considering leaving graduate school, and my work with Claire reinvigorated my motivation to continue research. She inspires me with her hands on expertise and serves as an role model in how to maintain excellence at work while also juggling family life and having fun. I am grateful to be able to call her a friend. Working on ProtoDESI was the best experience, hands down, I've had in my working life. I can't thank the DESI leadership enough for entrusting me with that role and giving me the support I needed. The scientists and engineers working on DESI are of the highest caliber, and I would like to thank the following in particular: Michael Levi, Joseph Silber, Robert Besuner, Pat Jelinsky, Michael Lampton, Klaus Honscheid, Ronald Probst, Dick Joyce, David Sprayberry, Arjun Dey, Bob Marshall, Lori Allen, Michael Schubnell, Steve Kent, Liz Buckley-Geer, Todd Claybaugh, Charles Baltay, David Rabinowitz, Armin Karcher, Connie Rockosi, Paul Martini, Stephen Bailey, David Kirkby, and Julien Guy. I'm afraid working on DESI has set an extremely high bar for my expectations of future project teams. I greatly thank my advisor, David Schlegel, for taking me on as a student. His positivity, excitement and approach to solving problems is inspiring. He has been extremely supportive through this process, eager to get me involved in interesting projects, and helpful in working through concepts and problems. I am glad I have the opportunity to continue working and learning from him.

Graduate school was more challenging than I expected. I have only been able to complete this process because of the support from my great friends and family. I have made life long friends at Berkeley: thank you to Halleh Balch, Trevor Bowen, and Robert Kealhofer for always being available have a beer and laugh over our (my) misery. I was so lucky to have old friends here at Berkeley when I arrived. Thank you to Rachel Hochman and Laura Lammers for showing me how to gracefully tackle the unique challenges of being in academia, and in particular, being a woman in science. My parents Eric and Phylis Fagrelius and my sisters Michal Fagrelius and Jeremy Morrison are forever my biggest supporters. Thank you for your never ending support. I am so grateful to have met Erik Endert during these last five years. He makes every year better. Thank you for being such an excellent partner and always making me laugh.

Contents

List of Figures

List of Tables

Chapter 1

Introduction

This thesis presents original work in support of the Dark Energy Spectroscopic Instrument (DESI). To effectively motivate this work, the introductory chapter describes the state of knowledge of dark energy (Sec. 1.1), describes in depth the baryon acoustic oscillation (BAO) method for measurement cosmological distances (Sec. 1.2), gives a review of large scale spectroscopic redshift surveys that have made possible BAO and RSD experiments (Sec. 1.3), and then an overview of the DESI experiment (Sec. 1.4). The original work of the thesis is presented in the following chapters. In chapter 2, I describe a novel approach to connecting fiber optics using fusion splicing, a method that will be used on the DESI optical cables. This work was originally published in the proceedings for the SPIE conference (Fagrelius *et al.* 2016). Chapter 3 describes the ProtoDESI project, which was the first on-sky test of DESI hardware. This chapter is based largely on a paper published in *Publications of the Astronomical Society of the Pacific* (PASP) (Fagrelius *et al.* 2018). Finally, chapter 4 describes a predictive sky background model that will be used for DESI survey optimization, which uses 5 years of BOSS/SDSS-III sky spectra.

1.1 Dark Energy

When Albert Einstein derived the field equations that describe his general theory of relativity, he believed that the universe was static. In his theory, which describes the curvature of spacetime due to mass and energy, he added a "cosmological constant" (Λ) to the geometric side of the equation to counteract the attractive gravitational force of matter (Eqn. 1.1). It has since been observed that the universe is not static, but expanding. Regardless, there is no reason to do away with this cosmological constant.

$$R_{\mu\nu} - \frac{1}{2} R\, g_{\mu\nu} + \Lambda\, g_{\mu\nu} = \frac{8\pi G}{c^4} T_{\mu\nu} \tag{1.1}$$

where $R_{\mu\nu}$ is the Ricci curvature tensor, R is the scalar curvature, $g_{\mu\nu}$ is the metric tensor, Λ is the cosmological constant, G is Newton's gravitational constant, c is the speed of light,

and $T_{\mu\nu}$ is the stress-energy tensors. In 1998, two independent teams (Perlmutter *et al.* 1999, Riess *et al.* 1998) measured the magnitude of Type Ia Supernovae at a range of redshifts ($0.16 < z \leq 0.86$ combined). Their results showed that the brightness of the supernovae decreased as a function of redshift consistent with an accelerating expansion rate of the universe. The rate of cosmic acceleration supports a cosmology with a geometrically flat universe that is not currently dominated by matter. If general relativity is the correct way to describe our universe, the accelerating expansion rate could indicate that there is a new form of energy. If we instead move the cosmological constant to the stress energy tensor ($T_{\mu\nu}$) side of the field equation, this unknown energy density ("dark energy") can be used to describe the source of cosmic acceleration. Any form of energy that is constant in time and space must have a repulsive gravitational effect, so it is possible that this dark energy is the cosmological constant and dominates the total energy density of the universe.

This discovery leaves us with some questions: does the acceleration of the universe arise from a new energy component (dark energy) or a breakdown of general relativity on some scales? If the acceleration is caused by dark energy, why is it the dominant energy today? Is the dark energy constant in time, corresponding to the cosmological constant? To answer some of these questions we can parametrize the dark energy equation of state (w_{DE}) as having a component that is constant in time ($w_\circ$) and one that changes with the scale of the universe (w_a) (Eqn. 1.2). If dark energy is the cosmological constant, $w_{DE} = w_\circ = -1$, and if this new energy density changes in time and space, w_a will be non-zero. Otherwise, general relativity is an incomplete description of our universe. In order to differentiate between these cosmologies, we want to measure w_{DE} by measuring the expansion history of the universe by its scale ($a = \frac{1}{1+z}$) and derivative as a function of redshift as parametrized by the Friedmann equation (Eqn. 1.3).

$$w_{DE} = w_\circ + (1 - a)\, w_a. \tag{1.2}$$

$$\frac{H^2(a)}{H_\circ^2} = \frac{\dot{a}}{a_\circ}^2 = \sum_i \Omega_{i,0} a^{-3(1+w_i)} \tag{1.3}$$

where w $= p/\rho$, with p being pressure and ρ being density for a fluid. The universe is observed to be homogenous and isotropic. The description of this space-time geometry, the Robertson-Walker metric, allows for different curvatures of space,

$$ds^2 = -c^2 dt^2 + a(t)^2 \left[\frac{dx^2}{1 - \kappa x^2 / R_0^2} + x^2 d\Omega^2 \right] \tag{1.4}$$

where $d\Omega = d\theta^2 + sin^2\theta d\phi^2$. If the value of κ is 0, the metric describes flat, Euclidean space. If instead the value of $\kappa = +1$, the metric describes three-dimensional space with uniform positive curvature, and if -1 it describes uniform negatively curved space having infinite volume. Current models indicate that our universe contains radiation, matter, and dark energy, currently dominated by the later two energy components (Dodelson 2003, Cervantes-Cota & Smoot 2011). We can constrain our knowledge of the curvature of the universe as

$$\Omega_\kappa = -\kappa/H_0^2 = 1 - [\Omega_r + \Omega_m + \Omega_{DE}]. \quad (1.5)$$

Therefore, our measurements of the expansion history of the universe will also inform our understanding of the curvature of space. Current best measurements indicate that we live in a spatially flat universe (Planck Collaboration *et al.* 2018), but even small deviations from that could have major implications on our understanding of the universe.

The expansion history of the universe can be measured by determining the scale of the universe across a large redshift range, requiring distance measurements to astronomical observables and their redshift ($z = \frac{\lambda_o}{\lambda_e} - 1$). There are several ways to measure distance, which will be discussed in depth below. Our goal is to measure the redshift objects as a function of their distance from us. As an object moves away from us, the emitted wavelength (λ_e) shifts so that the observed wavelength (λ_o) is longer than emitted. For optical wavelengths, the observed wavelength becomes "redder." Spectroscopic redshifts are measured by identifying a known spectral feature in the observed emitted spectrum, usually from stars and galaxies, and comparing the measured wavelength of that spectral line to the known rest wavelength. To effectively spectroscopically measure redshifts over a large redshift range it is important to use an easily identifiable spectral feature with sufficient signal to noise.

Photometry can also be used to measure redshifts, sometimes offering a more cost effective approach. Photometric redshifts (photo-z's) are obtained using the flux in several broad photometric bands to reconstruct a spectral energy distribution (SED). This was first done by Baum (1962), who measured the redshift of ~ 10 galaxies with 9 bandpasses. Koo (1985) followed this up with a new approach, showing that using only 4 unique photometric plates and color-color diagrams one could separate galaxies by type and redshift. A more popular approach was developed by Loh & Spillar (1986), using SED template fitting, and was used several times to study the redshift distribution of the Hubble Deep Field (Gwyn & Hartwick 1996, Fernández-Soto *et al.* 1999). Connolly *et al.* (1995) developed an approach used most commonly today for measuring the photometric redshifts that uses empirical training to create a linear regression model. Most of these early photo-z's were measured from pencil-like fields. Csabai *et al.* (2003) used the Sloan Digital Sky Survey (SDSS) imaging catalogue to measure photo-z's on a larger field of view with late type galaxies. They measured redshifts with $\delta_z \approx 0.03$ for r< 18 and $\delta_z \approx 0.1$ for $r \approx 21$. These redshift measurements can be used for cosmology, and a photometric redshift survey 10 times the volume of a spectroscopic redshift survey can produce similar power spectrum measurements. However, the loss of information due to smearing in the radial direction results in less precise redshift measurements. This effect significantly limits baryon acoustic oscillation (BAO) distance measurement accuracy, which will be discussed in length in sec. 1.2 (Seo & Eisenstein 2007, Glazebrook & Blake 2005, Blake & Bridle 2005).

Currently, the most common ways to make cosmological distance measurements are with standard candles and standard rulers, as summarized in Hogg (1999). Standard candles employ astronomical objects with a stable, known brightness that can be used to measure the luminosity distance (D_L) with the bolometric luminosity (L) and the flux from the object

(S): $D_L = \sqrt{L/(4\pi S)}$. The first standard candle was discovered by Henrietta Leavitt in 1921 when she found that there was a relationship between the period of Cepheid variable stars and their luminosity. While this standard candle is only functional in the relatively local universe, it is still being used today to calibrate distance ladders to measure the hubble constant today (H_0) (Riess *et al.* 2016). Another standard candle in the local universe ($z \ll 1$) has been spiral galaxies. Tully & Fisher (1977) determined a relationship between the luminosity of these galaxies and their mass, measured through the velocity of their spiral arms. While no longer used for cosmological distance measurements, it is still a valuable probe of galaxy evolution. Massive stars differ significantly in luminosity and size, but when Type II supernovae start expanding, they can be utilized as standard candles. Dubbed the "Expanding Photosphere Method" (EPM), Kirshner & Kwan (1974) modeled the photospheres of Type II SNe as blackbodies, the speed of the expansion measured by absorption lines in the SNe spectra. When the flux and expansion velocity are measured at several epochs, the distance can be measured, as demonstrated by Schmidt *et al.* (1992).

The most common objects used to measure luminosity distance today are Type Ia Supernovae, as measured in the discovery of the accelerating universe. These SNa have proven to be such great standard candles as the peak luminosity is so consistent. This is because their progenitors are white dwarf stars that collapse near the Chandrasekhar limit when enough mass is added to it, e.g. from a companion star, that electron degeneracy pressure is no longer able to hold off collapse; the peak luminosity is then related to this standard mass of the white dwarfs at collapse. As cosmologists have continued to use Type Ia supernovae in cosmology it has been found that they are "standardizable," meaning that there are several astrophysical features of the exploding stars that differentiate them ever so slightly from each other, and the supernovae can only be used as standard candles with some corrections to account for temporal and color differences (Phillips 1993, Tripp 1998, Kim *et al.* 2013).

Recently, electromagnetic detection of GW170817 offered another method of measuring cosmological distances. Gravity waves from a binary neutron star merger were measured using the LIGO-Virgo gravitational wave detectors, and at the same time (1.7 s later), gamma rays were measured from the same location as GRB 170817A with the Fermi Gamma Ray Burst Monitor (GBM) (Abbott *et al.* 2017). This momentous discovery offered a direct measurement of the luminosity distance, and offers a new probe ("standard siren") that will continue to be used in the future to measure distances to ever higher redshifts.

Standard rulers use a known scale on the sky to measure the angular diameter distance (D_A). As the distance to an object changes, the angle (δ) that the standard ruler subtends (r_s) changes as well, $D_A = r_s\,\delta$. One of the first successful measurements of a standard scale on the sky was of the intensity of the Cosmic Microwave Background (CMB), a measure of the large scale structure at the surface of last scattering after reconstruction (see Sec. 1.2). Using the Differential Microwave Radiometers (DMR) instrument on the COBE space telescope (Smoot *et al.* 1991), the large scale anisotropies of the CMB were first discovered. Measurement of the angular scale and amplitude of the first peak of the power spectrum was first confirmed by balloon-born experiments (BOOMERANG de Bernardis *et al.* 2002; MAXIMA Balbi *et al.* 2000) and an interferometer at the South Pole (DASI Halverson *et al.*

2002). Following these successful standard ruler measurements, groups started using galaxies to measure the same phenomenon that created the anisotropies in the CMB, allowing the scale to be measured at several redshifts. These Baryon Acoustic Oscillation (BAO), first measured by Cole *et al.* (2005) and Eisenstein *et al.* (2005), will be described in detail in the next section.

In 2006, in response to the growing consensus that dark energy is currently the dominant energy component in the universe and responsible for the cosmic acceleration, a "Dark Energy Task Force" (DETF) was assembled to assess the best ways to evaluate projects investigating cosmic acceleration. The report from the DETF (Albrecht *et al.* 2006) featured a figure of merit (FoM) to help differentiate the capability of projects to probe the properties of dark energy and its evolution with time. This FoM is defined as the inverse area of the error ellipse in the $w_\circ - w_a$ plane, enclosing 95% confidence. Larger values of the FoM correspond to stronger probes of the dark energy equation of state, indicating a project's ability to identify and differentiate between a constant dark energy or one that changes with time. The DETF evaluated 4 main probes with promise to gain insights into the cosmic acceleration: type Ia supernovae, baryon acoustic oscillations, mass of galaxy clusters, and weak lensing. They reported that none of these probes had sufficient power on their own to adequately constrain the dark energy equation of state, but a combination of several probes provides better constraints on cosmic acceleration.

In addition to understanding the dark energy equation of state, measuring the growth of structure as a function of redshift will provide complementary constraints on the theory of gravity, as large scale structure growth is constrained by dark energy (see Linder 2005 for a review). Standard candles and rulers can help measure the bulk flow of matter in the universe due to the accelerating expansion, but galaxy clustering can cause peculiar velocities in galaxies. These peculiar velocities are seen in the radial, or redshift direction along the line of sight, and are called Redshift Space Distortions (RSD). They deteriorate the BAO measurement, but can also offer a tool for measuring the growth of structure. Comparing the expansion history to the growth of structure will allow a test of general relativity and other theories of gravity. The RSD power spectrum can be written as the Kaiser approximation (Kaiser 1987):

$$P_g(k,\mu) = (b_g(z) + \mu^2 f(z))^2 \, P_m(k) \tag{1.6}$$

where b_g is the mass bias, μ is the cosine of the angle of observation relative to the wavenumber, and $f(z)$ is the log linear growth of rate of fluctuations, with $f = \Omega_M(a)^\gamma$. Models with the same expansion histories but different gravitation theories will have different values of γ. When $f(z)$ is fitted using a cosmological constant model (with general relativity), $\gamma = 0.55$ with accuracy to 0.2%. The amplitude of the power spectrum ($P_m(k)$) is degenerate with $f(z)$, so the main observable for the growth of structure is $f\sigma_8$, where σ_8 is the standard deviation of matter fluctuations in $8h^{-1}$Mpc and is used to normalize the power spectrum.

While measuring w_{DE} and the growth of structure are significant goals in the field of cosmology, there are also other interesting problems. The theory of inflation is widely regarded as the most probable explanation for certain observables, but some open questions remain.

While the primordial spectrum of density fluctuations can mostly be described as a power law, as in most things, the interesting physics emerges in its departure from this. Inflation predicts that the spectral index, n_s defined at some reference scale ($k_0 = 0.05\text{Mpc}^{-1}$),

$$n_s(k_0) = \left.\frac{d\ln P}{d\ln k}\right|_{k=k_0}, \tag{1.7}$$

is not exactly constant but has some dependence, or "running", with scale (i.e., $\alpha = dn_s/d\ln k \neq 0$). Additionally, inflation predicts that $n_s(k_0)$ deviates slightly from 1. Both a non zero measurement of α_s and non-unity measurement of $n_s(k_0)$ at a significant level would strengthen the case for inflation considerably. These inflationary parameters can be measured through the primordial power spectrum, strengthened by a large range of modes. Planck has measured the best constraints to date, with $n_s = 0.968 \pm 0.006$ (see Table 1.1) and a running of $\alpha = -0.003 \pm 0.007$ (Planck Collaboration *et al.* 2016c). These results can be complemented by galaxy surveys, most significantly by the Lyman-α forest.

Inflation also predicts a near gaussian distribution of primordial fluctuations, but the amount of primordial non-gaussianity differs from model to model. The departure from gaussianity ϕ_G, parametrized as f_{NL} in the primordial curvature fluctuation $\Phi = \phi_G + f_{NL}(\phi_G^2 - \langle\phi_G^2\rangle)$ could rule out the most simple models of inflation: a single field, slow roll model. This non-gaussianity can be measured in the CMB, and has been with COBE (Komatsu 2002), WMAP (Bennett *et al.* 2013), and Planck (Planck Collaboration *et al.* 2016b). It can also be studied with galaxy surveys by measurements of the dark matter halo bias, which was first shown by SDSS (Slosar *et al.* 2008).

In addition to inflation, the neutrino mass is also of interest in cosmology. We know that there are three neutrino mass eigenstates, each composed of different neutrino flavors, and we know the differences in the squares of masses (i.e. $\Delta m^2_{(21)}$, $\Delta m^2_{(32)}$). We do not know the absolute mass scale, however, nor the hierarchy of the masses. A normal hierarchy would imply that the two mass eigenstates that have a small separation have lower mass than the third, where an "inverted" hierarchy implies that the two closer together have a higher mass than the third. Cosmology can constrain these mass properties of neutrinos because after they transition to non-relativistic particles (some time after recombination) they behave similarly to dark matter and can impact BAO scales. The process neutrinos took to becoming non-relativistic provides a unique scale on the power spectrum, called the "free streaming scale". On small scales, defined as $k < k_{nr}$, with

$$k_{nr} \simeq 0.018\,\Omega_m^{1/2}\left(\frac{m}{1\text{eV}}\right)^{1/2} h\text{Mpc}^{-1}, \tag{1.8}$$

the power spectrum was reduced primarily because the growth rate of dark matter perturbations were reduced due to the absence of the gravitational effect from the free-streaming neutrinos (Lesgourgues & Pastor 2012). Power spectrum measurements from galaxy surveys have already developed constraints on the mass and mass hierarchy of the neutrinos (Riemer-Sørensen *et al.* 2012, Reid *et al.* 2010, Palanque-Delabrouille *et al.* 2015) .

Parameter	Value	Description
$\Omega_b\, h^2$	0.02226 ± 0.00023	baryon density
$\Omega_c\, h^2$	0.1186 ± 0.0020	cold dark matter density
$100\,\theta_{MC}$	1.04103 ± 0.00046	angular size of sound horizon ($100 \times r_s/D_V$)
τ	.066 ± 0.016	reionization optical depth due to Thompson scattering
$ln(10^{10}\, A_s)$	3.062 ± 0.029	log amp. of curvature pert. at $k_\circ = 0.05 Mpc^{-1}$
n_s	0.9677 ± 0.0060	scalar spectral index
Ω_{DE}	0.692 ± 0.012	Dark Energy density today
Ω_M	0.308 ± 0.012	Matter density today
σ_8	0.8149 ± 0.0093	density fluctuations at $8h^{-1}$ Mpc
t_0	13.799 ± 0.038	age of universe in Gyr
H_0	67.81 ± 0.92	Hubble parameter today (Hubble constant)

Table 1.1: Fiducial ΛCDM cosmological parameters based on Planck 2015 (Planck Collaboration *et al.* 2016a) assuming a spatially flat universe, using the temperature power spectrum (TT), polarization data for low-ℓ (lowP), and lensing reconstruction (lensing): TT+lowP+lensing.

The current consensus of cosmology can be described as spatially flat ($\kappa = 0$) ΛCDM, which includes dark energy as the cosmological constant and cold dark matter, assuming that $w_{DE} = -1$ and $\Omega_{tot} = 1$. This cosmology can be described with just 6 parameters determined from the acoustic peaks in the power spectrum of the anisotropies in the CMB. The location and size of these peaks are impacted by the photon-baryon ratio, matter-radiation ratio, redshift of the sound horizon, and optical depth at recombination, which was the surface of last scattering for the CMB photons. This fiducial cosmology, described in Table 1.1, is based on the most recent results from the Planck CMB experiment (Planck Collaboration *et al.* 2016a). Current and future experiments are looking to improve the uncertainties in these cosmological parameters and any deviation from this fiducial cosmology, which would provide greater insights into dark energy and potentially new physics. In order to differentiate between models of dark energy, w_{DE} should be measured to at least $\sim 1\%$, putting significant constraints on observational programs and hopefully providing the precision required to differentiate dark energy theories.

1.2 Baryon Acoustic Oscillations

During the period commonly referred to as inflation, quantum fluctuations in the inflaton field expanded with the exponential growth of the scale factor to a macroscopic field. In the early universe, the matter was largely ionized, and due to Thomson scattering, electrons, baryons and photons were tightly coupled as a plasma. The size of these fluctuations in the

photon/baryon plasma were less than the critical Jeans length (i.e. $\lambda \ll c_s t$), so photon pressure dominated over gravity and the perturbation oscillated like an acoustic wave (Peebles & Yu 1970). The perturbation of the dark matter, unaffected by the photon pressure, grew in place until the universe became matter dominated, at which time it started moving outward. As the universe expanded it cooled, and after $\sim 10^5$ years the baryons were sufficiently cooled to create neutral hydrogen atoms. During this recombination process, the mean free path for the photons increased and the acoustic waves were damped by diffusion on small scales ($\sim 8h^{-1}$Mpc), an effect known as Silk damping. The epoch of recombination lasted $\sim 70,000$ years, the midpoint defined as when the fractional ionization of electrons to baryons, $X = n_e/n_{bary} = 1/2$, occurring at a redshift of $z \sim 1370$ (Ryden 2003). Approximately 110,000 years later, the mean free path grew larger than the perturbations, and the photons streamed away and are measured as the CMB today. Without the photon pressure, matter was attracted to the gravitational potential wells at the over-density of dark matter, located at the source of the perturbation and at the peak of the baryonic acoustic wave, until reaching an equilibrium at an amplitude of $\sim \Omega_B/\Omega_M$. The baryons became the seeds of galaxy formation with the acoustic waves imprinted on them at large scales.

While the CMB has been measured as a constant blackbody background, the anisotropies contain rich information on the surface of last scattering at recombination. The same acoustic scales imprinted on the large scale structure of baryons have also been measured with excellent precision in the CMB power spectrum. The speed of the acoustic waves was set as the ratio of radiation pressure to energy density of the baryon-photon plasma. The plasma was dominated by photon pressure, and as radiation pressure is 1/3 of its energy density, $c_s = \sqrt{\delta p/\delta \rho} \simeq c/\sqrt{3}$. Using this speed it is possible to measure the distance travelled by the acoustic wave, setting our standard scale on the sky,

$$r_s = \int_0^{a_*} \frac{da}{a^2 H(a)} c_s(a) \tag{1.9}$$

where a_* is the scale at recombination. As originally shown by Hu & White (1996), this distance can be calculated using the photon-baryon and radiation-matter ratios as measured in the anisotropic CMB power spectrum, providing a fully calibrated standard ruler. The baryon acoustic oscillation scale is 150 Mpc, the distance travelled from initial perturbation until recombination.

As mentioned above, the baryons left at recombination became the seeds for galaxy formation. There is therefore a greater than random probability to find two galaxies separated by 150 Mpc ($\sim 100h^{-1}$ Mpc), with a mean density of $\bar{n}$ (Eqn 1.10). This excess probability can be expressed as a peak in the correlation function in configuration space, or positions in space according to FRW metric, (ξ_{12}) or small oscillations in the matter power spectrum, $P(k)$, in fourier space (Eqn. 1.11).

$$dP = \bar{n}^2 \delta V_1 \delta V_2 [1 + \xi_{12}(r)] \tag{1.10}$$

$$\xi(r) = \delta(x)\delta(x+r) = \int_0^{\inf} \frac{dk}{k} \Delta^2(k) \frac{sin(kr)}{kr} \tag{1.11}$$

The peak in the correlation function at a given redshift is a direct measurement of the radius of the sound horizon, our standard ruler, at that scale. In principle, the BAO is a simple method in that all is required is the three-dimensional positions of the galaxies, the relative separations of which are measured in the 1D correlation function or power spectrum. While the BAO standard ruler can be measured as D_A in the transverse direction, it can also be measured along the line of sight with $H(z)$, giving us a direct measurement of the growth of the scale factor. For experiments that are near the BAO threshold, these measurements can be combined as in equation 1.12, but the individual transverse and radial measurements provide stronger constraints.

$$D_V(s) = D_A(z)^{2/3} \left(\frac{cz}{H(z)}\right)^{1/3} \tag{1.12}$$

The relatively large size of the acoustic scale keeps this a mostly linear theory. At smaller scales, the nonlinearities and complexities of the interactions of matter can present systematic errors on our measurement of the BAO peaks. The peculiar velocities of galaxies due to interactions with other matter produce redshift space distortions (RSD), caused by large scale velocity flows and matter clustering, which can have a direct impact on H(z). The BAO signal is deteriorated by RSD, but measurement of the distortions offers insight into the growth of structure and the character of gravity throughout cosmic time as discussed above. Due to these bulk flows, matter can be moved by $\sim 10h^{-1}$ Mpc from its initial position, but these bulk flows are generated by exactly the same density perturbations that are being surveyed. This can be improved with "reconstruction", which is essentially a reversal of the gravitational effects that produce the peculiar velocities. This is possible because the galaxies we are measuring are the same causing the nonlinearities, so one can reverse the Z'eldovich approximation in which particles follow straight trajectories at rates predicted by linear perturbation, essentially running gravity backwards. In Eisenstein *et al.* (2007), they lay out a very simple process for reconstruction: compute the density field, fourier transform and filter with a gaussian kernel of $10 - 20h^{-1}$Mpc; predict linear motion and calculate the displacement field; move particles by the negative displacement field; and finally, account for linear redshift distortions. This concept was fully developed by Padmanabhan *et al.* (2012) and has been shown to improve measurement of the BAO peak in the correlation function by $> 20\%$ (see Fig. 1.1).

BAO is a weak signal, and so to get a precise distance measurement, a large sample of galaxies is needed. The statistical power of the BAO signal depends on the volume of sky surveyed, redshift range, and precision of redshift measurements. The acoustic oscillations in the matter power spectrum are predominantly in the range $0.1 - 0.2h\text{Mpc}^{-1}$, so to measure a representative universe we should have a sampling of at least $0.001h^3\text{Mpc}^{-3}$. The goal is to not be shot noise limited by moving towards a survey volume and source sampling such that cosmic variance is attempted, in which the sample variance is less than the variance between different sections of sky. With n density of galaxies, nP gives the relative contributions of shot noise and cosmic variance, which are equal when $nP = 1$. BAO surveys should aim

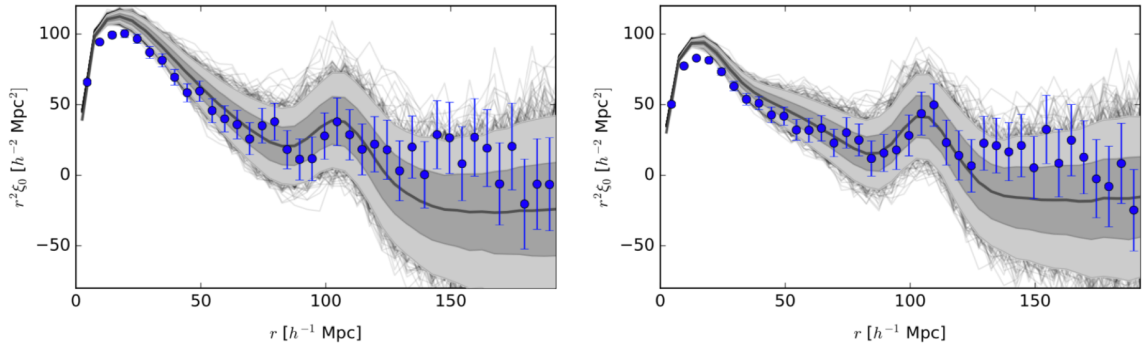

Figure 1.1: One dimensional correlation function for luminous red galaxies at a redshift of 0.72, using eBOSS (SDSS-IV) and BOSS CMASS (SDSS-III) galaxy samples. The left panel shows the pre-reconstruction correlation function and the right is the reconstructed correlation, which improves the rms errors $\sim 20\%$. (source: Bautista *et al.* 2017b)

for $nP > 3$ (Glazebrook & Blake 2005). Effectively constraining models of w_{DE} depends on our ability to measure $D_A(z)$ and $H(z)$ to a precision of 1%, in an effort to constraint dark energy theories. This error and be described as $\sigma \propto \sqrt{1/V_{eff}}$ (Feldman *et al.* 1994), where the effective volume is

$$V_{eff} = \left(\frac{nP}{1+nP}\right)^2 V_{survey}. \tag{1.13}$$

If a survey chooses to use photometric redshifts, the smearing of redshift measurements in the radial direction means that $D_A(z)$ can only be determined, while H_z information is lost. In this case, the error is increased by is multiplied by $\sqrt{\sigma_r/\sigma_{r,0}}$, where $\sigma_r = \sigma_0(1+z)\times dr/dz$ (Blake *et al.* 2005). Using a full Fisher matrix formalism, Seo & Eisenstein (2007) determine the cosmic variance limited BAO performance. For z $\sim$1, with a volume of 42.9 h^{-3}Gpc^3, the errors on D_A(z) and H(z) are 0.21 and 0.36 respectively, leading to $\sigma_w = 0.013$.

1.3 Large Spectroscopic Surveys

In order to complete a redshift survey to measure BAO, there are three main steps: create a target catalog through an imaging survey(s), make a selection of targets based on some magnitude cutoff, color selection, or other identifier, and then measure the spectra of targets to get their redshift. The surveys required to carry out such measurements, with large catalogs of galaxy redshifts across the sky with a variety of wavelength regimes, survey volumes, and galaxy targets, have rich datasets applicable to many astrophysical and cosmological studies. In addition to constraining cosmological parameters, large redshift surveys illuminate the large scale structure of the universe. If stars are included in the sample, as they have been for the SDSS surveys, they can also provide data for measurement of halo and galaxy stellar mass and biases, galaxy merger rates, and general comparison to N-body simulations

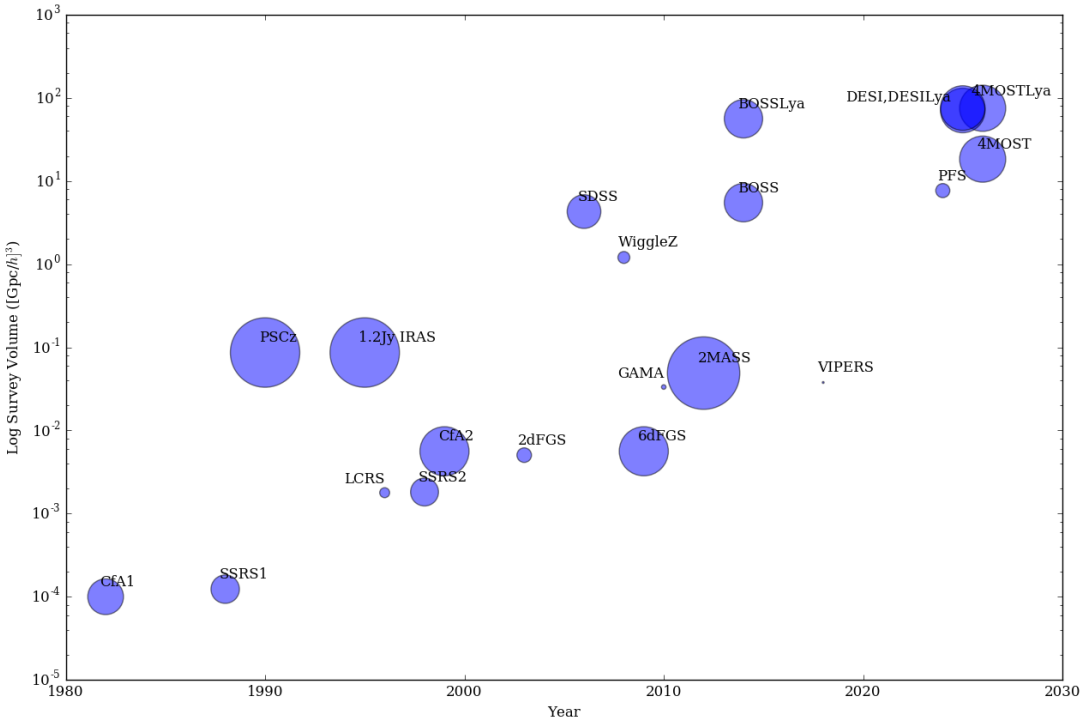

Figure 1.2: History of large spectroscopic redshift surveys. Survey completion date is plotted against the log survey volume, measured in $(\mathrm{Gpc}/h)^3$ using the cosmology listed in Table 1.1. The size of the date points corresponds to the relative area of the survey in deg^2.

for galactic distribution and evolution. Since the 1970's, ever-larger redshift surveys have been completed at a variety of redshift ranges, magnitude limits, and volumes (see Fig. 1.2). The next generation of large scale redshift surveys could revolutionize our understanding of the large scale structure of the universe and help create a 3D map of the universe out to $z \geq 3$.

1.3.1 History

In 1977, the Center for Astrophysics (CfA) completed a spectroscopic redshift survey, collecting ~ 2000 galaxies by 1982. Davis *et al.* (1982) built an intermediate resolution spectrograph for this purpose on the 1.5m telescope on Mt. Hopkins called the 'Z-machine'. They used the Zwicky catalogue (Zwicky *et al.* 1961) with a magnitude cutoff of $m_B \leq 14.5$, covering $\sim 9,000$ deg^2 at a mean redshift of $z \simeq 0.016$. This target selection reached galaxies beyond

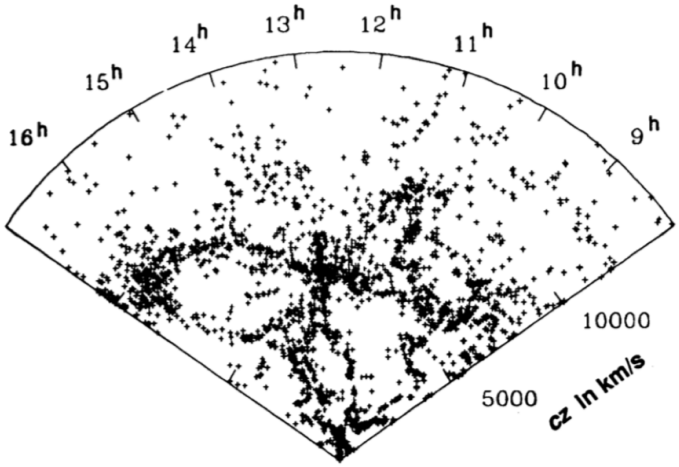

Figure 1.3: Results from the CfA2 survey as published in Geller & Huchra (1989). This segment, which consists of 2,500 galaxies, covers the declination range $26.5° \leq \delta \leq 44.5°$ and includes the "Great Wall", which is largest structure running across the northern hemisphere.

the local Virgo cluster in an attempt to measure a representative volume of the universe. Prior to this redshift survey, observations had indicated that other superclusters and voids existed, but it was believed that they were isolated, rare structures. The large scale structure measured with this first systematic redshift survey showed that "the natures of large scale clustering defies a simple qualitative description" (Davis *et al.* 1982), and the first view of the cosmic web encouraged larger surveys.

While the CfA1 survey was meant to represent a "fair sample" of the universe, the largest structures in the survey were comparable to the survey depth. It was decided to follow up the survey with one of similar size in the southern hemisphere to test the reproducibility of the findings in CfA1. Using the ESO catalog (Lauberts 1982), the Southern Spectroscopic Redshift Survey (SSRS) targeted 2028 galaxies in $\sim 5,700$ deg^2. Rather than using a magnitude cutoff, they used the face-on diameter of galaxies to make a target cut, allowing them to sample a similar number density as CfA1 (da Costa *et al.* 1988). The southern survey indicated that the clustering morphology seen in the northern dataset was reproducible, confirming that there are many voids between galaxies and galaxy clusters. The need for better sampling led to CfA2 and SSRS2, which pushed the limiting magnitude to $m_B \leq 15.5$ and a redshift of $z \simeq 0.05$. In the data of CfA2, the largest structure identified in a redshift survey, the "Great Wall", was discovered (Fig. 1.3), and the southern counterpart showed that the Great Wall isn't necessarily rare. Together the sample covered $\sim 30\%$ of the sky with $\sim 20,000$ galaxies (da Costa 1999), out to what are considered modest redshifts today.

These early surveys, as successful as they were, were completed one galaxy at a time. Multiplexing enabled much larger surveys, starting with the Las Campanas Redshift Survey (LCRS). Using 100 fiber optics feeding a spectrograph, LCRS on the 2.5m du Pont telescope

at Las Campanas, measured the redshift of 26,000 galaxies to a redshift of $z = 0.1$, covering ~ 700 deg^2. With the multiplexing, they were able to measure the spectra of more galaxies in less time as CfA2, from 1988 - 1994. There was no existing galaxy catalog suitable for targeting, so the LCRS team used the 1m Swope telescope to construct their own catalog. This survey led the way to the Sloan Digital Sky Survey (SDSS) and the 2dF Galaxy Redshift Survey (2dFGRS), which pushed large scale surveys to the next order of magnitude. The Sloan Legacy Survey, which includes both SDSS-I and -II, operated from 1998-2008, and included both imaging and spectroscopy. Using the 2.5m telescope at the Apache Point Observatory, with a 3 degree field of view and large format CCDs, close to 8,000 deg^2 was imaged in 5 bands (ugriz). From this imaging survey, two samples of galaxies were selected for spectroscopic follow up. The main galaxy targets were selected for their magnitude $r \leq 17.7$ out to a redshift of $z = 0.1$, and Luminous Red Galaxies (LRGs) had $r = 19.5$ out to a redshift of $z = 0.7$ (York *et al.* 2000). Using plug plates with 640 fibers and two spectrographs, the Sloan Legacy Survey took the spectra of ~ 2 million objects. The large scale structure of the universe, with all its voids and filaments could be explored for the first time, and one of the first measurement of the BAO scale was completed with the LRG dataset (Eisenstein *et al.* 2005).

Concurrently, at the Anglo-Australian Telescope (AAT), the two degree field galaxy survey (2dFGS) was underway, spanning 2,000 deg^2. The 2dF spectrograph measured the redshift of over 250,000 objects with a 400 fiber focal plate. Using sources from the APM galaxy catalog (Maddox *et al.* 1990), they made a cutoff at $b_J = 20.5$, using the Johnson-Cousins system, and targeted the southern Galactic hemisphere, complementing the SDSS dataset (Colless *et al.* 2001). This was followed up by the 6dFGS, which is a near-infrared survey that targeted the K band to $K = 12.65$ with a mean redshift of $z = 0.053$. This wavelength range enabled tracking of older stellar generations dominating the near universe. The measurements were made with a fiber spectrograph at the United Kingdom Schmidt Telescope (UKST), targeting $\sim 17,000$ deg^2, covering $\sim 41\%$ of the southern sky, and reaching 10 times more volume than the 2dFGS experiment (Jones *et al.* 2009).

Since optical surveys are limited to relatively high galactic latitudes in avoidance of the ecliptic plane, moving to different wavelength regimes like 6dFGS extends the sky coverage. Prior to 6dFGS there were several redshift surveys based on the galaxy and point source catalogs from IRAS, the Infrared Astronomical Satellite. Ending in 1983, the IRAS space mission detected 350,000 sources in four far-infrared bands: 12, 25, 60, and 100 μm. This full sky survey was completed on a space telescope cooled to $\leq 3K$ with 62 IR detectors (Neugebauer *et al.* 1984). Using this target catalog, the 1.2Jy IRAS survey covered $\sim 87\%$ of the sky with 2,663 galaxies, using almost every IRAS galaxy with a flux larger than 1.2Jy at 60μm (Fisher *et al.* 1995). The QDOT survey used a different approach that randomly selected 1 out of 6 of all IRAS galaxies with a flux greater than 0.6Jy at 60μm (Kaiser *et al.* 1991). Extending the use of the IRAS Point Source Catalog, the PSCz survey targeted 15,411 galaxies across 84% of the sky to a depth of 0.6Jy . This project combined existing and ongoing redshift surveys (CfA2, SRSS2) and newly-acquired data using the Faint Object Spectrograph (FOS) and Intermediate Dispersion Spectrograph (IDS) on the Isaac Newton

Telescope (INT), the Faint Object Red Spectrograph (FORS) on the AAT, and spectrographs at the CTIO 1.5m and INAOE 2.1m telescopes, and Naçay radio telescope (Saunders *et al.* 2000). They found that the luminosity function of galaxies in the far-infrared was largely insensitive to the Hubble flow. The larger sky-coverage and data uniformity that these IRAS surveys provided over their optical counterparts provided a reliable peculiar velocity field, helping us better understand redshift space distortions (da Costa 1999).

After the success of the Sloan Legacy Survey, momentum was growing to compile a dataset that could be used to more accurately measure the baryon acoustic oscillation length. The Baryon Oscillation Spectroscopic Survey (BOSS) used the 1.5 meter Sloan telescope, as a part of the SDSS-III project, with upgraded SDSS spectrographs. The BOSS instrument was able to fit 1,000 fibers into the plug plates by decreasing the size of the SDSS-II fibers by 2/3 to 2" per 120 μm. The gratings were replaced with VPH grisms and the CCDs were upgraded, but the basic optical design of the SDSS spectrographs remained the same. With the smaller pixels of the CCDs they were able to maintain 3 pixels/FWHM. The VPH gratings achieved markedly higher throughput over a somewhat larger wavelength range and spectroscopic resolution (Smee *et al.* 2013). This enabled measurements of redshifts with errors within a few tens of km/s (Bolton *et al.* 2012). Each BOSS spectrograph was fed 500 fibers from one half of a plug plate and had two arms, with the blue arm ranging 365-635 nm and the red sensitive to 570-1040 nm. The BOSS targets consisted of luminous galaxies up to $z = 0.7$ and measurements of the Lyman-α forest using quasars at $2.15 \leq z \leq 3.5$. The main galaxy target class was split at $\sim z = 0.4$ between the "CMASS" (for constant mass) and "LOWZ" samples, both of which were magnitude limited at $i = 19.9$. The BOSS survey increased the SDSS I & II imaging surveys by 2500 deg^2, reaching 10,000 deg^2 and targeting 1.5 million galaxies and 150,000 quasars (Dawson *et al.* 2013). In 2014, SDSS-IV started with a 6 year redshift survey called extended BOSS (eBOSS) which uses the BOSS spectrographs to obtain BAO measurements from galaxies at redshifts z$>$ 0.7, and improved Lyman-α forest BAO measurements at z$>$ 2. The extended survey adds more LRGs, emission line galaxies (ELGs), and quasars (QSOs) to the existing BOSS catalogue, producing distance measurements with precisions less than 2% (Dawson *et al.* 2016).

Using the other end of the spectrum to select targets, the WiggleZ survey used UV photometry from the Galaxy Evolution Explorer (GALEX) to identify ELGs. Combined with optical photometry from SDSS, the selection of NUV$<$ 22.8 allowed them to select more blue, star-forming galaxies. They ensured that their targets, consisting of 240,000 ELGs in the redshift range $0.2 < z < 1$ could be detected in the optical with $20 < r < 22.5$. The survey was carried out on the AAOmega instrument on the Anglo-Australian Telescope (AAT) covering a volume of $\sim$ 1Gpc^3 across seven unique sky areas with target densities of 350/deg^2 (Drinkwater *et al.* 2010). The Galaxy and Mass Assembly (GAMA) survey attempted to fill the gap between wide and shallow surveys like 2dF and SDSS, and deeper and narrower surveys. They achieved this using near-infrared target selection from UKIRT in addition to SDSS targets, with a moderate cutoff of $r < 19.4$ and a mean redshift of $z \sim 0.5$ (Baldry *et al.* 2010). Most recently, the VIPERS survey (VIMOS Public Extragalactic Redshift Survey) uses the VIMOS spectrograph on the VLT, making it the largest survey to

use an ESO telescope (Scodeggio *et al.* 2018). The survey has released the spectra of almost 90,000 galaxies in the redshift range $0.5 \leq z < 1.2$ with a limiting magnitude $i_{AB} \leq 22.5$ selected using the CFHT Legacy survey. Their goal is to have a similar survey size to 2dFGS and SDSS but with a higher redshift in order to obtain a dense sample within a larger volume over the general galaxy population.

While GAMA and VIPERS don't survey large volumes, they are excellent for studying RSD. Many of the surveys discussed above, while used primarily for distance measurements, can also be used to constrain gravity models. Models of gravity predict different values of $f\sigma_8$ (discussed in Sec. 1.1) as a function of redshift, as seen in figure 1.4. All current measurements of RSD support a flat ΛCDM cosmology, but reduced error bars on this measurement will significantly improve confidence in general relativity.

The next generation of large spectroscopic surveys will obtain millions of galaxy redshifts, revolutionizing our understanding of the large scale structure of the universe, hopefully pushing BAO distance measurements to sub-1% precision. In the next 5-10 years, two surveys will measure more than 20 million galaxy redshifts. 4MOST will be on the ESO VISTA telescope, and with $\sim$ 2400 fibers will take the spectra of 20 million spectra (de Jong *et al.* 2016). DESI, the Dark Energy Spectroscopic Survey, will measure up to 35 million spectra out to a redshift of at least 3, and is discussed in detail in Section 1.4. The Prime Focus Spectrograph (PFS) is being built for the 8-m Subaru telescope and plans to dedicate $\sim$ 100 nights to a BAO/cosmology survey covering a volume of $\sim$9 Gpc/h^3 using $\sim$ 2400 robotic positioners (Tamura *et al.* 2016). Within the next decade, there are also two space missions that will be dedicated to investigate dark energy: Euclid and WFIRST. Euclid, an optical/infrared survey being built by the European Space Agency (ESA) will measure w_{DE} through galaxy clustering and weak lensing methods (Racca *et al.* 2016). NASA also plans to launch a spacecraft to study dark energy with a mission called WFIRST: Wide-Field InfraRed Survey Telescope. It plans to probe the dark energy equation of state using three methods: Type Ia Supernovae, weak lensing, and a galaxy redshift survey to measure BAO (Spergel *et al.* 2015).

1.3.2 Current state of BAO

The first successful measurement of the BAO standard ruler was with the spectra of $\sim$40,000 SDSS LRGs, achieving a distance measurement at $z = 0.35$ with 5% precision and 3.6-σ confidence (Eisenstein *et al.* 2005). With additional data, from both the LRG and main galaxy samples from SDSS DR7, Percival *et al.* (2009) measured the BAO signal at a median redshift $z = 0.275$ ($z = 0.2$ for main galaxies and $z = 0.35$ for LRGs) with a precision of 2.7%. Later, with the use of density field reconstruction, the LRG measurement error was reduced to 2% (Padmanabhan *et al.* 2012) and a new measurement at the low redshift of $z = 0.15$ at 4% was made possible (Ross *et al.* 2014). The BAO signal was also measured using the LRG photometric redshift catalog using 600,000 galaxies (Padmanabhan *et al.* 2006, Blake *et al.* 2006). As expected, due mostly to redshift uncertainties, this approach

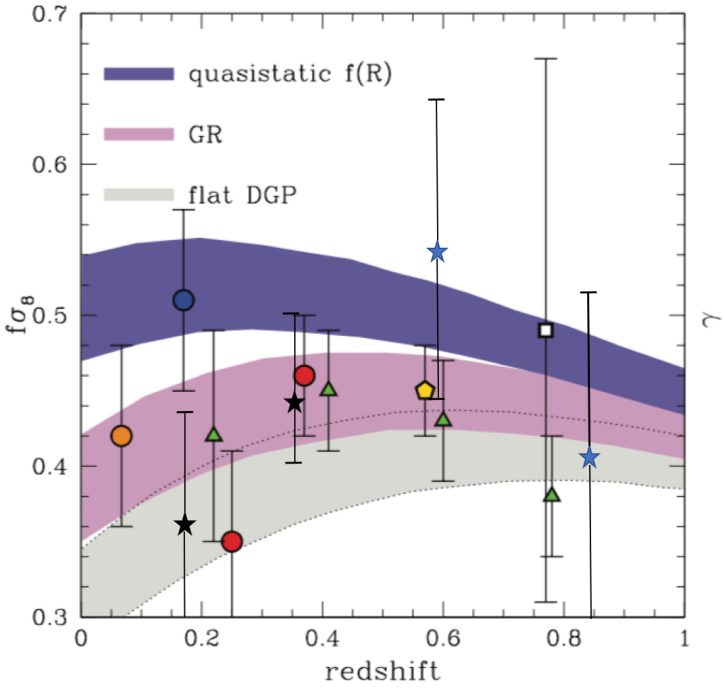

Figure 1.4: This figure has been updated from DESI Collaboration *et al.* (2016a), which shows measurements of the growth of structure ($f\sigma_8$) as a function of redshift. It also shows theoretical bounds for different models of gravity. All measurements made to date are consistent with general relativity. The green triangles show measurements made by WiggleZ (Blake *et al.* 2011b), the yellow pentagon is from the BOSS CMASS sample (Samushia *et al.* 2014), the orange and blue circles are from 6dFG (Beutler *et al.* 2012) and 2dFG (Percival *et al.* 2004) surveys, the red circles are from SDSS LRGs (Samushia *et al.* 2012), and the white square from the Vimos VLT Deep Survey (VVDS, Guzzo *et al.* 2008). The added points are the stars, with the black stars corresponding to the GAMA results (Blake *et al.* 2013), and the blue from VIPERS (Pezzotta *et al.* 2017).

gave measurement with a precision of 6.5% even using a catalog $\sim$ 10 times that of the spectroscopic analyses.

Analysis of the power spectrum of 2dFGRS galaxies at $z = 0.11$ (Percival *et al.* 2001, Cole *et al.* 2005) provided constraints on the matter content of the universe with a precision less than 10%. The WiggleZ survey, with its deeper survey, allowed BAO measurements to extend to higher redshifts, with measurements of the BAO at redshifts $z = 0.44$, 0.6, and 0.73 (Blake *et al.* 2011a). The WiggleZ catalog was re-analyzed using reconstruction, giving a distance measurement at each effective redshift with 3.4-4.8% accuracy (Kazin *et al.* 2014). The near-infrared 6dFGS survey measured the BAO signal at $z = 0.1$ with a precision of 4.5% (Beutler *et al.* 2011).

BOSS has presented the first opportunity to measure BAO with precision approaching 1%, with reconstruction used for all analyses. The first analysis of BOSS dataset in DR9 (Anderson *et al.* 2012) presented a 1.7% constraint on the angular averaged distance to z = 0.57, which has been improved to 1% with DR11 (Anderson *et al.* 2014). The LOWZ sample of BOSS, with a mean redshift of $z = 0.32$, has been presented in Tojeiro *et al.* (2014) with a 2% distance constraint. With the final data release (DR12), having a full sample of 1.2 million galaxies, distance measurements were made at $z = 0.32$, 0.51, and 0.61 with a 1% precision in the transverse direction and 1.2% for radial distance (Alam *et al.* 2017).

All distance measurements discussed above were made using galaxies as the tracer of large scale structure. The BOSS redshift survey also included quasars at redshifts out to $z = 3.5$. While these QSOs are tracers of the matter distribution on their own, they were also used as backlight to the lyman-α (Lyα) forest, which traces the large scale mass distribution due to the absorption spectra of the redshifted Lyα spectral feature (1216$\mathring{A}$ at rest) in the quasars by ionized hydrogen. Using the BOSS DR9 QSO auto-correlation, the BAO was detected at a mean redshift of $z = 2.3$ by Busca *et al.* (2012) and Slosar *et al.* (2013) with 3-5σ significance. This measurement was made again with DR11 Lyα spectra with a precision of 2% (Delubac *et al.* 2014). Font-Ribera *et al.* (2014) first studied the cross correlation between quasars and Lyα forest at $z = 2.36$. The latest results from DR12 give improved results for the Lyα forest auto-correlation (Bautista *et al.* 2017a) and updated results for the quasar-Lyα cross-correlation (du Mas des Bourboux *et al.* 2017). These Lyα BAO measurements are currently in tension with the Planck ΛCDM expectation by 1.8σ as seen in Fig. 1.5.

The extended BOSS survey (eBOSS) has started to release initial BAO measurements. Using $\sim 80,000$ LRGs at $z = 0.74$, they have made distance measurements with a precision of 2.6% (Bautista *et al.* 2017b). Using $\sim 150,000$ quasars between $0.8 \leq z \leq 2.2$, a distance to a mean redshift to $z = 1.52$ has been made to 3.8%, filling a hole in the BAO distance ladder. The combination of BAO as a cosmological distance measure and the luminosity distances measured by type-Ia supernovae are starting to create reasonable constraints on cosmological parameters and our understanding of dark energy (Fig. 1.6). The next generation of large scale spectroscopic surveys (DESI, 4MOST, PFS, Euclid, WFIRST) will supply the necessary statistical power to potentially differentiate between cosmologies and constrain our knowledge of the expansion history of the universe with the dependence of w_{DE}.

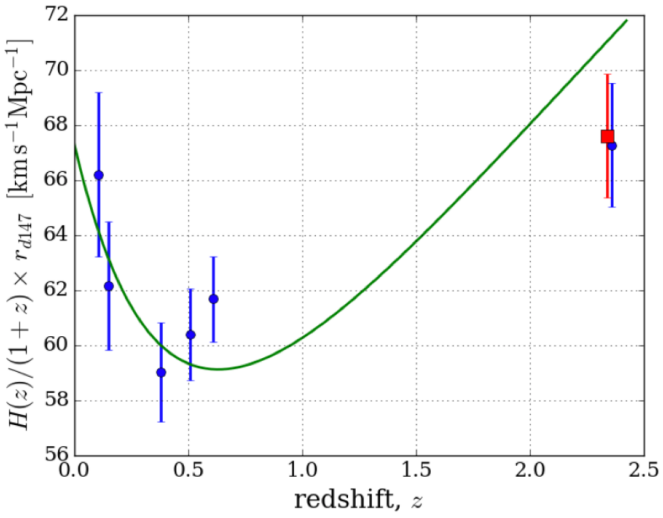

Figure 1.5: Hubble diagram with current BAO measurements not including the most recent results from eBOSS (SDSS IV). The green line represents the expectations of ΛCDM based on Planck results. The blue points come from the 6dFGS measurement at $z = 0.11$ (Beutler *et al.* 2011), the reconstructed SDSS measurement at $z = 0.15$ (Ross *et al.* 2014), and the DR12 BOSS measurements at $z = 0.32, 0.51, 0.61$ (Alam *et al.* 2017), and the quasar-Lyα cross correlation at $z = 2.36$ (Font-Ribera *et al.* 2014). The red point is from the paper this plot was taken from (Bautista *et al.* 2017a), as is the BOSS Lyα auto-correlation from a mean redshift of $z = 2.33$.

1.4 Dark Energy Spectroscopic Instrument

The Dark Energy Spectroscopic Instrument (DESI) is a dark energy experiment that will create a 3D map of the universe to a redshift of $z \sim 3.5$, measuring the spectra from 35 million galaxies and quasars. DESI is a Stage IV Dark Energy experiment in the parlance of the DETF report and is expected to improve the FoM by up to three times that of Stage II experiments, with a value of 133 using only the DESI galaxy BAO distance measurements. To achieve this, DESI employs 5,000 robotic fiber positioners to simultaneously place optical fibers on astronomical targets. The focal plate instrument, containing the robotic positioners, will sit behind a custom optical corrector, both of which will be installed at the primary focus of the 4-m primary mirror of the NOAO (National Optical Astronomy Observatory) Mayall telescope. The optical fibers will run from the robotic positioners at the prime focus down the telescope to ten 3-arm spectrographs, which cover a spectral range of 360-980 nm with a resolution of 2,000-5,000.

DESI will be installed at the Mayall telescope at Kitt Peak National Observatory (KPNO) in 2018-2019, followed by a dedicated 5 year science campaign. The DESI instrument is currently being built and will be finally integrated at the Mayall telescope. In the summer

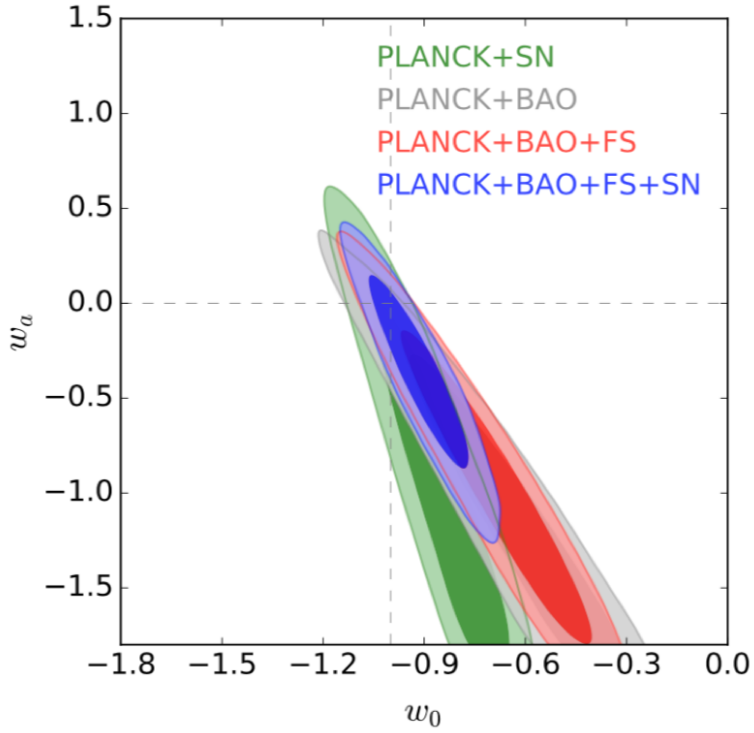

Figure 1.6: Current constraints on w_{DE}. Combining several probes gives us better constraints on cosmological parameters. Current measurement still support a ΛCDM cosmology. Here, SN is type Ia supernova data from the Joint Light-curve Analysis (JLA, Betoule *et al.* 2012) and FS means "full shape" data from galaxies without reconstruction. (source: Alam *et al.* 2017).

of 2016, a subset of the DESI subsystems were installed on the telescope to demonstrate capability of attaining targets with the DESI positioners/fibers. This on-sky test, called "ProtoDESI", is described in depth in Chapter 3. After the custom optical corrector is installed on the telescope, an intermediate "commissioning instrument" will be installed to test aspects of the guiding and focus capabilities. When the focal plane instrument, fiber optic cable, and spectrographs have been installed, a commissioning period will take place. After fully characterizing the instrument, we will enter the Science Validation period. During this time, the survey plan, targeting, and pipelines will be tested, and when they are confirmed to to work as designed, 5 years of science operations will take place with data products made public approximately once a year.

This section reviews the DESI project, covering its science objectives (Sec. 1.4.1), the survey plans and targeting (Sec. 1.4.2) and an overview of the instrument (Sec. 1.4.3). The majority of what is described here comes from the DESI Final Design Report (DESI Collaboration *et al.* 2016a, DESI Collaboration *et al.* 2016b), with updates since its publication in

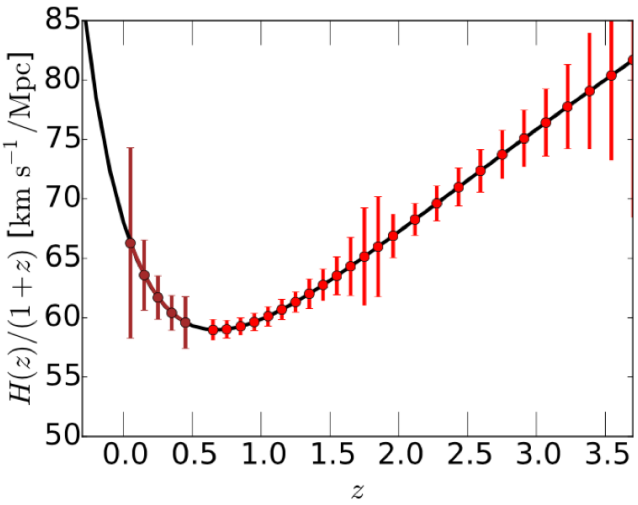

Figure 1.7: Hubble diagram with expected DESI BAO measurements. Each point on this Hubble diagram represents an expected BAO measurement by DESI. The errors on each distance measurement depend largely on the density of targets in the redshift range. For the range $0.05 < z \leq 0.4$, the bright galaxy survey will provide targets which are largely cosmic variance limited. LRGs, ELGs, and quasars are used as targets from $0.4 < z \leq 2.1$, and their density reduces with redshift. Beyond $z = 2.1$, the Lyα forest will be used to make the distance measurements.

2016. The following chapters of this thesis will discuss my specific contributions to DESI.

1.4.1 Science Objectives

The primary goal of DESI is to measure the spectroscopic redshifts of ~ 35 million galaxies and quasars with a precision of $\sigma_z(1+z) \sim 0.0005$. With this large dataset, the expectation is to measure the BAO scale in ~ 30 redshift bins with sub-percent precision (Fig. 1.7). These BAO measurements will be made using galaxies as tracers of the matter distribution, quasars at higher redshifts, and the Lyα forest as backlit by QSOs for $z \geq 2.1$. In order to achieve this precision, reconstruction must be completed, requiring the measurement of the anisotropies in the hubble flow. Using Fisher matrices, the DESI team estimated the expected precision of measurement by DESI based on target density and signal to noise $\bar{n}P$, and with the baseline survey of 14,000 deg^2, expect to make sub-percent distance measurements out to a redshift of 3, competitive with future space missions like Euclid and WFIRST (Fig. 1.8).

While measuring the BAO and growth of structure to better constrain dark energy and models of gravity are the main goals of DESI, its rich dataset will enable other science. In the field of cosmology, DESI will be able to contribute to the theory of inflation and the total mass of neutrinos. As mentioned above, the Lyα forest is an excellent complementary probe

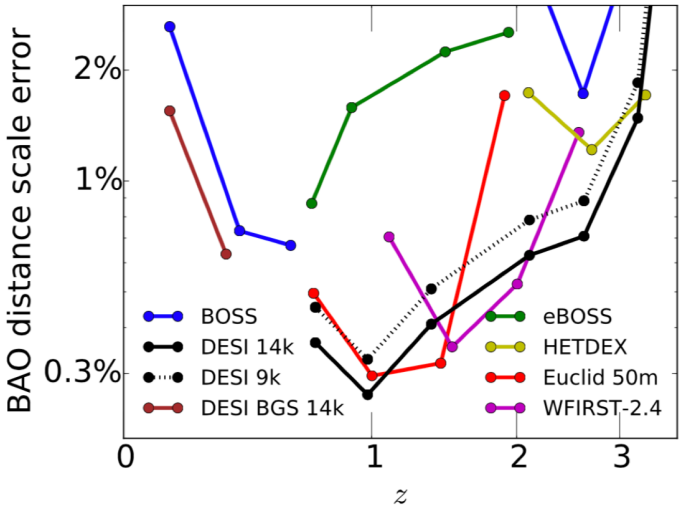

Figure 1.8: Precision of BAO distance measurements for current (BOSS, eBOSS) and planned projects as a function of redshift. The black and brown lines for DESI 14k represent the expected precision, with a back up of DESI 9k, (9,000 deg^2 survey). Euclid and WFIRST are both planned space missions dedicated to dark energy science.

of the spectral index (n_s) and its running (α_s), as their measurement is strengthened by a large range of scales. While Planck has the best constraints on these parameters (Planck Collaboration *et al.* 2016c), DESI will improve the errors on their measurements by a factor of 1.7 for n_s ($\sigma(n_s) = 0.0019$) and 2.7 for the spectral running ($\sigma(\alpha_s) = 0.0019$). Additionally, DESI expects to measure the departure from primordial gaussianity, parametrized by f_{NL}, with errors comparable to Planck. Forecasts show that DESI can produce a measure of f_{NL} with errors $\sigma(f_{NL}) \simeq 5$, and when combined with existing Planck data, this error could be reduced by a factor of two. Limits on the mass of neutrinos will be determined by the DESI power spectrum, with an expected 0.02 eV resolution on the sum of the neutrino masses (Σm_ν). If the sum of neutrino measurements is sufficiently low, then DESI will be able to exclude the inverted hierarchy at 2σ.

In addition to cosmology, DESI will contribute to the study of our own galaxy. During the bright galaxy survey (described below), a portion of the fibers will not have galaxy targets and therefore will target Milky Way stars. DESI expects to measure the spectra of ~ 10 million stars down to a magnitude of 17.5. These star spectra will provide radial velocity, effective temperature, surface gravity, chemical abundances, and approximate age for these stars. This dataset will help the study of the assembly history of the Milky Way and the distribution of dark matter.

1.4.2 Targets and Survey Design

The target selection for DESI will be made from the results of the ongoing "Legacy Survey" (Dey *et al.* 2018). This imaging survey includes optical photometry from three unique sites, and near-infrared photometry from the WISE/NeoWISE survey. The WISE space telescope supplies photometry to 20 and 19.3 AB mag for their W1 and W2 bands, having effective wavelengths of 3.368 and 4.618 μm. WISE was launched in 2009, and after imaging the entire sky twice, was decommissioned in 2011 (Wright *et al.* 2010). It was reactivated as NeoWiSE in 2013, and it continues to operate with its main goal to monitor "near earth objects" like meteors (Mainzer *et al.* 2014). The optical portion of the imaging survey is based on g,r,z photometry from the DECam Legacy Survey (DECaLS) for the North Galactic Cap (NGC) region at Dec $\leq 32°$ and the South Galactic Cap (SGC) region at Dec $\leq 34°$, and from the Mayall z-band Legacy Survey (MzLS) and the Beijing-Arizona Sky Survey (BASS) for the NGC region at Dec $\geq 32°$. DECaLS is operated at the 4-m Blanco telescope at Cerro Tololo using the Dark Energy Camera (DECam) built for the Dark Energy Survey (DES; Honscheid *et al.* 2010). This survey will reach depths of $g_{AB} = 24.0$, $r_{AB} = 23.4$, and $z_{AB} = 22.5$ and cover 9,000 deg^2. The g-band survey completion for data release 5 is shown in Fig. 1.9. The MzLS and BASS projects are both located at Kitt Peak National Observatory (KPNO) and will cover $\sim 5,500$ deg^2. MzLS, now completed, was run on the MOSAIC3 camera on the 4-m Mayall telescope (Dey *et al.* 2016), which happens to be the same telescope that will be used for DESI. The Bok 2.3m telescope is just down the hill from the Mayall telescope and is running the g and r band photometry with the 90Prime instrument. The filters for both MzLS and BASS were matched to those on DECam to ensure comparable datasets and depths. Additionally, 500 deg^2 of the MzLS and BASS footprints overlap with DECaLS for identification and correction of systematic errors.

Using the Legacy Survey results, DESI will select four unique target classes: bright galaxy sample (BGS), luminous red galaxies (LRGs), emission line galaxies (ELGs), and quasi-stellar objects (QSOs). The BGS is essentially a deeper version of the SDSS main galaxy survey, increasing the number of targets by 10 in the redshift range $0.05 < z < 0.4$. These galaxies will mostly be selected by a magnitude cut in the r-band and their redshifts measured predominantly by the 4000$\mathring{A}$ absorption bands and the H-alpha emission line. The LRGs are high stellar mass objects with a lack of ongoing star formation. DESI will target LRGs from $0.4 < z < 1.0$, identifying them in the g and r bands for the lower redshift population ($0.4 < z < 0.6$) and measured using the 4000$\mathring{A}$ continuum break. Above $z = 0.6$, the 4000$\mathring{A}$ break is no longer visible so we can use the 1.6 μm "bump", which can be identified using the WISE W1 photometry. Reaching out to $z = 1$, DESI expects to target 350 LRGs/deg^2. The largest target group is the ELGs, with a density of 2400 galaxies/deg^2. The redshift of these typically late-type spiral and irregular galaxies with strong star formation rates are measured with the OII doublet (3726, 3729$\mathring{A}$) from ionized HII regions. These galaxies are generally bluer than LRGs and are selected using all the optical photometry, selected in the range $0.6 < z < 1.6$. Finally, QSOs or quasars, are used in two distinct ways. From $0.9 < z < 2.1$ they are used as direct tracers of the large scale

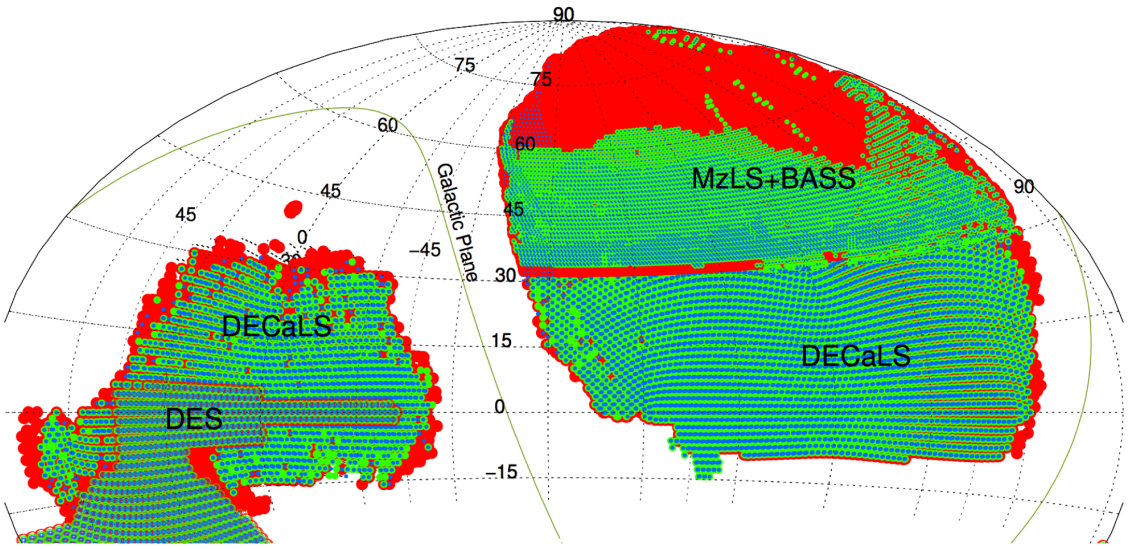

Figure 1.9: The current imaging coverage (as of April 2018) of the Legacy Surveys. Red, green and blue dots represent regions where there is at least a single z, r or g band observation, respectively. The MzLS z-band survey is now complete; BASS g and r-band observations are expected to be completed in July 2018; and DECaLS is scheduled to complete all grz observations by January 2019.

structure. Above that range, they are used as backlight sources for the Lyα forest, which comes from the absorption of the Lyα (1216$\mathring{A}$ in rest frame) spectral line from the quasar in non-ionized hydrogen. For redshifts below 2.1, the QSO target density is expected to be 170/deg^2 and $\sim$ 50/deg^2 above that. The distribution of these targets can be seen in Fig. 1.10.

The baseline DESI survey covers 14,000 deg^2. The survey is planned for 5 years, during which time $\sim$ 35 million galaxies and quasars will be have redshifts measured. The field of view of the instrument will be 7.5 deg^2, so the survey footprint can be split into 2,000 unique tiles. The DESI program plans to visit each footprint an average of 5 times to achieve the required signal to noise, so there will effectively be 10,000 dark time observations. DESI will be the sole instrument on the Mayall telescope, so will use all available dark, gray, and bright time.

1.4.3 Instrument

The DESI instrument will provide unprecedented multi-object spectroscopy, requiring a novel design. New corrector optics will provide a 3 degree diameter field of view that feeds a focal plate containing 5,000 robotic positioners that can be reconfigured within 3 minutes to measure the spectra of a new set of galaxies. Optical fibers mounted to the positioners

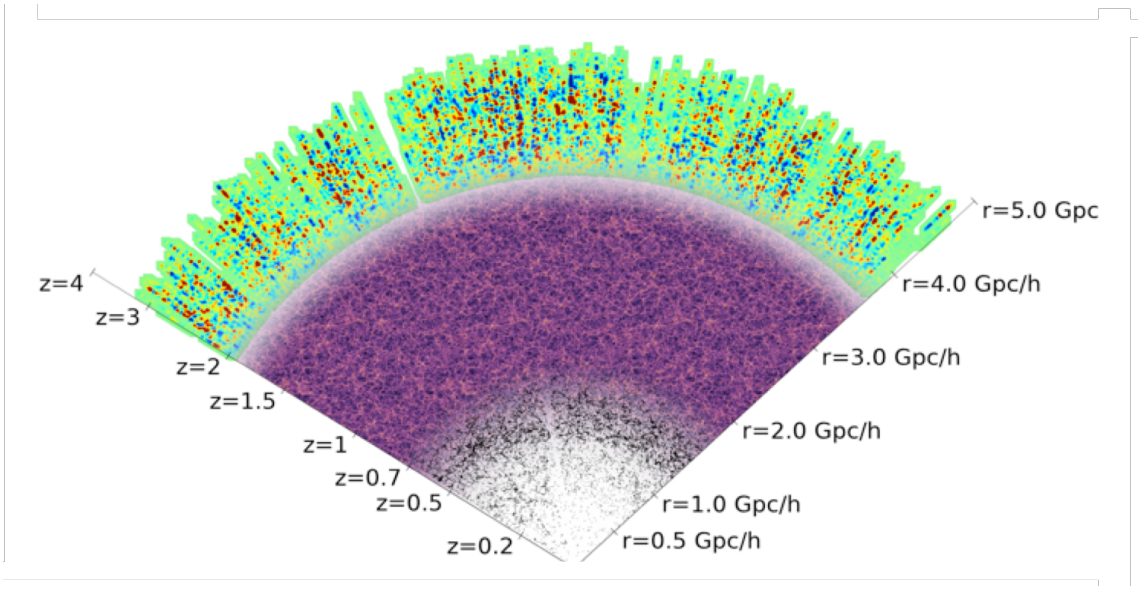

Figure 1.10: Redshift distribution of DESI targets. The white section represtents the BGS targets, which are mostly cosmic varaince limited and extend to $z = 0.4$. For redshifts $0.4 < z \leq 2.1$, the targets are comprised of LRGs, ELGs and quasars (purple region). Above $z = 2.1$, the green represenets the Lyα forest using quasars as the backlight. In total, DESI expects $\sim$10 million galaxies from BGS, 4 million LRGs, 17 million ELGs, and 2.5 million quasars, for a total of $>$ 30 million.

will run 50-meters down the telescope to feed ten broad-band spectrographs, each containing three detectors. The spectrographs will cover a spectral range of 360-980 nm with a resolution of 2,000-5,000. All commands and data transfers will be run by the Instrument Control System (ICS), and the data acquisition system will ensure that all targets are reached over the 5 years of operations, and the data is analyzed and archived quickly. Below, I describe the telescope and corrector optics, the focal plane instrument and fiber optic cable, the spectrographs, and finally the ICS and data systems.

Telescope and Corrector Optics

The instrument is being built at several institutions and will be integrated after delivery to the telescope. DESI will be mounted on the 4-meter Mayall telescope at Kitt Peak National Observatory (KPNO), which is located 56 miles southwest of Tucson, AZ, in the Schuk Toak District on the Tohono O'odham Nation. KPNO is administered by the National Optical Astronomy Observatory (NOAO) in Tucson. The Mayall telescope is a reflector telescope with a 4-meter primary mirror that sits on an equatorial mount (Fig. 1.11), and is the largest of the 22 optical telescopes located on Kitt Peak. It was commissioned in 1973, and nearly identical to the 4-meter Blanco telescope at the Cerro Tololo Inter-American Observatory in

Figure 1.11: View of the 4m Mayall telescope from inside the dome. The primary mirror sits on an equatorial mount. The current mosaic corrector at the prime focus will be replaced for DESI.

Chile, also operated by NOAO and commissioned in 1976. The Mayall currently supports regular scientific observing by visiting astronomers, as it has done throughout its life; it will be converted to sole-purpose use for DESI. The Mayall was chosen to host DESI because of its unique combination of adaptable optical and mechanical designs, and availability of the large block of dedicated survey time needed to carry out the DESI project.

The corrector is designed to provide a larger field of view to the focal plate, allowing 5,000 fibers to be arranged over 7.5 deg^2. The design includes four large fused silica elements. The two smaller lenses have aspheres on one surface each; all other silica surfaces are spherical. An atmospheric dispersion compensator (ADC) is included in the design in order to meet blur requirements at off-zenith angles. This compensator includes two large wedged borosilicate lenses. The optical layout of these 6 elements are shown in Fig. 1.12. The focal surface created by the corrector isn't completely flat, but has a slight curve. The 6 lenses each sit in their own cell, with C1-C4 having cells with flexure systems, and the ADCs having rotating cells. The cells are then integrated into a barrel, which is a single shell with 4 sections with an interface to the focal plate instrument. The barrel, which is secured at the prime focus of the primary mirror in a cage attached to the telescope structure with a ring, has a hexapod for rapid adjustment of focus and alignment relative to the primary mirror. The DESI hexapod, designed like the DECaM hexapod (Flaugher *et al.* 2015), includes six actuators that have mechanical joints at each end that attach to motion plates with their own control system. Figure 1.13 shows how the barrel sits in the prime focus of the focal plate and attaches to the focal plane instrument and cables.

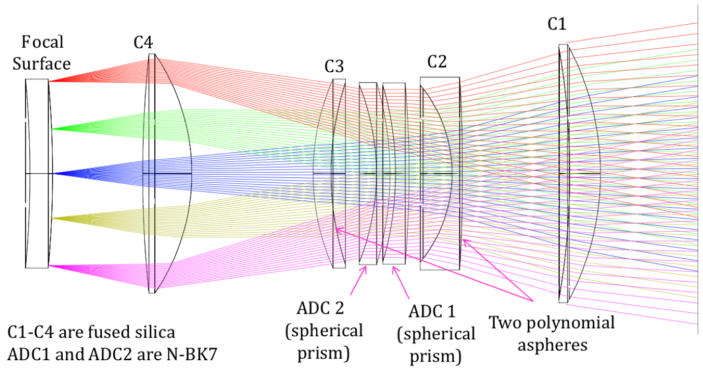

Figure 1.12: Optical layout of DESI corrector. Light from the primary mirror (coming from right), is focused onto a curved focal surface with a linear field of view of 3.2 deg.

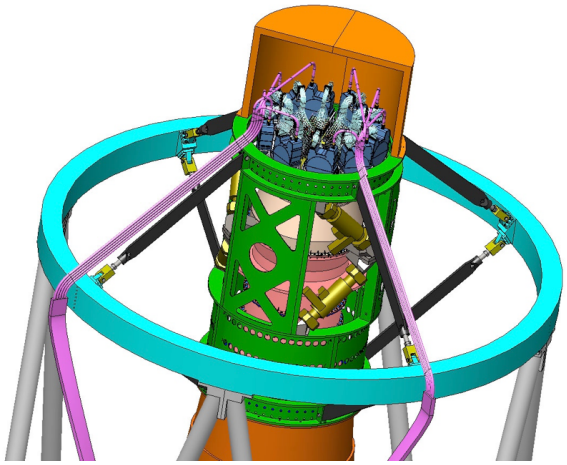

Figure 1.13: View of prime focus of telescope. Includes the ring (blue), cage (green), barrel (pink), and hexapod inside the cage (gold) in addition to the focal plate and cables (pink) and cover (orange).

Focal Plane and Fiber Optics

The focal plane subsystem is comprised of three main parts: focal plane assembly, focal plane enclosure, and the Fiber View Camera (FVC) (see Fig. 1.14). The focal plane assembly is separated into 10 identical modules called "petals", each including 500 robotic positioners, a Guide, Focus and Alignment camera (GFA), 10 field illuminated fiducials (FIFs), and 2 GFA illuminated fiducials (GIFs). These are mounted in an aluminum structure with precision machined through-holes for the positioners and fiducials. A petal fully assembled with fiducials and positioners is shown in figure 1.15. The focal plane assembly also contains the electronics to command each positioner and all structure needed to manage the interface between the fibers and robotics positioners. The focal plane enclosure manages the thermal output of the focal plane, ensuring that the heat generated by the robotic positioners doesn't distort any images. The focal plane assembly and enclosure are both mounted at the prime focus of the telescope, behind the corrector.

The FVC is mounted in the Cassegrain cage 12.25 m from the prime focus, oriented to image the front of the focal plane. The images of the front of the focal plate, with the fiducials illuminated and science fibers back-lit, are used for metrology. Centroids for each point imaged by the FVC provide a feedback mechanism for identifying the location of the fibers. The FVC uses a Finger Lakes Instruments[1] Proline PL501000 with a Kodak KAF50100 CCD, controlled with an Intel NUC over USB. The sensor has 6132×8176 pixels with a 6 μm pitch and receives light through a blue narrow band filter. Using a Canon telephoto lens with an effective focal length of 600 mm stopped to f/19, the focal plate is de-magnified by 21.7 so that the diffraction-limited full width half maximum (FWHM) of each fiber spans 2 pixels, maximizing the SNR. The lens and camera will be attached to an adapter plate, which is installed in the Cassegrain cage, and the heavy (≈4 kg) Canon lens will be supported within a cage to minimize flexure due to gravitational loading.

The DESI robotic positioners are used to reconfigure the focal plane, gaining access to new targets on a short time scale. Each positioner holds a single optical fiber, and has two 4 mm DC brushless motors, enabling it to access any point within a 6 mm radius patrol disk. The motors are arranged so that there are two rotational degrees of freedom with parallel axes (Schubnell *et al.* 2016). This style of positioner is often referred to as theta-phi, where the central motor defines the θ axis, and the eccentric motor defines the ϕ axis. The motors do not include individual rotary encoders. Instead, the positioning control loop is closed by directly imaging the backlit fiber tips with the FVC. Each unit has an external thread coaxial with a precise cylindrical datum feature, and screws into the focal plate like a sparkplug. A flange co-machined into the unit positions the fiber tip 86.5 mm forward of the plate's mechanical mounting surface. They were designed to be mounted on a grid spaced by 10.2 mm, allowing for an overfilled focal plate on DESI with patrol areas overlapping. This will require anti-collision algorithms ensuring that robots do not run into each other during reconfiguration.

[1] www.flicamera.com

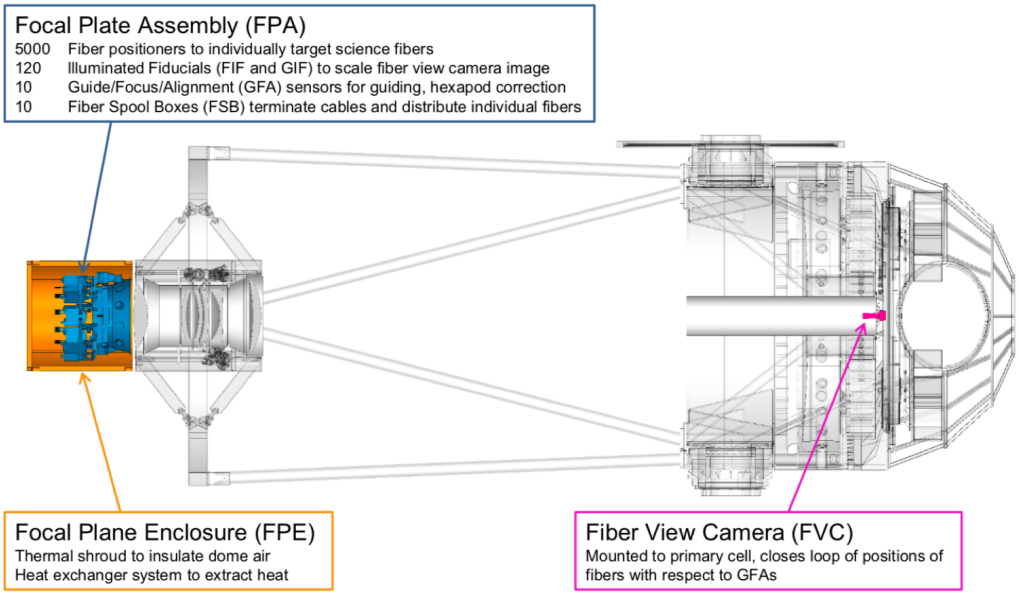

Figure 1.14: Focal plate subsystem consists of the focal lane assembly, its enclosure and the FVC which sits in the cassegrain cage fo the telescope.

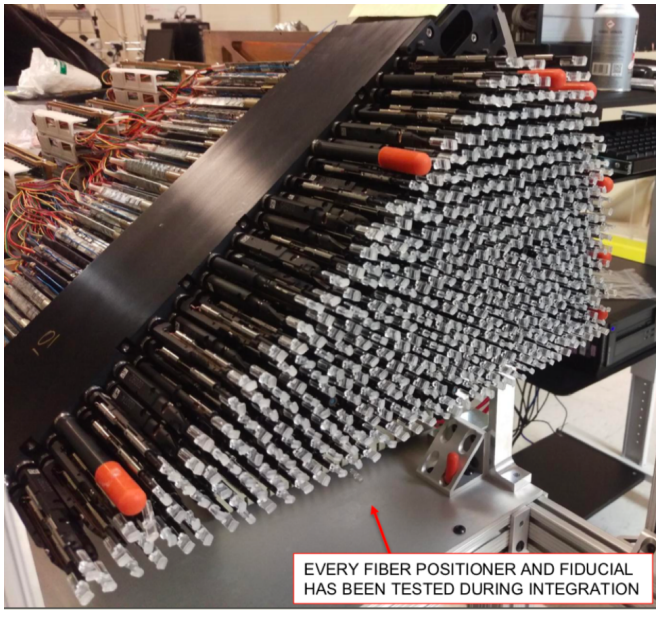

Figure 1.15: Petal populated with 500 fiber positioners and fiducials (FIFs). Each positioner has a clear plastic cap on the front to protect the optical fiber. The GFA module has not yet been installed in this petal.

The fiducials each consist of four 10 μm pinholes etched in a black coating on a glass block that are back illuminated by a 470 nm LED. Their main function is to provide reference points on the focal plate relative to the movable fibers. By imaging the front of the focal plate with the FVC it is then possible to measure the absolute position of the science fibers despite the distortions introduced by the corrector optics. The locations of the pinholes were measured relative to the outside diameter of the fiducials with an accuracy of 1.5 μm. The centers of the fiducials were measured with an accuracy of $\approx 5\mu$m for the two types of fiducials. The FIFs will be mounted similarly to the positioner, having the same length and spark plug installation feature. The GIFs will be attached directly to the GFAs to link the location of the guider images to the positioner locations.

There will be 10 GFAs on the focal plane, 6 being used for guiding and 4 for focus. The only difference between these being the filter used. For the focus modules, a dual thickness filter will be used, placing stars ~ 1.5 mm above and below the focus, making them appear as donuts. The guider filter will be flat, centered in the red. The cameras, housing an e2v CCD230-45 sensor, was custom-designed and built by LBNL and IFAE in Barcelona to minimize mechanical footprint while maximizing sensor area on the focal plate. The GFA sensor has 15 μm pixels read out by 4 separate amplifiers with excellent dark current performance and read noise. Each sensor sees ~ 29 arcmin^2, and with a magnitude limit of $r_{AB} = 17$, will have at least 10 guide stars for every observation.

The fiber positioners are installed into the focal plate from the front. For ease of integration, a 3 meter section of optical fiber is attached to the positioner by clamping onto a glass ferrule glued to the tip of the fiber. This section of the fiber is then attached to a fiber cable that is routed down the telescope to the spectrographs in the coudé room (see Fig. 1.16). This attachment is done with fusion splicing, which will be described in detail in Chapter 2. The DESI optical fiber is a broadband Polymicro FBP fiber with a core diameter of 107 μm and a numerical aperture of 0.22. The fibers from one petal, all 500, are collected as one cable so that each petal connects to one spectrograph. This cable is constructed of 10 tubes that are spirally wound around a core of Aramid-yarn. This is then covered with a conduit and PVC coating, following the technique developed by Durham University for under-sea construction of optical cables.

Spectrographs

Each of the identical spectrographs will accept one fiber optic cable with 500 fibers. The ends of the fibers will be bonded into a v-groove block which will sit at the slit. Each fiber will sit 230 μm from the next on a curved slit to counteract the curve of the focal plane. Using dichroics, the light will be split from the f/3.57 collimated beam to three different cameras. The blue camera, which will use a ITL STA4150A detector from the University of Arizona Imaging Technology Lab, will be used in the range from $360 < \lambda \leq 555\mu$m with a resolution $R = \lambda/\Delta\lambda = 2,000 - 3,200$. The red and infrared arms will both use LBNL 250μm thick CCDs, the red detector sensitive to $555 < \lambda \leq 656\mu$m with resolution $R = 3,200 - 4,100$ and the infrared from $656 < \lambda \leq 980\mu$m with $R = 4,100 - 5,000$. The light is spread using

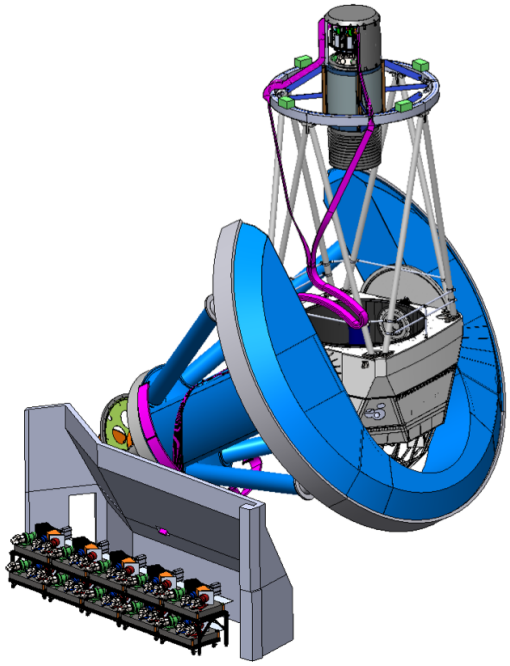

Figure 1.16: DESI optical cable routing. The cable, shown here in pink, runs $\sim$ 50m around telescope from positioners on the focal plate to spectrographs in the coudé room at the base of the telescope.

volume phase holographic (VPH) gratings, and each camera uses 5 lenses in a reflective Schmidt design. The detector arrays have 4096×4096 15μm pixels and are each housed in their own cryostat. Figure 1.17 shows the designed total throughput for the three cameras and their measured values with $\sim$ 70% efficiency across the whole redshift range. The point spread function (PSF) will be $\sim$ 3 pixels with 95% of the enclosed energy within 100μm. There is a shutter in front of the slit, and when closed, an LED can be illuminated to send light back down the fibers so they can be imaged by the FVC. Figure 1.18 shows the layout of the spectrograph and an as-built version.

ICS and Data Systems

The DESI ICS performs all control and monitoring functions required to operate DESI. This includes all data acquisition and flow, connection to the Mayall TCS, monitoring infrastructure, maintenance of an operations database, guiding, coordinate transformations, subsystem coordination, and user interfaces. At the core of the ICS is the DESI Online System (DOS). This includes an application framework for the subsystems' distinct software. It is built on Pyro[2], an object-oriented communication package which enables efficient command and

[2]https://pypi.python.org/pypi/Pyro4/

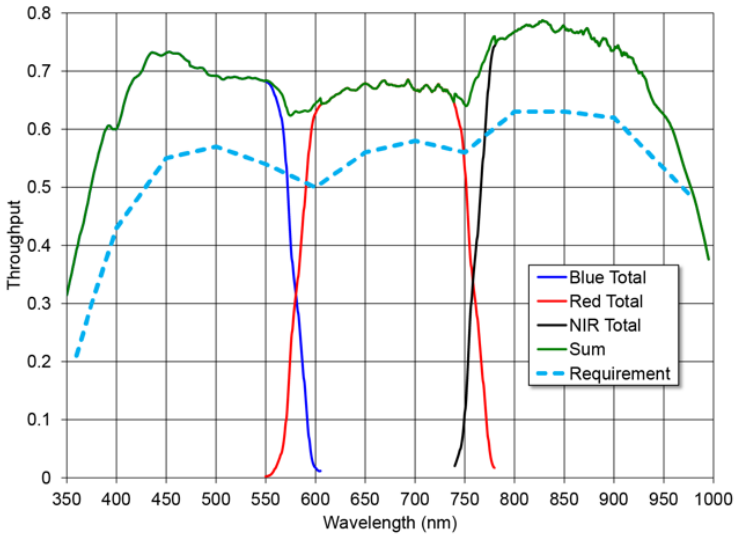

Figure 1.17: Throughput of the DESI spectrographs. For each arm of the spectrograph, the requirement is exceeded, with a total throughput of $\sim 70\%$.

data transfer. DOS also contains all of the user interfaces, which display exposure sequences, real-time telemetry, and image previews. The Observation Control System (OCS), which orchestrates exposure sequences, is based on the architecture developed for the DECam on the Blanco telescope, which was successfully deployed in 2012 (Honscheid *et al.* 2010). The OCS controls the flow of data from one subsystem's software to another using a sequence oriented architecture. DESI will collect a large amount of metadata and telemetry information, which will be recorded in the operations database.

Data Systems on DESI is responsible for all target selection and survey planning, the data pipelines, and then transfer, archiving, and distribution of the data products. Using the Legacy Imaging surveys, target lists are being assembled and mock surveys run to determine the most efficient target allocations and field selection. During operations, the Next Field Selector will be used to efficiently select the target area and assign specific targets to fibers. Once the raw data is collected, calibrations will be performed. Then the spectrum is extracted, sky is subtracted, and then each spectrum will be classified and its redshift measured. It is expected that there will be $\sim$ 10TB of raw data per year transferred from KPNO to NOAO in Tucson, and then to NERSC in Berkeley where it will be archived. After running the data through the pipelines, there will be $\sim$ 100 TB/year of data products that will be made available as data releases approximately once per year throughout the 5 years of operations.

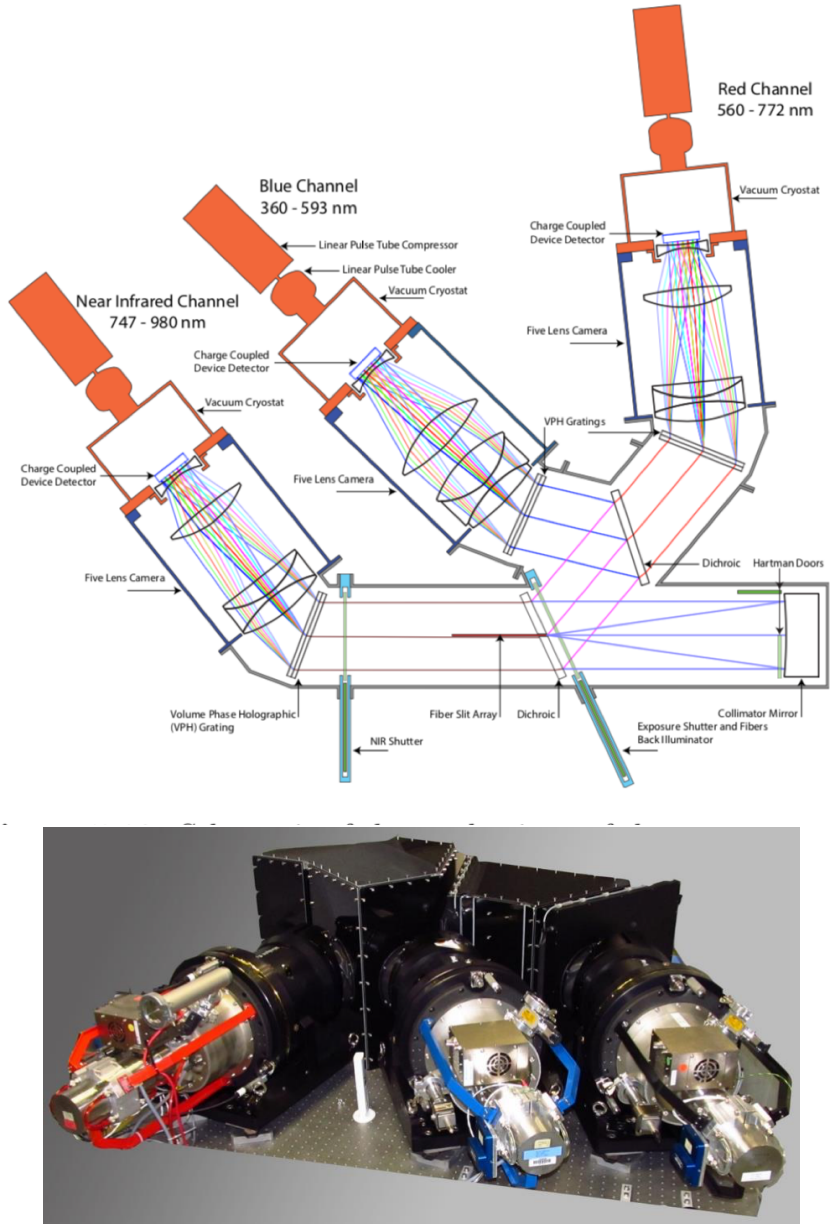

Figure 1.18: Top: Optical layout of a DESI spectrograph. Features include 3 cameras, cryostat for each detector, VPH gratings, dichroics, and a shutter with an LED back-illuminator. Bottom: As built version of the first DESI spectrograph.

The following chapters of this thesis describe my contribution to the DESI project. I start by describing a novel technique for connecting the DESI optical fibers using fusion splicing I helped develop (chap. 2). I then describe ProtoDESI, the first on-sky test of DESI hardware completed at the Mayall telescope on Kitt Peak. During ProtoDESI, under my leadership, we confirmed the capability to align fiber optics with targets using the DESI robotic positioners and maintain guiding (chap. 3). Finally, I introduce a sky model that I developed using 5 years of BOSS sky spectra. This sky model will serve as a planning tool for DESI, both during survey planning and observations. This model, and improvement on previous models, will enable the DESI survey to operate more efficiently (chap. 4).

Chapter 2

Fiber Splicing

Optical fibers play a critical role in the DESI design. They make possible unique focal plane designs and the ability to separate the spectrographs from the focal plane by a large distance ($\sim$ 50m). This allows the spectrographs to be stationary and housed in a thermally stable environment, improving the stability and performance of the instrument. To implement DESI's unique design, it is necessary to have two sections of fibers during subsystem integration that are connected before installation on the telescope. The typical way of connecting optical fibers is with commercially available optical fiber connectors, but to maintain high throughput, the DESI team will be using fusion splicing to connect the fibers. This chapter first discusses the use of optical fibers for astronomical applications, focusing on several properties of these fibers. I will discuss the near field and far-field behavior of the output of fibers and how best to measure these effects (sec. 2.1). This is followed by a discussion of the DESI requirements for the fiber system, the DESI design and implementation, and measured performance (sec. 2.2). Finally, I will describe fiber splicing, its specific implementation on DESI, and performance results from splicing (sec. 2.3).

2.1 Fiber Optics in Multiobject Spectroscopy

Since the 1970's, optical fibers have been used in astronomy to capture light from the sky. While applications have ranged from radial-velocity spectroscopy and interferometry to photometry, one of the most successful applications has been in multi-object spectroscopy (Parry 1998). The first instrument to use fiber optics in this way was MEDUSA at the Steward Observatory in Tucson, AZ, which used 20 fibers to simultaneously measure the spectra of 8 galaxies across 20 arcminutes (Hill *et al.* 1980). The fibers were set in a plug plate, similar to more recent implementations like the SDSS spectrographs. The continued use of optical fibers in multi-object spectroscopy is largely driven by their flexibility as they are able to gather light from anywhere in the focal plane and deliver them to any number of spectrographs. Additionally, their relatively high throughput and strong scrambling characteristics make them ideal for large redshift spectroscopic surveys.

The fibers most commonly used in astronomy are step-index multimode fibers with fused silica cores. While there are some applications for single-mode fibers, they will not be discussed here (Parry 1998). The silica cores of these fibers, able to accept a range of input modes, are covered with a cladding with a lower index of refraction than the core. Optical fibers can be treated like waveguides with the allowed modes determined by the difference in the index and the diameter of the fiber core. The critical angle for total internal reflection is defined as:

$$\theta_c = \arcsin\left(\frac{n_{clad}}{/} n_{core}\right) \tag{2.1}$$

where n is the index of refraction. Modes with incident angles less than this critical angle can propagate freely, but modes with an incident angle above the critical angle are considered "lossy".

There are several ways that throughput can be reduced in fibers. First, there is absorption and scattering due to the material properties of the fibers, dominated by absorption bands of OH in the infrared and metal ion impurities in the blue. These are referred to as "mode independent" losses in Ramsey (1988). Mode dependent losses will here on be referred to as "Focal Ratio Degradation" (FRD), which is the phenomena that étendue, or the spreading out of light in area and angle (AΩ) is not conserved. This means that the input light cone of a beam becomes more divergent in the output, decreasing the energy density by spreading the light. The input beam, with a $f/\#$ defined as the ratio of the telescope's focal length to its diameter, becomes faster. If your spectrograph has a specific acceptance aperture, some light will not make it to your detector.

FRD can be caused by a variety of phenomena, but is mostly attributed to microbending of the fiber and end preparation effects. It was shown by Poppett & Allington-Smith (2010) that the dependence on length of fiber is minimal, although length of the fiber can have implications on the overall throughput of the fiber. While the FRD dependence on length was predicted theoretically, it could not be confirmed experimentally. Instead, for fibers without microbending, the majority of the FRD can be attributed to a FRD-generating zone (FGZ), which is contained to a few millimeters at the tips of fibers and is mostly caused by fiber termination (Allington-Smith *et al.* 2013). When using optical fibers in astronomy, or most applications, it is necessary to have a very clean, smooth, normal face at the end of the fibers. There are two common ways to prepare the ends: cleaving and polishing. Cleaving is accomplished by tensioning the fiber and then nicking it with a diamond blade. Polishing the fiber uses progressively finer grades of abrasion, ending with a solution of colloidal silica. There are varying levels of success with both of these processes, but in both cases it has been observed that stress imparted to the fiber ends during this preparation are the largest contribution to FRD not attributed to bending (Poppett & Allington-Smith 2010). It has also been observed that any pressure on a fiber, even securing it with a piece of tape, can increase the FRD. Additionally, any small-scale imperfections in the bulk of the fiber can scatter power between modes and contribute to the FRD. These include variations in the core size and material inhomogeneities.

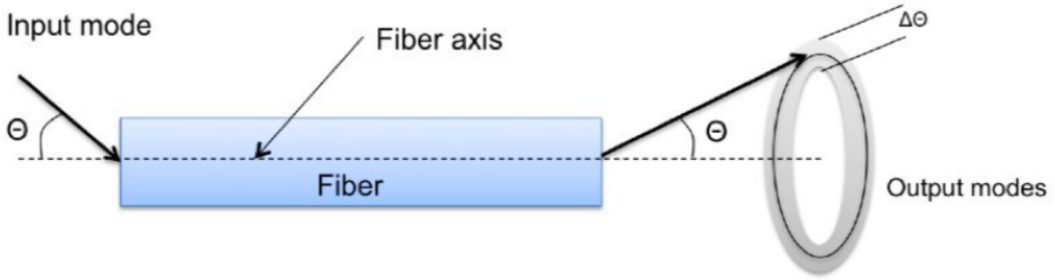

Figure 2.1: Illustration of collimated FRD. For a given input mode and angle, the output spreads out over some $\Delta\Omega$. The FWHM of the output ring defines the Focal Ratio Degradation and is impacted by bending, length of the fiber and any modifications or damage to the fiber.

The FRD can be parametrized by the ratio of input and output $f/\#s$ (f_{in}/f_{out}), and can be measured in several ways, as shown by Carrasco & Parry (1994). The first has a full light cone enter a fiber and measures the encircled energy within an angular limit of light that exits. This test can be designed to replicate the instrument by including a scaled obscuration modeling the telescope, and controlling the aperture such that a well specified $f/\#$ of light enters the fiber. The full cone test is a direct representation for how the fibers will behave in an instrument, specifically how much energy will be enclosed within some $f/\#$ for a given illumination geometry. While this test requires careful alignment of the input light cone with the fiber axis, a more simple test can be performed to quickly determine the growth of FRD. This is done by shining collimated light into the fiber at a single input angle, which is azimuthally scrambled by the fiber and creates a ring (Fig. 2.1). If you shine a single mode of collimated light into the fiber, the output is a ring that is centered at θ_i:

$$f_{in} = \frac{1}{2\tan(\theta_i)} \tag{2.2}$$

In this test, if the fiber is long enough that the light is completely azimuthally scrambled, the full width half maximum (FWHM) of the ring corresponds to the FRD (Fig 2.2). While the full cone test directly represents the behavior in the instrument, the results from the collimated FRD test are equivalent, except at very small angles. The shape of the ring was studied by Haynes *et al.* (2011) who found that its profile can best be described as a Voigt, which is a combination of gaussian and lorentzian functions. They separate FRD into three components: diffraction, model diffusion, and scattering, the latter of which can be modeled as a lorentzian in most cases. When scattering effects are reduced (using anti-reflection coatings for example), the rings can be well approximated as a gaussian.

While FRD largely impacts the far-field intensity distribution of output light, near-field intensity is also important. The final point spread function (PSF) on the detector is the

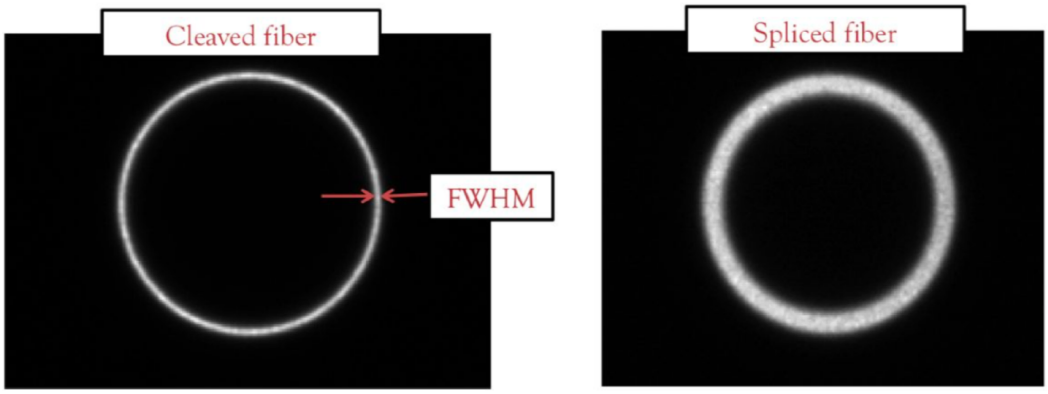

Figure 2.2: Output from collimated FRD test. These images were created by sending collimated light at a set wavelength (470nm) in to the fiber end at a set angle. When the fiber is stressed the FWHM increases as seen here. Note: We don't expect this large of an increase in the FWHM after splicing DESI fibers.

image of the output end of the fiber convolved with the spectrograph optics. Therefore, changes in the near-field pattern can change the PSF, especially in the wavelength direction. It was measured in Poppett *et al.* (2014) that there is a near-field pattern on DESI-like fibers, likely caused by end preparation (Fig. 2.3), but that it is quite stable for on-axis illumination. Any structure in the on-axis pattern was "frozen" in as evidenced by imaging the end of the fiber while spinning it on its axis. The end of the fiber was imaged with a very fast microscope objective, using the setup shown in figure 2.4, to ensure that all of the higher order modes are collected. The pattern does change, however, with the injection angle. Changes in the PSF based on target location present significant challenges to spectroscopic redshift surveys as it makes sky background subtraction more difficult, so it is critical that the injection angle changes very little during the survey.

2.2 DESI Optical Fibers

The light cone from the DESI focal plane corrector enters the fiber optics at $f/3.86$ averaged over the field-of-view. Due to the collimator design, the input beam ranges from $\sim f/3.7 - f/4.1$. The spectrograph is designed to accept $f/3.57$, so the DESI requirement is that $\geq 90\%$ of the output light from an input of $f/3.9$ will arrive at the detector. This requirement, together with the bulk throughput requirements on the DESI fiber, will ensure that the fiber system's throughput exceeds 50% over the full wavelength range (Fig. 2.5). The throughput can be compared to the FWHM of the ring in a collimated FRD test for a given $f/\#$ by measuring the enclosed energy for the same input in a full cone test. For the DESI fibers, the results indicate that for an input of $f/3.9$, a $\sim 0.8\%$ decrease in throughput at $f/3.57$

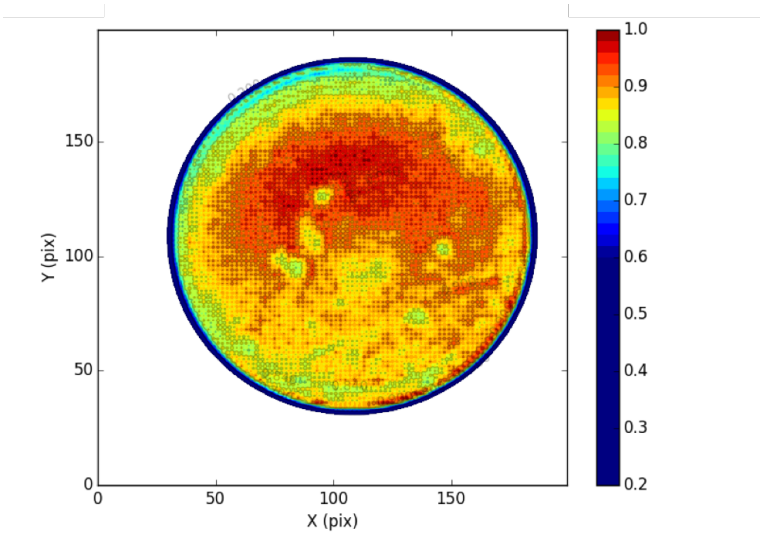

Figure 2.3: Near-field distribution of light. This is an image of the end of the fiber with a input of on-axis uniform illumination at 622 nm light at $f_{in} = f/4$. The fiber is $\sim$ 2m in length with a splice in the center.

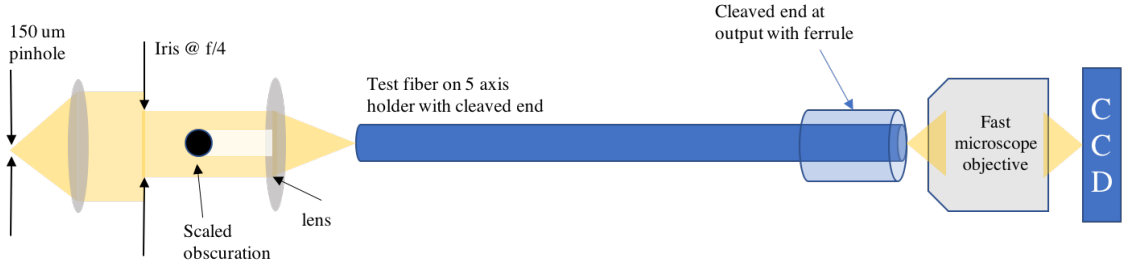

Figure 2.4: Test configuration for imaging end of fibers in full cone tests.

corresponds to a 0.1 degree increase in the FWHM of a ring. Therefore, to meet the DESI requirement, the increase in the FWHM cannot degrade by more than $\sim$ 1 degree for the whole fiber system. The total FRD will be impacted by microbending due to the robotic positioner, end preparation effects, and inhomogeneities along the length of the fiber, in addition to the fiber connection. DESI also has a requirement on the spectral stability, corresponding to the near field pattern. The FWHM of the PSF in the wavelength direction on the detector should change no more than 3% between observations. The challenge of the fiber system is to maintain low FRD at each step in the fabrication, installation and operation processes to meet the requirement.

As mentioned earlier, the fiber positioners are installed from the front of the focal plane. They are slid in and secured with a precision thread. To facilitate this installation, a 3 meter fiber is installed in the positioner and pushed through the hole in the aluminum petal.

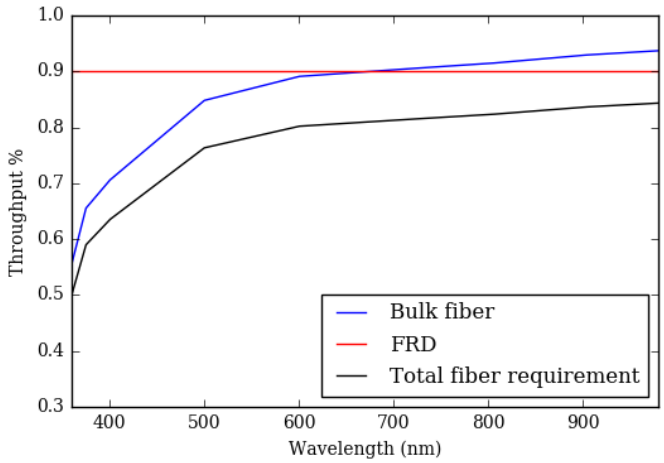

Figure 2.5: Throughput requirement for DESI fiber system. The decrease in throughput due to FRD should be no more than 10%. The bulk throughput requirements are set mostly by the capability of commercially available fiber optics.

When all 500 positioners and fibers are installed in the petal, they are connected to the $\sim$ 50m fiber optics cable that ends at the spectrograph slit. The 3 meter fiber optic is called the Positioner Fiber Assembly (PFA). The fiber chosen to be used on DESI is a broadband optical fiber (Polymicro FBP) with a 107μm diameter core and a numerical aperture (NA) of 0.22, where $NA = \sqrt{n_{core}^2 - n_{clad}^2}$ describes the acceptance angle of the fiber. It is a low-OH step-indexed fused silica fiber, which reduces the OH spectral absorption features in the red/infrared. The cladding has an outer diameter of 150μm and its width helps eliminate evanescent surface loss. The fiber is coated with polyimide for strength and protection with an outer diameter of 170 μm.

Since end preparation is so critical for reducing FRD, much care is been given to this process. The PFA ends are cleaved, rather than polished. Then a glass ferrule is slid onto the ends and secured with UV curing glue. Additional polyimide tube is secured to the ferrule to provide more support to the end of the fiber, and then covered with hytrel. The input end is AR coated with ion deposition, which reduces the reflection and scattering losses from 4% to 1.5%. The end of the fiber is secured to the positioner with a set screw holding the glass ferrule, which is later glued in place. Each step in the PFA production can add some FRD. Also, there as been some FRD increase measured from the microbending of the fiber during actuation of the positioner to some extreme locations within the patrol radius (Poppett *et al.* 2014). Of the $\sim$ 1 degree of allowed FWHM increase in collimated FRD, 0.5 degrees has been allocated to the fiber connections.

Connector type	Uncoupled FRD (FWHM deg.)	Coupled FRD (FWHM deg.)
FC + FC 'Standard'	0.6 - 0.7	-
MTP × 32 + SMA 'Standard'	0.5 - 1.8	2.0-3.9
DMI + DMI	2.5 - 3.5	3.4-4.3
GHD + GHD	-	5.5

Table 2.1: FRD measurements of the mechanical connectors for individual fibers (uncoupled) and when two fibers are connected (coupled). Ferrule Connectors (FC) could not actually be joined to each other. The Diamond Micro Interface (DMI) and Glenair High Density (GHD) connectors showed large increases in coupled FRD. The Mechanical Transfer Push-On (MTP) connectors proved the best option, and were further investigated.

2.3 Fiber Splicing

The most common way to connect fiber-optic cables is with mechanical connectors, and a variety of connectors are widely used in many industries, including science applications. In the fall of 2012, the DESI team tested a number of the commercially available connectors using the collimated FRD test and found that the performance did not meet our requirements (Edelstein *et al.* 2012). The results (Table 2.1) indicated that the best performance achievable when coupling two connectorized fibers was using multi-fiber Mechanical Transfer Push-On (MTP) connectors, planned to be used by the PFS instrument on Subaru (de Oliveira *et al.* 2014), with a minimum FRD increase of 3 degrees on average. The available options for connecting two fibers all exceed the FRD budget for the DESI fiber connection (0.5 deg increase of FWHM). While other groups have measured better FRD performance with connectors, using specialty gels and using extreme care in end preparation, the results still indicate they wouldn't be sufficient for DESI with a minimum of 1.1 degree increase in FWHM (Haynes *et al.* 2010, dos Santos *et al.* 2014) . The performance of these tests encouraged DESI to investigate other solutions rather than optimize performance with existing connector types.

2.3.1 Splicing Process

Fusion splicing is a method to connect two fiber optics using heat. With very low levels of loss, two unbuffered ends of fibers can be aligned, melted with an electric filament, and carefully pushed together to create a solid bond. There are several commercial machines available for fusion splicing optical fibers, used mostly in telecommunications and the medical industry. These industries generally use single mode fibers. This is the first known use of fusion splicing for astronomical spectroscopy.

To produce the best possible splices with minimal FRD, each fiber to be spliced must

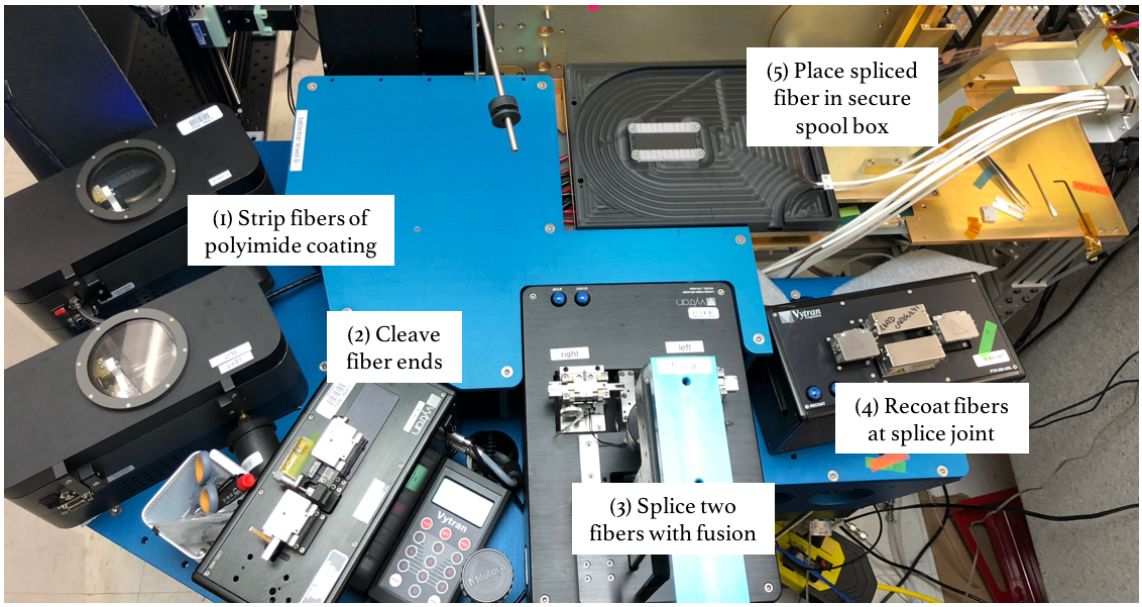

Figure 2.6: The commercial machines used in the splicing process looking down on the work table. From left to right: 3SAE Plasma Station stripper, Vytran LDC-400 Fiber Cleaver, Vytran LFS-4100 Fusion Filamnet SPlicer, and Vytran PTR-200 Fiber Recoater. The fibers are then placed in a spool-box that secures 25 spliced fibers.

undergo several processes. The fibers must be stripped and cleaved before splicing, and it is recommended that they be recoated after splicing to protect the spliced joint and stripped fiber. Bare fiber optic glass is susceptible to contamination, and any particles that bond to the glass can weaken the fiber and splice, leading to deterioration over time. For this reason, it is important to complete all steps of the splicing process in rapid sequence in a clean environment. Figure 2.6 shows all the commercial products used for splicing the DESI splices. They are arranged in an ergonomic way to enable quick transition between steps.

Fusion splicing with an electrical filament is only successful with clean fiber optic glass, so any fiber coating must be removed. The DESI fibers are coated with 20μm of polyimide which cannot be easily removed with common solvents or wire strippers. Most methods of stripping polyimide are hazardous and leave the fiber mechanically and chemically altered. We use the 3SAE Plasma Station, which uniformly removes the polyimide from a section of fiber using "3-Phase Plasma Technology". The ion etching maintains the mechanical integrity of the fiber by tapering the amount of coating on the fiber over a short length rather than having a sharp cutoff (Fig: 2.7). Care must be taken to ensure that all coating is removed as even a thin layer of remaining polyimide can impact the performance of the splice. When the polyimide is fully removed from a short (10mm) length of fiber, the impact on the FRD is negligable, but if the polyimide is heated during splicing, it can migrate into the glass and modify the NA of the fiber.

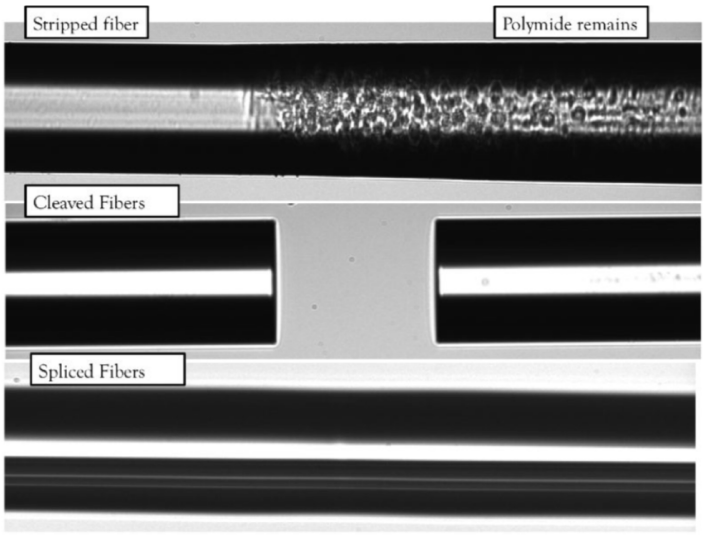

Figure 2.7: Images of fibers as they go through splicing process. Top: Part of the fiber has all polyimide removed and the amount is tapered until the fiber is fully coated on the right. Center: Two fibers that have been stripped and cleaved individually. Bottom: Two fibers spliced together. There is some faint indication of the splice in the center of the image.

Critical to the success of a splice is the cleaving of the fiber. Using the Vytran LDC-400 Fiber Cleaver, we are able to reproducibly cleave fibers using the tension-and-scribe method. We cleave through stripped fiber and consistently get cleaved ends with an angle of less than 0.5 degrees. The fibers can be transferred from the cleaver to the splicing machine, the Vytran LFS-4100 Fusion Filament Splicer, with custom inserts so that the fibers are not handled directly. Because heating of the coating can reduce performance, it is important that the tapered polyimide is far from the filament in the splicing machine. Once two stripped, cleaved fibers have been placed in the splicing machine, the LFS-4100 aligns the fibers, heats them, and then pushes them together. Using the collimated FRD test, we found that we achieve the lowest FRD when we spliced with the lowest heat that would still create a good bond (Table 2.2).

To protect the fibers after splicing and maintain their strength over time, it is important to recoat the bare glass. We are using the Vytran PTR-200 Fiber Recoater, which includes a linear proof tester to ensure that the splice was strong. The recoater deposits a UV-cured material on the spliced section and overlaps part of the polyimide on either side to seal the gap. After recoating, the DESI spliced fibers will be placed in a fixture that will secure each fiber individually, ensuring that the spliced section of fiber is not bent. Each fiber will be verified with the collimated FRD test, and if it is found to exceed the performance requirement it will be restripped, cleaved and spliced. Our results indicate that the performance of this splicing process is very stable. When the production process is optimized, the amount of rework expected is minimal.

Power	FWHM @ f/3.9 input
high	1.2
optimum (DESI)	0.9
low	1.7

Table 2.2: Heat impact on splicing performance. The FRD is impacted by how much heat is applied to the fiber. It was found that the performance is best when the splice power is as low as possible, while still making a good bond. The low power value represents a bad bond. Past a certain optimal power, the performance decreases with heat. The "high power" is actually the typical power used for splicing single mode fibers of this size.

2.3.2 Splicing Results for DESI Fibers

We used several tests to evaluate the splice performance. We used the collimated FRD results to test the splice parameters and stability of the splice process. However, our primary goal was to measure the enclosed energy for an input angle of $f/3.9$, ensuring that 90% of the input light can be collected by the $f/3.57$ collimator of the spectrograph. During the full light cone test, we also confirmed that the near field output of the fiber was stable at several offset angles ($\pm$ 2 deg.) by imaging the output of the fiber.

We tested our splicing process with 3m DESI fibers using a 470nm LED. As mentioned above, the requirement on the splice is that it introduce no more than 0.5 degrees of additional FRD. Therefore, with an average FWHM for a 3m cleaved and un-ferrulized (bare) fiber of 0.7 ± 0.1 degrees, we can accept fibers with an FRD of $< 1.2 \pm 0.1$ degrees after splicing. This FRD increase must account for all steps of the splicing process, i.e. stripping, recleaving, splicing, and recoating (Fig: 2.8). After splicing 25 fibers in the same configuration, $> 90\%$ of the splices would achieve this goal on the first splice with an average final FWHM of 0.93 ± 0.14 degrees (Fig: 2.9). With this relative FRD increase of ~ 0.25 degress, we expect a corresponding decrease in enclosed energy at f/3.57 of 2%.

We performed a full cone test to measure the solid angle FRD, and our results indicate that $> 90\%$ of the input light into these fibers will be collected in $f/3.57$ (Fig: 2.10), meeting the DESI requirements. Most of the light will enter the DESI fibers on-axis, but our results indicate that we will still meet our requirements if the light from the telescope is ± 70 arcminutes off-axis. The near field tests indicated that that the intensity is relatively stable, with centroid shifts of less than 20 microns as a function of input angle. Given the DESI spectral resolution, this will meet the science requirement (Fig: 2.11).

It should be noted that these results are from taking fiber from one batch of fiber, cleaving it, then splicing it back together. For the final DESI product, the PFA and fiber able will be prepared independently and the fibers will come from different batches of optical fibers. This will likely mean that the sizes of each side of the splice are slightly different, impacting the FRD performance. Also, in the full fiber system, the pre-splice FRD will be larger due to the length, but our results indicate that the splicing process will not introduce more that

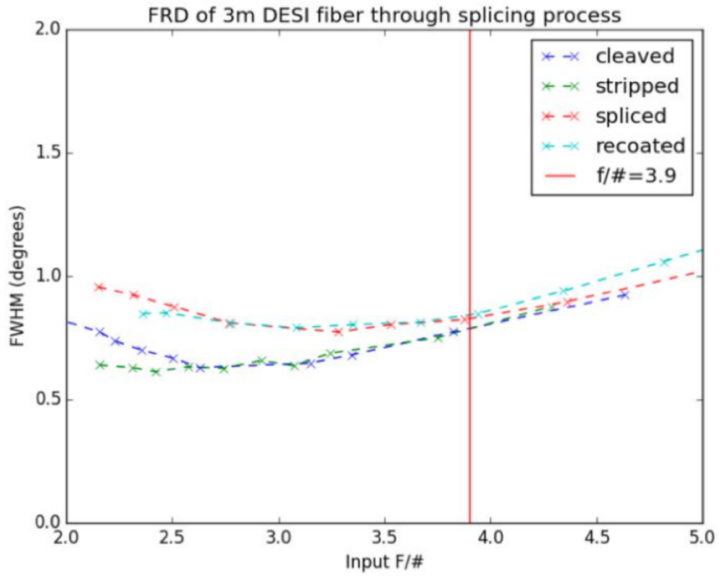

Figure 2.8: Collimated FRD curve for a DESI fiber (length = 3m) fiber as it moves through the splicing process, starting with cleaved and coated fiber ("cleaved:), then stripped and re-cleaved ("stripped"), "spliced", and then "recoated".

0.5 degrees of FRD. Recent production experience, using optical fibers from different batches for the PFA and the cable, indicates that the increase to FRD is still within requirements. It is found that in general, $FRD_{splice} = \sqrt{FRD^2_{PFA} + FRD^2_{cable}}$, with FRD measurements prior to splicing ranging from 0.65 to 2 deg.

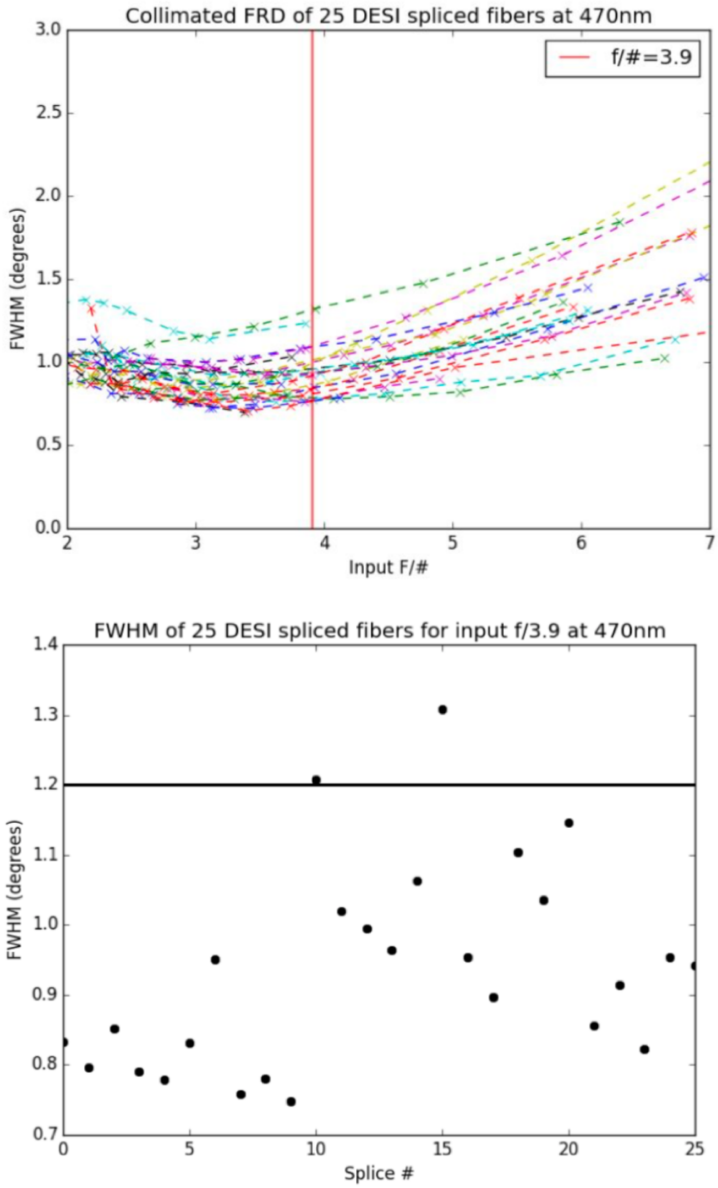

Figure 2.9: Upper: FWHM vs. input angle for 25 fibers spliced in the same configuration. Lower: FWHM of each spliced for an input angle of f/3.9. 90% of the splices (all data points below the horizontal line) have a FRD measurement that meets the requirement with an average value of 0.93 degrees. This corresponds to a $\sim$ 0.2 degree FRD increase for the splice process.

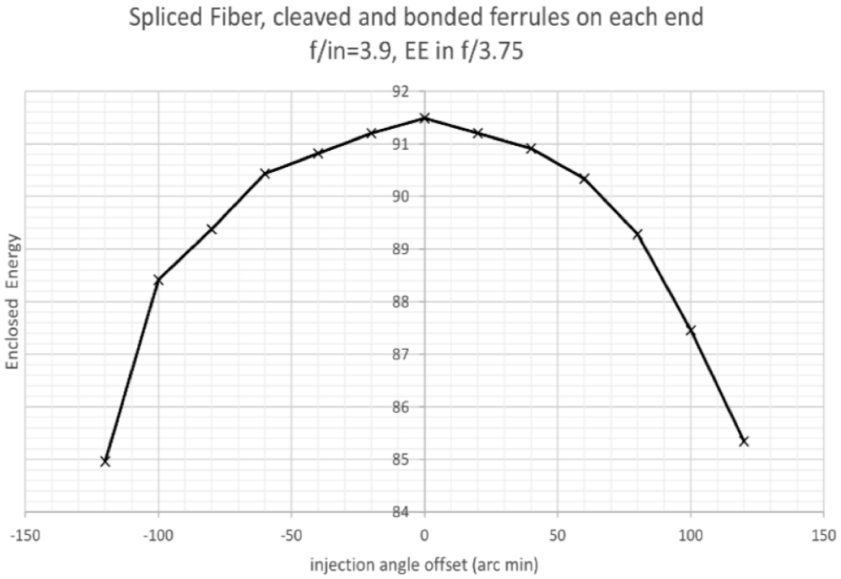

Figure 2.10: Full cone FRD test indicating that the spectrograph collimator will collect 90% of the light incident on the spliced fiber.

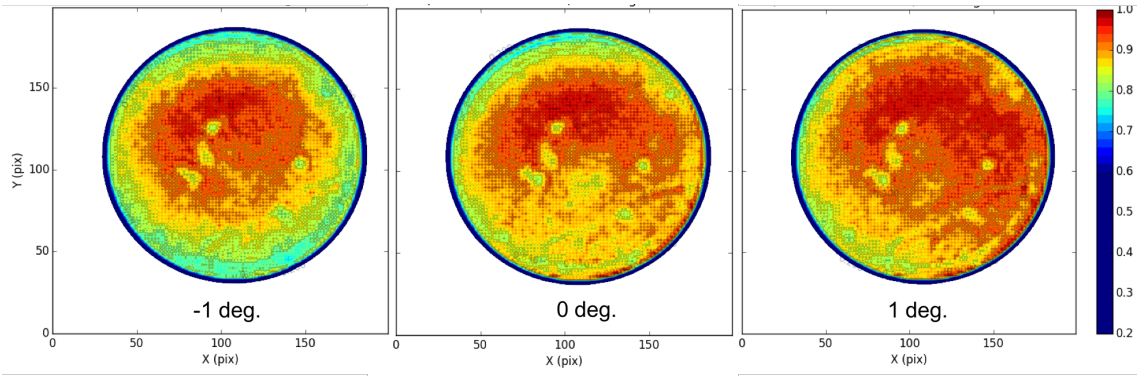

Figure 2.11: Near Field images of end of a DESI fiber after it was spliced, showing relatively stable output over range of input angles (± 1 deg.). The splices were done with two 2m fibers. The input to the fibers was f/4 uniform beam, using a scaled obscuration for realism, at 622 nm. The plot axes are in pixels and the scale is normalized flux.

Chapter 3

ProtoDESI

In order to measure the spectra with the 107 μm diameter DESI optical fibers, sampling the focal plane with an average plate scale of $\approx$0.014 arcseconds/μm, the robotic positioners must arrive at their target with $\leq$10 μm RMS error and maintain pointing for the duration of the DESI observation. This level of precision had been tested in the lab, but not fully demonstrated on-sky with positioners and other key DESI components integrated together. In order to reduce the risk related to these technical challenges, a prototype instrument was built and commissioned on the Mayall 4-m telescope in the summer of 2016. This prototype, called ProtoDESI, is a subset of DESI subsystems that was used for the first on-sky test of critical functions for the larger DESI instrument.

ProtoDESI included three robotic positioners, a guiding camera, a fiber metrology camera, and a subset of the instrument control software. It did not include long optical cables or spectrographs, like the final DESI Instrument will, but it did include shorter fibers that fed an imager for monitoring alignment with targets. The focal plate instrument was small enough to fit in the existing prime focus bay of the Mayall telescope with the existing corrector. During the time installed on the KPNO Mayall telescope from August 14, 2016 to September 30, 2016, ProtoDESI demonstrated that the Mayall telescope could be guided using the DESI architecture and that the DESI robotic positioners moved such that light from targets could be captured by the DESI optical fibers and remain stable. Additionally, the commissioning of ProtoDESI required early and careful integration of many critical subsystems in the DESI design, aiding in the completion of DESI and informing commissioning plans.

On-sky subsystem testing for large complex, instruments is a common and useful practice as demonstrated by projects such as: 2MASS (Kleinmann *et al.* 1994), HETDEX (Tuttle *et al.* 2016), and DECam for the Dark Energy Survey (Kuehn *et al.* 2013). This approach will become even more critical as the size and complexity of cosmology instruments increases, and has been adopted by LSST (Sebag *et al.* 2014). Most of the commissioning instruments referenced above were used for early testing of almost-complete facilities. ProtoDESI is unique in that it represents an early on-sky proof of concept for operations and a testbed for new technologies prior to a telescope upgrade, an approach that aims to reduce risks during

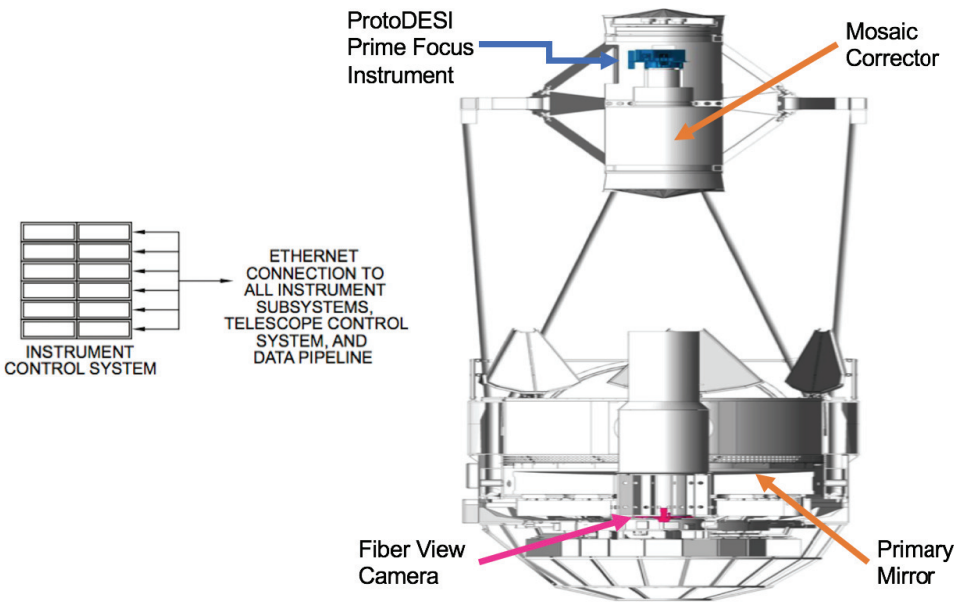

Figure 3.1: Layout of the ProtoDESI experiment. The prime focus instrument (blue) is mounted behind the Mosaic corrector and the FVC (pink) is mounted behind the primary mirror in the Cassegrain cage. ProtoDESI also includes the ICS and TCS.

the development stage.

This chapter describes in detail the design of the ProtoDESI instrument as-installed (Sec. 3.1). It then outlines the subsystem tests completed in the lab and on the telescope, which provides a benchmark for performance (Sec. 3.2), and which has some overlap with the description of the DESI instrument in Chapter 1. When all subsystems demonstrated compliance with their design requirements, we completed an operations campaign that tested ProtoDESI's ability to guide the telescope and align fibers with targets. I describe the operations in Sec. 3.2.4 and the results in Sec. 3.2.8. Finally, I discuss key lessons learned from ProtoDESI that will be considered in the DESI integration and commissioning phases (Sec. 3.3).

3.1 Instrument Description

The ProtoDESI instrument is a subset of DESI subsystems, including a much simplified prime focus instrument with three positioners, fiducials and a Guide, Focus and Alignment (GFA) camera, a Fiber View Camera (FVC) for positioning feedback, the Telescope Control System (TCS), and the DESI Instrument Control System (ICS) (Fig. 3.1). Rather than measuring the output of a 50-meter fiber cable with the DESI spectrographs, ProtoDESI confirmed fiber pointing and stability with a fiber photometry camera (FPC) that imaged

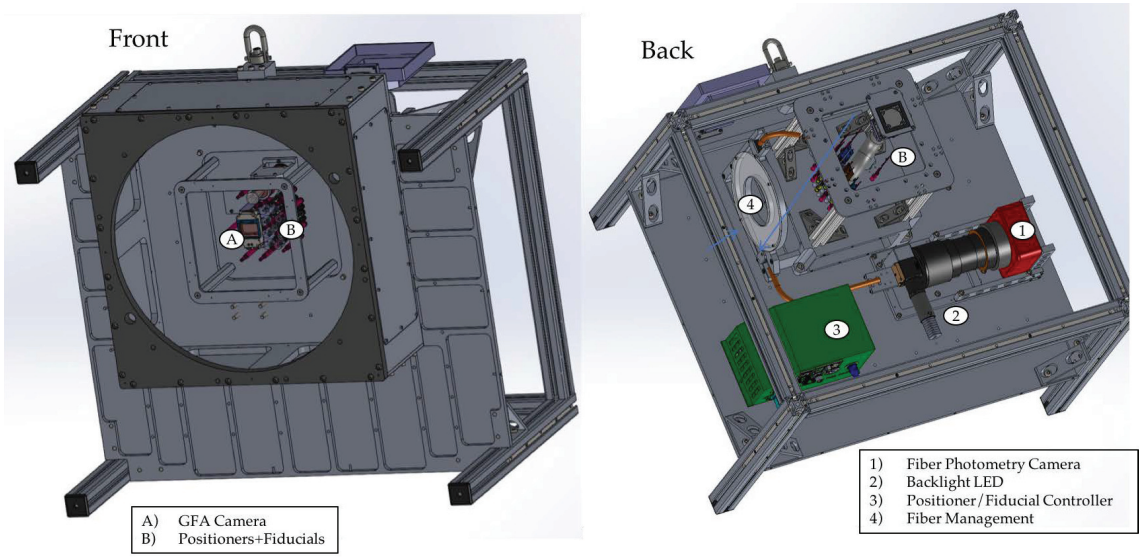

Figure 3.2: Computer-aided design (CAD) model of the ProtoDESI prime focus instrument. Light was incident on the front (left image) of the focal plate, which was mounted directly to the Mosaic corrector.

the ends of the short 3-meter fibers mounted on the prime focus instrument. The prime focus instrument (Fig. 3.2), which included the fibers and the robotic fiber positioners, illuminated fiducials, GFA and the FPC, sat behind the existing Mosaic corrector The FVC was installed in the Cassegrain cage of the Mayall telescope where it could image the front of the focal plane. The following gives a detailed description of the instrument as-installed.

3.1.1 Prime Focus Instrument

The prime focus instrument was designed so that it could be installed like the Mosaic prime-focus camera, requiring no modifications to the telescope. The instrument is $750 \times 800 \times 500$ mm with a total mass of ≈80 kg, and was mounted behind the f/3.2 refractive Mosaic corrector which has a 0.8 degree field of view (FOV). The flat focal plate held 16 fiducials (point sources fixed to the focal plate), three robotic positioners, one GFA camera, and a backup finder scope camera. The focal plate was mounted to a support structure which housed the fiber management system, FPC, and all power and control electronics. The instrument received all power and network connections in the prime focus bay via a single feedthrough in the instrument. The front mounting plate of the ProtoDESI instrument (Fig. 3.2, left) was machined to match the mounting surface of the Mosaic3 wide-field imager (Dey *et al.* 2016). Therefore, it could be installed directly to the corrector using the same lifting and installation procedures used for Mosaic3, using pins to accurately align the focal plate before securing it.

Robotic Positioners

The DESI robotic positioners are used to reconfigure the focal plane, gaining us access to new targets on a short time scale. Each positioner holds a single optical fiber, and has two 4 mm DC brushless motors, enabling it to access any point within a 6 mm radius patrol disk. The motors are arranged so that there are two rotational degrees of freedom with parallel axes (Schubnell *et al.* 2016). This style of positioner is often referred to as theta-phi, where the central motor defines the θ axis, and the eccentric motor defines the ϕ axis. The motors do not include individual rotary encoders. Instead, the positioning control loop is closed by directly imaging the backlit fiber tips with the FVC (described below). The robotic positioners were built by the University of Michigan. Each unit has an external thread coaxial with a precise cylindrical datum feature, and screws into the focal plate like a sparkplug. A flange co-machined into the unit positions the fiber tip 86.5 mm forward of the plate's mechanical mounting surface. They were designed to be mounted on a grid spaced by 10.2 mm, allowing for an overfilled focal plate on DESI with patrol areas overlapping. This will require anti-collision algorithms ensuring that robots do not run into each other during reconfiguration. ProtoDESI did not include this capability so the positioners were placed such that their patrol areas did not overlap. The fiducials were mounted in the same way on the focal plate, having the exact same length so that the fibers and fiducial pinholes all lie in the same focal surface. The optical fiber was attached to the positioner with a set screw that holds a glass ferrule glued to the tip of the fiber (Fig. 3.3). Each individual positioner includes an integrated custom electronics board that powers and controls the brushless motor function. The positioners received 7.5 V and commands were sent using the CAN bus protocol from a petal controller (PC) based on a BeagleBone Black[1] microcomputer. The PC also managed the thermal control system, consisting of four temperature sensors and two fans. One of the fans cooled the GFA and the other created positive pressure across the front of the focal plate to avoid deposition of dust on the optics.

Optical Fibers

Three meters of DESI fiber were attached to each positioner to carry light from the front of the focal plate to be imaged by the FPC on the back of the prime focus instrument. The optical fiber is broadband Polymicro FBP fiber with a core diameter of 107 μm and a numerical aperture of 0.22. The length of the fiber ensured that the output of the fibers was sufficiently azimuthally scrambled, avoiding any near field structure. The light cone from the Mosaic corrector to the focal plane is $\approx$f/3.2, with a platescale of 0.017 arcsec/μm, so each fiber saw 2.4 arcsec^2 of the sky.

[1] https://beagleboard.org/black

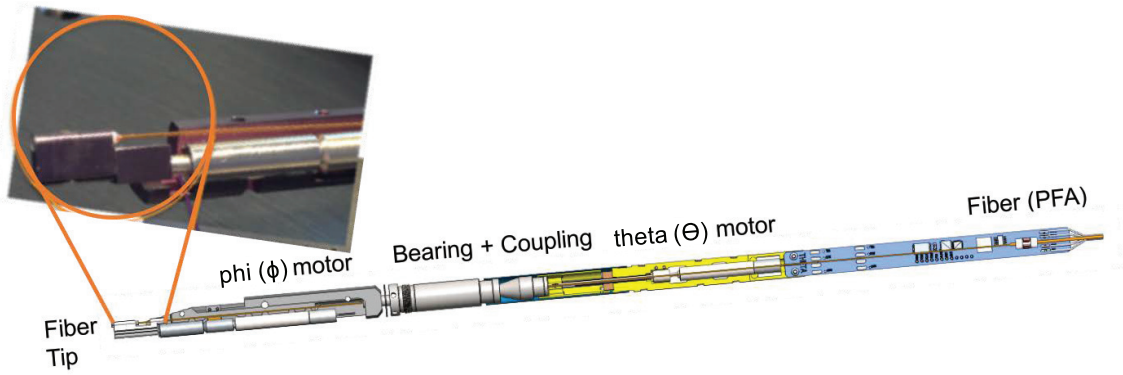

Figure 3.3: The DESI robotic positioner. Magnified is the fiber tip, glued into a glass ferrule and secured to the positioner with a set screw. The positioner measures 29 cm in length from the ferrule to the bottom of the custom electronics board.

Fiducials

The fiducials, built by Yale University, each consist of four 10 μm pinholes etched in a black coating on a glass block that are back illuminated by a 470 nm LED (Fig. 3.4). Their main function is to provide reference points on the focal plate relative to the movable fibers. By imaging the front of the focal plate with the FVC (See Sec.3.1.2) it is then possible to measure the absolute position of the science fibers through the distortions introduced by the corrector optics. The locations of the pinholes were measured relative to the outside diameter of the fiducials with an accuracy of 1.5 μm. The centers of the fiducials were measured with an accuracy of $\approx 5\mu$m for two types of fiducials. Two of the 16 fiducials were mounted directly to the GFA camera body, hereafter referred to as GFA Illuminated Fiducials (GIFs). Using a metrology system in the laboratory, developed at Lawrence Berkeley National Laboratory (LBNL) for this specific purpose, the locations of the GIFs were measured relative to the GFA CCD sensor. First, the illuminated GIFs were imaged using an external camera mounted on motorized stages, and the x-y locations of each GIF pinhole centroid was recorded. Next, an LED-generated circular dot, aligned with the center of the external camera sensor, was projected onto the GFA sensor. The projected dot was stepped over the GFA sensor in a grid pattern, and at each step a GFA exposure was taken. The LED centroid location on the GFA sensor and the stage x-y coordinate was recorded. This tied the x-y location of the GIF pinholes to the x-y locations of GFA pixels. The remaining fiducials, Field Illuminated Fiducials (FIFs), were mounted directly to the focal plate. The location of the FIFs, relative to the focal plate surface, were determined using a Coordinate Measuring Machine (CMM). After the GFA + GIF assembly was installed on the focal plate, the location of the GIFs relative to the FIFs was measured using the FVC, linking the coordinate systems of the focal plate and of the GFA sensor.

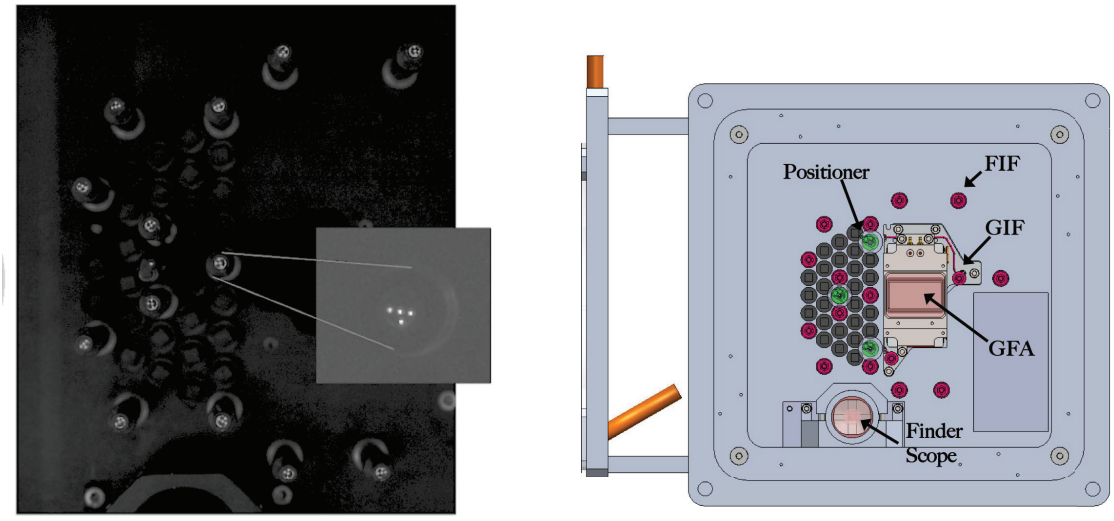

Figure 3.4: **Left:** Illuminated fiducials with 4 pinholes each mounted on the focal plate. **Right:** Schematic drawing of the front view of the focal plate. Locations of the fiducials (pink), fibers (green), and empty holes (black) are identified along with the GFA (rectangular camera at center) and the finder scope (circular camera towards bottom).

Guide, Focus and Alignment Camera

Located in the center of the focal plate, the GFA sent ≈30 arcmin^2 images to the ICS to be used in field identification and telescope guiding. The camera, housing an e2v CCD230-45 sensor, was custom-designed and built by LBNL and IFAE in Barcelona to minimize mechanical footprint while maximizing sensor area on the focal plate (Fig. 3.5). The GFA sensor has 15 μm pixels read out by 4 separate amplifiers. A custom SDSS r'-band filter was mounted to the camera to reject light from the blue fiducial LEDs and backlit fibers. The GFA required 3.3 V, 5 V, 15 V, and 32 V power inputs, supplied by linear regulated AC-DC supplies connected to an interlock so that if the FPGA on the GFA exceeded 60° C the power would be externally shut down, avoiding damage to the CCD. The cameras ran at ambient temperature and were cooled only by a fan dispersing heat behind the sensor. The data from the GFA was delivered directly over ethernet to the ICS where images were assembled for guiding.

In addition to the GFA, the focal plate contained a finder scope camera. This was to be used in the event that we were unable to align fibers with targets, we would have a way to connect images from two areas on the focal plate (finder and GFA) for troubleshooting. The finder camera selected was a SBIG[2]-STi Monochrome camera with a SEMI KAI-340 CCD, also with an SDSS r'-band filter. Besides confirming its functionality, we did not use the finder camera during operations of ProtoDESI.

[2]SBIG Astronomical cameras distributed by Diffraction Limited (diffractionlimited.com)

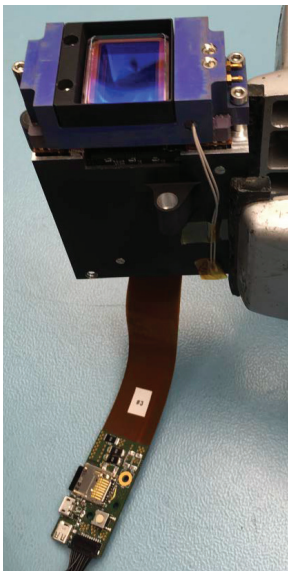

Figure 3.5: ProtoDESI GFA camera. The custom enclosure houses an e2v CCD with a Kapton tape cable to the electronics, giving access to power and ethernet connections.

Fiber Photometry Camera

Light from the targets ran down the fibers to the FPC where all 3 fibers were imaged in a fixed pattern. As the name suggests, the FPC provided aperture photometry on the output of the fibers, with the goal to achieve ≈1% relative photometry error for each fiber. The system was designed such that the output of the fibers did not move in the FPC images, nor did they change shape (azimuthal scrambling), but as a star moved across a fiber brightness of the output would change. In addition to imaging the fibers, the FPC assembly also backlit the fibers using a beam splitter and a 470 nm LED. The LED output was adjusted using a Mightex USB/RS232 controller[3] so that the fibers had the same brightness as the fiducials. The FPC is an SBIG STF-8300M containing a KAF-8300 CCD with 3326×2504 pixels with a 5.4 μm pixel size. Using a Canon 50 mm f/1.4 lens, the fiber output was imaged with a magnification of 1. Like the GFA and fiber camera, the FPC also had an SDSS r'-band filter with 0.15 μm bandwidth to reject the 470 nm light from the fiducials and backlighting LED. The FPC and LED were commercial-off-the-shelf parts with standard power supplies. The control software ran on an Intel NUC[4] that was mounted on the back of the prime focus instrument and connected to the LED and FPC via USB.

[3]Mightex Universal LED Controller (www.mightexsystems.com)

[4]Intel mini PC using Intel Core i3 Processor (https://www.intel.com/content/www/us/en/products/boards-kits/nuc.html)

3.1.2 Fiber View Camera

The FVC was mounted in the Cassegrain cage 12.25 m from the prime focus, oriented to image the front of the focal plane (Fig. 3.1). The images of the front of the focal plate, with the fiducials illuminated and science fibers back-lit, are used for metrology. Centroids for each point imaged by the FVC provide a feedback mechanism for identifying the location of the fibers. Since the robotic positioners don't include encoders, these images are critical to ensuring that fibers arrive at their commanded locations. The FVC used for ProtoDESI was nearly identical to that which will be used for DESI —a Finger Lakes Instruments[5] Proline PL501000 with a Kodak KAF50100 CCD, controlled with an Intel NUC over USB. The sensor has 6132×8176 pixels with a 6 μm pitch and receives light through a blue narrow band filter. Using a Canon telephoto lens with an effective focal length of 600 mm stopped to f/19, the focal plate was de-magnified by 21.7 so that the diffraction-limited full width half maximum (FWHM) of each fiber spanned 2 pixels, maximizing the SNR. The lens and camera were attached to an adapter plate which was installed in the Cassegrain cage, and the heavy (≈4 kg) Canon lens was supported within a cage to minimize flexure due to gravitational loading.

3.1.3 Telescope and Telescope Control System

The Mayall telescope at KPNO is a 4-meter optical telescope on an equatorial mount. Together with its sibling, the Blanco telescope at Cerro Tololo Inter-American Observatory in La Serena, Chile, it is one of the last of its kind ever built, and will support the DESI corrector which provides a 3.2 degree FOV. It currently serves regular scientific observing, and will be converted to sole-purpose use by DESI in 2018. Before major modifications are made to accommodate DESI, ProtoDESI was designed to be mounted behind the existing Mosaic corrector.

In preparation for DESI, and prior to ProtoDESI, the Mayall Telescope TCS was upgraded very similarly to the Blanco telescope in support of the Dark Energy Survey (DES; Abareshi *et al.* 2016; Sprayberry *et al.* 2016). This upgrade included new encoding hardware, servos, and the telescope control software. The new system is fully digital with a programmable servo controller. Evaluation of the new system during the Mosaic z-Band Legacy Survey (MzLS) showed the RMS pointing error to be 3-4 arcseconds with a settling time after slew of less than 10 seconds, with minimal dependence on the slew angle. With these improvements, the TCS provided open loop tracking with stability better than 0.17 arcsec/min (10 μm/min on the focal plate) RMS error, exceeding expectations for ProtoDESI. Additionally, the Mayall telescope control room was moved and enlarged to meet the needs of the large DESI commissioning team, and the ProtoDESI team acted as "beta" testers, leading to additional improvements.

[5] www.flicamera.com

3.1.4 Instrument Control System

The DESI ICS performs all control and monitoring functions required to operate DESI. One important aspect of the ProtoDESI project was early integration of several DESI hardware subsytems with the ICS prior to DESI commissioning. Wherever possible, ProtoDESI was run with elements of the ICS similar to the expected final version. This included all data acquisition and flow, connection to the Mayall TCS, monitoring infrastructure, operations database, guiding, PlateMaker (Sec. 3.1.4), subsystem coordination, and user interfaces (Fig. 3.6). Additionally, the computing hardware architecture, similar to the design for DESI commissioning, was used for the first time. This included three server class racks, a disk array, and two iMac observer consoles (Honscheid *et al.* 2016).

At the core of the ICS is the DESI Online System (DOS). This includes an application framework for the subsystems' distinct software. It is built on Pyro[6], an object-oriented communication package which enables efficient command and data transfer. DOS also contains all of the user interfaces, which display exposure sequences, real-time telemetry, and image previews. The Observation Control System (OCS), which orchestrates exposure sequences, is based on the architecture developed for the DECam on the Blanco telescope, which was successfully deployed in 2012 (Honscheid *et al.* 2010). The OCS controls the flow of data from one subsystem's software to another using a sequence oriented architecture. The structure of the OCS was validated through a variety of routine sequences, including guiding, taking dark and flat images, and a dedicated object exposure sequence customized for ProtoDESI that will be described in Section 3.2.5. DESI will collect a large amount of metadata and telemetry information, which will be recorded in the operations database. The operations database is implemented using PostgreSQL and ProtoDESI served as a testing ground for its architecture and user interfaces. The observers also had access to an electronic log book to keep a record of observation sessions, in particular any issues that came up during observing.

PlateMaker Software

One of the key elements of the ICS is PlateMaker, responsible for making all critical coordinate transformations to place fibers on targets. ProtoDESI tested the data flow to and from PlateMaker, and its performance enabled us to meet our goals. During an exposure sequence, PlateMaker runs through several processes, including calculating apparent target positions, guide star identification, and calculating fiber positioner locations based on FVC images.

The initial target positions are provided to PlateMaker in tangent plane coordinates, with the field center and a list of astrometric standards including potential guide stars. For ProtoDESI, astrometric standards and guide stars were selected from the NOMAD (Naval Observatory Merged Astrometric Dataset) catalog, and later the Gaia DR1 catalog (Gaia Collaboration *et al.* 2016). PlateMaker applies offsets, rotations, scale and skew corrections (Eq. 3.1), then incorporates aberrations, refraction and polar axis misalignments to produce

[6]https://pypi.python.org/pypi/Pyro4/

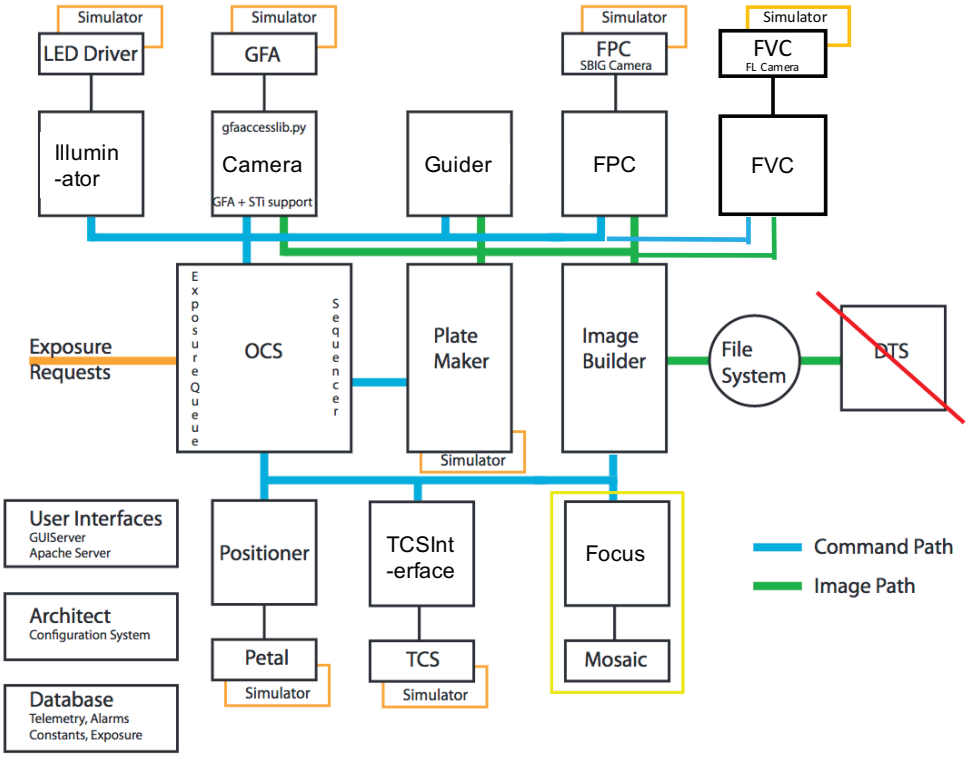

Figure 3.6: Schematic view of the ProtoDESI ICS. Exposure requests are submitted to the OCS application that coordinates operation of the instrument using dedicated applications for the illuminator, GFA camera, FPC, the positioners as well as an interface to the May-all telescope control system (TCSInterface). Instrument focus is controlled via the focus application and the existing Mosaic corrector focus motor. Guide images are processed by the guider application and corrections signals are sent to the TCS via the TCSInterface. The OCS uses PlateMaker to transform the requested on-sky coordinates to either focal plane or FVC coordinates and images of the back illuminated fibers taken with the FVC are analyzed to confirm that all positioners have reached the requested target postions. After an exposure is taken, the Image Builder application collects data from the GFA and FPC cameras, combines it with telemetry and meta data information and writes everything as a multi-extension FITS file to disk. Note: the Data Transfer System (DTS) was not used on ProtoDESI.

the final apparent targets (Eq. 3.2). The corrected target locations are output along sky North (ξ) and sky East (η) rather than RA/DEC:

$$\begin{aligned}\xi_0 &= [(y-y_0)\,\cos\theta_0 + (x-x_0)\sin\theta_0]\,\frac{sp}{3600}\\ \eta_0 &= [-(x-x_0)\,\cos\theta_0 + (y-y_0)\sin\theta_0]\,\frac{sp}{3600}\end{aligned} \tag{3.1}$$

where x_0, y_0 are the locations of the telescope boresight, θ_0 is the rotation of the GFA relative to the ProtoDESI focal plate x-y plane (positive angle from +x axis to +y axis), s is the focal plane scale factor, and p is the pixel size of the GFA (15 μm);

$$\begin{aligned}\xi = \xi_0(1+R+A+R\sin^2\psi\tan^2 z) +\\ \eta_0 R\cos\psi\sin\psi\tan^2 z - \theta\eta_0\\ \eta = \eta_0(1+R+A+R\cos^2\psi\tan^2 z) +\\ \xi_0 R\cos\psi\sin\psi\tan^2 z + \theta\xi_0.\end{aligned} \tag{3.2}$$

R and A are the factors for refraction and aberration, ψ is the position angle of zenith, z is the zenith angle, and θ is the position angle of the sky in the North direction relative to the focal plane sky North direction, including contributions from precession, polar axis misalignment, and overall rotation of the ProtoDESI focal plate.

In order to derive focal plate coordinates from the sky coordinates (ξ,η), one needs to know the distortion map of the corrector (Kent *et al.* 2016). In general, one can not assume that the telescope/corrector system is fully symmetrical, requiring a more general model than 1D polynomials. For DESI, these non-axisymmetric components are modeled as follows. The wavefront error W can generally be written as a function of the exit pupil coordinates (ρ,ψ) (Eq. 3.3) using Zernike radial polynomials R_l^s:

$$\begin{aligned}W(\rho,\psi;r,\theta) = \sum_l\sum_s [A_{ls}\cos(\psi-\theta)\\ +B_{ls}\sin(\psi-\theta)]R_l^s(\rho).\end{aligned} \tag{3.3}$$

The coefficients A_{ls} and B_{ls} can be written as a function of position in the focal plane using one form of spin-weighted Zernike polynomials ${}^*_sZ_n^m$:

$$(-1)^s(A_{ls}+iB_{ls}) = \sum_n\sum_m ({}^*a_{nm}^{ls} - i\,{}^*b_{nm}^{ls})\,{}^*_sZ_n^m, \tag{3.4}$$

where

$${}^*_sZ_n^m = R_{n-s}^{m+s}(r)\,e^{im\theta}. \tag{3.5}$$

In these equations, $-n\le m\le n-2s$, $n+m$ is even, and ${}^*a_{nm}^{ls}$, ${}^*b_{nm}^{ls}$ are complex and Hermitian on index m. Distortion corresponds to terms with $l=s=1$. For computational purposes, the complex summations are rewritten as a pair of real summations. To complete

the generalized 2-d fit of the distortion pattern, as described in Kent (2018), DESI will need to fit 16 terms are needed (compared with 42 needed for a more traditional mapping). For ProtoDESI, 10 terms are needed since, unlike DESI, the focal plate is flat. Initial values for the a and b coefficients are obtained by making fits to raytraces of the corrector optical design. The initial focal plate locations for the target fibers are calculated assuming that the telescope has been re-positioned to point precisely at the field center.

With the initial acquisition images from the GFA, PlateMaker identifies stars based on pattern matching with the catalog. Knowing the apparent sky coordinates that correspond to the GFA pixels coordinate space, plus the known location of the GIFs relative to the GFA pixels, PlateMaker computes the apparent sky coordinates at the location of each GIF using the known optical distortion pattern to extrapolate the GFA astrometric solution to the GIFs.

After the initial move, the fibers and fiducials are backlit, and the FVC images are taken to measure their locations. The GIF pinholes, having known astrometric coordinates, are used to calibrate the FVC pixel space. The true location of the fibers are determined from the FVC images and offsets from their targets are calculated. These are transformed back to the focal plate and interpreted as delta movements for the positioners; the process is repeated until at least 2 fibers are within the required 10 μm RMS error of their desired locations. At the same time, the FVC pixel coordinates of the backlit fiducials are compared with the lab-based metrology coordinates of each fiducial in the focal plane and used to generate updated coefficients in Eq. 3.3. Images of the focal plane by the FVC and on-sky images from the GFA were required to initialize the PlateMaker software algorithms, after which it operated as an integrated application of the OCS.

3.2 Installation and Operations

The ProtoDESI prime focus instrument was assembled at LBNL, where functional capabilities were tested and the performance was benchmarked prior to shipment to KPNO. The ProtoDESI focal plate instrument arrived at Kitt Peak on Aug. 14, and after a quick ($\approx$1 hr.) installation (Fig. 3.7), a functional test was performed that confirmed that all subsystems had survived shipment, received adequate power and could be commanded with an external control system via ethernet. Prior to this, the FVC was shipped to KPNO, integrated with the 600 mm lens and mounted in the Cassegrain cage of the telescope. The ICS hardware was configured and all software installed so that testing could begin with the arrival of the prime focus instrument. The fully assembled prime focus instrument was shipped as one piece requiring minimal preparation when it arrived at Kitt Peak.

Our commissioning campaign included subsystem tests that ocurred both in the lab and integrated on the telescope. These tests characterized the performance of the subsytems and determined their compliance with requirements. The commissioning test sequence increased in complexity with time, beginning with tests that used stand alone software that could be done in the lab and then with the dome closed. These included positioner accuracy, FPC and

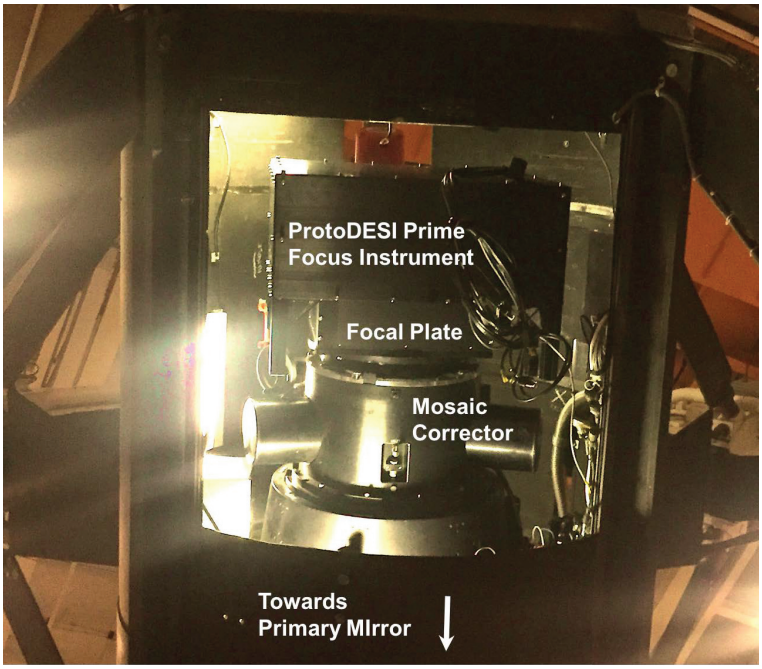

Figure 3.7: The ProtoDESI prime focus instrument as mounted behind the Mosaic corrector after installation. The bottom of this image is in the direction of the primary mirror.

FVC tests. We then moved to on-sky testing for the GFA, the first successful image taken on Aug. 25. When these tests were complete, the ProtoDESI instrument was sufficiently integrated and characterized to attempt guiding and aligning fibers with targets, at which time we moved into the operations phase (Sec. 3.2.4). Below we describe the tests and results that comprised the commissioning campaign, organized by subsystem.

3.2.1 FVC Centroiding

The purpose of the FVC is to provide a feedback mechanism to PlateMaker and the robotic positioners, helping ensure that the positioners are centered on targets. To achieve this, the FVC is required to deliver centroid locations of the fiducials and backlit fibers to 1/30 of a pixel, corresponding to a precision of less than 3 μm on the focal plate. While the FVC was used in the lab as discussed in the next section, characterization of the true FVC performance had to be completed on the telescope due to the separation from the focal plate and presence of corrector optics. To test the accuracy and stability of the FVC, a dataset was collected at different times of day with a variety of dome conditions and exposure times. The LEDs that backlit the fibers and the fiducial brightness were adjusted so that the flux on the FVC at all exposure times was more or less the same. Using the large dataset collected, we first evaluated the precision of our measurement of the fiducial locations (defined as the center of the fiducial). To compare images with the same exposure time to one another, we

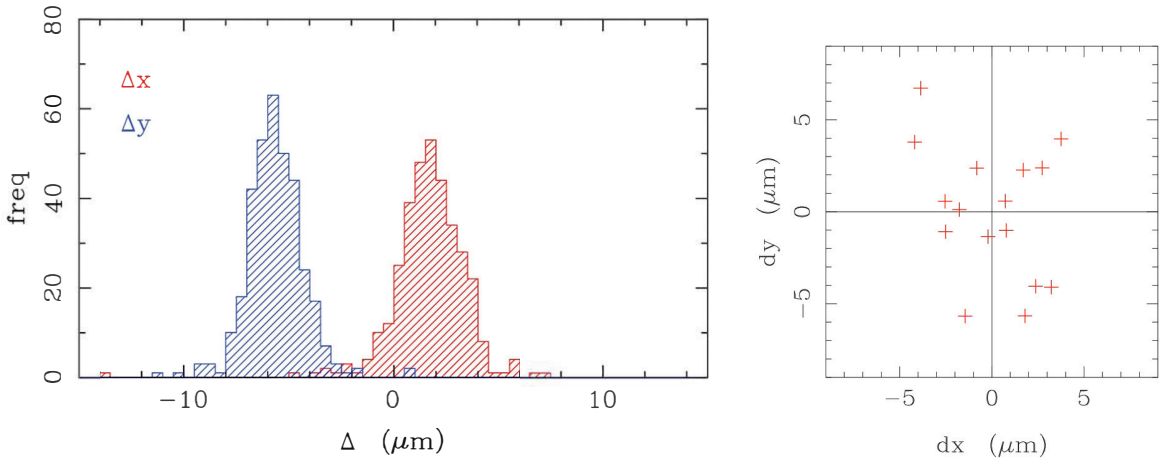

Figure 3.8: **Left:** Difference between the metrologically measured location of a single fiducial and its location measured by the FVC. These results are consistent with the 5 μm precision of the CMM used. **Right:** The average FVC offset of all 16 fiducials from their metrologically measured position.

used a linear transformation to put all exposures into the same coordinate system, since the position of the camera relative to the focal plane could change. Taking the mean error of all fiducial measurements vs. exposure time it was found that the precision requirement could be met for the fiducials with exposure times as low as 0.5 seconds.

This analysis was insensitive to distortions of the Mayall corrector lens. With the dataset of ≈450 exposures, we were able to solve for the distortions to third order. With this distortion calculation, each image could be pre-corrected to get an even better calculation of the average deviations of the fiducial locations. It was found that all the fiducials were offset in a random distribution from the CMM metrology measurements made at LBNL (Fig. 3.8), consistent with the ±5 μm precision of the CMM used. The distortion map derived from the FVC images were consistent with that used by PlateMaker in Section 3.1.4. Using this distortion map, the positions of the fibers could be accurately measured. The results (Fig. 3.9) indicate that the centroids of the fibers can be measured with the same precision as the fiducials and meet requirements at all exposure times of 0.5 seconds and above (the design exposure time was 2 seconds). During DESI, more of the FVC FOV will be used so additional distortion errors are likely to be encountered. However, there will be many more fiducials (100 FIFs, 20 GIFs) to enable additional constraints.

3.2.2 Positioner Accuracy Tests

In order to test the performance of the positioners it is necessary to use a fiber view camera, without which it is impossible to determine the true location of the fibers. Before running

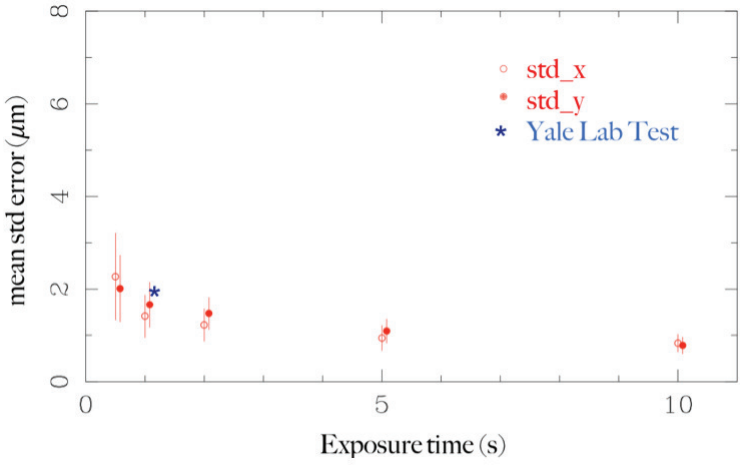

Figure 3.9: The standard error on the FVC centroid measurements of the fibers after correcting for distortions. Each point represents the mean of 70 images. The blue asterisk represents the in-lab results prior to delivery.

the accuracy tests it is necessary to run a positioner calibration sequence. The robots are commanded to move blindly to a series of pre-defined points. FVC images are taken at each point, and the measured positions are used to calculate 6 calibration parameters: kinematic radius of theta and phi axes, angular zero points of each axis, and the (x,y) center of the robot in focal plane coordinates. In accuracy tests, all positioners are also moved blindly on a grid of pre-selected points. The locations of the fibers are measured by the FVC and sent back to the positioner software where a delta correction move is calculated. Each positioner performed corrective moves (submoves) 3-4 times attempting to get closer to the target position, with an FVC measurement after every move. When the test was complete, the maximum, minimum, and RMS error were calculated for each submove (Fig. 3.10).

The positioners were designed to arrive at their commanded position with an RMS error of less than 5 μm with $\leq$3 corrective moves, ensuring an on-sky RMS accuracy of $\leq$10 μm. While additional corrective moves may reduce RMS error, during DESI operations reconfiguration of all positioners is expected to be complete to the required accuracy within 45 seconds. The initial blind move of the positioners, with no feedback from the FVC, is required to arrive within 100 μm of the commanded position. These requirements are expected to be met under all possible operating conditions for DESI.

The three ProtoDESI positioners were tested both at the University of Michigan and at LBNL prior to shipment to Kitt Peak. We did not have the laboratory space to use the FVC with a 600 mm lens, but we used a similar Canon lens with a focal length of 100 mm, placed it $\approx$2 meters from the focal plate so that when imaging the fibers they had the same demagnification of $\approx$22 as expected on the telescope. After adjusting the fiducial brightnesses to that of the backlit fibers, we imaged the front of the focal plate with the FVC. The initial tests of the positioners at University of Michigan indicated that

Environment	Blind Move Max Error (μm)	Submove 3 RMS error (μm)
Requirement	100	10
UM, pre-shipment	22	0.4
LBNL, integrated with ProtoDESI	35	3
Telescope, dome closed, no PlateMaker	60	25
Telescope, dome opened, no PlateMaker	50	14
Telescope, dome opened, PlateMaker	≈50	4-6

Table 3.1: Positioner Accuracy Test Results

their performance was excellent, exceeding the requirements. When the positioners were integrated in the ProtoDESI focal plate at LBNL, the performance was slightly diminished, likely due to the test configuration and conditions (e.g., stray light, floor vibrations), but all positioners still met the requirements.

The first tests conducted after completion of the initial functional tests on the telescope were the positioner accuracy tests. When mounted on the telescope the performance decreased significantly compared to results from lab testing. At the third submove, the RMS error was ≈20 μm with the dome closed, decreasing to ≈10-14 μm when the dome was opened. This change in performance on the telescope corresponded to dome seeing effects, as our ability to measure the locations of the fibers with the FVC was impacted by the changes in air density.

After identifying the dome seeing issue, tests were run with an open dome and sufficient circulation, but the accuracy requirements were still not met. The software used for these early commissioning tests was not fully integrated in ICS, as the test did not require the OCS and image building. Because of this, the transformations from FVC centroid measurements to focal plate coordinates was completed using a linear scaling by the stand alone positioner software, which proved to be an inadequate model of the corrector's optical transfer function. On September 18, we integrated a subset of the PlateMaker algorithms into the accuracy test software, correctly translating the FVC centroids to x-y locations on the ProtoDESI focal plate. With this additional functionality, the RMS error finally dipped below 5 μm and continuously met the requirement of ≤10 μm RMS error (Table 3.2.2). Once we were meeting the requirement, we did so within 1-2 corrective submoves. During this testing campaign, it was determined that the positioner calibration sequence needed to be run at least once a night.

3.2.3 FPC Performance

The requirement on the photometry camera was ≈1% relative photometry error for each fiber, meaning that the difference in output between sequential measurements with a given fiber with a stable input would not change more than that amount. This corresponds to a

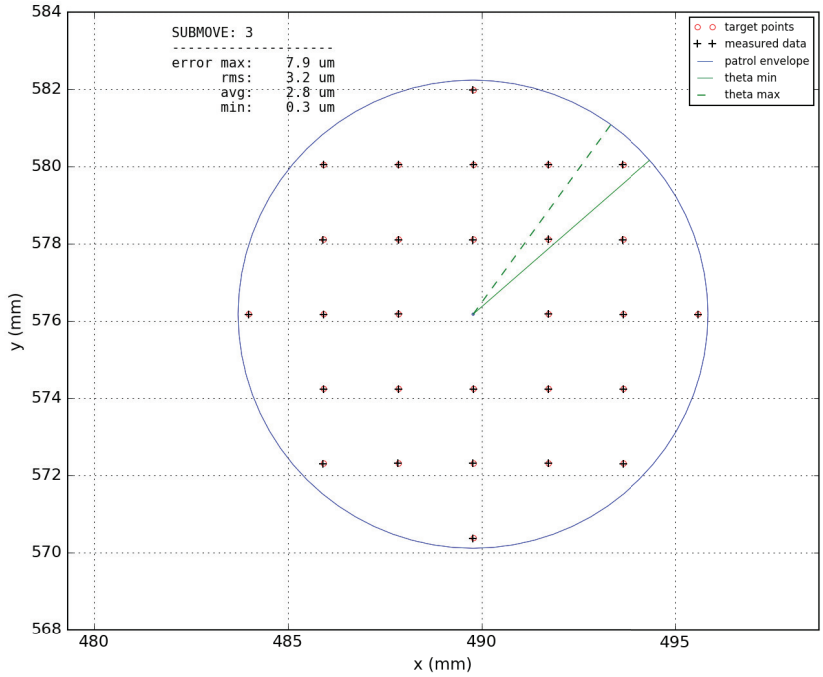

Figure 3.10: Output of a positioner accuracy test performed at LBNL on a positioner installed on ProtoDESI, which is identical to those performed at Kitt Peak. This test was performed on Aug. 8, 2016 and contains a grid of 28 positions within the patrol area. Each point on the plot represents a location within the patrol area which is targeted up to four times with increasing accuracy. After three corrective submoves, the positioner meets the requirements with an RMS error of 3.2 μm.

few microns error on the measurement of the centroid location of the star within the fiber. While in the lab, we did not project targets on the robotic positioners, but created a diffuse light source that could illuminate all three positioners, simultaneously measuring the output of the fibers as the positioners moved. Preliminary data analysis of the FPC images was performed and the camera was characterized, indicating that we would meet the requirement. On the telescope, using the calibration screen in the telescope dome, we took several series of 11 flat-field images with the FPC, each at a different exposure time. For each exposure time, the output from each fiber from the flat illumination remained constant in sequential observations with $\leq$0.8% error, meeting our measurement goals.

Since our objective was to measure the relative photometry, overall throughput was not a priority; however, care was taken to handle the fibers and maintain the minimum bending radius. Despite this care, one of the fibers appeared to be offset in the fiber array block such that the output did show some structure (Fig. 3.11). While each fiber did have a different throughput, when aligned with a star, they all had sufficient signal to noise with a FWHM of $\approx$25 pixels. The throughput differences in these fibers are not a concern for DESI as the

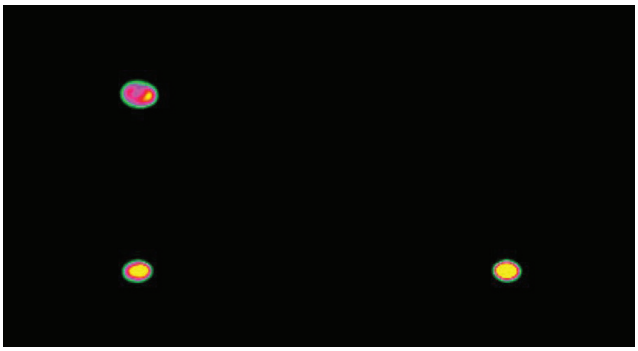

Figure 3.11: Output of the three fibers during a 10 second flat-field image taken with the FPC. The upper left fiber has clear structure in the output.

routing and termination will be quite different. The linearity of the camera was measured in the lab (Fig. 3.12) and then again on the mountain, with comparable results. Additional analysis of the FPC images taken on the telescope indicated that the location of the center of the fiber images moved up to 20 pixels from image to image, likely due to a shift of the camera relative to the fiber array block for different telescope pointings.

There were several fields that only had targets for one fiber at a time, while the other fibers were pointed at the sky background. This gave us a unique opportunity to look at the brightness of the night sky, helping to establish the signal to noise of the camera. We measured the signal from the night sky to be ≈4500 ADU for a 10 second exposure (Fig. 3.13), consistent with 20.6 mag/arcsecond^2 in the r-band as listed in the KPNO Direct Imaging Manual[7] appendix. The noise from these sky measurements, nevertheless, was much larger than expected. While we expected a SNR of 6 we measured closer to half that. The source of the noise was not identified, but it is possible that the DC voltage camera offset value of the FPC was not entirely steady but shifted the signal by variable amounts.

3.2.4 GFA testing

While the GFA cameras on DESI will be responsible for guiding, focus and alignment, the ProtoDESI GFA was only used for guiding and alignment. It was designed to measure centroids of guide stars with 30 milliarcsecond (mas) accuracy at 1 Hz. The GFA used on ProtoDESI was a prototype, and our experience with it was extremely useful in improving the final design for DESI. The GFA was the final subsystem to be integrated with the focal plate at LBNL. Before shipping the prime focus instrument to Kitt Peak, there was only time to complete functional tests, confirming that the CCD sensitivity was sufficient to reconstruct an image with adequate SNR. There was not enough time to fully characterize the camera and optimize its parameters prior to installation on the telescope, but a preliminary gain measurement was made in the lab. The initial results indicated that the ADC was using

[7]https://www.noao.edu/kpno/manuals/dim/

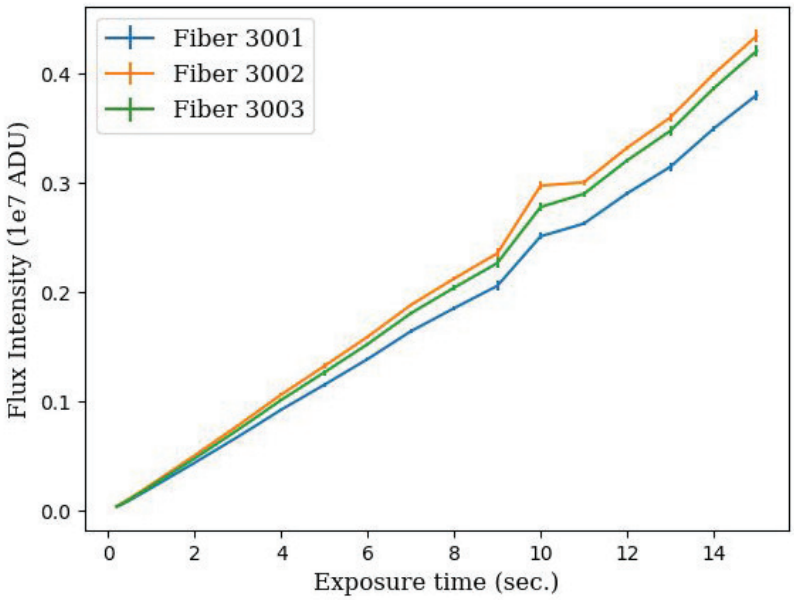

Figure 3.12: Relative throughput and linearity of each fiber. These measurements were made using dome flats after the prime focus instrument was installed on the telescope. Data with 10 s exposure time were taken at a different CCD temperature, hence the outliers. Fiber #3001 and #3003 had 87.0% and 95.5% respectively of the throughput of #3002, the best performing fiber.

only a small part of the dynamic range available and that the system was non-linear due to differences in the four readout amplifiers.

During integration with the focal plate, it was discovered that there was a loose connection in the Kapton flex cable which ran from the GFA to its power and ethernet connectors. This was addressed before shipment, but on the mountain it was found that the problem persisted and when it caused the GFA to shut down, it required opening the prime focus instrument and manually rebooting the camera. Towards the end of the ProtoDESI campaign, the firmware was modified, enabling reboot via software. The origin of the GFA shutdowns was not explicitly identified, but we postulate there were two causes. First, during slew of the telescope, the loose connection of the flex cable could temporarily break the power connection. More commonly, however, the interlock system installed on the power sources (see Sec. 3.1.1) would shut down if the temperature of the GFA's FPGA exceeded 60C. The cooling mechanism for the camera was a fan that pulled air from behind the CCD to outside the focal plane, and while this was expected to run continuously, the fan sometimes shut off. If the fan was turned off for more than ≈1 minute, the GFA would approach the maximum allowed temperature.

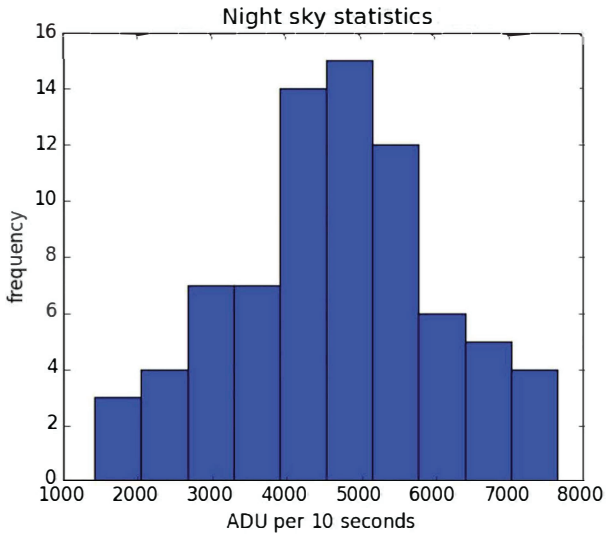

Figure 3.13: Histogram of 77 night sky measurements from a single fiber over a few independent FPC image runs. The best fit maximum, assuming a Gaussian distribution, is 4500 ADU, which is consistent with the expected sky brightness in the r-band at Kitt Peak. However the breadth of the distribution, 1500 ADU, was about twice its expected breadth.

After installation on the telescope, while the GFA was powered on, significant pattern noise was seen in the images making guiding impossible. Initially this issue was assumed to be with the ethernet interface and was temporarily fixed by replacing the ethernet switch. It was eventually determined that there was a design error in the camera electronics that caused interface issues. With this resolved, the GFA delivered images with sufficient SNR to meet its requirements for guiding (see Sec.3.2.9). Gain measurements made on the telescope were found to be inconsistent with that measured in the lab, however, some detector parameters were determined from on-sky images while ProtoDESI was installed. Using images of the trumpler37 field on Sept. 16 and 17 and assuming a gain of 4.5 e^-/ADU, a value that was not verified, the throughput was measured to be 0.46 combining the atmosphere, telescope reflectance, CCD QE, corrector and filter throughput. The read noise was measured to be 20 ADU/pixel and the dark current was ≈80 ADU/pix/sec at an ambient temperature of ≈ 20C, dominating the sky noise.

Once all subsystems were confirmed to function as expected, ProtoDESI moved on to its main goals: align a fiber with a target and maintain alignment for the duration of a DESI exposure. Prior to attempting the sequence of events that would align fibers with targets, we evaluated our guiding capabilities. The first successful object exposure sequence was accomplished on Sept. 14, 2016 when fibers illuminated by light from three stars were imaged by the FPC. After achieving acquisition of targets with the fibers, we extended the exposure sequence to include additional steps to measure the instrument's performance.

These included telescope dithers to sample the pointing precision and alignment stability tests. Our goal was to build a dataset that would allow us to confirm the precision and stability to 5 μm, but due to non-ideal weather, we were only able to complete a subset of our planned tests. This section describes our operations approach. The results from all guiding, pointing precision, and stability tests are discussed in section 3.2.8.

3.2.5 Object Exposure Sequence

Prior to a night of observing, we identified a number of fields that had enough bright stars for guiding and stars in the patrol areas of the three positioners to serve as fiber targets. From the list of available fields, one was selected based on time of the night and weather conditions, and the RA/DEC coordinates of the field center were given to the telescope operator. Once the telescope was in place, telescope control was switched to the OCS and the field information was uploaded, including the locations of the guide star(s) and fiber targets. While the OCS was capable of directly commanding the TCS to the field, for safety reasons, any telescope slew greater than 5 degrees required manual authorization for operation by the telescope operator. We then moved the prime focus stage in 50 μm steps, using GFA images at each step to find the best focus by analyzing how the PSF (Point Spread Function) of bright stars changed. The exposure sequence began with a full frame GFA image which PlateMaker analyzed to identify the guide star(s). With a guide star selected, the OCS entered guide mode, sending the ROI (Region of Interest) of the GFA image around the guide star to the guide software and forwarding guider corrections to the TCS. After entering guide mode, fiducials were turned on, fibers were backlit, and positioners made their first blind move. The initial fiber target locations were calculated relative to the guide star in GFA pixel space, converted to focal plate x-y coordinates by PlateMaker, and provided to the positioner software. The positioner software converts the x-y positions received from PlateMaker to the θ-ϕ basis for the robotic positioners. Once the positioners completed their blind move, an image was taken with the FVC and a list of centroids of all fiducials and fibers in FVC pixel space was sent to PlateMaker where they were converted to x-y positions on the focal plate. The measured locations of the fibers were compared to their commanded positions, and offsets were calculated and sent to each positioner. The positioners then attempted to correct their position, and the iteration with the FVC was completed up to 3 more times until at least 2 of the positioners were within the required 10 μm of the targeted locations. Passing GFA and FVC images through the PlateMaker software, as described in Section 3.1.4, the fibers were aligned with the targeted locations. At this point the fiducials and backlighting LED were turned off and a 10-second image was taken with the FPC, completing the sequence.

3.2.6 Dither Patterns and Stability Measurements

After achieving the primary goal of ProtoDESI, namely acquiring targets by aligning fibers with stars and maintaining pointing, the remaining two weeks of operations were spent

running tests to evaluate the performance of our pointing and stability. To determine the stability, we took a 10 second FPC image approximately twice a minute for at least 20 minutes. The pointing accuracy of our system was measured by moving either the telescope or positioners in a 5×5 dither pattern in an attempt to maximize the flux through the fibers. Assuming the true target location is where the flux through the fiber is at a maximum, we moved the telescope in either 1 or 2 arcsecond steps in a grid around the initial acquisition position of the fiber. The two step sizes were chosen so that we could identify an approximate maximum in a reasonable (<30 minute) amount of time. The larger step size of 2 arcseconds is just slightly bigger than the angular extent of the fiber so that the flux incident area for each step was independent and did not overlap. We also performed some dither patterns with the positioners, which could be dithered with much smaller step sizes. Unfortunately, the telescope was dithered in steps of RA/DEC and those of the positioners were x-y positions on the focal plane, so the dither patterns could not easily be compared. The next version of PlateMaker will allow DESI to compare positioner and telescope dithers. The results from these tests are discussed in Section 3.2.10.

3.2.7 Guide Modes

During the object exposure sequence, guide stars were primarily selected by PlateMaker based on astrometry, but the guiding software could also be controlled directly by the observer. There were three guiding modes readily available for ProtoDESI: self, direct, and catalog. Before running the full object exposure sequence, we tested our guiding capabilities in self mode, in which the guiding software chooses a guide star from a full frame GFA image. The star selected had the highest SNR among those meeting several requirements, including: isolation within a 16-pixel radius, having a round PSF, located away from the edge of the image, and not being blended, saturated, or flagged for some other reason. The direct mode used a guide star pre-selected by the operator, identified in GFA pixel space. In this direct mode we were able to explicitly test our ability to measure guide signals on stars over a range of brightness (see Sec. 3.2.9).

When we moved to full exposure sequences, the catalog mode was used, in which PlateMaker was responsible for selecting the guide star. Once the telescope slewed into place, a full frame image was taken to confirm the current position. PlateMaker could then identify the guide star and select a pixel on the GFA for alignment. At this point, the guider reconfigured the GFA to operate in ROI mode, after which only postage stamp images of the guide star were received. In order to move the guide star to the selected pixel with the required accuracy, correction moves were sent to the TCS every few seconds. After achieving stability, the guider prompted the OCS to continue with the object exposure sequence (Fig. 3.14).

3.2.8 Target Selection

The initial selection of ProtoDESI target fields was based on their accessibility given the observing dates, and designed to cover a range of sky positions and observing airmass. The

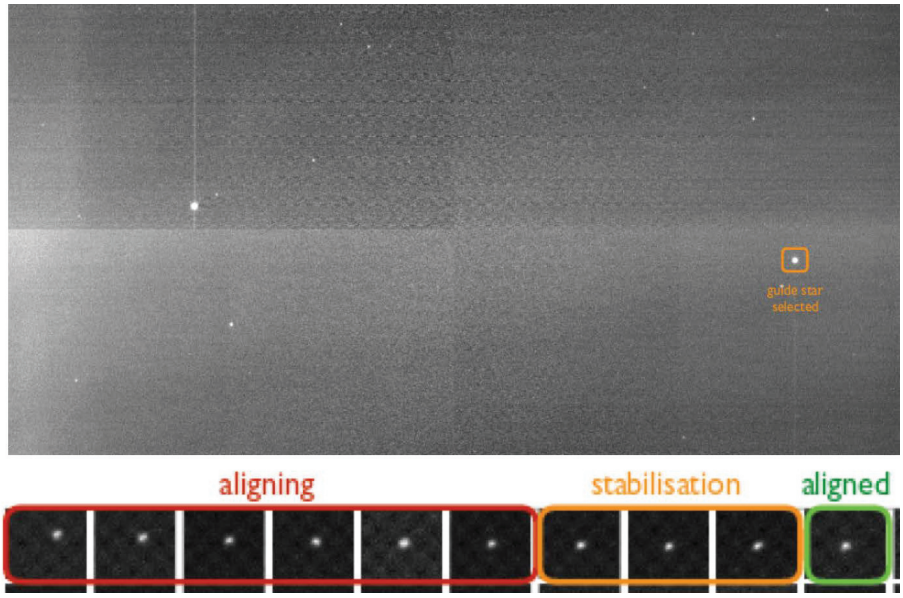

Figure 3.14: **Top:** Full frame GFA image with the guide star identified. **Below:** The guider moves into ROI mode and sends correction signal to the TCS to align and stabilize the guide star.

fields chosen each included a few guide star candidates ($r_{\rm AB} < 17$) near stars separated such that they could be reached with the fiber positioners. The selected targets were bright ($8 \leq r_{\rm AB} \leq 12$) for pointing accuracy measurements. Our target files included the coordinates of the field center and also the coordinates of the three fiber targets. For some target files, we offset the positioners so that only one would be aligned with a star and the other two not used. The coordinates were first identified using the NOMAD catalog, but then moved to the Gaia DR1 catalog which had much better precision astrometry. All fields attempted are listed in Table 3.2. We re-observed targets from night to night to trace repeatability. Figure 3.15 shows an example field, trumpler37, which we used to test both pointing accuracy and guiding, as it contained stars with a range of brightnesses in the GFA FOV.

The results in this section are collected from tests of the integrated system required to meet the primary goals of ProtoDESI, including: guiding tests, which required the GFA and telescope, and pointing accuracy and stability tests, which required all subsystems to be working together as described in the object exposure sequence. A summary of these results of these tests, as well as key results from the commissioning phase, are listed in table 3.3.

3.2.9 Guiding

The requirement for the DESI guiding system is that it be capable of delivering a tracking error signal to the TCS better than 100 mas RMS, of which 30 mas come from GFA errors, and of acquiring a guide signal for stars as faint as $r_{\rm AB} = 17$. This ensures that at least

Name[a]	# attempts[b]	RA[c]	DEC[c]	Catalog[d]
hour0	47	2.4206	28.6358	NOMAD
hour18_5	55	277.1659	32.9500	NOMAD
hour21	86	314.3166	31.2828	NOMAD
hour3	25	43.9392	30.8636	NOMAD
trumpler37	50	324.4944	57.5317	NOMAD
n7789a	7	359.5963	56.7387	NOMAD
33001	4	276.4567	29.8505	NOMAD
33002	5	276.5449	30.0056	NOMAD
33003	3	276.5676	29.7067	NOMAD
33011	10	315.6318	29.7147	NOMAD
33012	4	315.7199	29.8698	NOMAD
33021	46	0.2883	30.0809	NOMAD
33022	7	0.3767	30.2360	NOMAD
33023	6	0.3994	29.9371	NOMAD
33031	13	44.9427	29.7678	NOMAD
33032	1	45.0308	29.9229	NOMAD
53001	30	324.3935	57.1716	Gaia DR1
53002	74	324.3951	57.7616	Gaia DR1
53003	13	324.4151	57.7216	Gaia DR1

Table 3.2: Target List. **(a)** The names have no special significance, except in some cases they are the name of a recognizable field (trumpler37 and n7789a) and some correspond to the hour angle at which to use them. **(b)** Not all attempts were successful. **(c)** The RA/DEC coordinates are for the field center. **(d)** While the catalog for selecting the targets changed from NOMAD to Gaia DR1, the field identification by PlateMaker continued to use the NOMAD catalog.

10 guide stars will be available in any DESI target FOV, given calculated star densities at any galactic latitude (Bahcall 1986). With a FOV $\approx 29.3\,\mathrm{arcmin}^2$, the GFA camera could usually see up to five bright stars ($15 \leq r_{\mathrm{AB}} \leq 19$).

Determining whether or not the ProtoDESI guiding system met the 100 mas requirement was not possible, as the overwhelming majority of the guiding error came from atmospheric seeing. However, based on SNR measurements, the GFA contribution to this error budget easily met the 30 mas requirement, as shown in Fig. 3.16 for a $r_{\mathrm{ab}} = 12.27$ guide star. The guider correction signals were dominated by motion of the image centroid resulting from atmospheric scintillation, made clear by the correlation between the guiding error and centroid location. Based on these results, DESI will increase the exposure time of the GFA images, and given the large FOV for DESI it is expected that the seeing effects will average out.

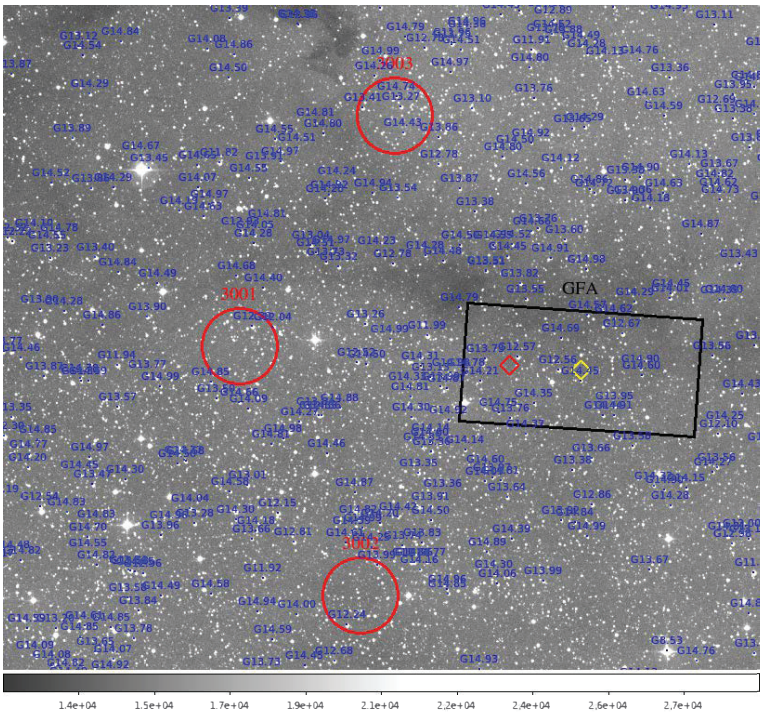

Figure 3.15: Trumpler37 field, used on ProtoDESI to test pointing accuracy and guiding. The red circles represent the patrol area of each fiber and the black box is the GFA FOV.

Using the direct guiding mode described above, we tested the GFA guiding sensitivity as a function of star magnitude. The GFA had sufficient SNR on 17 mag stars to acquire a guiding signal (Fig. 3.17), but failed at magnitudes greater than 17.5. Since DESI will likely have more than 10 guide stars at any time, Fig. 3.17 also shows the expected guiding errors for 10 stars. The guider was run in a direct feedback mode and another mode with a closed loop proportional-integral-derivative (PID). The results of both modes are comparable as we did not have time to tune the PID loop. With additional tuning of the PID loop, changes made to the GFA and guiding software, and increase of exposure time, we are confident that DESI can meet the guiding requirements even with these faint stars. Finally, the guider demonstrated capability of maintaining a guide signal for more than an hour (Fig. 3.18).

3.2.10 Pointing Accuracy and Stability

The expectations for pointing were that we align the center of the fiber with the target center within 10 μm and maintain that pointing accuracy for the duration of a DESI exposure time. While we previously showed that we could point the fibers to within 10 μm of where they were commanded (Sec. 3.2.2), we needed to confirm that this corresponded to actual targets on-sky. To explore how well we were pointing, we dithered the telescope around its initial position as described above. By calculating the intensity-weighted centroid using 25

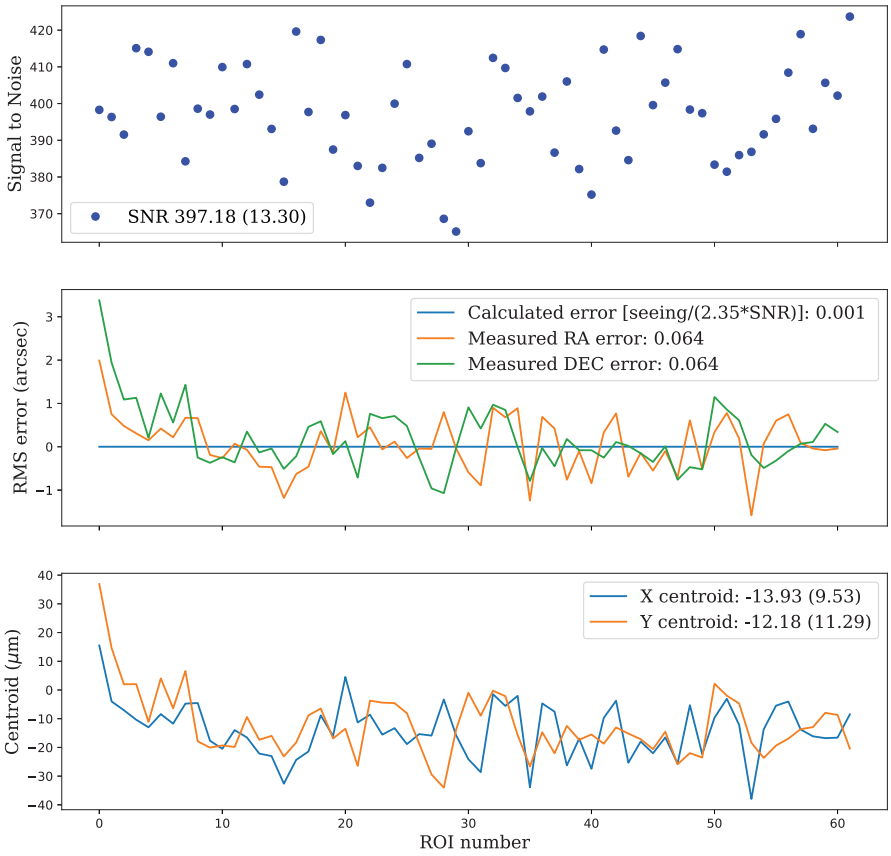

Figure 3.16: Guiding statistics for a guide star of $r_{\rm AB} = 12.27$. All values in parentheses are the RMS errors on the mean. The SNR was sufficiently high (top panel) to yield a statistical centroiding error less than 30 mas RMS (blue line, middle panel), which is the combined RA/DEC error calculated directly from the SNR that would be expected. Despite excellent SNR, the actual correction signals sent to the telescope were much larger than expected (RA/DEC errors in middle panel); the difference is primarily due to atmospheric seeing. The centroid location of the star in the guider images moved quite a bit (bottom panel). There is a clear correlation between the change in centroid location and the measured RMS error, with a plate scale on the focal plate of 0.017 arcsec/μm.

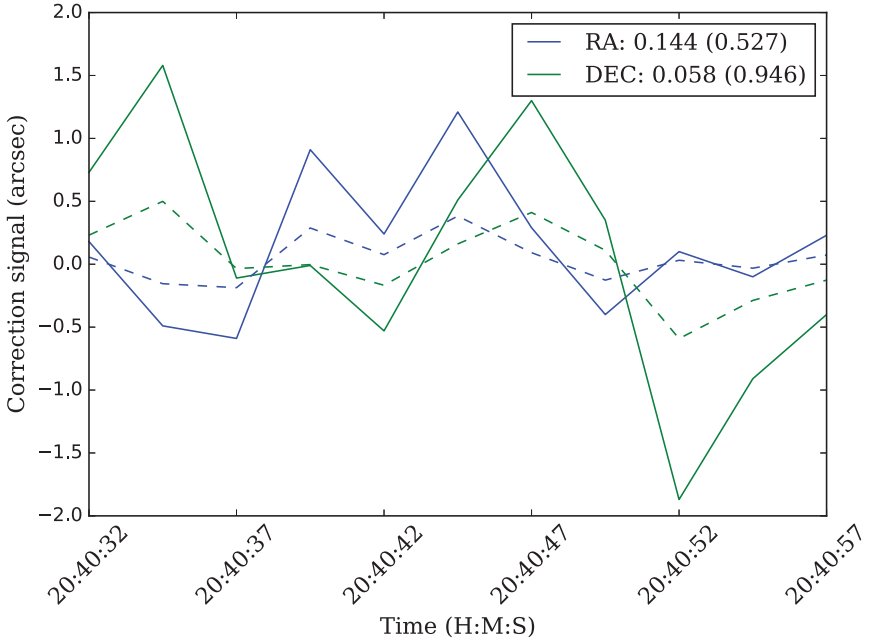

Figure 3.17: Guiding signal from a 17.09 mag star on Sept. 27, 2016. These guide correction signals were sent to the TCS for ≈5 min. on a night with 0.83" seeing. The correction signal was determined from 1-second GFA images, with the mean value listed with the RMS error in parentheses. The solid lines represent the actual measurements, and the dashed lines are the theoretical correction signal from the statistical properties of using 10 guide stars, reducing the RMS error considerably.

measurements for each dither grid, we determined where the peak intensity lay in RA/DEC space and the initial pointing offset from the targets. On average, the fibers appeared to be offset from the targets by 1.38 ± 0.30 arcsec in magnitude for all fibers and successive acquisitions (Fig. 3.19).

Several factors contributed to these offsets. First, two survey catalogs were used for generating target coordinates, NOMAD and Gaia DR1. It was found that the offset in the positioners decreased slightly when using the astrometry from Gaia DR1, even though the field identification by PlateMaker continued to use the NOMAD catalog. Second, an apparent tilt across the focal plate was identified in GFA images by measuring a differential in the focus across the CCD. To investigate this, telescope dithers were performed at several focus levels and it was found that when the GFA was in focus, which is where we measured the focus, the output of each fiber was at a different focus. This can be seen in Fig. 3.20, which shows two dithering tests results for two fibers, and fiber 3001 (upper panel) is much more spread out than 3003 (lower panel). Fiber 3001 was furthest from the GFA and therefore most affected by the tilt. The target was re-acquired and the dither pattern repeated, showing

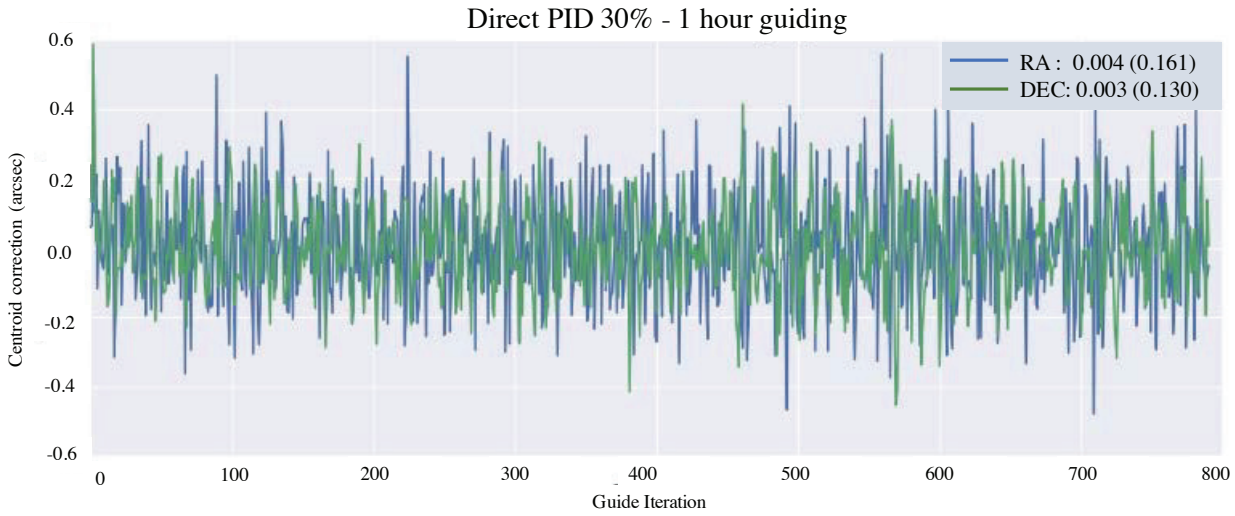

Figure 3.18: The guiding correction signals sent to the TCS for one hour, about three times the duration of a typical DESI exposure. During this guiding test, the proportional integral derivative (PID) was set to 30%.

that this result was reproducible. We returned to certain fields several times in a given night and throughout the weeks to test the repeatability of the offsets. The dithers from these fields gave visibly consistent results for repeat tests (Fig. 3.21), with slight variations in their weighted offset. This tilt was later confirmed on a CMM to be 0.3 degrees after ProtoDESI was removed from the telescope and shipped back to the laboratory, corresponding to $\Delta z \approx 160\,\mu$m across the GFA and greater than 200 μm focus error for the positioner placed furthest from the GFA.

The pointing stability of a ProtoDESI observation depended on both the pointing accuracy and stability of a fiber positioner and the guiding accuracy of the combined GFA+telescope system. In order to assess the pointing stability, we first acquired a target and then took a series of 10 second FPC images, two per minute, for a period of 20 minutes (corresponding to a typical DESI exposure duration). The fibers remained at the initial target acquisition with no offsets applied. The results showed fluctuations of ≈30% in fiber spot intensity around the mean value, with some 10-second integrations resulting in fiber spots 70% below the peak value. This may be the result of imperfect initial target acquisition, i.e., where the fiber was not centered on the target star, but instead on the wings of its PSF. As a consequence, the normal atmospheric seeing fluctuations resulted in a larger-than-expected spot intensity variation. In fact, we saw that the guide star centroids vary considerably over this time period after averaging over the 10 second FPC exposure times (Fig. 3.22).

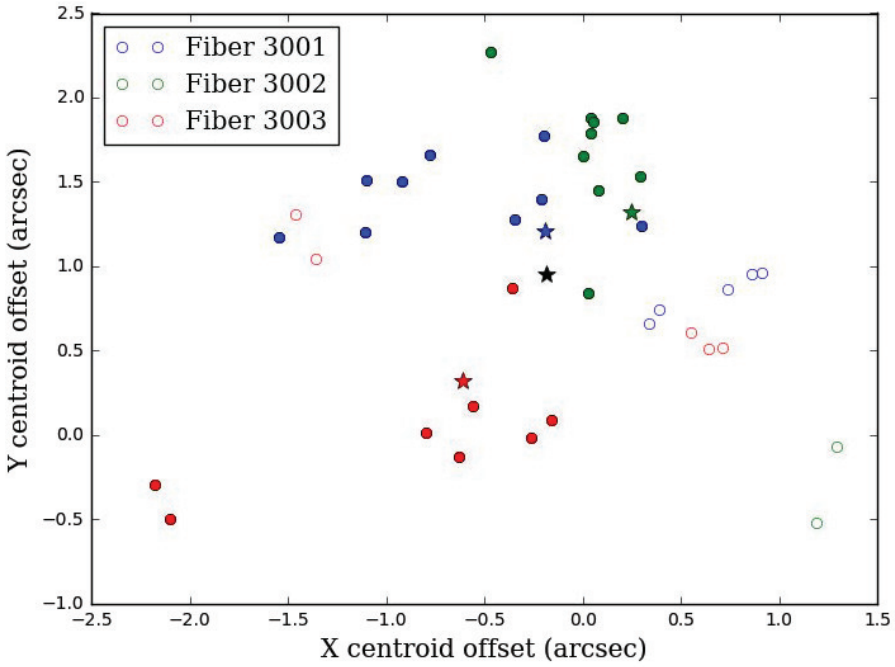

Figure 3.19: Scatter plot showing the results of successful target acquisition tests to measure positioning accuracy. Each color represents one of the three fibers, and each point is the offset measured from a telescope dither sequence. The filled circles show the results from targets selected from the Gaia DR1 catalog and the open circles are from the NOMAD catalog. The stars are weighted mean offsets for each fiber and the black star is the vector mean offset.

Description	Requirement	Result	Ref.
Positioner Accuracy[a]	$\leq$10 μm	6 μm	3.2.2
FVC Centroid Precision[b]	3 μm	$\leq$3 μm	3.2.1
FPC Relative Photometry	1%	$\leq$0.8%	3.2.3
GFA Centroid Accuracy[c]	30 mas (@ 1Hz)	$\approx$10 mas	3.2.9
Guiding Sensitivity (r_{AB})	$\leq$17	17.5	3.2.9
Pointing Accuracy[d]	0.17 arcsec	1.38 $\pm$ 0.3 arcsec	3.2.10

Table 3.3: Key ProtoDESI Requirements and Results. **(a)** Test on-telescope with dome open. **(b)** Requirement met at exposure times as low as 0.5 sec. **(c)** Requirement changed to a lower frequency. **(d)** See Sec. 3.3 for discussion of the discrepancy between requirement and result.

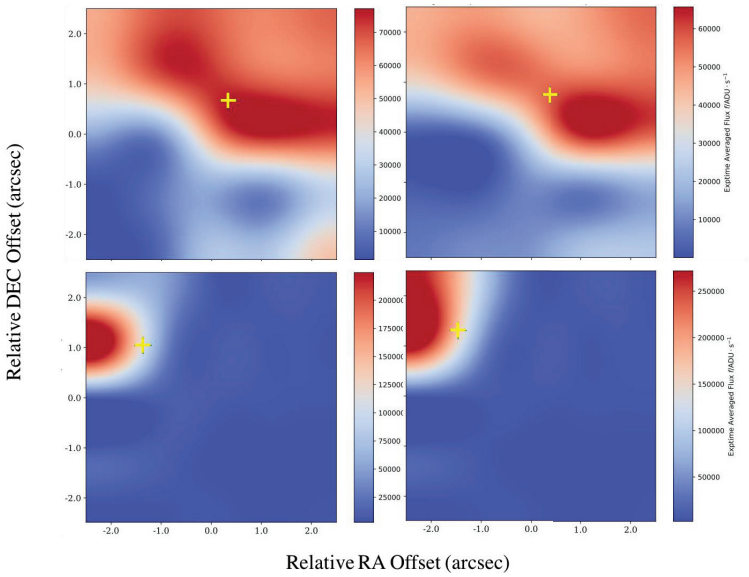

Figure 3.20: A series of two consecutive 5×5 telescope dither observations of field trumpler37. The telescope was moved in steps of 1 arcsec and the results for fibers 3001 (top) and 3003 (bottom) are shown. There is a significant difference in focus for the two fibers. There is a systematic offset of 1-2 arcsec, represented by the yellow crosses, from the initial telescope pointing for both positioners. The coordinates for these stars were derived from the NOMAD catalog, whose astrometry may be worse than that of Gaia DR1.

3.3 Discussion of Results

The scope and scale of the investment in the DESI project necessitate a plan to retire risks associated with achieving its science goals. This is achievable during the development stage by targeting hardware and software interfaces lying on the critical path, representing both technical and programmatic risks. ProtoDESI's construction and operations were conducted with a small team, due in large part to the desire to impact the overall DESI project and schedule as minimally as possible. This resulted in two issues: some of the hardware was not in its final performance condition; and the team was over-stretched in terms of personnel and working hours. Despite these challenges, ProtoDESI exemplifies an effective approach to exercising interfaces, gaining operational experience, and identifying improvements to the instrument on a useful time scale. Furthermore, a small dedicated team was able to uncover and resolve problems, as well as retiring risks associated with system performance, and build a basis for commissioning plans.

This experiment was designed to test the pointing accuracy and stability of the robotic fiber positioners and the target acquisition and guiding capabilities of the GFAs. We successfully demonstrated these to varying levels of accuracy and were able to recommend changes in design or operations for the larger DESI project. Key improvements will be made to the

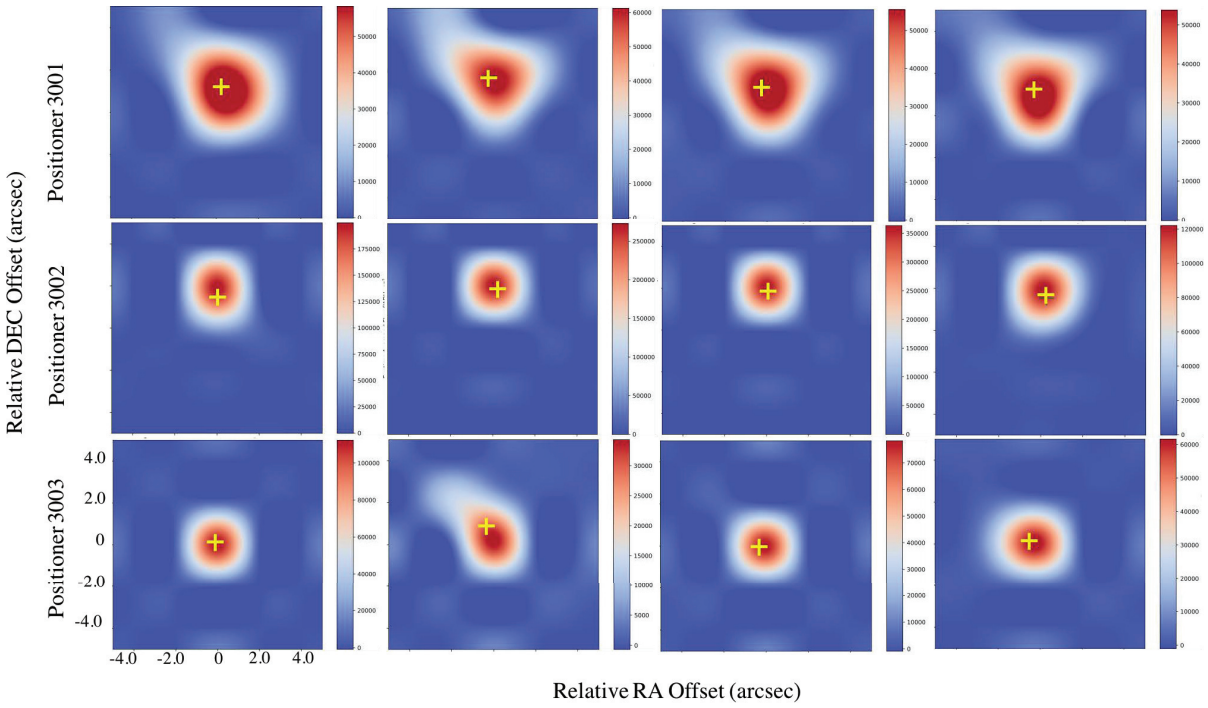

Figure 3.21: A similar 5 × 5 telescope dither on field 53002, with the stellar coordinates derived from the Gaia catalog. Signals from all three fibers are plotted, each column showing the results from a unique object exposure sequence. The acquisition sequence was repeated four times on the same night. The dither steps were 2 arcsec, so we should expect all of the light to be contained in a single tile. The yellow cross is the location of the flux-weighted centroid in each dither sequence, and the color bar show the exposure time-averaged flux in ADU/sec. Fiber 3001 seems out of focus and fiber 3002 is offset by ≈2 arcsec. Note that even for a single positioner (row) there were slight differences in the flux from one observation to the next.

GFA and its operation, including the GFA thermal system, electronics design issues associated with the ethernet link, and requiring the GFA to send full frame images to the guider software at a rate of 0.1 Hz rather than ROIs at 1 Hz. Other hardware design improvements will include mechanical bolstering of the FVC lens and modifications to the robotic positioners. Operational and process oriented issues were also identified during ProtoDESI and have already impacted the development of DESI assembly, integration, and test procedures and ongoing commissioning planning. These include early development of data models and interfaces, clear plans for precision metrology integrated across subsystems, and lab-testing of the instrument in every configuration expected to be used on the telescope.

There are several sources that contributed to our pointing error: focal plate tilt, FPC DC offset variations, atmospheric turbulence, astrometric errors, and metrology errors. While each of these will be addressed individually, their combined impact will be apparent only

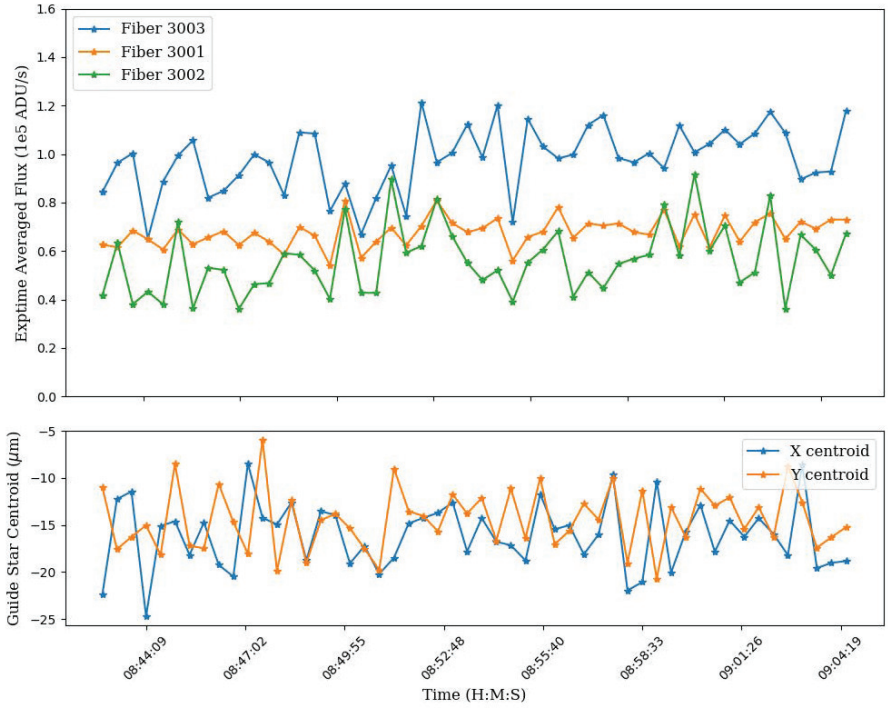

Figure 3.22: Stability tests for all three fibers on September 25, 2016 for field 53002. Each fiber was aligned with a different target and 10-second FPC images were taken in succession over a 30-minute period. The measured flux fluctuates up to 25% over this time period. We again see correlations between the averaged GFA guide star centroid location and the fluctuations in the target flux.

after DESI is installed. However, the accuracy achieved with ProtoDESI is well within expectations given the limitations on metrology and incomplete characterization of the Mosaic corrector and FVC optical distortions. The DESI team is confident that with improvements, DESI will achieve its science goals.

Chapter 4

BOSS Sky Background

In order to complete the DESI survey in the five years allocated, the survey must be implemented as efficiently as possible. One approach to increasing efficiency is the use of an accurate, predictive sky background model. This chapter describes a model developed for this purpose using data from BOSS, the largest spectroscopic survey to date. The first section of the chapter starts with a detailed description of the DESI survey and the ways in which a sky background model will impact its planning and implementation (sec. 4.1). Then we describe published sky measurements and existing models of the sky background in section 4.2. With the goal of testing existing sky models on a large spectroscopic data set and measuring the brightness of the night sky above Apache Point Observatory (APO), we turn to the BOSS spectra. Section 4.3 describes the BOSS sky spectra data set, consisting of $\sim$ 1 million unique sky spectra taken across a large observational parameter space. In order to study the continuum sky independent of the airglow lines, we fit each line in the sky spectra (sec. 4.3.4). We then describe our model in section 4.4, starting with the inter-airglow line continuum sky and then discussing specific airglow and terrestrial lines. Finally, we compare our results to other measurements of the sky and discuss the implications of applying the results to DESI and other surveys in sections 4.4.5, 4.4.6, and 4.4.7. Some of the preliminary results from this work was recently published in the proceedings for SPIE (Fagrelius & Schlegel 2018).

4.1 DESI Survey

The baseline DESI survey covers 14,000 deg^2 with a field of view of 7.5 deg^2, so the survey footprint can be split into 2,000 unique tiles. The DESI project will be the sole instrument on the Mayall telescope so will have access to all dark, gray, and bright time available for the survey. The dark/gray program will be allocated $\sim 1,940$ hours per year for 5 years, during which time we plan to visit each footprint ~ 5 times, giving us a total of 10,000 observations. Dark time is defined when the moon is below the horizon and the sun altitude $< -15°$, while *gray time* is defined when the moon illumination is less than 60%, the product of the moon

Program	Sun Alt.	Moon Ill.	Moon Alt. × Moon Ill.	Layers	Reference Exp. Time (s)
Dark	$< -15°$	-	$< 0°$	4	1000
Gray	$< -15°$	< 0.6	$< 30°$	1	1000
Bright	$< -13°$	-	$> 30°$	3	300

Table 4.1: Definition of Dark, Gray and Bright DESI Programs. The bright time survey is defined as any time not dark or gray.

illumination fraction and the moon altitude is less than 30°, and the the sun altitude $< -15°$ (see Table 4.1). Approximately 20% of the dark/gray program will occur during gray time. For these observations, the survey plan will be to target emission line galaxies (ELGs), for which the spectral feature for redshift measurements lands in the redder wavelengths and is therefore not as impacted by the brightening in the blue wavelengths by scattered sunlight and moonlight. Due to weather predictions at Kitt Peak, it is expected that 57% of the dark/gray time will be useful, meaning the dome is open and the seeing is less than 1.5 arcsec. Therefore, the dark program needs to complete 10,000 observations with 5,500 observing hours over the 5 years of operations. The bright time program, during which the bright galaxy survey (BGS) and Milky Way Surveys will be completed, is all observing time when the sun altitude $< -13°$ and any time not defined as dark or gray. There will be ~ 200 hours per year during which time the BGS program will cover the 14,000 deg^2 footprint in 3 passes. We expect a total of 6,000 observations during bright time with an average exposure time of ~ 12.5 min.

The exposure time of each observation during the dark/gray program will vary, but is generally set as the time needed to achieve a signal-to-noise ratio (SNR) of > 7 for the OII doublet in ELGs, DESI's largest target class. The SNR can be calculated as:

$$\mathrm{SNR} = \frac{S \times t}{\sqrt{(S + Sky + n_{pix} \times DC) \times t + n_{pix} \times RN^2}} \tag{4.1}$$

where S is the flux from the source (in detected photons per second), t is the exposure time (in sec), *Sky* is the flux from the sky background (photons per second), DC is the dark current (photons per sec), RN is the read noise (photons), and n_{pix} is the number of pixels. For many of the DESI sources, the source flux will be low, and the noise will be dominated by the sky background. In this case,

$$\mathrm{SNR} \simeq S \times \sqrt{\frac{t}{Sky}} \tag{4.2}$$

Our ability to achieve our SNR goal depends greatly on the sky background. If the sky gets brighter by a factor of 2, it will take twice as long to achieve the necessary SNR. On average, each observation is allocated 1,980 seconds (10,000/5,500). Of this, 180 seconds

are allocated to the telescope slew and reconfiguration of the focal plane (using robotic positioners), leaving 30 minutes for the observation.

The redshift of a reference ELG for the DESI target class is $\simeq$1.189. At that redshift, the OII doublet, which is 3726.032, 3729.815 $\AA$ at rest, is shifted to 8156, 8162 $\AA$. The combined flux of the doublet has a median value of F[OII] = $1.4 \times 10^{-16} erg/cm^2/s$ (see section 7.6.5 in DESI Collaboration *et al.* (2016b)). Our reference exposure is assumed to be taken at zenith with 1.1 arcsec seeing and an exposure time of 1000 seconds. The DESI simulations with the instrument throughputs, pixel scales, and baseline dark sky continuum value in that redshift range to be $3 \times 10^{-17} erg/cm^2/s/\AA$ for this reference exposure, we can easily reach a SNR = 10. If, however, the sky brightness doubles to $6 \times 10^{-17} erg/s/cm^2/\AA$, which is certainly possible based on BOSS observations during dark conditions, the exposure time would need to double to maintain this SNR. The limiting SNR is 7, which for the reference exposure described above, dictates that F[OII] = $0.8 \times 10^{-16} erg/cm^2/s$, so if you have to double the sky background, you would get a S/N of 5.

Of course, the sky background will not only impact the SNR of our emission line galaxy (ELG) redshift measurement. In fact, the 4000$\AA$ break line that is used to measure the bright galaxy survey (BGS) and luminous red galaxies (LRGs) will often be more impacted by scattered moonlight and sunlight, which is why LRGs will be targeted only during very dark time rather than gray time. The BGS program will operate when the moon is above the horizon, so will be significantly impacted by scattered moonlight. Understanding the shape and parameters of this scattered moonlight, brightest in the blue part of the spectrum, in addition to the scattered sunlight during twilight, will enable us to determine the set of galaxies we can successfully measure redshifts for during this bright time. Furthermore, when DESI uses quasars (QSOs) as backlights to the lyman-α forest, the strength of the broadband sky continuum can impact our sensitivity to the absorption strength of the low-flux continuum of the quasars. The SNR for all emission lines depends not only on the overall brightness of the sky, but also whether the emission lines land between or on sky airglow lines. Therefore, it is important to study not only the continuum brightness but also the location, strength, and variability of the airglow lines.

Having a good model of the sky background will enable better planning of the survey, increasing efficiency and helping to ensure we are able to complete the program in 5 years. Long term planning is occurring now to determine survey time and redshift completion rates. This "quick survey" uses mock catalogs (rather than simulated spectra) to simulate DESI observations, then creates fiber assignments and generates final redshift catalogs. Observations are simulated by creating a list of prioritized fields for the night using the "Next Field Selector" (NFS), pulling randomized values for the dome being open based on measured averages, selecting seeing and transparency values from measured distributions, using ephemerides to calculate the moon's phase, altitude, and separation. Using that meta data, the DESI simulation modifies the reference exposure (1000 sec, 1.1 arcsec seeing, airmass of 1) in order to meet the SNR goals[1]. Currently, our simulations indicate that we could

[1] https://github.com/desihub/surveysim/

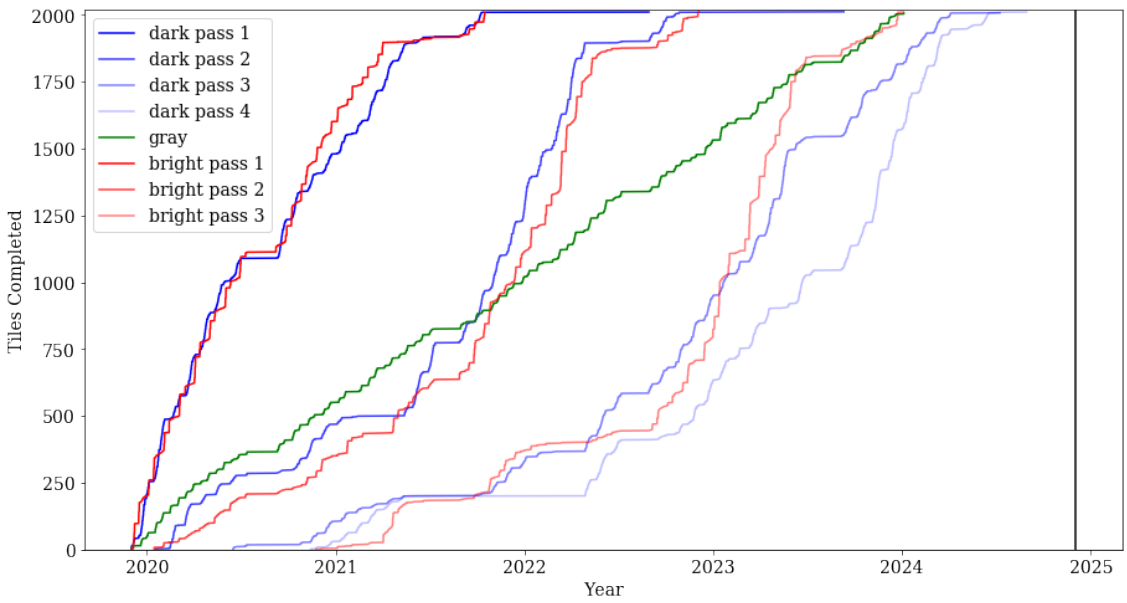

Figure 4.1: Projected DESI survey completion as run with desisim.py. Each line for the dark and bright time are different passes. The vertical black line signifies the end of the 5 year survey. This simulation was run with the current DESI sky model, which uses the UVES dark spectrum and the Krisciunas & Schaefer (1991) moon model.

finish the survey in ∼4 years, giving us 20% contingency (fig. 4.1). This estimate will be more reliable with a better model of the sky background based on measured distributions of observing parameters, possibly having a serious impact on our overall survey plan due to longer exposure times.

During the survey validation and operations phases of the DESI survey, a predictive sky model will prove exceptionally useful. The NFS implements the survey in real time based on current and past observing conditions, which tiles have already been observed, and what fields are available on the sky. Estimating the sky brightness based on past and current conditions will ensure that the best field is selected. Also, if unique observing conditions exist, like the zodiacal light is exceptionally high at a given lat./lon. or the terrestrial light is higher at a given azimuth, the NFS can reprioritize a field for a later time.

DESI also plans to employ a dynamic exposure time calculator (ETC). There will be ∼20 fibers per DESI observation pointed at the sky that will run to a photometry camera. This camera will have relatively short integration times (∼60 sec) which will track the brightness of the sky background in a narrow continuum dominated band during the DESI exposure. These data, along with seeing measurements from the guider cameras, will be fed to the dynamic ETC, which will update the needed exposure time to reach the required SNR for an observation. This approach will make the survey more efficient by possibly ending an exposure early, and also will ensure data uniformity. While the predictive sky model

described in this chapter will be used when selecting the field and not during the observation of the field, the real-time measurements from the sky camera can be used to calibrate this sky model. Additionally, this study will inform the design of this sky camera in identifying the most useful bands to observe the sky, and studying how changes in the brightness of a narrow continuum band scale with other parts of the spectrum and atmospheric emission (airglow) lines.

The current sky model for DESI includes a static dark sky spectrum based on measurements made by UVES (Hanuschik 2003, see fig. 4.2) with a model for scattered moonlight based on Krisciunas & Schaefer (1991). The model of the scattered moonlight was completed for V-band brightness, and is then converted to a spectrum using the assumed moon's spectrum (solar spectrum) and the wavelength dependent extinction curve. The brightness of the moon is modeled as a function of the phase angle of the moon (α), separation between the moon and the target (ρ), and airmass of both the moon as the target (X, X_m). Using the extinction coefficients from KPNO integrated over the V-band (k_V), this brightness is:

$$B_{moon} = f(\rho)\, 10^{-0.4(m+16.57)}\, 10^{-0.4 k_V X_m} (1 - 10^{-0.4 k_V X}), \tag{4.3}$$

where

$$m = -12.73 + 0.025|\alpha| + 4 \times 10^{-9} \alpha^4. \tag{4.4}$$

The scattering function $f(\rho)$ is dominated by components from Rayleigh scattering $f_R(\rho)$, and aerosol or Mie scattering $f_M(\rho)$, which are modeled as

$$\begin{aligned} f_R(\rho) &= 10^{5.36} * (1.06 + cos(\rho))^2 \\ f_M(\rho) &= 10^{6.15 - (\rho/40.)} \end{aligned} \tag{4.5}$$

This scattered moon brightness can be converted to the V-band as

$$V_{scatt} = (20.7233 - \log(B_{moon}/34.08))/0.92104 \text{ mag/arcsec}^2 \tag{4.6}$$

The zenith extinction used comes from measurements made at KPNO, as shown in figure 4.3. While this sky model accounts for the large changes in the night sky due to scattered moonlight, it doesn't account for changes in the dark time sky brightness.

4.2 Measurements of the Night Sky Background

The light of the night sky is comprised of contributions from sources that originate above the earth's atmosphere, light that is generated in the upper layers of the atmosphere, and terrestrially emitted light back-scattered off the troposphere. The major sources that originate outside of the atmosphere are unresolved milky way stars (integrated starlight; ISL), zodiacal light which is sunlight scattered off interplanetary dust, and moonlight. There is some light coming from unresolved extragalactic sources and diffuse galactic light, but their contribution for ground based observations is minimal enough to ignore for the most part.

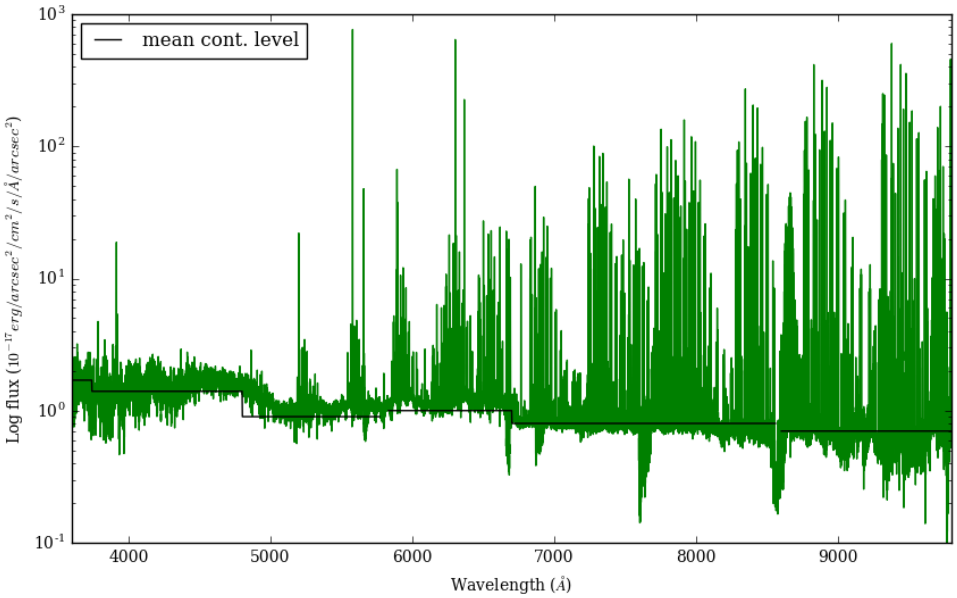

Figure 4.2: UVES sky spectrum used in the DESI sky model. The black line is the mean continuum values as published in table 3 of Hanuschik (2003).

Airglow emissions are generated in the upper levels of the atmosphere by the decay of excited electronic states that produce light, called chemiluminescence. Airglow, zodiacal light, ISL, and moonlight are all then scattered in the troposphere. This scattering comes mostly from Rayleigh scattering, which is isotropic in nature, and Mie scattering off of aerosols. This basic model is expressed as:

$$I_{Sky}(\lambda) = (I_{Airglow}(\lambda) + I_{ISL}(\lambda) + I_{Zodi}(\lambda) + I_{Moon}(\lambda)) \times e^{-\tau_0(\lambda)\,X} + I_{Terra}(\lambda) \qquad (4.7)$$

where $\tau_0(\lambda)$ is the zenith optical depth accounting for the scattering effects, X is the airmass of the observation, and *Terra* accounts for all terrestrial light components, like light pollution. In addition to wavelength dependence (λ), most of these terms show spatial and temporal dependence, which will be discussed below. See Leinert *et al.* (1998) for an excellent review of this model. Astronomers have long studied the brightness of the night sky to evaluate the darkness of sites to be used as astronomical observatories. There has also been considerable work on developing a model of the night sky based on the contributing light sources, helping to determine appropriate exposure times.

Several studies have been conducted to evaluate the brightness of the night sky at observatories and planned sites, in large part to evaluate the impact of light pollution from growing population centers. Most of these earlier studies (Mattila *et al.* 1996, Leinert *et al.* 1995, Walker 1988, Pilachowski *et al.* 1989, Krisciunas 1990, Kalinowski *et al.* 1975), were

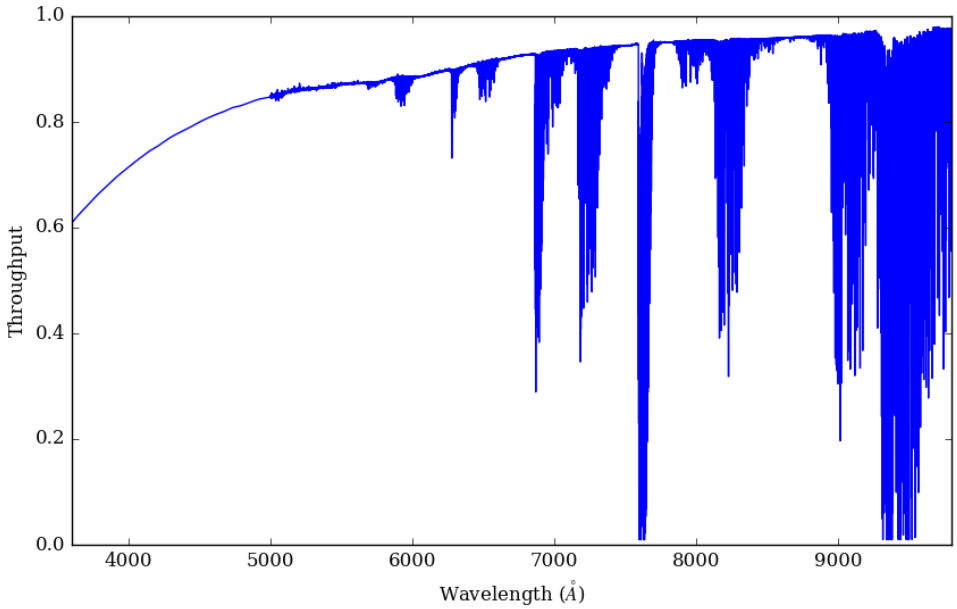

Figure 4.3: KPNO zenith atmospheric throughput. This is derived from the measured extinction (ext), where $T(\lambda) = 10^{-0.4*ext}$.

carried out on small telescopes with photomultipliers, primarily in B and V bands, with Vega used as the reference. The results indicated that there is decent agreement on the brightness of the night sky at the darkest observatory sites in the world, measuring average values of B$\sim$22 mag/arcsec^2 and V$\sim$23 mag/arcsec^2. The duration and number of observations for these studies vary considerably (see table 4.2), but they all report variability in the brightness of the dark night sky on both long and short timescales after correcting to zenith brightness. Below I review these and other night sky measurements, their dependence on specific sources and other parameters, and current available models.

4.2.1 Correlation with Solar Activity

Many published results have observed correlation between the long term variability of the brightness of the night sky and solar activity. The first indication of this correlation came from Rayleigh (1928) and Rayleigh & Jones (1935), who observed that the flux of the OI airglow line (5577 $\AA$) increased with the sunspot number. The solar wind excites more airglow emission, so an increase is expected in both the airglow emission lines and the airglow continuum (see sec. 4.2.5). Rather than using sunspot numbers, more recent programs have found strong correlation with the solar flux density measured at 10.7 cm (Walker 1988, Mattila *et al.* 1996, Leinert *et al.* 1995, Krisciunas 1990, Pilachowski *et al.* 1989, Neugent & Massey 2010). Walker (1988) found that the sky changes as much as 0.8 mag in B and 1 mag in V, and Mattila *et al.* (1996) measured a factor of 1.5 change in flux in the pseudo-continuum (3500-6500$\AA$) over 9 years of observations. Since the sun completes a full cycle in ∼11 years, going from minimum to maximum activity, if a survey lasts long enough it can fully track this correlation (see fig. 4.4). More recent measurements of the difference between solar maximum and minimum measure a value of 0.4 mag (Benn & Ellison 1998b, Pedani 2009). Krisciunas (1997) made measurements over a full sunspot cycle (no. 22) at Mauna Kea, finding that the dark sky brightness during solar maximum is comparable to the sky when a quarter moon is above the horizon. They measure the change in V-band over the solar cycle to be 0.7 mag, but find that the $\langle B-V \rangle$ color is stable, suggesting that much of the change is due to the flux in the OI line that is present in both bands. Measurements covering solar cycle no. 23 were completed by Patat (2008) at Cerro Paranal, finding changes of ΔV = 0.5 mag. Comparing the results from solar cycles 21, 22, and 23, there is some indication that the impacts of the solar activity on the night sky are not identical across solar cycles. Additionally, the mechanism for the solar wind's impact on airglow is still poorly understood. In a study at CTIO, Krisciunas *et al.* (2007) measure a time delay in the activity of the sun of 5 days, corresponding to a solar wind of $\sim$ 350km/s. However, Patat (2008) found best correlation with a time lag of ∼30 days, with differing time delays for specific airglow emission lines.

4.2.2 Dependence on Airmass

The relationship between the brightness of the sky and increasing airmass, or zenith height, is somewhat complicated. As sky measurements are made at higher airmass, light from sources outside the atmosphere encounter a larger scattering cross section, producing higher extinction values. However, more airglow emission is expected to be seen when observing a larger effective area of the atmosphere. Additionally, when observing closer to the horizon, more light from terrestrial sources will be seen if light pollution in the area exists. This additional contribution from airglow in a thin layer at height (h) from the earth (radius R), is described by van Rhijn (1921), as a function of zenith distance (z_D):

$$I(z_D) = I(0)/\sqrt{1-(R/(R+h)^2 sin^2(z_D))}. \tag{4.8}$$

Site	U	B	V	R	I	# Nights	Years	Ref.
San Benito Mt.	–	22.25	23.25	–	–	17	1976 - 1987	Walker (1988)
Kitt Peak	–	22.9	21.9	–	–	12	1986 - 1988	Pilachowski *et al.* (1989)
Mauna Kea	–	22.8	21.9	–	–	~ 75	1985 - 1996	Krisciunas (1997)
McDonald Observatory	–	22.8	21.8	–	–	8	1972 - 1973	Kalinowski *et al.* (1975)
La Silla	–	22.8	21.7	20.8	19.5	40	1978 - 1988	Mattila *et al.* (1996)
Calar Alto	22.2	22.6	21.5	20.6	18.8	18	1989 - 1993	Leinert *et al.* (1995)
San Pedro Martir	22.68	23.10	21.84	21.04	19.36	18	2013 - 2016	Plauchu-Frayn *et al.* (2017)
Mt. Graham	21.20	22.8	21.8	20.8	19.8	23	2008	Pedani (2009)
Cerro Tololo	22.1	22.8	21.8	21.2	19.9	–	1992 - 2006	Krisciunas *et al.* (2007)
Cerro Paranal	22.4	22.7	21.7	20.9	19.6	650	2001 - 2007	Patat (2008)
Cerro Alto	22.4	22.9	22.0	21.4	19.25	~ 6	2004 - 2007	Sánchez *et al.* (2007)
La Palma	22.0	22.7	21.9	21.0	20.0	63	1987 - 1996	Benn & Ellison (1998b)

Table 4.2: UBVRI mag/arcsec^2 measurements from observatories at zenith during dark time.

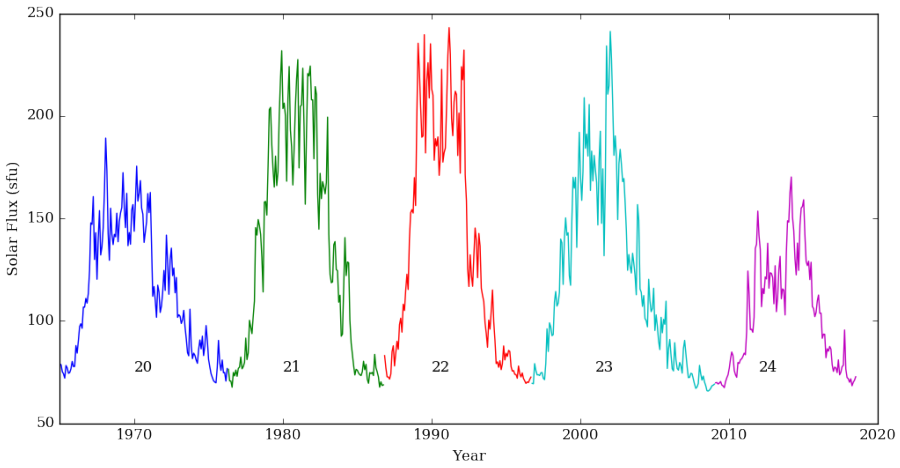

Figure 4.4: Solar activity for cycles 20-24. This is the monthly average data at 2800 MHz (10.7cm) since 1965, measured in solar flux units where 1 sfu = 10^{-22} W/m^2/Hz.

Depending on the fraction of the brightness of the sky that results from airglow, ranging from 50% to 80% depending on the solar activity (i.e., $0.5 < f < 0.8$), the change in the brightness of the sky can be approximated as:

$$\Delta m(z_D) = 2.5\log(f * z_D + (1 - f) * I(0))/I(0). \tag{4.9}$$

It has been observed that even at dark sites with negligible light pollution, the sky increases in brightness by at least 0.1 mag from airmass 1 to ∼1.4 (Leinert *et al.* 1995, Krisciunas 1990), and up to 0.3 mag (Benn & Ellison 1998b, Pedani 2009), consistent with this model.

4.2.3 Zodiacal Light and ISL

Zodiacal light is solar flux that is scattered off interplanetary dust, or, for light $> 4\mu$m, it is absorbed and re-radiated. The zodiacal light intensity is a function of heliocentric latitude ($\lambda - \lambda_\odot$) and ecliptic latitude (β), heliocentric distance, and position relative to the symmetry plane of the interplanetary dust. Leinert *et al.* (1998) models the contribution to the night sky brightness from zodiacal light as:

$$I_{ZL} = (f_R * I(\lambda - \lambda_\odot, \beta) * f_{abs} * f_{co} * f_{SP}) * e^{-\tau(\lambda)}, \tag{4.10}$$

where f_R is the heliocentric distance in AU, f_{abs} gives the wavelength dependence taken from a solar spectrum, f_{co} is a factor that accounts for the redenning of the spectrum in the redder wavelengths, and f_{SP} describes seasonal variations as caused by the location of the observer relative to the symmetry plane of interplanetary dust. This redenning was updated in a study by Aldering (2001) based on additional measurements. The dependence of the zodiacal light intensity on the ecliptic latitude and longitude ($I(\lambda - \lambda_\odot, \beta)$) was measured

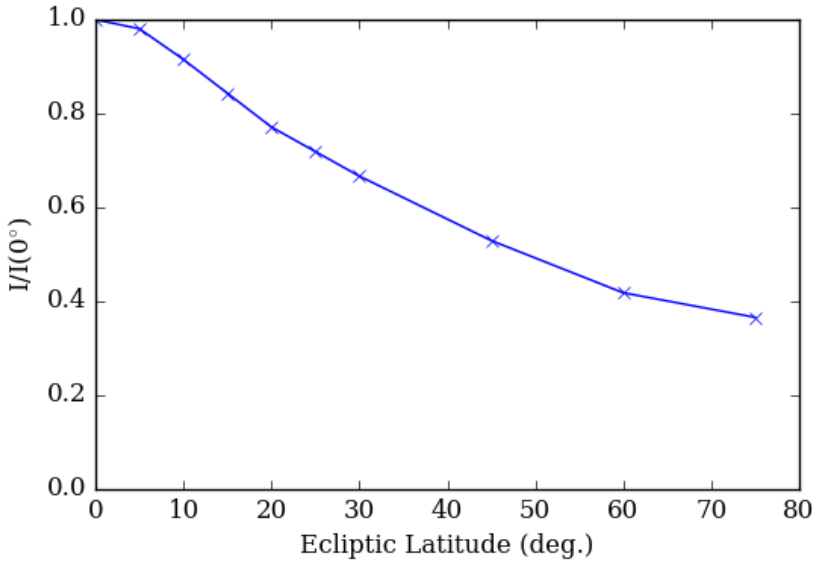

Figure 4.5: Zodiacal light dependence on ecliptic latitude as measured by Levasseur-Regourd & Dumont (1980) at a helio-ecliptic longitude of 180°.

by Levasseur-Regourd & Dumont (1980) at 500nm (see fig. 4.5), which can then be scaled using the solar spectrum. There is an excess of brightness at the anti-solar point called "gegenschein", which is German for countershine. It is caused by the backscattering peak of the scattering function off of interplanetary dust and appears as an oval shape extending $\sim 20°$ around a heliocentric ecliptic longitude of $\sim 180°$. It is believed that annual variations in the zodiacal light of about 10% can be caused by the orbital motion within interplanetary dust (Leinert & Mattila 1998).

The night sky brightness dependence on ecliptic latitude has been verified by many groups (Benn & Ellison 1998b, Mattila *et al.* 1996, Bernstein *et al.* 2002, Patat 2003). In some cases, in order to properly study the impact of the solar flux density, some studies identified the specific contribution from the zodiacal light and removed it. By making observations at several ecliptic latitudes, and using space based measurements of the zodiacal light as reference (Mattila *et al.* 1996, Plauchu-Frayn *et al.* 2017, Levasseur-Regourd & Dumont 1980), it is believed that $\leq 50\%$ of the dark night sky continuum comes from zodiacal light. Therefore, on moonless nights, more than half of the continuum comes from airglow, which is likely why there is such strong dependence on the solar activity.

Integrated Starlight (ISL) is the light from all unresolved stars that makes it into our telescope. Contributions from unresolved stars in the Milky Way is regarded as the third major source of "diffuse" night sky brightness, after airglow and zodiacal light. In the visible, this is dominated by hot stars, white dwarfs and main sequence stars and dependent

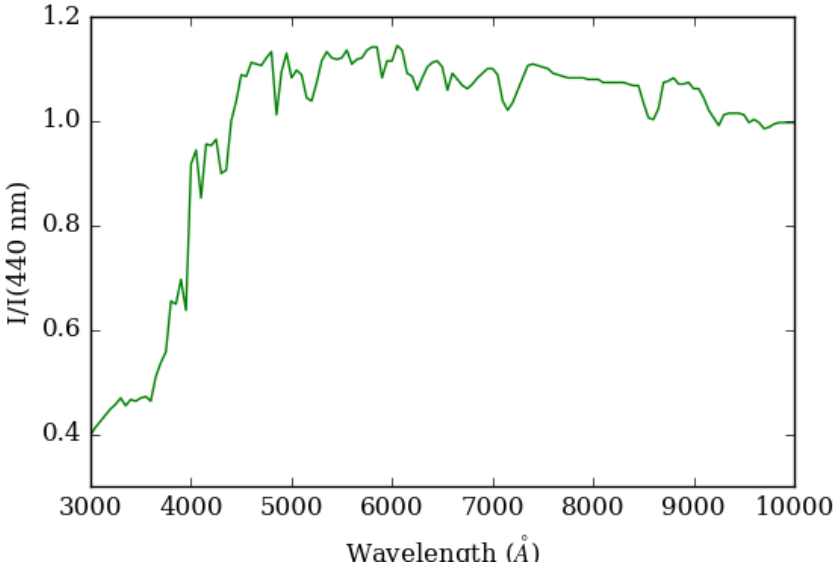

Figure 4.6: Spectrum of ISL from Mattila (1980) normalized to 440nm to be multiplied by the galactic latitude and longitudinal dependent flux from Toller (1981).

on galactic latitude and longitude. This is modeled as:

$$I_{scattISL} = (I_0(l,b) + I_{melchior} \times I_{ISL}(\lambda)) * e^{-\tau_{eff}(\lambda)}. \tag{4.11}$$

In this model from Leinert *et al.* (1998), the galactic latitude and longitudinal (l, b) dependence comes from data from the Pioneer 10 space mission, measured at 440 nm (Toller 1981). The values from the Pioneer data only include starlight from stars less bright than $V = 6.5$ mag, so to include the light from brighter stars, Melchior *et al.* (2007) measured that an increase of ∼16% was appropriate at 440 nm. The spectral dependence of ISL ($I_{ISL}(\lambda)$) was measured by Mattila (1980) as seen in figure 4.6. While many of the more recent models of the night sky include ISL (see Noll *et al.* (2012)), it is generally too dim of a component to really measure in most of these broad-band photometric studies from the ground.

4.2.4 Nightly and Seasonal Variations

Sky brightness variations on shorter timescales (months and throughout a given night) have been measured, with variations of up to 20% observed in a given night. The strength, scale and source of these shorter timescale variations is not particularly agreed upon, however. Zenith dark sky brightness variations on very short timescales (minutes), especially at redder wavelengths, are mostly attributed to the known variability of the OH lines (Leinert *et al.* 1998). Walker (1988) found that the sky got darker during the night by 0.4 mag until 6 hours after twilight, which was confirmed by Leinert *et al.* (1995). This observation has

become known as the *Walker Effect* as few have observed the same strong change. Some have observed decreases in brightness after twilight (Sun altitude $< -15°$) of $\sim$0.1 mag (Benn & Ellison 1998b, Patat 2008), but most sites had no indication of this (Mattila *et al.* 1996, Plauchu-Frayn *et al.* 2017). It is thought that perhaps these variations are due to varying contributions of zodiacal light at high ecliptic latitudes or changes in the release rate of energy in the atmosphere.

Seasonal variations have also been investigated by some, but it requires a sufficiently large data set that most programs did not have. While Benn & Ellison (1998a) didn't see convincing evidence for seasonal variations, they expected to see some broadband changes of $\sim$ 1 mag due to the NaI doublet (5890, 5896 $\AA$), which has been seen to be brighter in the winter than summer (Allen 1973). Actual seasonal variations were detected by Patat (2008) with a data set of $\sim$ 10,000 images on 650 nights over 6 years. They report a periodic modulation over a year with brighter dark sky measurements in Mar./Apr. and Oct./Nov. after correcting for the zodiacal contribution and solar flux dependencies. Patat (2008) suggests that the seasonal variations may be related to solar activity, as analysis of the proton number flux from the sun is both correlated with the brightness of the sky and shows the same seasonal pattern.

4.2.5 Airglow

Airglow is produced when the sun's energy ionizes atoms and dissociates molecules in our atmosphere, which then recombine to create "chemiluminescence". It is related to aurora, which is caused by energetic particles entering the atmosphere. These chemical reactions create strong emission lines as well as a diffuse continuum in some segments of the optical spectrum. The reactions occur in different parts of the atmosphere. For example, the O_2 Herzberg lines in the region 2400 - 3000 $\AA$, the strong OI line at 5577$\AA$, the NaI doublet at 5890, 5896 $\AA$, and the OH Meinel bands all are created at an altitude of 90 - 100 km in the mesopause. The OI lines, 6300 and 6364 $\AA$, and any H-α lines originate at $\sim$ 300 km in the ionosphere (Ingham 1972, Benn & Ellison 1998a). The most prominent airglow lines, and perhaps those most important for astronomy, are NI (5200 $\AA$), OI (5577$\AA$), NaI doublet (5890, 5896 $\AA$), OI lines (6300, 6364 $\AA$), O_2 lines (8605, 8695 $\AA$), and the OH Meinel bands (Meinel 1950), with each band identified by the upper and lower vibration levels (ν) with bandwidths which can have $\Delta\nu = 1$ - 9 (i.e. (9,1) or (6,0)). All lines in a specific OH Meinel band are strongly covariant. Barbier (1956) split all airglow emission lines into "covariance groups", observing that their changes were correlated. These groups consist of the green lines [OI (5577), O_2, airglow continuum in blue], sodium group [NaI D, OH], and the red lines [OI (6300,6364), NI (5200)]. These covariances were confirmed by Patat (2008), who additionally found that the NI and OI 5777$\AA$ were strongly correlated.

It was mentioned above that the solar cycle impact on long scale variations in sky brightness was first observed with the 5577 $\AA$ line. This correlation is also seen with other OI, OII, NI (5200 $\AA$) and NaI doublet lines (Patat 2008, Yee *et al.* 1981). Some of these lines have also shown significant seasonal dependence. Takahashi *et al.* (1984) found that OI 5577 $\AA$

and the NaI doublet lines show a maxima in Apr./May and Oct./Nov., also seen by Patat (2008). See Roach & Gordon (1973) for a comprehensive review of these specific lines and their behavior.

High resolution spectrographs have been turned on the night sky, mostly with the goal of measuring and identifying all airglow lines and providing an atlas for observational planning. The most current of these, and the one currently used in the DESI model, comes from Hanuschik (2003). This night sky atlas was compiled from 44 observations using an echelle spectrograph at the 8.2m VLT at Paranal in Chile, with resolutions from 43,000 - 45,000. Building on work by Rousselot *et al.* (2000), this study extended the spectral coverage to 3400 - 10400 $\mathring{A}$ using publicly available science exposures with the moon below the horizon. While the absolute scale of the final strongly averaged sky spectrum still suffered from some systematic effects and variability from night to night, they found that their results are similar, if not an improvement on, a similar study from Keck (Osterbrock *et al.* 1996). The final data product provided the positions, widths, and fluxes for 2810 airglow emission lines with an average accuracy of 17m$\mathring{A}$ (fig. 4.2).

In addition to the emission lines, some of the airglow processes produce diffuse continuum light. The most ubiquitous of these is caused by collision induced transitions of O_2 producing light from 500 - 9000 $\mathring{A}$ and 7000 $\mathring{A}$ – 2.2μm, and NO_2 producing light from 4000 - 5500 $\mathring{A}$ (Sternberg 1972). While it is difficult to separate the light from these different reactions in astronomical data, laboratory experiments have been able to identify other potential sources of airglow continuum (Evans *et al.* 2011 and sources therein). It is believed that the airglow continuum accounts for more than 50% of the dark night sky inter-airglow line continuum, which also includes zodiacal light and ISL. There are few measurements of it, but a spectrum in the range from 4100 - 8200 $\mathring{A}$, was published by Sternberg & Ingham (1972) with a measured range of values of from $\sim$0.1 - 0.2 $\times 10^{-17} erg/cm^2/s/\mathring{A}/\text{arcsec}^2$ up to $\sim$ 7300$\mathring{A}$. From the $\sim$ 1000 low-resolution spectra from Patat (2008), Noll *et al.* (2012) measured the airglow continuum from 3700 - 8700 $\mathring{A}$ (fig. 4.7). They measured a value of $\sim$0.29 $\times 10^{-17} erg/cm^2/s/\mathring{A}/\text{arcsec}^2$ at 7200 $\mathring{A}$. Both Noll *et al.* (2012) and Sternberg & Ingham (1972) see a bump in the airglow continuum spectrum at $\sim$ 6000$\mathring{A}$.

In addition to creating an airglow line atlas, Hanuschik (2003) also estimated that the continuum flux is roughly constant at 1-2 $10^{-17} erg/s/cm^2/\mathring{A}/arcsec^2$, as can be seen in figure 4.2. This measurement of the continuum doesn't remove the zodiacal and ISL contributions, so is just a mean measurement of the inter-airglow line diffuse continuum light. Besides this estimated continuum flux from UVES, there are few published values of the inter-airglow line continuum. There has been considerable interest in determining the near-infrared brightness (Y, J, H bands), since for instruments that can resolve the OH line forest, faint object spectroscopy is limited by the inter-line sky continuum. The results are reported in a variety of ways, so they are listed in Table 4.3 in flux units ($F_\lambda = 10^{-17} erg/s/cm^2/\mathring{A}$) per arcsec^2, and for those reported in AB magnitudes I use the mean effective wavelength. Sullivan & Simcoe (2012) write that they believe that the measured continuum is dominated by the wings from the line spread functions of instruments, and therefore extremely difficult to actually measure the underlying continuum. This might be the case with H band

Location	$\lambda(\mu m)$	F_λ/arcsec^2	Ref.
Fritz Peak	0.857	0.304 (0.213 - 0.682)	Noxon (1978)
Observatoire de Haute Provence	0.82*	0.682 (0.454 - 0.908)	Sternberg & Ingham (1972)
Cerro Paranal	0.82*	0.65 ($\pm$0.169)	Noll *et al.* (2012)
Magellan	1.02 (Y)	0.99 ($\pm$0.036)	Sullivan & Simcoe (2012)
Magellan	1.22 (J)	1.10 ($\pm$0.030)	Sullivan & Simcoe (2012)
Magellan	1.65 (H)	1.21 ($\pm$0.022)	Sullivan & Simcoe (2012)
Cerro Paranal	1.19	2.00	Cuby *et al.* (2000)
Cerro Paranal	1.7	2.69	Cuby *et al.* (2000)
Gemini	1.67	1.02 ($\pm$0.250)	Ellis *et al.* (2012)
Mauna Kea	1.66	0.704 ($\pm$0.167)	Maihara *et al.* (1993)
La Palma	1.65 (H)	$\sim$0.36	Oliva *et al.* (2015)

Table 4.3: Airglow Continuum measurements. F_λ is measured in $10^{-17} erg/s/cm^2/\mathring{A}$. (*) values are to indicate that these measurements are of only the airglow contribution to the continuum, having explicitly removed all zodiacal light.

measurement by Maihara *et al.* (1993), which is almost double the more recent results, but Oliva *et al.* (2015) found that about 65% of the reported value by Maihara *et al.* (1993) are due to emission features from primarily hot-OH. There are fewer results in the visible. One of the earliest results measured a continuum flux value of measured a flux of 0.304 $\times 10^{-17} erg/cm^2/s/\mathring{A}$/arcsec^2 at 8570$\mathring{A}$ (Noxon 1978), which is considerably lower than the measured values from Sternberg & Ingham (1972).

4.2.6 Terrestrial Light

Terrestrially generated light that is back-scattered off the troposphere is largely from the light pollution from population centers. As cities grow, the light from housing and street lamps can be seen at observatories. Predominantly, the light seen in dark night sky spectra comes from three types of lamps: mercury lamps, high pressure and low pressure sodium lamps. Each of these have a unique spectrum, which was measured by Osterbrock *et al.* (1976). The strongest of these lines are listed in table 4.4. More recently, cities are replacing these lamps with LED lighting, and while they are likely overall less bright, they have broad-spectrum emission impacting the whole spectrum. While increases in brightness from street lights and other terrestrial light sources are expected only when looking towards the horizon, Sánchez *et al.* (2007) measured typical street lamp lines in spectra taken at zenith.

Garstang (1989) developed a model to determine the brightness of the sky of a particular location (observatory) based on the light from cities surrounding that location. This model, estimating the increase in sky brightness at an airmass of 1.4, depends on the population P (# people) and distance D (km) to cities and towns near the observatory, can be simplified

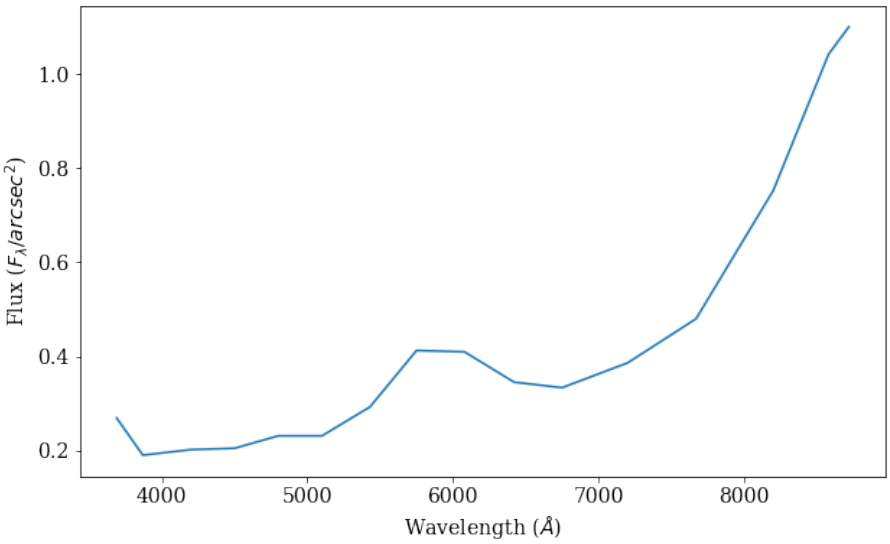

Figure 4.7: Airglow continuum measurements from Noll *et al.* (2012).

Lamp Ref.	Name	Wavelength ($\AA$)
Mercury	HgI	4047, 4048
-	NaI	4165, 4168
Mercury	HgI	4358
-	NaI	4420, 4423
HP Sodium	NaI	4665, 4669
Mercury	HgI	4827, 4832
HP Sodium	NaI	4983
Mercury	HgI	5461
HP Sodium	NaI	5683, 5688
Mercury	HgI	5770, 5791
LP Sodium	NaD	∼5893
LP Sodium	NaI	6154, 6161

Table 4.4: Bright emission lines from typical street lamps. HP and LP stand for high and low pressure respectively, each having unique spectral emission lines.

as (Pedani 2009):

$$\Delta m \sim (PD^{-2.5}/70) \tag{4.12}$$

The model was tested by Pilachowski *et al.* (1989) at Kitt Peak and found that an increase in the B band of ~ 0.06 mag was consistent with Garstang's calculation, but the sky was darker in the V band than predicted. At Mt. Graham, near Kitt Peak, Pedani (2009) found increases of ~ 0.13 mag which is quite a bit higher than Garstang's predicton, likely due to changes in lighting not predicted in 1988. In contrast to Sánchez *et al.* (2007), no broadband evidence of terrestrial light was detected at altitudes above 45° by Plauchu-Frayn *et al.* (2017) and Krisciunas *et al.* 2007). It is clear that observatory sites in proximity to large population centers, especially if there are no local sky protection laws in place, suffer from brighter night sky conditions.

Building on the work on broadband measurements by Pilachowski *et al.* (1989), several decades of spectro-photometric observations were made at Kitt Peak. Starting in 1990, Massey *et al.* (1990) first obtained spectro-photometry of the night sky during dark time, pointing at a variety of azimuths and zenith angles to test the contribution from terrestrial sources. In addition to taking measurements at zenith, they looked toward four locations on the horizon when the moon was below the horizon at a zenith angle of 60°: Tucson (64°), Phoenix (340°), Nogales (142°), and "Nowhere" (180°). The spectra were taken from 3800 - 6500 $\AA$, giving spectrophotometric measurements for the B and V bandpasses. One decade later, this study was completed again to track the impact of the growth of Tucson and Phoenix. Massey & Foltz (2000) made 10 measurements very similar to those made in 1989 and found that while the brightness of the sky had increased in the last decade, the increase was minimal relative to the growth of the population centers. They measured that the sky brightness had increased 0.5 mag/arcsec^2 towards Tucson and less than that in other directions.

The study was conducted again a decade later when Neugent & Massey (2010) took 30 measurements throughout the year during dark time. They showed that the night sky had stayed mostly constant over the two decades from 1990 - 2010, and in fact was somewhat darker toward Tucson in 2010 that in 2000, likely due to effective lighting ordinances. Since the data of these three studies spanned a couple solar cycles, they were able to test the impact of solar flux on the dark sky brightness. It is likely that some of the brightening seen from 2000 to 2010 is due to the solar cycle, as 2000 was during a solar maximum and 2010 was during a solar minimum. Table 4.5 shows the broadband measurements taken from their spectra from these three studies at both zenith and towards Tucson at a zenith angle of 60°. The table also includes the adjusted values when accounting for solar flux by averaging over the solar flux during the month observed and scaling the flux using the assumption that the sky changes by ~ 0.4 mag from solar minimum to maximum. All of the synthetic broad band magnitudes are calculated after removing the bright OI 5577$\AA$ line, replacing 17$\AA$ on each side of the line with an average value. This study also showed some dependence of the sky brightness on the seasons, showing that the sky is brighter during the winter months than the rest of the year.

Year	Azimuth	V	B	Solar Phase	V′	B′
1988	Zenith	21.95	22.84	0.29	22.07	22.96
	Tucson	21.63	22.71		21.75	22.83
1999	Zenith	21.72	22.67	0.57	21.95	22.90
	Tucson	21.14	22.20		21.37	22.43
2009	Zenith	21.95	22.79	0.00	21.95	22.79
	Tucson	21.46	22.50		21.46	22.50

Table 4.5: Brightness of Night Sky above Kitt Peak from 1989 - 2010 in mag/arcsec^2. The highly variable OI line (5577 $\AA$) was removed for these synthetic B and V-band brightness. The measurements towards Tucson were taken at an altitude of $\sim 30°$. Prime values are for solar flux corrected values where the magnitudes were scaled under the assumption that the sky brightness changes by ~ 0.4 mag from solar minimum to solar maximum with the solar phase representing the time to solar minimum.

4.2.7 Moonlight

Many of the studies mentioned above took observations in only dark times with the moon below the horizon. Walker (1987) made some measurements of the sky when the moon was above the horizon, but still separated by 90° from the observation. At Mauna Kea, Krisciunas (1990) made 21 observations of the sky with the moon in the V-band, finding that the Walker (1987) results defined a lower envelope and determining that the amount of scattered moonlight observed is a "complex function of the moon's phase, elevation angle, and angular distance on the sky between the moon and position where the sky brightness is measured (...)" Adding about a dozen more observations to this data set, Krisciunas & Schaefer (1991) attempted to determine that complex function, as described above in §4.1). Their moon model, the most used model since being published, predicts the moonlight brightness with an accuracy of 8-23%. While this model only gives the B band brightness, Noll *et al.* (2012) showed that it can be converted to a spectrum using a site's specific extinction curve. This model was extended by Jones *et al.* (2013) using spectra from Patat (2008), for which 141 spectra of the observations occurred with the moon above the horizon, comprising 26% of the full data set. After subtracting the zodiacal light using the prescription in Leinert *et al.* (1998), they used 3D single scattering calculations to provide a scattered moonlight spectrum. They start with a solar spectrum and apply an albedo model:

$$I^* = I_{sol} \frac{\Omega_M}{\pi} A \left(\frac{384,400}{M_{dis}} \right)^2 \tag{4.13}$$

where Ω_M is the solid angle of the moon (6.4177×10^{-5} sr), M_{dis} is the distance to the moon (384,400 is the average), and A is the albedo model as developed by Kieffer & Stone (2005)

using data from the ROLO survey. After applying the single scattering calculations (see Wolstencroft & van Breda (1967) and Staude (1975)), the scattered moonlight as observed at a given target azimuth (Az_0) and zenith distance (z_0) is:

$$I_{scatt}(\mathrm{Az}_0, z_0) = \frac{C_{scatt}(\lambda)}{4\pi} \int_0^{s_2(z_0,\sigma_0)} n(\sigma)P(\theta) \times I^*(\mathrm{Az}_M, z_M)e^{-\tau}ds \tag{4.14}$$

In this equation, $n(\sigma)$ is the column density and $P(\theta)$ is the scattering phase function ($P(\theta) = 3/4 * (1 + cos(\theta)^2)$ for Rayleigh scattering). C_{scatt} is the scattering cross-section, which is equal to the extinction cross section C_{ext}, unless absorption occurs, where

$$C_{ext}(\lambda) = \frac{\tau_0(\lambda)}{\int_0^{s(z=0,\omega)} n(\omega')d\omega'} \tag{4.15}$$

4.2.8 Twilight

Astronomical observations typically occur after "astronomical twilight", when the sun is more than 18° below the horizon. This level of twilight is differentiated from nautical twilight at 12° and civil twilight at 6° below the horizon. The scattered sunlight during twilight can significantly impact the brightness of the sky. Modeling the scattered light can be challenging, however, because there are multiple scattering effects in place. Few astronomical measurements have been made of the twilight, but in expectation of new observatories at the high latitude Dome C site in Antarctica, new interest has arisen. Patat *et al.* (2006) modeled the UBVRI brightness as a second order polynomial:

$$m = a_0 + a_1(\alpha - 95) + a_2(\alpha - 95)^2 \tag{4.16}$$

where m is the surface brightness in mag/arcsec^2, α is the sun zenith distance in the range $95° \leq \alpha \leq 105°$ and the coefficients are fit for each band and listed in table 1 of Patat *et al.* (2006).

4.3 BOSS Sky Spectra

The Baryon Oscillation Spectroscopic Survey (BOSS) is the largest spectroscopic redshift survey to date. As discussed in Section 1.3.1, the BOSS survey, which ran as part of SDSS-III, used upgraded SDSS (Sloan Digital Sky Survey) spectrographs. These spectrographs are installed on the Sloan Foundation 2.5m Telescope at APO located in southern New Mexico. While the optical design remained mostly the same, the size of the fibers was reduced to 120μm so that 1,000 fibers could be fit over the 3° field of view of the telescope. The two BOSS spectrographs, each having a red and a blue arm, have VPH grisms with updated detectors covering a wavelength range of 360 - 1040 nm. The fibers were plugged into aluminum plates pre-drilled for selected targets. Fibers 1-500 fibers went to the first

spectrograph, and fibers 501-1000 were sent to the second spectrograph (Smee *et al.* 2013). BOSS targeted two main classes: large red galaxies at z ∼0.6 (CMASS) and lower redshifts of z < 0.4 (LOWZ), and quasars from z > 2.1 that were used as backlights of the lyman-α forest. The survey ran for five years (2009-2014), with the final data release (DR12) including spectra from ∼1.7 million galaxies and quasars (Alam *et al.* 2015).

The survey target area consisted of ∼2500 unique plates (tiles) used in ∼13,500 observations. Up to 9 plates per night, prepared months ahead of time, were plugged and then mapped to identify each fiber. Each individual spectrum was specified by the plate number, MJD (Modified Julian Date), and fiber number. For each observation, a minimum 80 fibers were drilled to look at empty sky, measuring the sky background primarily for sky subtraction. There were ∼1 million unique sky spectra taken over the five years of the survey. Each exposure was 900 seconds, providing us a large, uniform, well-calibrated data set to study the night sky.

The large spectroscopic data set of sky observations from the 5 years of BOSS gives us a unique opportunity to test and confirm the observational models described above. It also gives us the first published spectra of the night sky above APO, useful for comparing to the other top observing sites in the world. In some cases, since the BOSS data set is so much larger than others described here, we can possibly create higher fidelity models of the mean sky behavior and its variations. Together with our knowledge of the terrestrial light sources at Kitt Peak, we can create a predictive model to be used for DESI planning.

4.3.1 Overview of Data

A total of 2475 plates covered the BOSS footprint. The plate drilling was based on the RA/DEC of the tile center, the locations of each of the 1000 targets, and hour angle (HA) planned for the exposure. Each plate required no fewer than 3 exposures of 900 seconds to reach the required SNR. While it was a priority to finish a plate in a given night (3+ exposures), that was not always possible, and the plate would be observed on subsequent nights without replugging the fibers. This resulted in 13,634 unique observations taken over ∼ 800 days from 2009 - 2014. Each plate was split in half, with the first half-plate containing 500 fibers that went to the first spectrograph ('b1','r1') and the second half-plate going to the second spectrograph ('b2','r2'). For each half-plate, no fewer than 25 fibers were drilled to look at dark sky, with an average of 90 per plate.

Some observations were identified as "bad" and were re-observed at a later time. They were identified as such for a variety of reasons:

- used as a commissioning plate
- no good flats
- out of focus
- plate re-drilled for new HA
- new fiber plugging needed
- plate set for a specific year but not finished (< 3 observations)

- repeat tile
- coma on a spectrograph
- used as astrometric plate with bright stars

All observations labelled as bad were removed from the data set. Additionally, we removed other observations from three plates that were initially marked "good" for the following reasons: sky fiber test plate, second spectrograph wasn't working, and the observation was forced to complete before ready. All of those removed account for 538 observations.

For each observation, the pipeline identifies bad pixels that are major outliers in a plate or were effected by cosmic rays. We reject any pixels that have the following identifiers. In the case of some of these, the whole spectrum is rejected.

- BADFLAT: The flat-field contains less than half the light expected from neighboring fibers at the same wavelengths. Occurs for unplugged or damaged fibers
- BADSKYFIBER: The sky fiber spectrum is not consistent with other sky fibers on the plate and has been removed from the sky model vectors.
- FULLREJECT: The extraction has rejected at least 60% of the pixels for this fiber at a given wavelength.
- PARTIALREJECT: The extraction has rejected at least 20% of the pixels for this fiber at a given wavelength.
- NOPLUG: Fiber was not properly mapped.
- BADTRACE: The spatial trace of the fiber on CCD encountered an error so spectra may have lowered flux values and unreliable error estimates due to uncentering
- NOSKY: No sky spectra at a given wavelength, typically at the extreme blue and red wavelengths.

After rejecting these pixels we have a total of 2448 unique plates with 13,055 observations. Our final data set has ∼1,200,000 individual sky spectra ranging from 360-1040 nm.

These represents a uniform data set covering a wide range of observations parameters. Figure 4.8 shows the number of sky spectra measured over 5 years of BOSS. The spectra marked as "dark" were taken when the observation was taken in an airmass of less than 1.4, the moon is below the horizon, the sun is at least 15° below the horizon, and the target is more than 10° from the galactic plane. As seen in figure 4.9, the BOSS observations cover all altitudes above 50° with some down to 30°. The majority of the BOSS observations occurred with the moon below the horizon and sufficiently after twilight, but figure 4.10 shows that the data set contains some spectra that enable us to test scattered moonlight and twilight models.

BOSS provides an excellent opportunity to probe the impact of solar activity on the brightness of the night sky as the observing time covered half of solar cycle 24. Figure 4.11 shows the measurement of the solar flux as daily measurement made at the Dominion Radio Astrophysical Observatory (DRAO) in Penticton, British Columbia and Ottawa of the solar

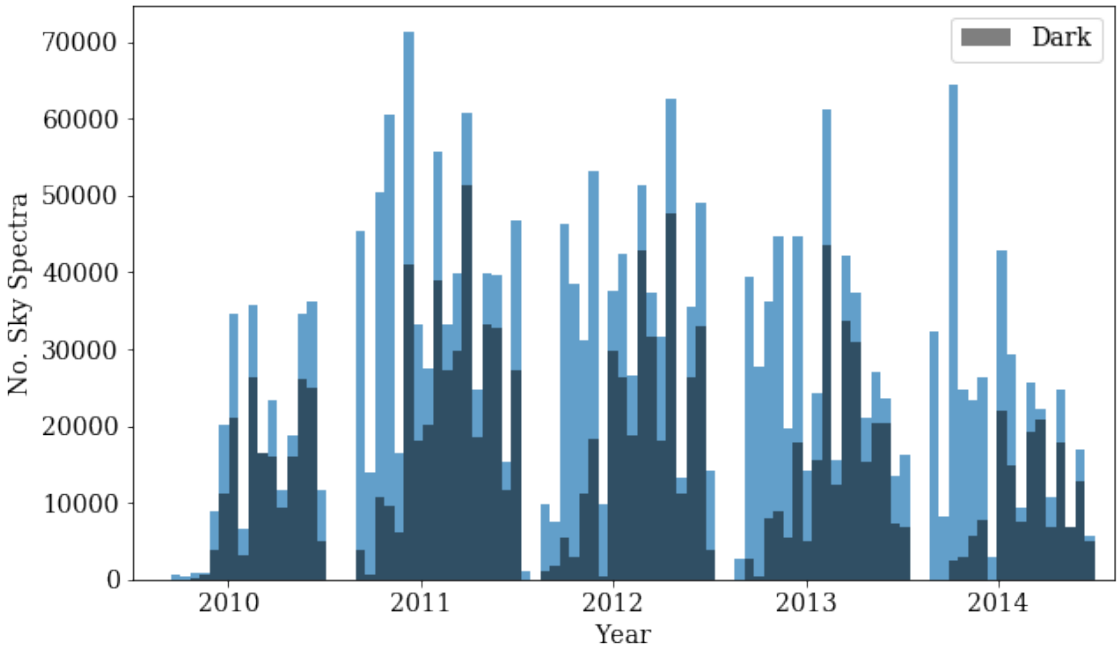

Figure 4.8: Distribution of sky spectra during the BOSS survey from 2009 - 2014. The dark time observations are when airmass < 1.4, moon altitude $< 0°$, sun altitude $< -15°$, and galactic latitude $> 10°$.

flux density at 2800 MHz[2]. This solar flux originates from the sun's chromosphere and is sensitive to the number of sunspots. Its value, which changes day-to-day, is an excellent measure of the sun's overall activity. The red points in figure 4.11 identify the sampling of this solar flux for the dates corresponding to BOSS observations, covering half of solar cycle 24 and a range of solar activity.

As discussed in section 4.2.3, the brightness of the night sky is also very dependent on zodiacal and integrated starlight. These depend on the ecliptic and galactic latitude and longitude respectively (fig. 4.12). The BOSS data set maps out most of the sky, although we don't have sufficient data to study the anti-solar point (gegenschein). Additionally, our ability to probe shorter time scales is quite good with this data set. We have many measurements in each month to help identify any dependence on season, and ~ 30 observations are taken throughout a night (fig. 4.13). Often these measurements were not taken at the same airmass or location on the sky, but correcting for these we can determine how the night sky changes during a night at APO.

[2]Daily values at ftp://ftp.geolab.nrcan.gc.ca/data/solar_flux/daily_flux_values/fluxtable.txt

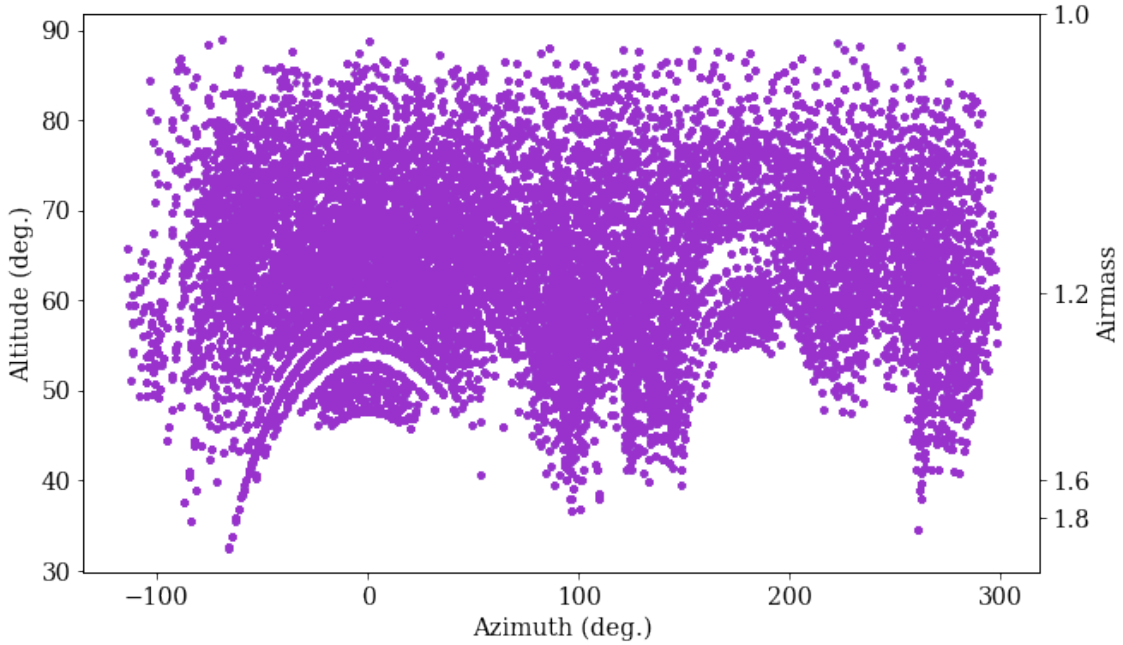

Figure 4.9: The altitude and azimuth of the measurements made during the BOSS survey. Airmass is related to altitude by $X = (1 - 0.96 * \sin^2(90 - \text{Alt})^{-0.5}$

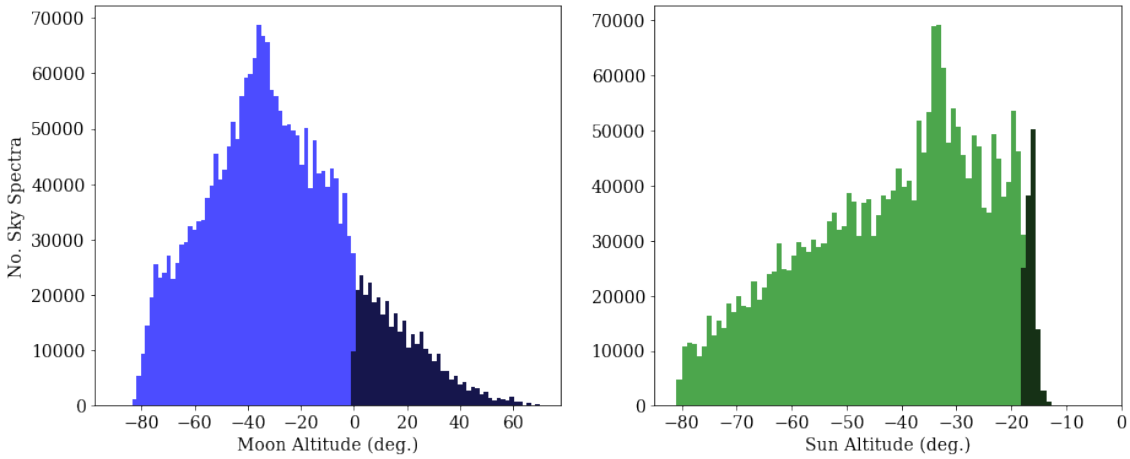

Figure 4.10: Moon and Sun altitude for BOSS observations. Darker sections for when moon altitude is above horizon and when the observation is before or during twilight.

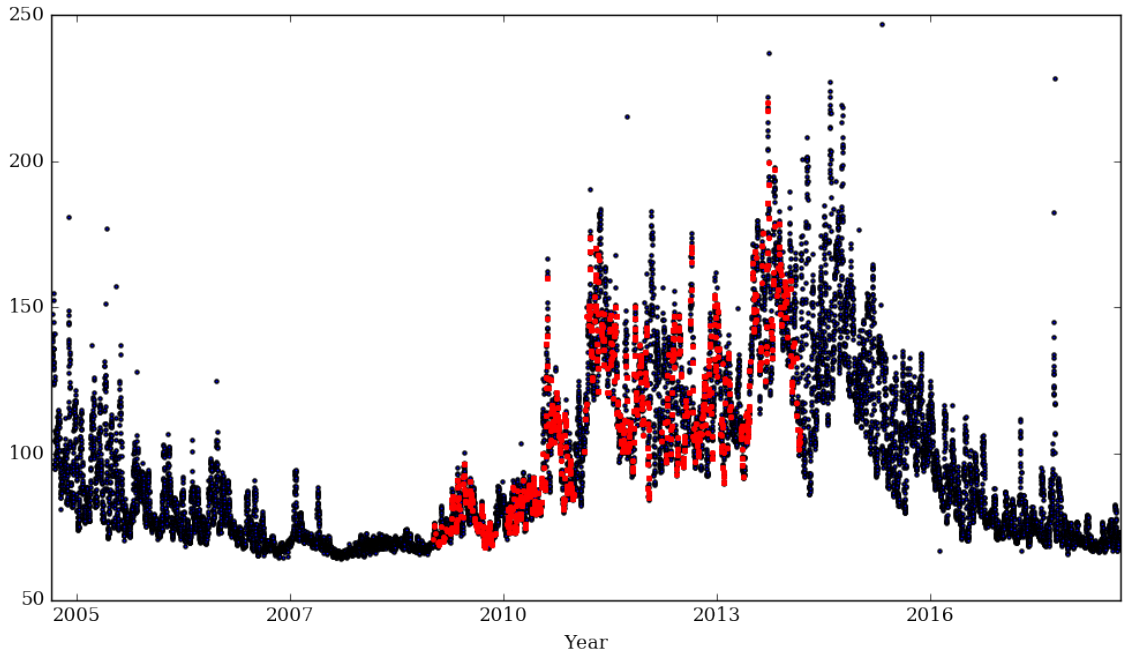

Figure 4.11: Daily measurements of the solar flux for solar cycle 24. The red points are those solar flux measurements taken during the day of a BOSS observation, sampled in this analysis.

4.3.2 Cloud Data

There is a mid-infrared all sky cloud camera (IRSC) at APO continuously taking thermal-IR images at 10μm (Hull *et al.* 1994). These wide field images (135° × 135°) were used during SDSS-III to determine the photometricity of the sky as a function of time. An example image of a cloudy night is shown in figure 4.14. Analysis of the images through a night was used to identify periods of time that were cloudy or clear (Hogg *et al.* 2001). Approximately every 15 minutes, they would find the mean variance of all the sky images taken during that time period. If the variance was below a specified threshold, the time segment was considered photometric. Using this identifier, we can determine the effect of clouds on the brightness of the sky, splitting our data set into photometric and non-photometric observations (fig. 4.15).

4.3.3 Flux Calibration

In general, flux calibration contains all steps to convert electron counts on the detector to useful units describing the flux from the target as a function of wavelength. The main steps are to remove pixel-to-pixel and fiber-to-fiber variations, apply a wavelength solution, and then remove atmospheric extinction and solve for the fiber acceptance ratio based on the

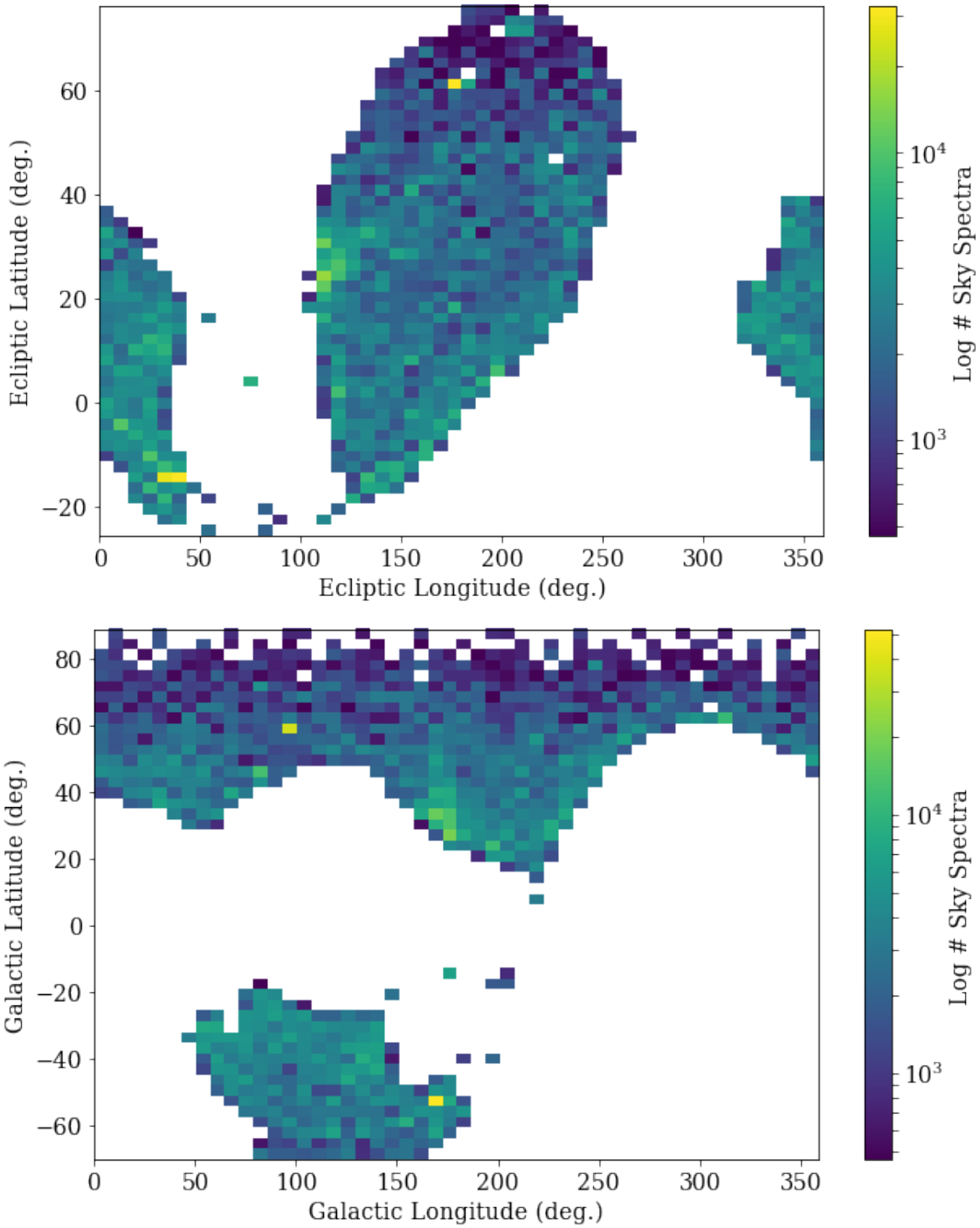

Figure 4.12: **Left**: Map of the BOSS observations as a function of their ecliptic latitude and longitude, which is correlated with zodiacal light. **Right**: Map of the BOSS observations as a function of their galactic latitude and longitude which is correlated with ISL.

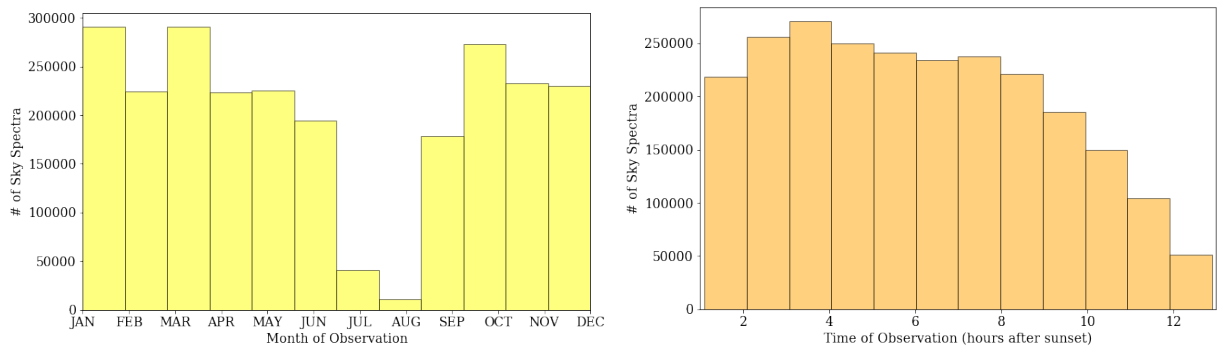

Figure 4.13: **Top:** Distribution of sky spectra throughout a year, which can be used to determine the relationship between night sky brightness and the season of observation. The lack of data in August is due to shutdowns for dome work during the monsoon season. **Bottom:** Distribution of sky spectra throughout a night plotted as hours after twilight, which helps us study the short timescale variations in the sky brightness.

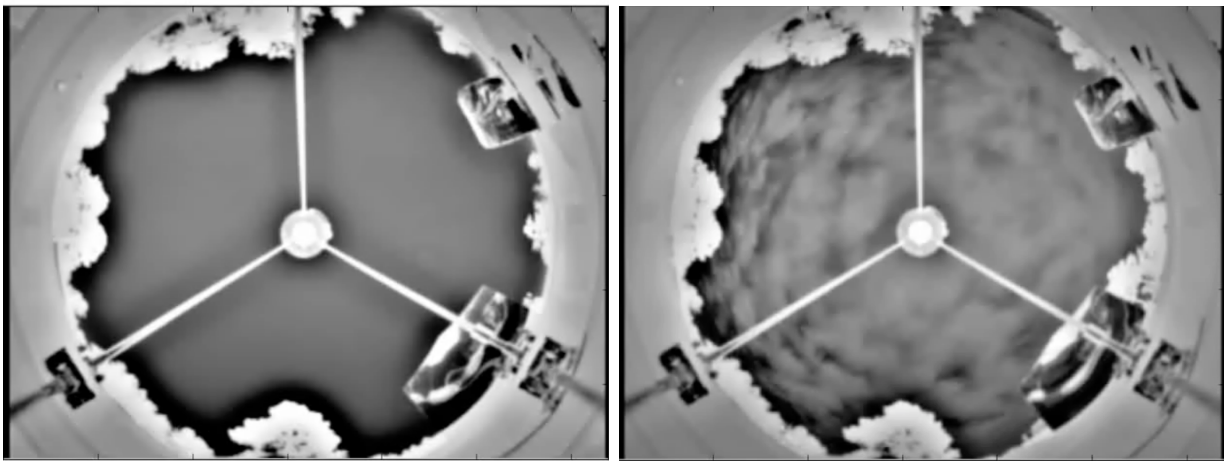

Figure 4.14: **Left:** Image taken with the APO IRSC at 10μm under clear conditions. **Right:** Image taken during cloudy conditions.

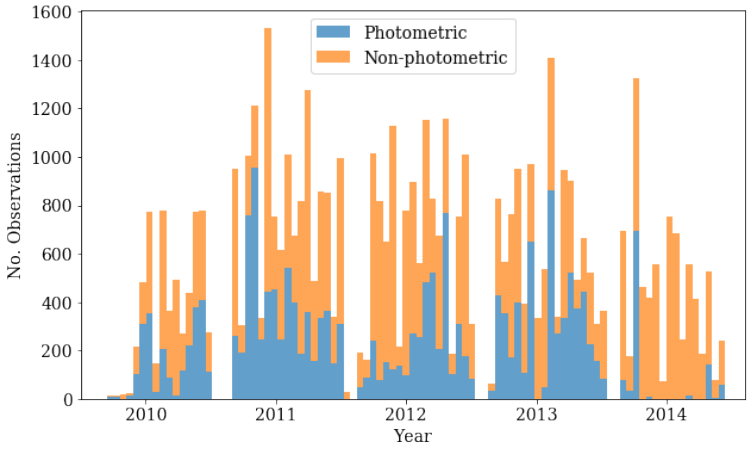

Figure 4.15: Distribution of photometric observations during BOSS survey.

seeing. After the target exposure is completed, the pipeline would run the analysis using the calibration data appropriate to the given science exposure. A single IDL script was responsible for converting the raw data into a FITS file with a header, a 4096×4096 floating point data image, and a corresponding inverse variance image. To get to this point, the amplifier bias was subtracted and then the inverse gain was multiplied to convert from ADU to electrons. The variance was calculated as:

$$\mathrm{Var}_i = e_i + RN^2 + (0.01 \times e_i)^2 \tag{4.17}$$

where e_i is the gain corrected data in a pixel, RN is the read noise, and the final term accounts for the 1%-level multiplicative uncertanties in the per-pixel flat-field response of the CCDs. The calibration pipeline had to be run separately for each spectrograph due to slightly differences in the camera optics and CCDs.

Each observation started with flat-fielding to correct pixel and fiber variations. To do this, there are 8 flat field petals at the top of the telescope that can be illuminated with either broadband quartz lamps or several arc lamps, further discussed in §4.3.4. The flat field frames were optimally extracted, using a gaussian profile and polynomial for scattered light. The arc lamp frames were used to create a wavelength solution so the spectra could be normalized and stacked to create a "superflat" for each camera of each spectrograph. The superflats were then resampled and fitted to the ratio of the extracted spectrum of a fiber to the superflat, creating fiber-flats for each plate. The image and inverse variance were then corrected by both superflats and fiber-flats. These "flattening" corrections are of order unity as all variations are very small. The superflats corrected for pixel-to-pixel variations of 0.3% RMS and the fiber-flats accounts for $\sim 5\%$ RMS variations from fiber to fiber.

The sky fibers were combined to generate a 2-dimensional model of the sky vs. wavelength as a function of fiber number. This sky model was then subtracted from each fiber spectrum, leaving us with sky-subtracted target spectra in units of flat-fielded electrons,

which are saved as spFrame-cc-eeeeeeee.fits, where cc is for the camera ['b1','r','b2','r2'] and the identifier e is for the unique image or exposure number[3]. The **spFrame** file contains both the sky-subtracted flat-fielded electrons (HDU[0]) and the sky spectrum subtracted (HDU[6]), as well as the inverse variance (HDU[1]), wavelength solution as a trace set (HDU[3]), the fiber plugging solution (HDU[5]), and the pixel mask (HDU[2]).

The final data product for BOSS spectra is the flat-fielded electron flux converted to physical flux densities as observed above the atmosphere. Each plate observed $\sim$ 16 spectrophotometric standard stars, low-metallicity F star sub-dwarfs in this case. The calibration from counts to flux density includes the throughput of the telescope and instrument and the acceptance of light within the fiber, without disentangling those various terms. This calibration file was saved as **spFluxcalib**, identified by camera and exposure number with a single vector as a function of wavelength. In order to co-add or compare spectra from multiple exposures requires consistency in the spectrophotometry, so for each plate, the "best" exposure was selected and all spectra were remapped to that using a multiplicative vector per fiber. These correction files are saved as **spFluxcorr** for each camera and exposure, with values of unity for the best exposure or a vector per fiber for all other exposures. Remaining spectrophotometric errors due to large spatial scale centering and guiding errors were saved in **spFluxdistort** files for each day of observation (plate/MJD).

Due to optical distortions, the pixel scales are not consistent across wavelength or fiber number. Each spectrum is re-sampled to the same wavelength grid using a B-spline of order 3 with a break point density of 1.2 times the final wavelength sampling. The final sampling is uniform to log-wavelength with a dimensionless spacing of R $= 10^{-4}/binsize$, corresponding to $10^{-4} \times c \times \ln(10) = 69.029764$ km/s. For each observation, the spectrophotometric flux in units $10^{-17} erg/s/cm^2/\mathring{A}$ for each fiber subtending π arcsec^2 ($\varnothing$ 2 arcsec) was saved as a **spCFrame** file, identified by camera and exposure number. This flux was computed by:

$$\text{spCFrame(flux)} = \text{spFrame(ff}e^-) \times \frac{\text{spFluxdistort} \times \text{spFluxcorr} \times \text{R}}{\text{spFluxcalib}} \tag{4.18}$$

where the calibration vector is the inverse of the **spFluxcalib** file and ffe^- is flat-fielded electrons.

The BOSS data products are designed to recover accurate spectrophotometry for point sources. This approach to calibrating flux is designed to recover the total flux of point sources despite fiber acceptance losses, and therefore increases the apparent surface brightness of the sky within the 2-arcsec diameter fibers. Since the sky flux should be treated as a surface brightness, rather than the flux from a specific object, we do not want to implement these flux correction steps for this project. I have re-analyzed these data to recover accurate spectrophotometry on surface brightness (like the night sky), under the assumption that the telescope and instrument response is reasonably constant over the five years of observation. For this study we use a single calibration vector to convert flat field electrons to flux and do

[3]See the data model at: https://dr13.sdss.org/datamodel/files/BOSS_SPECTRO_REDUX/RUN2D/PLATE4/spFrame.html

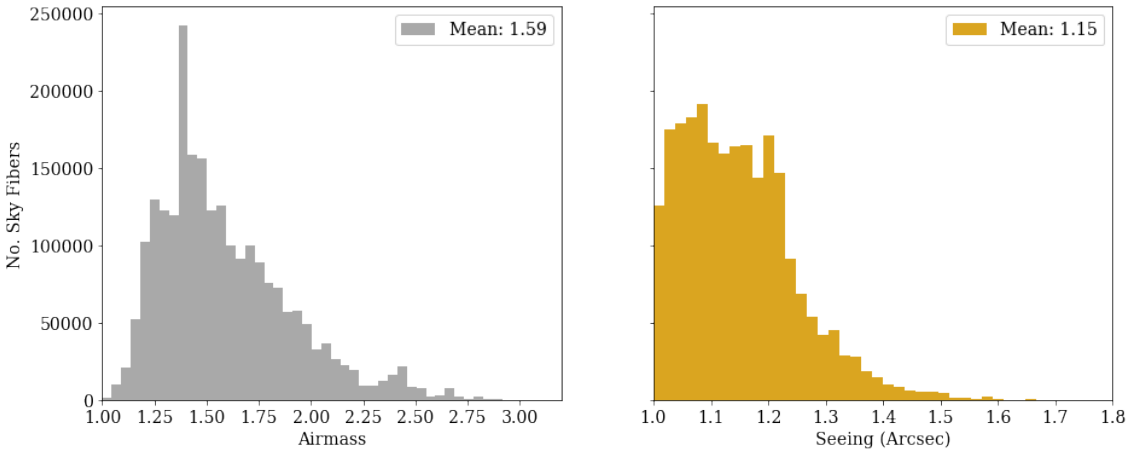

Figure 4.16: Distribution of seeing and airmass for BOSS observations

not include the flux corrections (**spFlucorr** and **spFluxdistort**). We define spCalib(Plate = 3985, Exposure = 114439) as this flux calibration vector, taken from a night with very good seeing (1.0673 arcsec) and low airmass (1.0043), minimizing any adjustment to the flux due to seeing and extinction. From figure 4.16, it's clear that this is one of the best observing nights from the BOSS exposures. If we model the PSF as a gaussian and assume the standard star used for the calibration is centered on the fiber, 97.3% of the flux will make it into the fiber, with some light scattered into the wings, which can be calculated back in. For the fibers looking at blank sky identified as 'SKY', the sky-subtracted flux (spFrame HDU[0]) is just the residuals from the sky subtraction. Therefore, to get a measure of the total flux from the sky background, we add this back in to the sky flux saved in spFrame HDU[6]. To get our final flux calibrated sky spectra in $10^{-17} erg/s/cm^2/\AA$ we perform the following calculation:

$$\text{SkyFlux} = (spFrame[0] + spFrame[6]) \times \frac{R}{spCalib(3985, 114439)} \times 1.027 \tag{4.19}$$

We converted the flux for each sky spectrum (∼1.2 million) in our BOSS data set using this approach, giving us the surface brightness of the sky over a range of 360 - 1040 nm with minimal flux calibration errors.

4.3.4 Airglow Line Fitting

The inter-airglow line continuum sky background is not always impacted in the same way or by the same phenomena as the airglow emission lines. For this reason, we are interested in studying the behavior of the continuum independently. This is fairly straight forward to do in the blue part of the spectrum as there are few airglow lines, but becomes increasingly challenging as you move to the redder wavelengths. For the OH Meinel bands in particular,

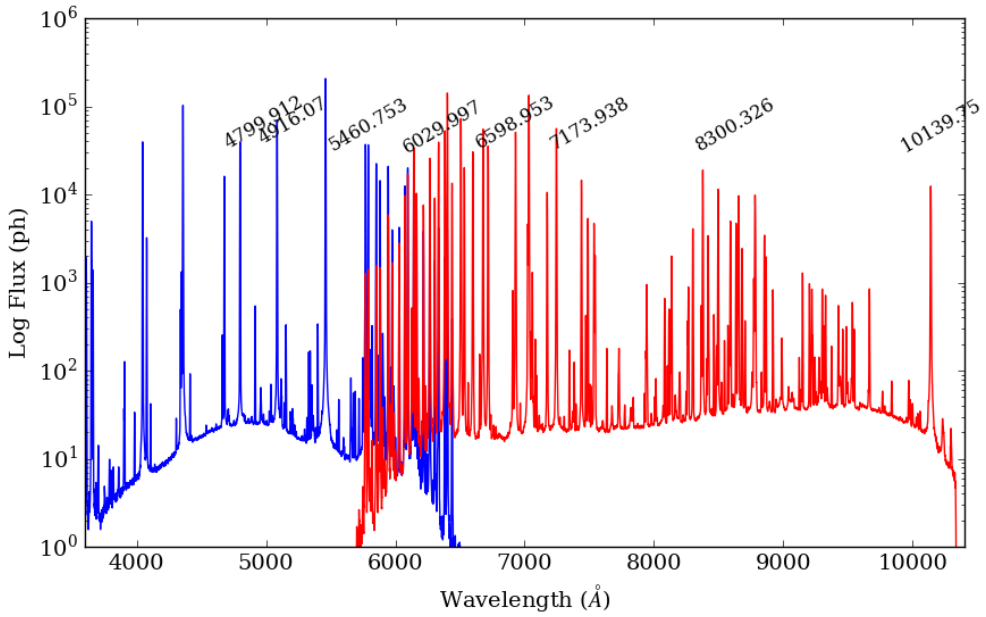

Figure 4.17: Sample BOSS arcline spectrum. Identified are several bright lines well separated from others which were used to model the line spread function. The blue spectrum is from the blue detector on the first spectrograph and the red is from the red detector from the same spectrograph.

the line spread functions of individual lines overlap. In order to model and then remove all the lines from our spectra, we used the arc lamp spectra used for wavelength calibration because they have very high signal to noise with essentially no background. The arc lamps include Mercury, Cadmium, and Neon with trace amounts of Argon. They produce 45 distinct lines in the blue and 65 in the red, and some of these are separated well enough to model the line spread function of the BOSS spectrograph (see fig. 4.17).

The point spread function (PSF) measured on the detector is the PSF of the camera optics and entrance aperture convolved with scattering from the diffraction grating. We use "line spread function" to describe the part of the PSF in the wavelength direction on the detector. In other words, the line spread function describes the width of a monochromatic point source in the wavelength direction. The PSF of the BOSS spectrographs can be well approximated as a gaussian, which is essentially the cross-sectional shape of the fiber convolved with the entrance aperture. The scattering due to the VPH diffraction gratings can be derived from the equation that describes the diffraction from N slits, adopted for a grating. Woods *et al.* (1994) measured the scattered light properties of several diffraction gratings and they found that the appropriate scattered light profile can be expressed as a simplified version of that

equation:

$$\begin{aligned} Y_{fit} &= \left[\frac{sinc(b)}{sinc(b_0)}\right]^2 \frac{0.5}{N_{eff}^2 sin^2(a)} + C \\ a(\lambda) &= \pi(\lambda/\lambda_0) \\ b(\lambda) &= \pi \frac{\lambda - \lambda_{blaze}}{\lambda_0} f \end{aligned} \tag{4.20}$$

where b_0 is the value of b at λ_0 which is the reference wavelength for the grating, λ_{blaze} is the blaze wavelength where maximum efficiency is achieved, f is the ratio of the groove width to spacing and C is a constant background term. For this model, N_{eff} is the effective number of grating grooves that are illuminated with no imperfections.

The above equation can be further simplified as a Lorentzian function, which is the final model developed for VPH gratings by Woods *et al.* (1994). The line spread function for the IRIS2 grism spectrograph and the AAOmega VPH spectrometer fit well to a function of a gaussian plus a lorenztian (Ellis & Bland-Hawthorn 2008). We have taken a similar approach to fitting the BOSS arclines. If we model the line spread function as only a gaussian function, we find that 25% of the total line flux is outside the core (greater than FWHM of gaussian) (see fig. 4.18). Not only does the model require a description of the scattered light in the wings, but the core is actually best modeled as the sum of two gaussian functions, separated by $\sim 1\mathring{A}$. As the core is essentially the convolution the cross-sectional shape of the fiber (top-hat function) with a circular aperture, this is not surprising. The core is then convolved with a lorentzian function to account for the scattering from the VPH diffraction grating, having a form similar to that used by Woods *et al.* (1994). The line spread function has nine free parameters: three for each gaussian, two for the lorentzian, and a constant background term (D):

$$I(\lambda) = \left[A\, e^{-(\lambda-(\lambda_0+\delta_a))^2/2\sigma_a^2} + B\, e^{-(\lambda-(\lambda_0-\delta_b))^2/2\sigma_b^2} * C\, \frac{\mathrm{w}^2}{(\lambda-\lambda_0)^2+\mathrm{w}^2}\right] + D \tag{4.21}$$

with $\delta_{a,b}$ being the offset from the reference wavelength (λ_0), $\sigma_{a,b}$ is the standard deviation of the gaussian function, and $\mathrm{w} = \frac{\lambda_0}{N_{eff}} \frac{1}{\sqrt{2}\pi}$. See figure 4.19 for example fits for a line in both arms of the spectrograph, which were all performed using the non-linear python fitter *lmfit*[4].

For all arc line fits across the wavelength range, one gaussian is $\sim 0.85\mathring{A}$ above the center wavelength and the other is below the center wavelength by $\sim 0.6\mathring{A}$. Both have $\sigma \approx 1$ with amplitudes that scale with the total flux quite similarly. The amplitude of the lorentzian function also increases mostly linearly with a given value of N_{eff} except with lines of small total flux that have fairly small scattering wings. The non-linear fits didn't settle on a single value for N_{eff}, but there were a range of values depending on the amplitude of the lorentzian (see fig. 4.20). Using the fits of several arc lines from several unique observations, we found

[4] https://lmfit.github.io/lmfit-py/

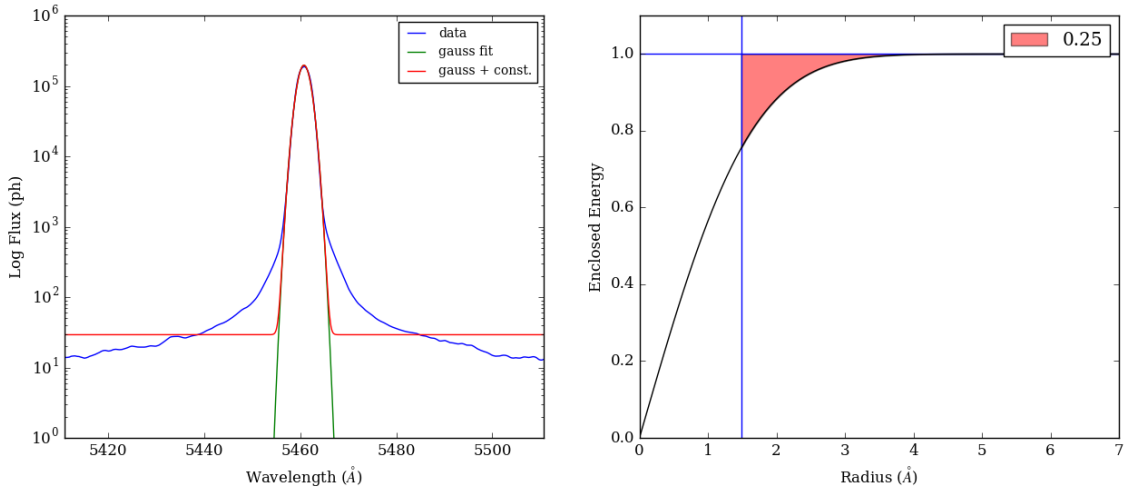

Figure 4.18: Gaussian fit of arclines. 25% of the light is outside of the FWHM in the wings.

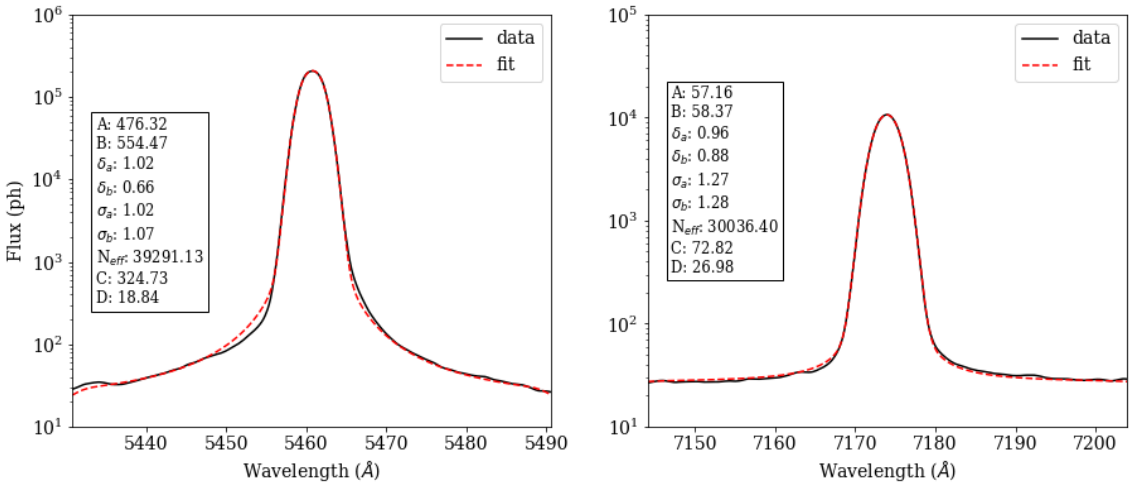

Figure 4.19: Line spread function for arclines. The nine parameters used to fit the lines are identified.

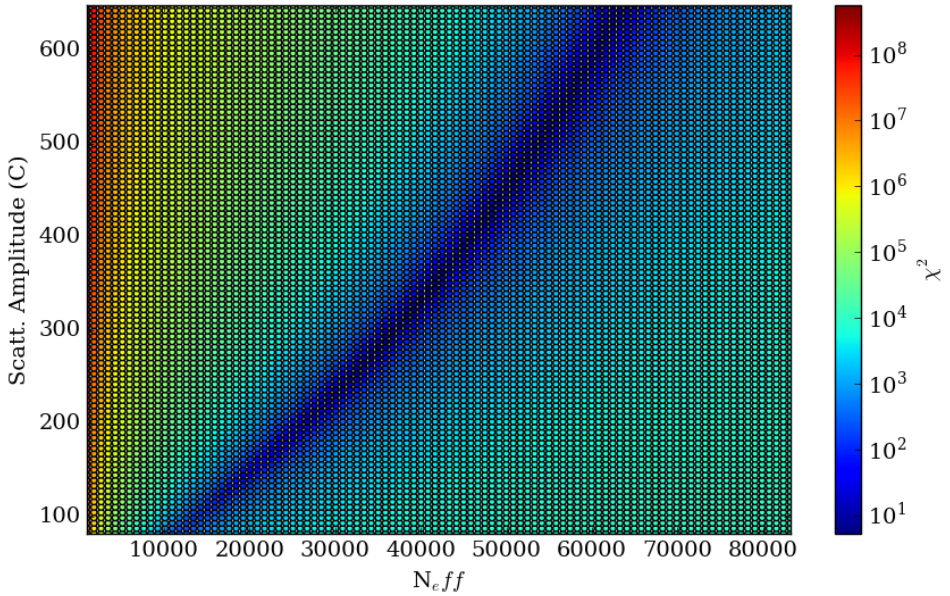

Figure 4.20: Non linear fit χ^2 for different N_{eff} values and scattering amplitudes. This is the fit for an arc line at 546 nm. The best fit is $N_{eff} \sim 50,000$.

the best N_{eff} for blue is $\sim 50,000$ and for red is $\sim 40,000$. While this value is supposed to describe the number of effective illuminated grating lines, this interpretation doesn't fit with the fact that it has strong covariance with the the amplitude of the lorentzian, which in turn has high covariance with the gaussian amplitudes. We therefore cannot confidently attribute this fitted value to the physical illumination of lines.

We used this line spread function model to identify and remove the airglow lines from the BOSS sky spectra. We used the airglow line list compiled by Cosby *et al.* (2006) which was put together based on the Hanuschik (2003) measurements and is comprised of 2808 emission lines from 3140 - 10430 $\mathring{A}$. The wavelength positions are listed as their positions in air, so we convert them to vacuum using the formula from Edlén (1966), where $\lambda_{vacuum} = \lambda_{air} \times n$,

$$n(\lambda) = 1 + 10^{-18}\left(8432.13 + \frac{2406030}{130 - (1/\lambda)^2} + \frac{15977}{38.9 - (1/\lambda)^2}\right) \tag{4.22}$$

with λ measured in μm. We reduced the Cosby list to 241 lines by taking only those with a peak intensity above 150 R/nm ($> 5 \times 10^{-17} erg/cm^2/s/\mathring{A}$) and separated by more than 0.3 nm, from 360 - 1040 nm. We added to this list 19 of the street lamp lines from table 4.4, mostly in the bluer wavelengths. Each line was windowed by 1-5$\mathring{A}$ around the emission line, fit to eqn. 4.21 with a fixed N_{eff}. The windowed section in the spectrum was then replaced by the fit constant (D). The remaining continuum spectrum is then smoothed with a gaussian

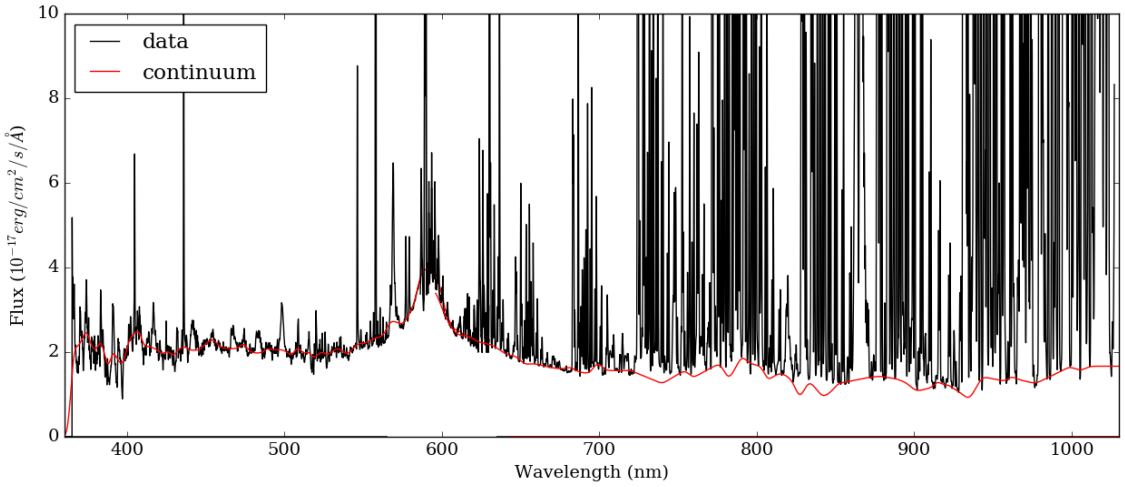

Figure 4.21: BOSS sky continuum flux fit.

kernel and the original spectrum minus the continuum includes the airglow and lamp lines without the continuum background (figure 4.21). For the red spectrograph, some sections of airglow lines were too tightly packed to get reliable measurements of the continuum level, so we selected several points between lines to use as a reference, interpolating them before using the gaussian kernel.

4.4 Sky Model

Our goal for this model of the night sky above APO is intended to enable us to predict how the sky spectrum differs from the dark zenith spectrum (see fig. 4.22 - 4.25) given available observational parameters. Since the sources of light for the continuum differ in some cases from those for specific airglow lines, it's useful to look at them separately rather than using broadband measurements. Using the spectra of the continuum, with the airglow lines removed, we can evaluate the sky background continuum across the full BOSS wavelength range (360 - 1040 nm), which overlaps with the DESI wavelength range. Section 4.4.1 details the continuum model derived from the large spectroscopic data set. We use fit airglow lines to model the individual behavior of interesting airglow lines, which is done in section 4.4.2. We do the same for terrestrial light, both the broadband contribution as well as specific lamp lines (sec. 4.4.3). These models are completed using the flux averaged across a half-plate for specific observations, corresponding to the sky fibers among the 500 fibers that go to each spectrograph. After describing our model, we evaluate the improvements it offers to the current DESI sky model (sec. 4.4.4), compare our results to other measurements (sec.

4.4.5), and then discuss the implications our measurements could have on future ground and space based observations in sections 4.4.6 and 4.4.7.

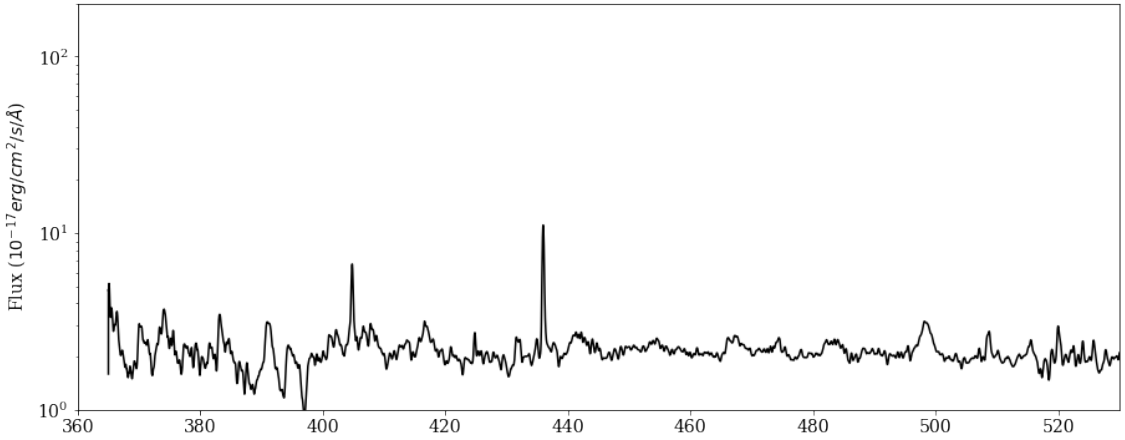

Figure 4.22: Dark zenith spectrum. Average of spectra that are photometric, with the moon below horizon, sun altitude $< -18°$, galactic and ecliptic latitude $> 15°$ and airmass < 1.01. This shows the spectrum from 360 - 530 nm.

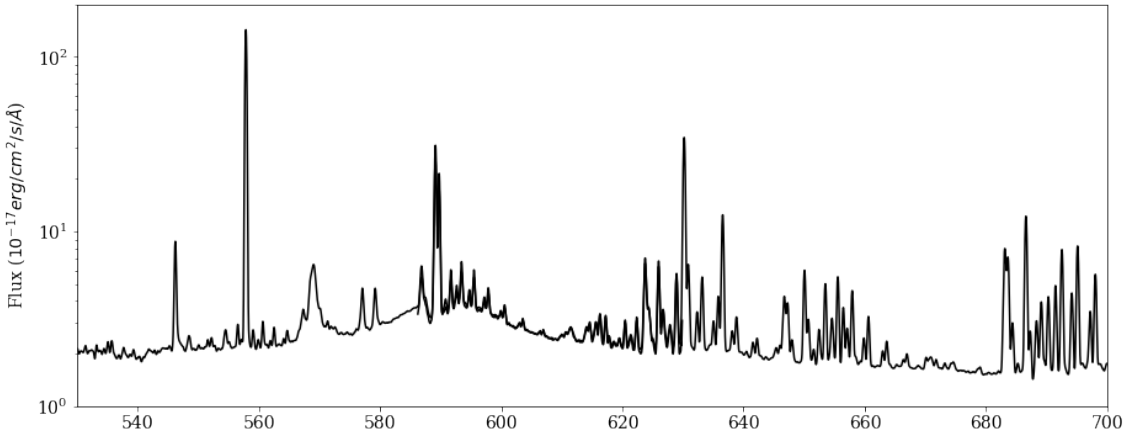

Figure 4.23: Same spectrum as 4.22 from 530 - 700 nm

4.4.1 Continuum Emission

The dark continuum sky background is primarily composed of ISL, zodiacal light, and airglow continuum. When the sun is near the horizon, scattered sunlight (twilight) greatly increases the brightness of the sky, even at sun altitudes less than $-14°$. When the moon is above the

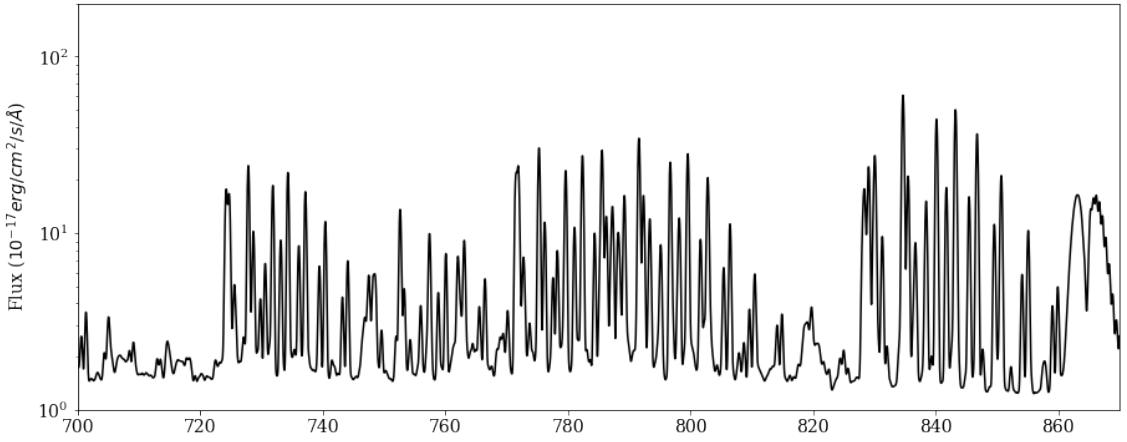

Figure 4.24: Same spectrum as 4.22 from 700 - 870 nm

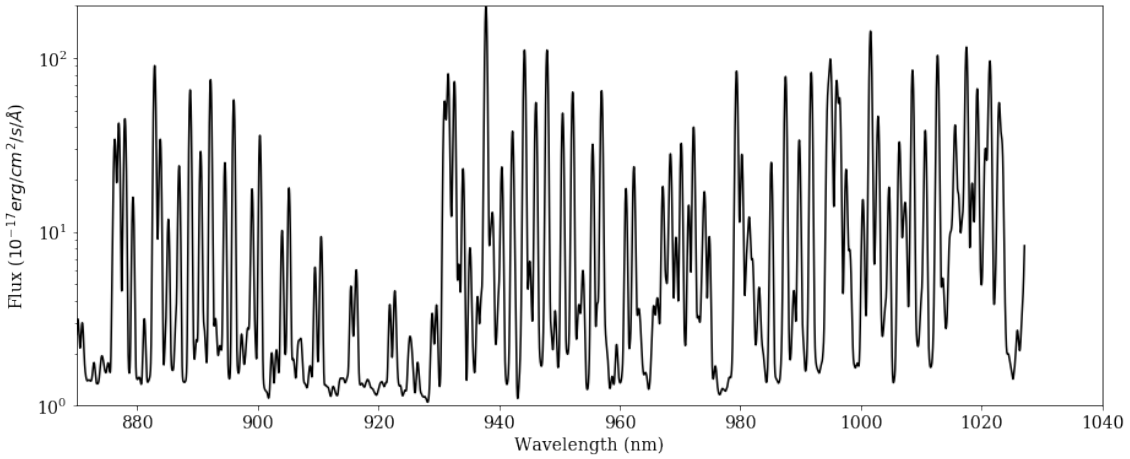

Figure 4.25: Same spectrum as 4.22 from 870 - 1030 nm

horizon, scattered moonlight dominates the continuum, especially at blue wavelengths. We model the full continuum, including all these sources, $\mathrm{I}_{cont.}(\lambda)$ as:

$$\begin{aligned} I_{cont.}(\lambda) =& [c_{AM}(\lambda) \cdot X + c_{zodi}(\lambda) \cdot I_{ZODI}(\beta) + c_{isl}(\lambda) \cdot I_{ISL}(l, b) \\ &+ c_{SF}(\lambda) \cdot I_{SF}(\text{sfu})[\text{MJD} - i] + c_{seas}(\lambda) \cdot I_{seas}(month) \\ &+ c_{hour}(\lambda) \cdot I_{hour}(\text{t.s.s.})] \times \Delta T(X, \lambda) \\ &+ c_{twi}(\lambda) \cdot I_{twi}(\alpha, \delta) \times e^{\tau_T(\lambda) \cdot X} \\ &+ c_{moon}(\lambda) \cdot I_{moon}(\text{Alt}_M, \text{Ill}_M, \delta_M) \times e^{\tau_M(\lambda) \cdot X} + c_{AC} \end{aligned} \tag{4.23}$$

The model has 12 input parameters and 33 fitted coefficients. We describe each component of this model below in detail, but for reference, the linear coefficients for the dark time model

are c_{AM} for airmass, c_{zodi} for zodiacal light, c_{isl} for ISL, c_{SF} for solar flux, c_{seas} for seasonal dependence, and c_{hour} for the time of night measured as the time since sunset (t.s.s). The dark model is multiplied by an effective transmission curve $\Delta T(X, \lambda)$ that accounts for the additional extinction for observing at higher airmass. Additionally, the twilight (c_{twi}) and scattered moonlight (c_{moon}) components are multiplied by factors to account for additional scattering effects (τ_T, τ_M). The constant term (c_{AC}) accounts for any additional continuum flux not accounted for by the other elements. We first fit the model using data only from dark time, defined as when the airmass is less than 1.4, the moon is below the horizon, and the sun is below the horizon by at least 18°, and the observation is above the galactic plane by 10°. The coefficients measured with that data selection are c_{zodi}, c_{isl}, and c_{SF}, along with some other parameters associated with those sources. These coefficients are then saved and used to model the twilight model, which is done with data at any airmass having the moon below the horizon and the sun altitude greater than −20°. Then we add in data with the moon above the horizon, and model the scattered moonlight (c_{moon}). Finally, we fit all data, including observations taken in non-photometric conditions, with the final model, while keeping all parameters frozen, to determine the remaining variance.

Airmass

As discussed above, the change to night sky brightness due to airmass is complicated because while a larger scattering cross-section for extinction is encountered at a higher airmass, it also produces more airglow. Equation 4.9 indicates that the relationship between flux and airmass can be approximated as linear, which can be seen with the dark data set (figure 4.26). We model the increase in sky flux linearly as $c_{AM} \cdot X$, where X is airmass as recorded in the observation meta data. In the case of the BOSS sky spectra, the spectra are calibrated so that they measure the above atmosphere flux at zenith. There is some additional extinction not accounted for due to this approach to calibration. As you can see from figure 4.27, the additional extinction due to moving from an airmass of 1 to 1.4 results in a mean throughput reduction of between 1% and 10%. In the model we represent this as $\Delta T(X, \lambda)$, which is defined as:

$$\Delta T(X, \lambda) = 1 - \left[10^{-0.4 \cdot k_0(\lambda)} - 10^{-0.4 \cdot k_0(\lambda) \cdot X}\right] \tag{4.24}$$

where $k_0(\lambda)$ is the extinction coefficient at zenith for KPNO (see extinction curve in fig. 4.3). This differential throughput reduction is applied to the zodiacal, ISL, and solar flux components of the dark sky model as well.

Figure 4.28 plots the coefficient c_{AM} as a function of wavelength, showing that the mean coefficient is ∼1, decreasing almost linearly with wavelength. It is not clear exactly what causes the decrease in the fit coefficient towards the red, but it is likely because most of the airglow continuum processes produce light in the blue (i.e. NO_2; sec. 4.2.5). The spike in the coefficient around 598 nm suggests two things. The calculation of the continuum in this area is challenging as it is difficult to extract the emission lines from the NaI doublet from the broader continuum emission, however, it is possible that the strength of NaI broadband emission in this region is more impacted by airmass relative to other airglow emission sources.

We are likely observing both of these effects in the airmass fit coefficient. The difference in flux between an airmass of 1 and 1.4 ranges from 0.3 - $1.5\times10^{-17} erg/cm^2/s/\mathring{A}$ for the inter-airglow line continuum. This is consistent with past measurements of $0.1-0.3$ mag increase from airmass 1 to 1.4 (sec. 4.2.2). Our confidence in this model is tested by comparing the reduced χ^2 of the model fit to changes in the fit coefficient, to which our model is robust (figure 4.29).

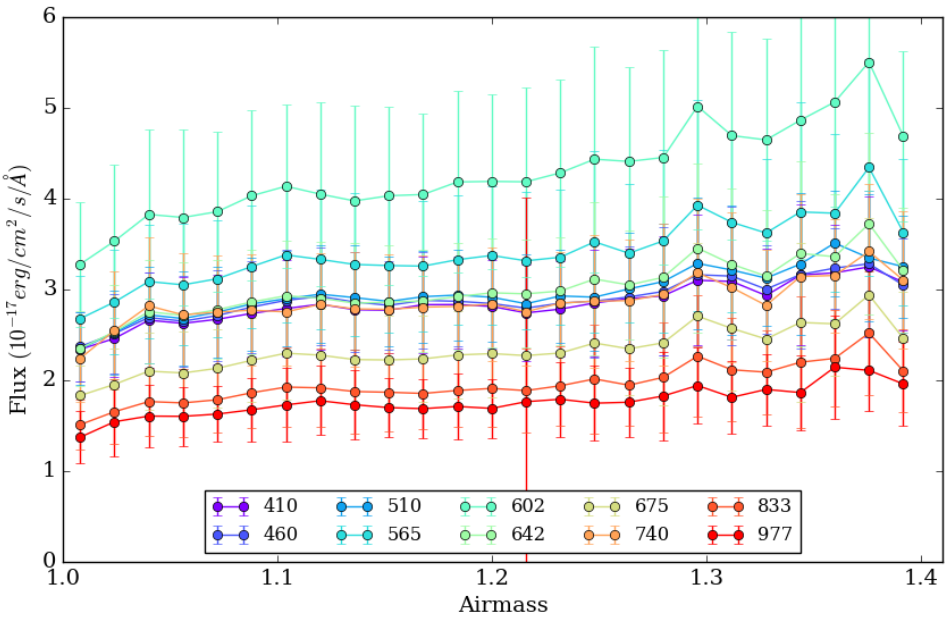

Figure 4.26: Airmass vs. sky flux during dark time. Each line represents a different wavelength (in nm) as identified in the key. There is a linear relationship between airmass and the flux.

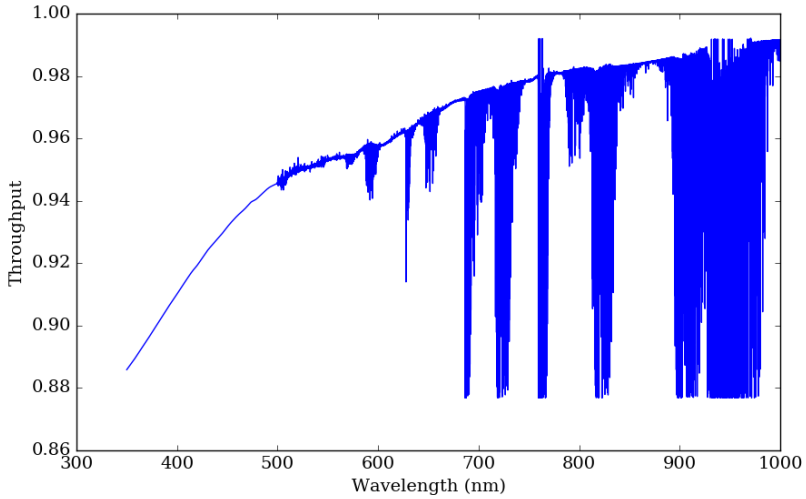

Figure 4.27: Difference in atmosphere throughput from airmass of 1 to 1.4. This is determined as 1 - $(10^{-0.4 \cdot k_0(\lambda)} - 10^{-0.4 \cdot k_0(\lambda) \cdot 1.4})$, where $k_0(\lambda)$ is the zenith extinction coefficient.

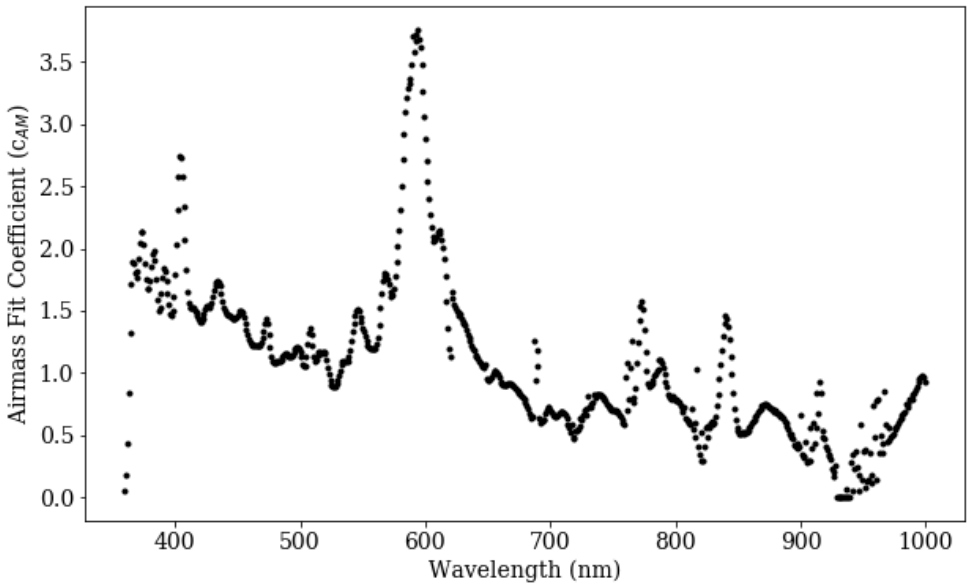

Figure 4.28: Fit coefficient for airmass dependence (c_{AM}) as a function of wavelength. The relationship decreases as a function of wavelength, with higher values where the measurement of the continuum is less certain near bright airglow lines.

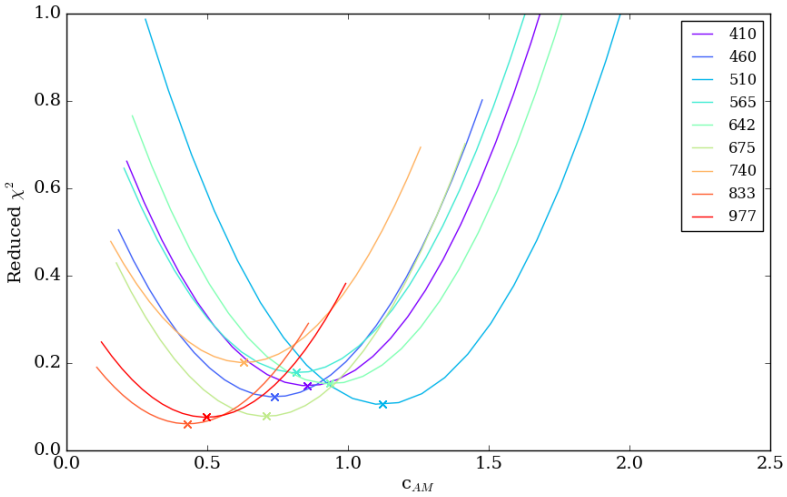

Figure 4.29: Stability of the fit coefficient for dependence on airmass (c_{AM}). Each line represents the fit for the flux in a given wavelength band. There is a clear minimum value, giving stability to our model.

Zodiacal Light

To model the contribution of the zodiacal light to the continuum, we use the map of zodiacal light intensity as a function of heliocentric ecliptic latitude and longitude ($I(\lambda - \lambda_\odot, \beta)$) as measured by Levasseur-Regourd & Dumont (1980). Since the dependence on ecliptic longitude is minimal, we just take the map in Levasseur-Regourd & Dumont (1980) for a helio-ecliptic longitude of 180°, expressed in the model as ($\mathrm{I}_{ZODI}(\beta)$). The $\mathrm{I}_{ZODI}(\beta)$ term is in units of flux ($10^{-17} erg/cm^2/s/\mathring{A}$) at 500 nm, converted from the published values of $S10_\odot$, where 1 $S10_\odot = 1.28 \times 10^{-9} erg/cm^2/s/\mathring{A}/sr$. The wavelength dependence of our model is defined by $\mathrm{c}_{zodi}(\lambda)$, which should follow a solar spectrum, slightly redenned as discussed in sec. 4.2.3. In figure 4.30, the dark sky data is plotted as a function of ecliptic latitude. The data indicates that the sky is much brighter than would be expected from zodiacal light alone, with each solid line showing the expected normalized flux as a function of ecliptic latitude for several longitude values.

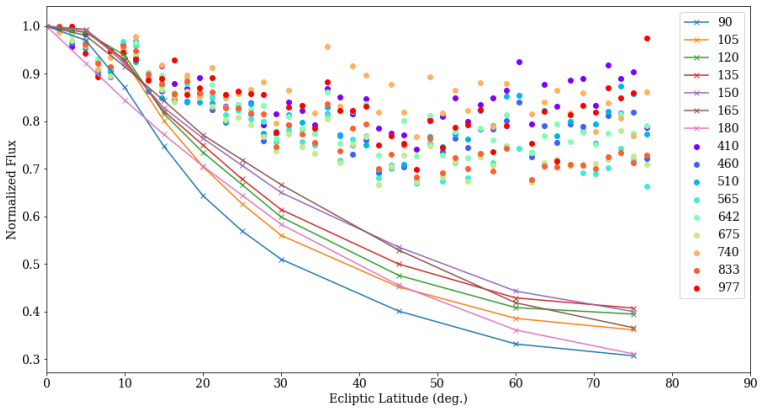

Figure 4.30: Ecliptic latitude vs. relative sky flux. The points represent the binned data from several wavelengths (in nm). Each solid line shows the expected relative amount of zodiacal light for ecliptic latitudes. The solid lines are identified by their helio-ecliptic longitude (in deg.) as measured by Levasseur-Regourd & Dumont (1980).

After fitting the full model, we compare the residuals without zodiacal, (i.e. data - [$I_{cont.}(\lambda)$ - $c_{zodi}(\lambda) \cdot I_{ZODI}(\beta)$]) and plot this against the ecliptic latitude (figure 4.31). We find that zodiacal light accounts for 30% on average, ranging from 15 - 50% of the total continuum flux, which is consistent with past measurements (sec. 4.2.3). This suggests that using a space based platform, instead of a ground-based telescope, would see a 2-5 times decrease in the inter-airglow line sky background continuum.

The wavelength dependence of the fit tracks the solar spectrum almost exactly up to $\sim$ 550 nm (figure 4.32). The spectrum at wavelengths greater than 600 nm is brighter than we would expect from redenning as described in Aldering (2001), who calculated the above atmosphere zodiacal contribution. Therefore, this additional zodiacal light must be attributed to atmospheric scattering effects, where more red light is scattered back into our field of view. It is interesting to note the strong absorption feature at $\sim$ 740 nm. These results are in good agreement with the predictions of the Noll *et al.* (2012) scattering calculations for zodiacal light, except for the peaks between 550 and 600 nm, the source of which is unknown to the writer.

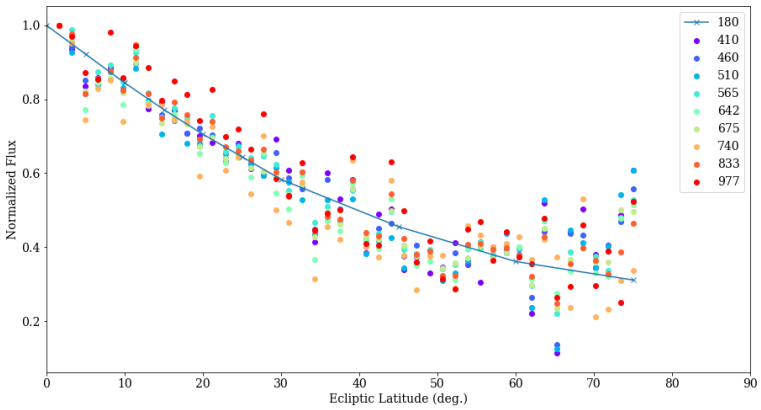

Figure 4.31: Ecliptic latitude vs. normalized zodiacal contribution for different wavelength bins (in nm) as identified in the key. This shows the dark model residuals plus the zodiacal model, calculated by data - $[I_{cont.}(\lambda)$ - $c_{zodi}(\lambda) \cdot I_{ZODI}(\beta)]$. The solid blue line shows the model for expected zodiacal intensity for a helio-ecliptic longitude of 180°.

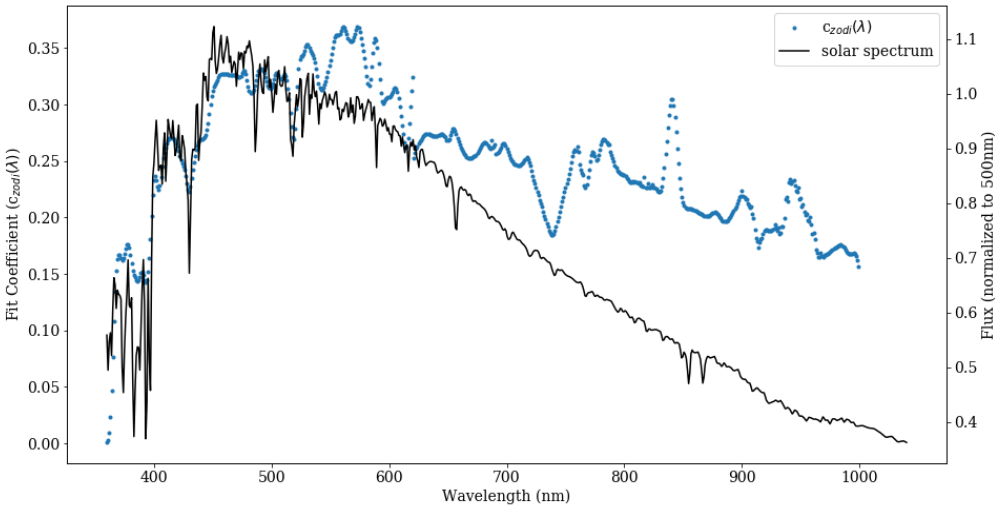

Figure 4.32: Wavelength dependence of zodiacal light as measured by its linear coefficient $c_{zodi}(\lambda)$. The black solid line shows the solar spectrum normalized to 500 nm and the blue points show the model coefficients.

ISL

We base the model for the ISL contribution on the measurements made by Pioneer 10 space mission measurements at 440 nm as a function of galactic latitude and longitude, $I_{ISL}(b, l)$ (Toller 1981), with the wavelength contribution fitted with the linear coefficient $c_{isl}(\lambda)$. We find that the contribution is extremely small, at most 2% of the total continuum, and not detected at several wavelengths. This is fairly consistent with the findings of Bernstein *et al.* (2002) who measured that the ISL flux is 12-24% of the total zodiacal flux. The wavelength dependence for the fit coefficient generally decreases towards the red, with absorption features around 598 nm, 780 nm, and between 900 and 1000 nm (figure 4.33). In most cases, it would be acceptable to remove this term from the model.

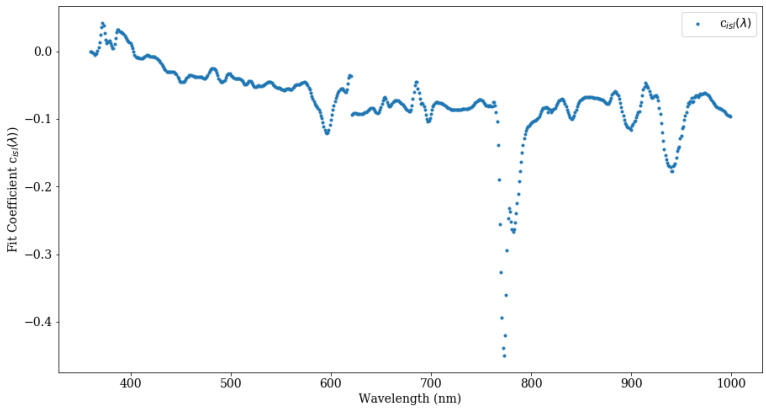

Figure 4.33: Fit coefficient for ISL vs. wavelength.

Solar Flux

To model the impact of the solar flux, we use the daily measurements of the solar flux density at 2800 MHz (10.7 cm) from Dominion Radio Astrophysical Observatory (DRAO) in Penticton, British Columbia and Ottawa. This daily measurement is made in "solar flux units" (sfu), where 1 sfu = 10^{-22} W/m^2/Hz. Preliminarily, if we plot our dark continuum sky against the solar flux, the result is quite linear (fig. 4.34). If we split our dark zenith data set, with airmass between 1 and 1.01, into observations with solar flux density less than 100 sfu and those above that level, we see that the impact from solar flux is independent of airmass (fig. 4.35).

Learning from past experiments (Patat 2008, Krisciunas *et al.* 2007), we also expect there to be some time delay between the observation and the date of the solar flux measurement. Therefore, we model the sky emission caused by solar activity as a linear response to the measured activity with a time delay allowing for the travel time of particles from the sun to the earth and time for the earth's atmosphere to respond: $c_{SF}(\lambda) \cdot I_{SF}(\text{sfu})[\text{MJD} - i]$ where

i is the time delay since the date of the observation (MJD). The linear coefficient $c_{SF}(\lambda)$ transforms to units of our flux ($10^{-17} erg/cm^2/s/\AA$) and accounts for any changes due to wavelength.

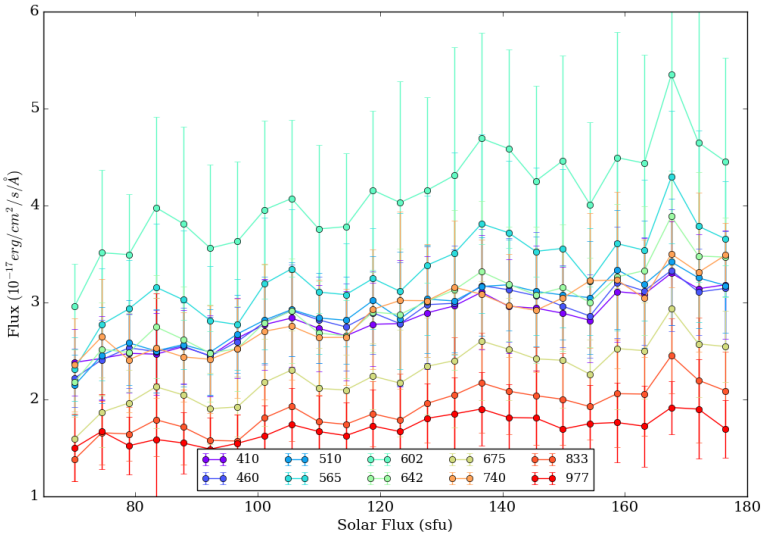

Figure 4.34: Dark sky flux vs. solar flux measurements with no time delay. Each line represents the flux of a specific wavelength (in nm) as indicated in the key.

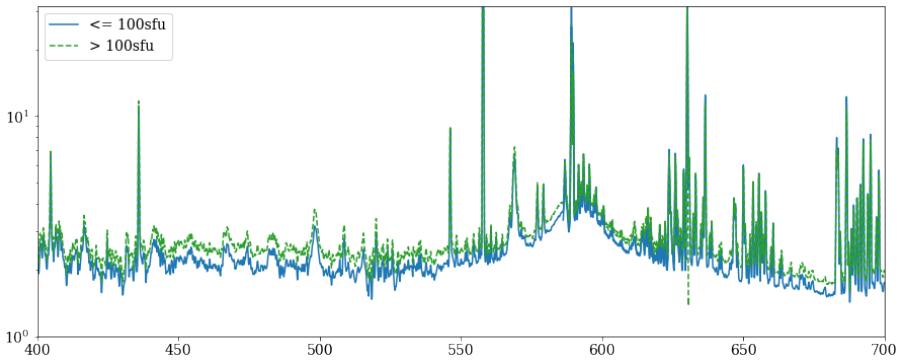

Figure 4.35: Dark zenith spectra for observations with different mean solar flux density. The data used to make these mean spectra are composed from observations taken at an airmass of between 1 and 1.01, showing that the solar flux effect is independent of airmass. The full spectrum has been windowed from 400 - 700 nm to highlight difference in spectra, but the offset is evident across the whole wavelength range.

The model fit for the time delay coefficient (i), using dark time data with airmass values up to 1.4, is between 4.5 and 5 days (fig. 4.36). If we re-fit the model for different time delay factors, the minimum χ^2 is different than the model fit value in some cases, especially the red, and it is evident that there are two minima over $\sim$ 50 days (fig. 4.37). The first minimum for the time delay varies from 4.5 - 13 days, and the second minimum occurs $\sim$ 25 days later. It is not clear why the model prefers a fit at $\sim$ 4.8 days rather than 10 at the redder wavelengths. However, the solar wind is approximately 300 - 500 km/s, so to travel from the sun to the earth takes 3.5 $\sim$ 5.8 days, which is consistent with the fit time delay factors as plotted in figure 4.36. The time delay in the correlation between the sky background and daily solar flux density values was measured by Krisciunas *et al.* (2007) to be $\sim$ 5 days, and by Patat (2008) to be $\sim$ 30 days, as discussed in section 4.2.1. Our results seem to support both of these findings. It is not clear why the time delay changes with wavelength or why there are two minima. Additional research here would be interesting, especially if there were an opportunity to combine data sets from different solar cycles.

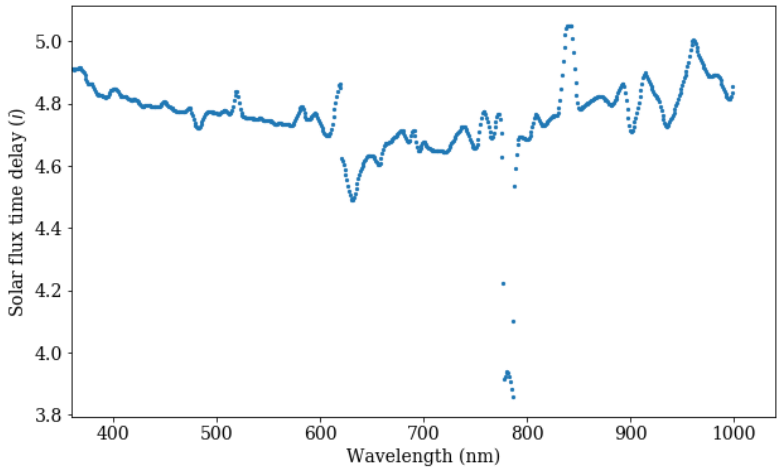

Figure 4.36: Model fit for time delay (i).

The airglow continuum, as measured through its relationship with the solar activity, accounts for more than half the dark sky continuum. Therefore, it is important to include changes in the solar cycle into any sky model. The linear coefficient, $c_{SF}(\lambda)$, is approximately constant at 0.01 (fig. 4.38), meaning that there is little wavelength dependence on the impact of the solar flux. Figure 4.39 shows the continuum contribution from this solar flux model for an observation with low solar activity (orange line) and one with higher solar activity (blue). We find that the difference in sky brightness in B band, due only to the solar flux, corresponds to $\sim$ 1.1 mag increase from solar minimum to maximum. This is slightly higher than previous measurements, ranging from 0.4 to 1 mag as discussed in section 4.2.1.

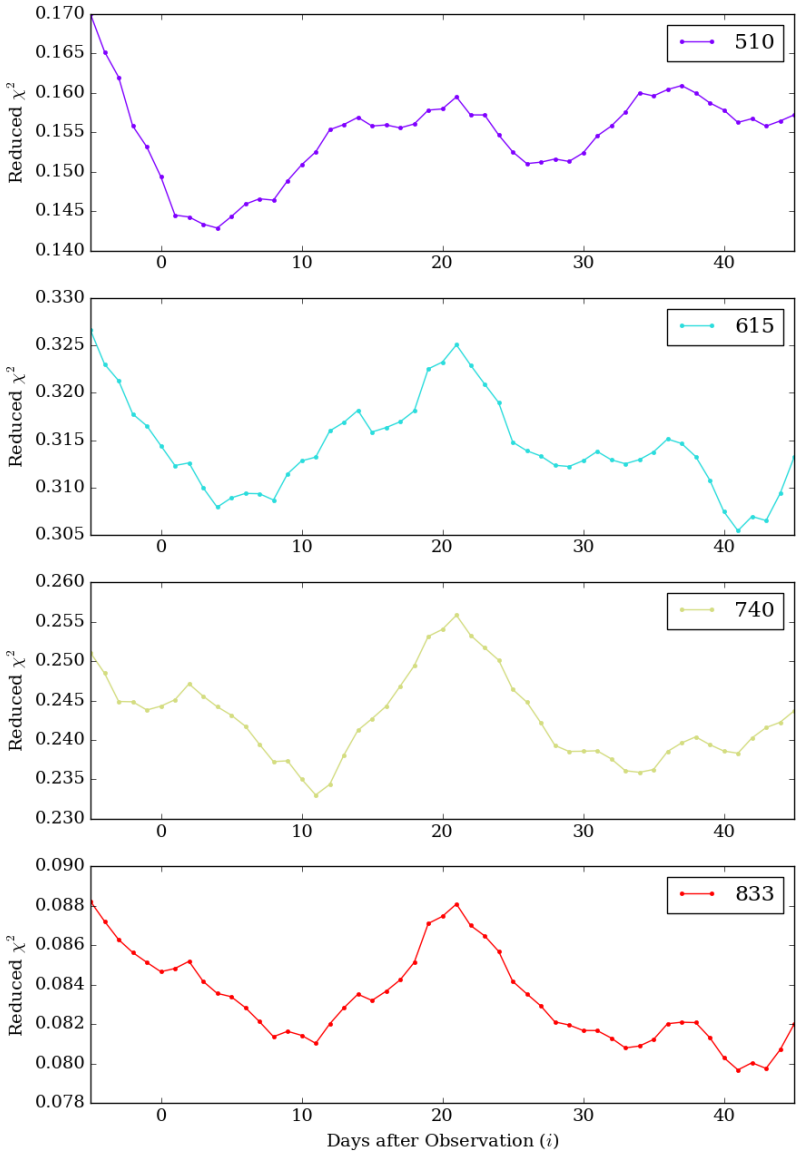

Figure 4.37: Reduced χ^2 for the model fit over a range of solar flux time delays (i) for several wavelength bins (in nm) as identified in the key for each panel. The first minimum ranges from 4-10 days, and in some cases there is a second minimum $\sim$ 25 days following the first.

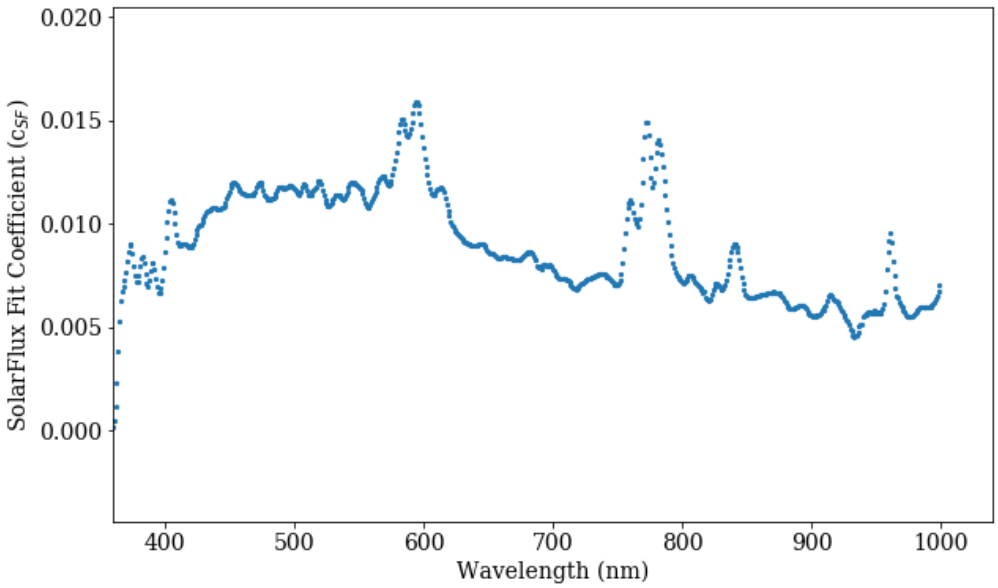

Figure 4.38: Solar flux fit coefficient vs. wavelength. The value is mostly constant with a slight decrease in the redder wavelengths.

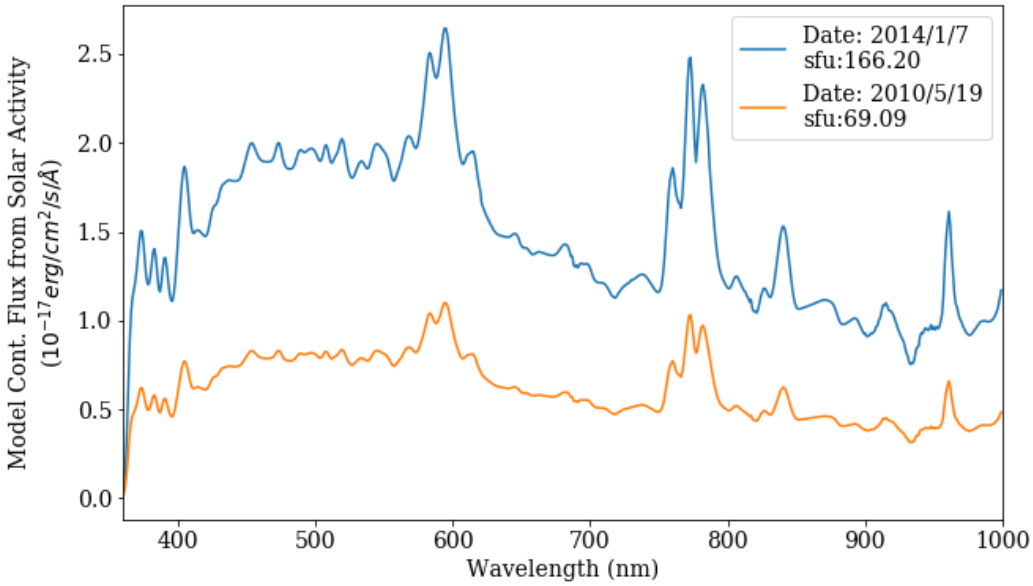

Figure 4.39: Contribution to continuum flux from solar flux. Each line is the continuum flux as calculated from $c_{SF}(\lambda) \cdot I_{SF}(\text{sfu})[\text{MJD} - i]$, where the date and solar flux is identified.

Seasonal and Nightly Variations

The data appears to support the addition of seasonal sky brightness variations and time-of-night variations independent of the solar activity. With 5 years of observations, there are 5 independent measurements of seasonal terms and hundreds of measurements dependent on time of night. We modeled the time dependence of the observations by their month and time of observation as time after sunset. The dependence on the season, $I_{season}(month)$, is modeled by a linear combination of unique coefficients for each month, giving a delta brightness from January.

$$\begin{aligned} c_{seas}(\lambda) \cdot I_{seas}(month) = & c_{feb}(\lambda) \cdot FEB + c_{mar}(\lambda) \cdot MAR + c_{apr}(\lambda) \cdot APR + c_{may}(\lambda) \cdot MAY \\ & + c_{jun}(\lambda) \cdot JUN + c_{jul}(\lambda) \cdot JUL + c_{aug}(\lambda) \cdot AUG + c_{sep}(\lambda) \cdot SEP \\ & + c_{oct}(\lambda) \cdot OCT + c_{nov}(\lambda) \cdot NOV + c_{dec}(\lambda) \cdot DEC \end{aligned} \tag{4.25}$$

For each observation, 1 is used for the month of the observation and 0 for all others (FEB - DEC). The results (fig. 4.40) indicate that the sky is brighter in October and November at all wavelengths. The increase in November can account for up to $\sim 0.5 \times 10^{-17} erg/cm^2/s/\mathring{A}$ relative to February, which seems to be the darkest month. This increase in Oct/Nov is consistent with past measurements, as discussed in section 4.2.4, but we do not see any

increased brightness in Apr./May as others have seen. It is not clear why the sky brightens during these months, a phenomena that has now been observed at astronomical sites across the globe.

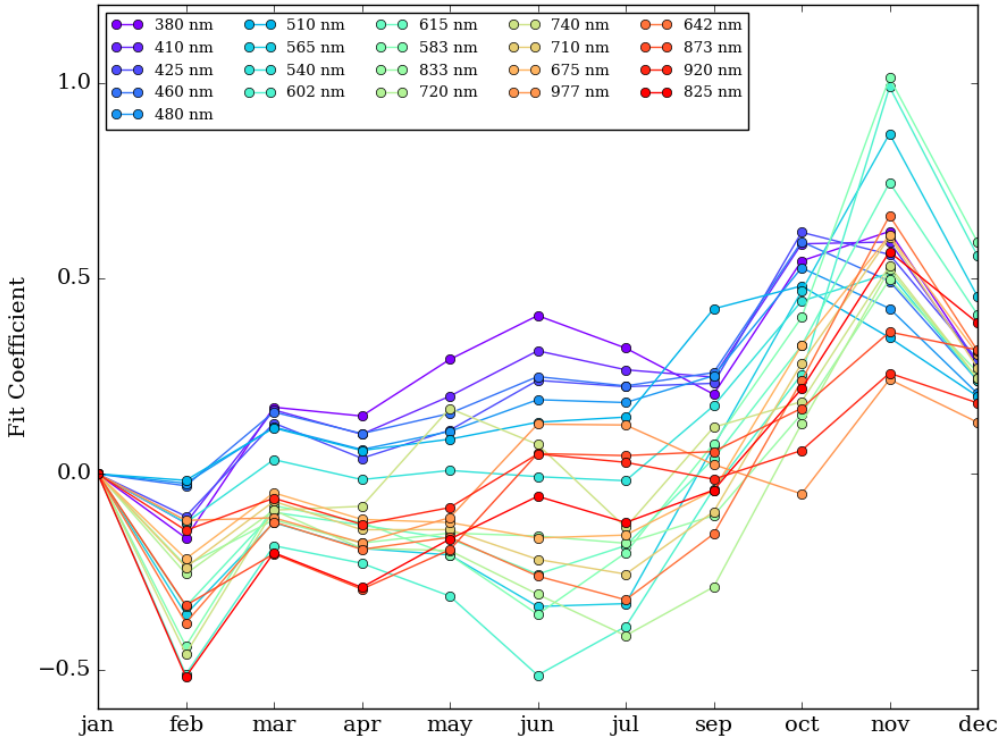

Figure 4.40: Seasonal dependence of sky brightness. This measures the relative brightness to January. There is no data point for August as there was no data taken at that time due to the monsoon season. Each line represents the fit in a different wavelength bin, as identified in the key.

The observation time was modeled similarly, measured as the time after sun set. We have split the time between sunset and sun rise into 6 fractions of the night, such that I_{hour}(t.s.s.) represents the brightness delta from the first sixth of the night, with the input being 1 for the observing time fraction (H2 - H6):

$$c_{hour}(\lambda) \cdot I_{hour}(t.s.s.) = c2(\lambda) \cdot H2 + c3(\lambda) \cdot H3 + c4(\lambda) \cdot H4 + c5(\lambda) \cdot H5 + c6(\lambda) \cdot H6 \quad (4.26)$$

The results for the dark sky observations indicate that at most wavelengths, especially in the red, there does seem to be a darkening throughout the night, brightening in the last

sixth of the night (fig. 4.41). Since the effect is stronger at redder wavelengths, this may be the reason that other programs, mostly using B and V broadband measurements, didn't observe the effect. The stronger effect at 740 nm is likely related to the absorption feature at that wavelength. Overall, the dark sky brightness dependence on time of night is small, accounting for a maximum change of $\sim 0.15 \times 10^{-17} erg/cm^2/sec/\mathring{A}$ over a night. While our our model supports the *Walker Effect* (Walker 1988), with the sky getting darker after twilight and then brighter halfway through the night, we measure a smaller effect.

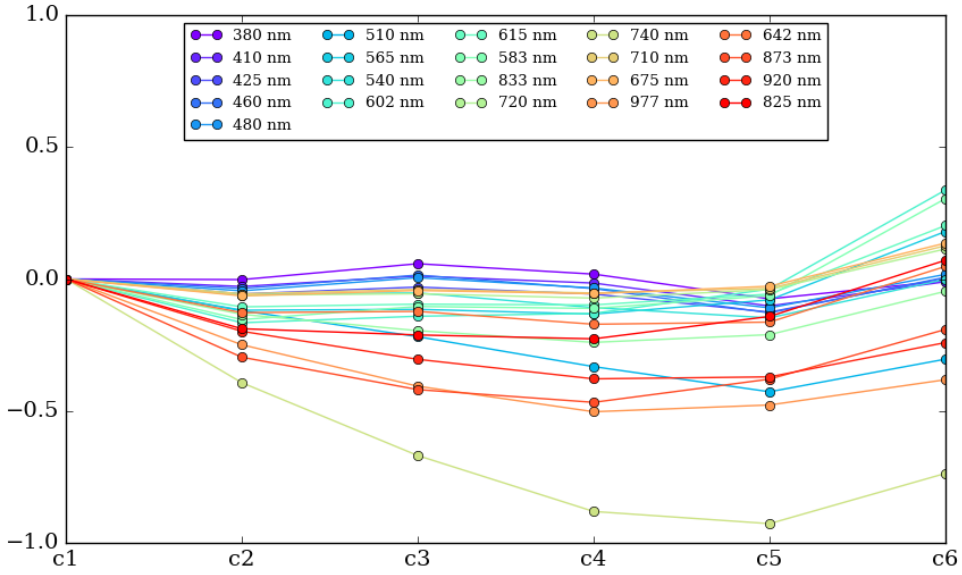

Figure 4.41: Changes in sky brightness throughout a night as measured, as the time since sunset. The night is split into six fractions from sunset to sunrise (c1-c6). Each line represents the fit for a given wavelength bin as identified in the key.

Twilight

When the sun is above $-20°$ altitude, some of its light will back-scatter off the atmosphere into the field of view. This is predominantly dependent on the altitude of the sun and the separation between the sun and target. Figure 4.42 shows that the brightness of the sky increases exponentially when above $-18°$, which is the definition of astronomical twilight. It rises much faster in the blue wavelengths as the intensity follows the solar spectrum. The dependence on sun separation is mostly linear (fig. 4.43). Additionally, we expect there to be some scattering of the sunlight in somewhat complicated ways (Patat 2003), which we model as and effective optical depth ($\tau_T(\lambda)$). The full model is defined as:

$$c_{twi}(\lambda) \cdot I_{twi}(\alpha, \delta) \times e^{\tau_T(\lambda) \cdot X} = \left[c_{T1}(\lambda) \cdot \alpha^2 + c_{T2}(\lambda) \cdot \alpha + c_{T3} \cdot \delta^2 + c_{T4} \cdot \delta\right] \times e^{-\tau_T(\lambda) \cdot X} \quad (4.27)$$

where α is the sun altitude and δ is the separation between the target and the sun's location, both measured in degrees. The linearized vector coefficients, denoted C_{T1} through C_{T4}, and the effective optical depth τ_T, are the parameters to be fit by the twilight model, using the previously fitted parameters from the dark model.

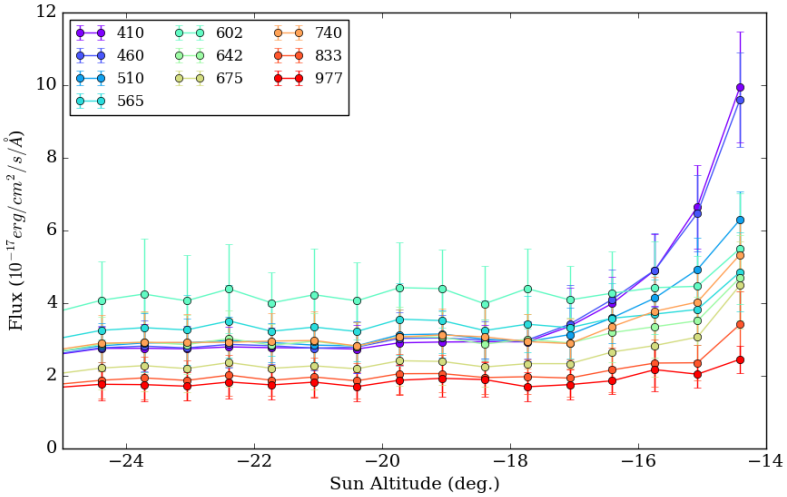

Figure 4.42: Brightness of sky as a function of sun altitude. There were no observations with the sun above an altitude of $-14°$. Each line represents the continuum data for a given wavelength bin as identified in the key (in nm).

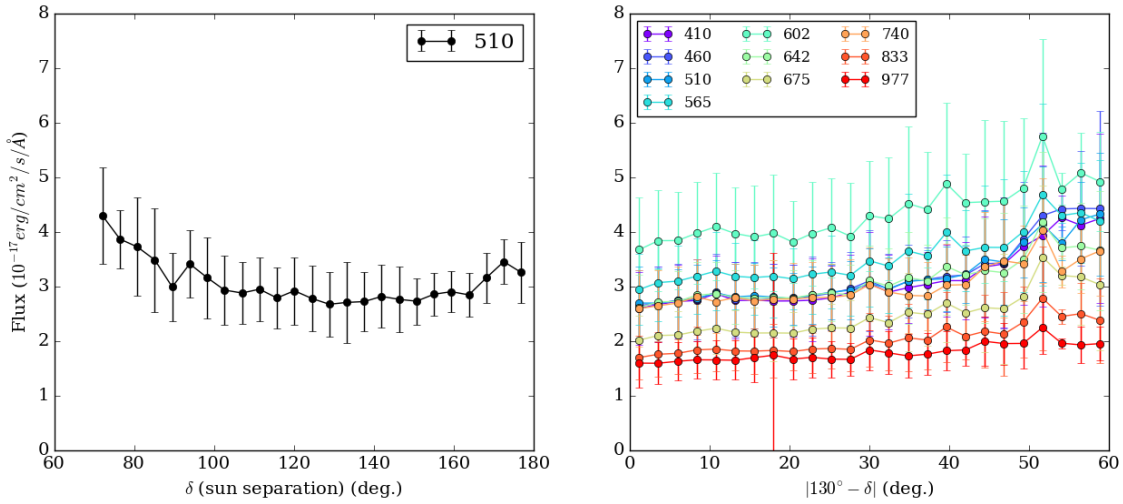

Figure 4.43: **Left:** Continuum data at 510 nm as a function of sun separation (δ) in degrees. **Right:** Continuum data as a function of sun separation, plotted as $150^\circ - \delta$. Each line represents the continuum data for a given wavelength as identified in the key (in nm).

This model was fit using data with the moon below the horizon and the sun above -20° altitude ($-14^\circ > \alpha > -20^\circ$), with no airmass constraints. There were not enough photometric observations during twilight so we also included non-photometric observations. Figure 4.44 plots the flux contribution from twilight plus the constant term c_{AM} for a couple observations, not including other sources in the dark model. The wavelength dependence of the results suggest that most of the sunlight at redder wavelengths is scattered out of the field of view. The normalized solar spectrum is shown for reference. It is clear that twilight is significantly impacted by the sun separation.

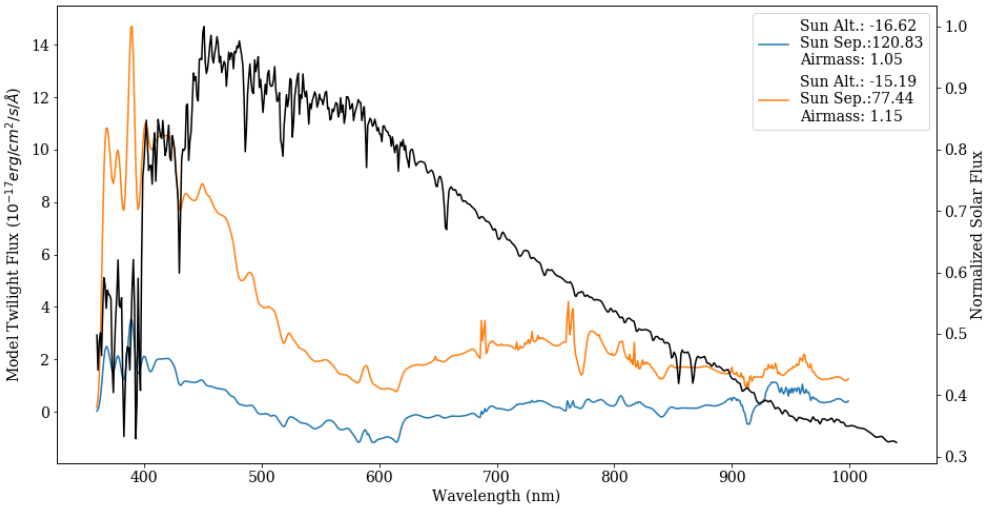

Figure 4.44: Sample twilight spectra from twilight model for different values of α and δ. These are calculated from the model in eqn. 4.27 plus the constant c_{AC}. The brighter spectrum (orange) is most impacted by the relatively small sun separation angle. The black solid line is the normalized solar spectrum for reference.

The effective throughput for the twilight, calculated as $e^{-\tau_T(\lambda)\cdot X}$, using the fitted effective optical depth parameter, is used to account for all additional scattering effects. This is plotted in figure 4.45 for an airmass of 1. It shows a very similar shape as that for Rayleigh and Mie scattering, resembling the extinction for a target at very high airmass. Inclusion of terms describing twilight will be critical for observations during the DESI gray and bright programs, as the flux can increase by factors of 5 or more in the blue wavelengths.

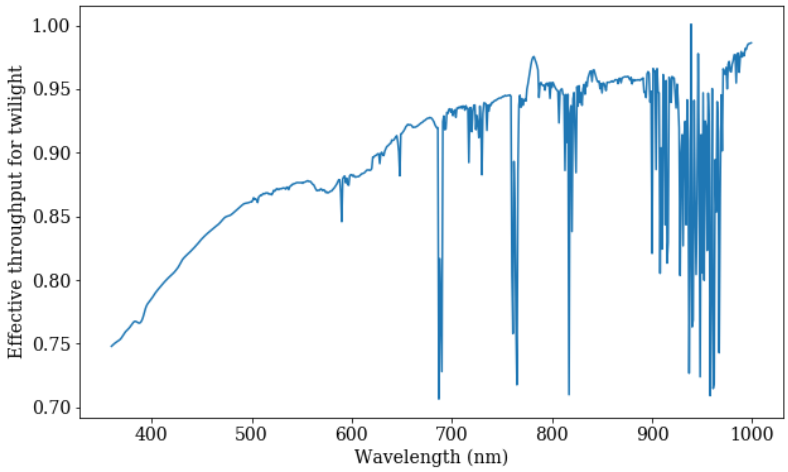

Figure 4.45: Effective throughput for twilight which shows the additional scattering of the twilight. This is calculated as $e^{-\tau_T(\lambda)}$, with $\tau_T(\lambda)$ being a fitted coefficient.

Moonlight

When the moon is visible, it dominates the sky continuum emission at all optical wavelengths. This can be experienced with the naked eye, with few visible stars available to the gazer when there is a bright moon. During a moonless and cloudless sky, visible stars seem to multiply. The light from the moon that is scattered into our field of view is predominantly a function of the moon phase and moon altitude (fig. 4.46), but also depends on its separation from the target of the observation (fig. 4.47). The scattered moonlight also depends on the albedo, or reflectivity of the moon, defined as:

$$lnA(\lambda) = \sum_{i=0}^{3} a_{i,\lambda} g^i + \sum_{j=1}^{3} \Phi^{2j-1} + d_{1,\lambda} e^{-g/p_1} + d_{2,\lambda} e^{-g/p_2} + d_{3,\lambda}\, cos[(g - p_3)/p_4] \tag{4.28}$$

where g is the lunar phase ($g = 0°$ for full moon and 180° for new moon), Φ is the solar selenographic longitude that defines if the moon is waxing or waning, and the constants $a_i, b_i, d_i,$ and p_i are all defined in Kieffer & Stone (2005). To account for the complex scattering functions of moonlight, I've added an effective optical depth, τ_M. The final model for the apparent scattered moonlight is then:

$$\begin{aligned} c_{moon}(\lambda) \cdot I_{moon}(\mathrm{Alt}_M, \mathrm{Ill}_M, \delta_M) \cdot e^{\tau_M(\lambda)\cdot X} & \\ = [c_{M1}(\lambda) \cdot \mathrm{Alt}_M^2 + c_{M2}(\lambda) \cdot \mathrm{Alt}_M + c_{M3}(\lambda) \cdot \mathrm{Ill}_M^2 & \\ + c_{M4}(\lambda) \cdot \mathrm{Ill}_M + c_{M5}(\lambda) \cdot \delta_M^2 + c_{M6}(\lambda) \cdot \delta_M] & \\ \times A(\lambda) \times e^{-\tau_M(\lambda)\cdot X} & \end{aligned} \tag{4.29}$$

where Alt_M is the moon altitude, which is $90^\circ - \mathrm{z}_M$ as used in eqn. 4.14, Ill_M is the moon illumination fraction, related to the moon phase, and δ_M is the separation between the target and the moon. The linearized vector coefficients, denoted by C_{M1} through C_{M5}, and the effective optical depth τ_M, are the parameters fit by the moon model.

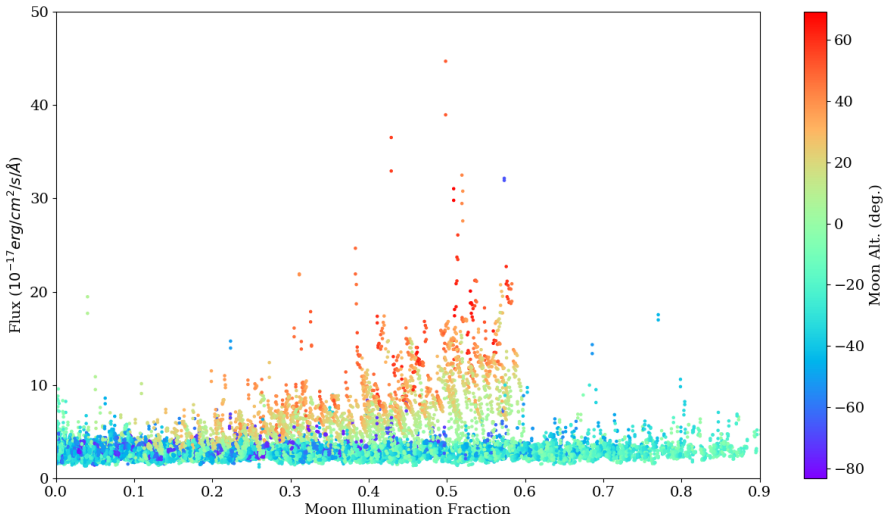

Figure 4.46: Sky brightness as function of moon illumination and moon altitude at a wavelength of 510 nm. The color coding indicates the moon altitude. There were few BOSS observations with the moon above the horizon when it is illuminated more than 50%.

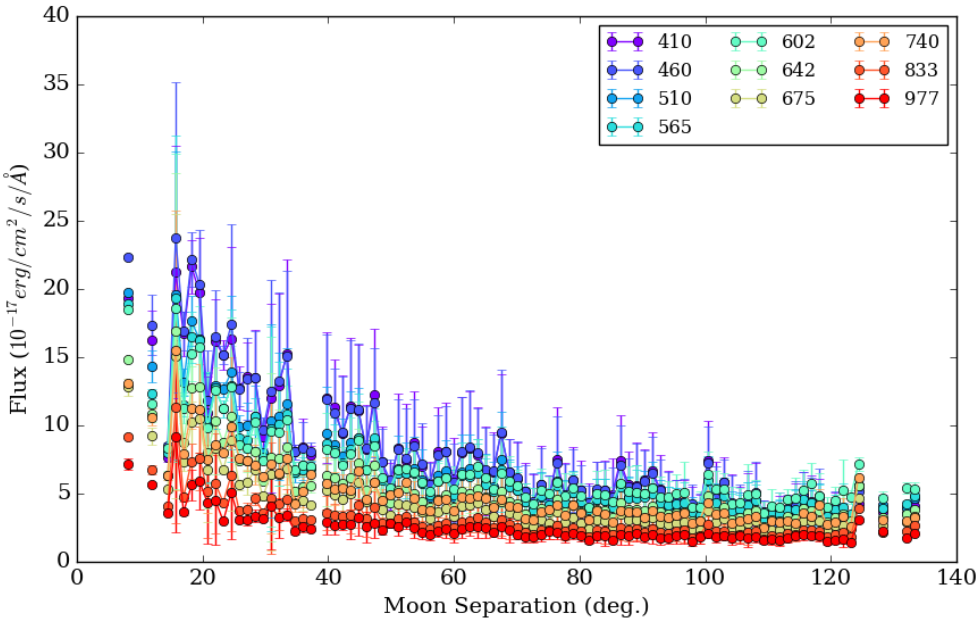

Figure 4.47: Sky brightness dependence on the angular separation of the moon from the target. Each color indicates the continuum flux for a specific wavelength bin (in nm) as indicated in the key.

Figure 4.48 plots the contribution from the moon model plus the constant term c_{AC} for observations with differing moon parameters. The normalized solar spectrum is shown for reference. These are made using the fitted coefficients and values identified in the key in eqn. 4.29, which calculates the scattered light contribution from the moon as a function of wavelength. Similar to twilight, light at redder wavelengths is scattered out of the field of view. The wavelength dependence is similar to the model in Noll *et al.* (2012). Figure 4.49 plots the fit for the effective optical depth, showing the redistribution of light due to scattering. It is not clear why this doesn't resemble the effective throughput curve for twilight (fig. 4.45). Additional work is needed to evaluate the differences between this model and that used for the DESI simulations.

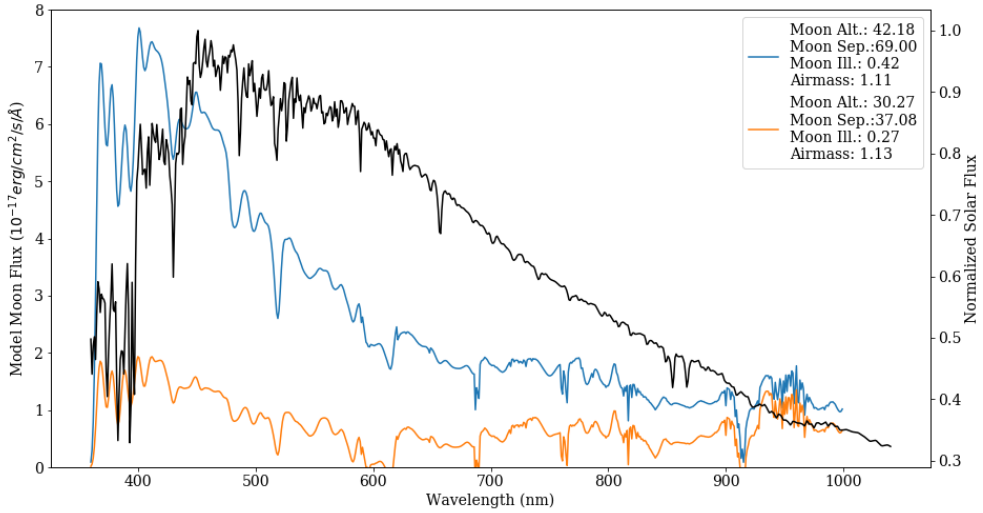

Figure 4.48: Sample moon spectra calculated using the moon model. The black solid line is the normalized solar spectrum for reference.

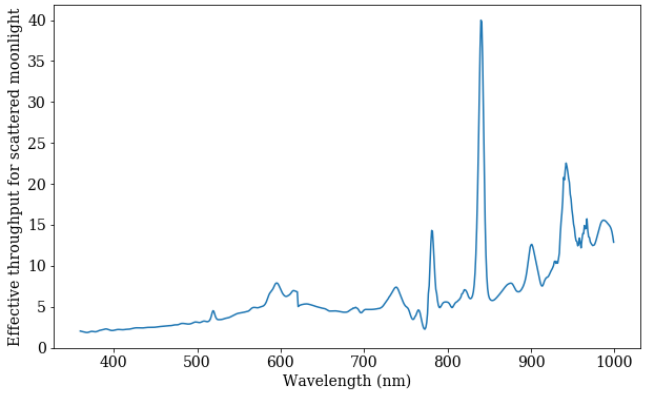

Figure 4.49: Effective throughput for scattered moonlight calculated at $e^{-\tau_M(\lambda)}$, where $\tau_M(\lambda)$ is a fitted coefficient.

4.4.2 Airglow Emission Lines

In this section we look at several airglow lines that have interesting attributes or have been well studied in the past. There are several airglow lines that are of particular interest. These lines are NI (5200$\AA$), OI (5577$\AA$), NaD (5890, 5896 $\AA$), red OI lines (6300, 6364 $\AA$), and red

O2 lines (8605, 8695 $\mathring{A}$). We measured the flux in these lines by taking 5$\mathring{A}$ on either side of the line and summing the flux. The dark time flux distributions of these lines are shown in figure 4.50. Of these, the OI lines 5577 and 6300 $\mathring{A}$, and the NaI doublet contain high flux even during dark time. The NaD light comes both from street lamps and airglow, and is correlated with the continuum emission around those wavelengths. The strength of airglow lines isn't always correlated with the continuum flux, as seen in figure 4.51.

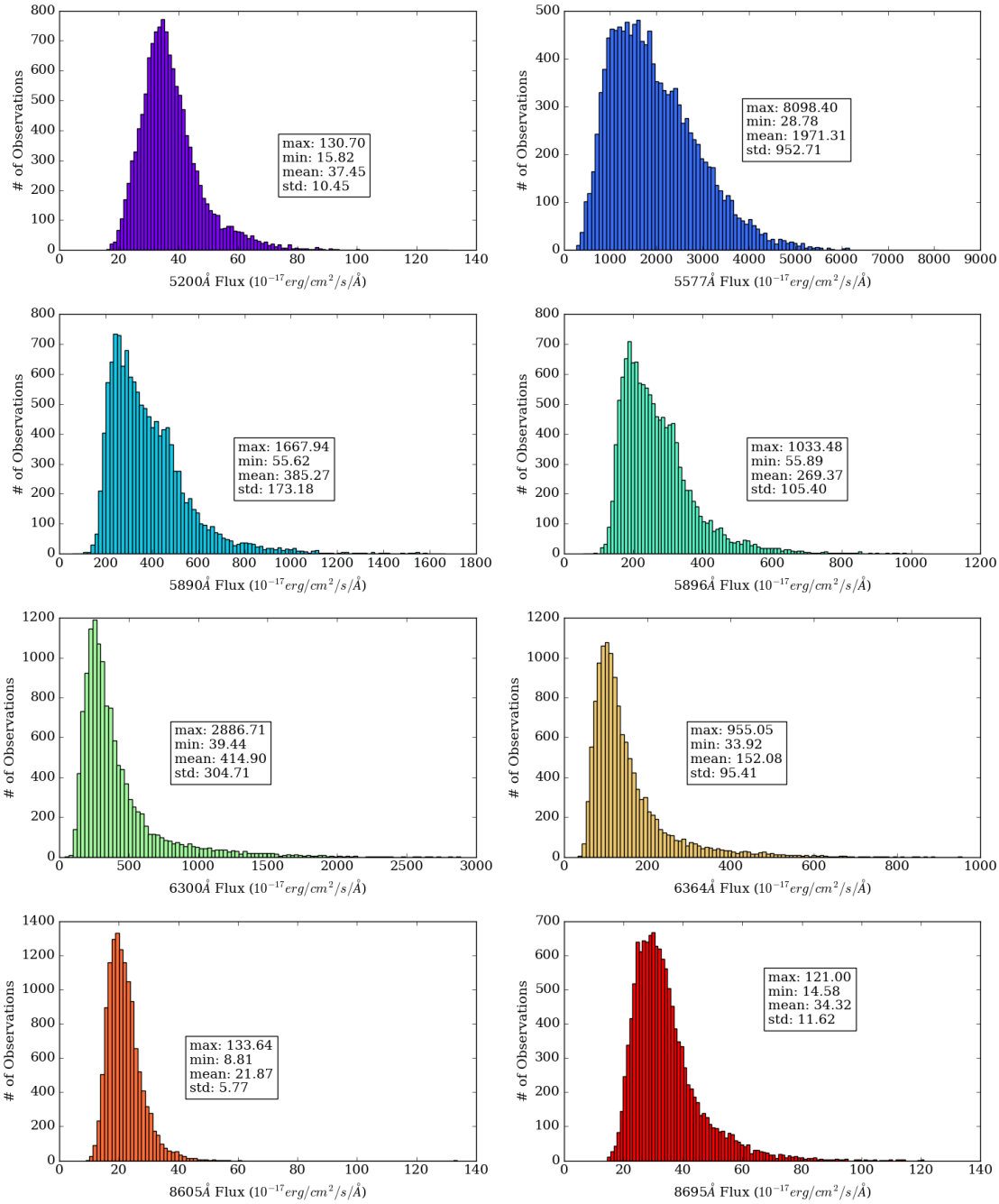

Figure 4.50: Flux distribution of airglow lines in dark time

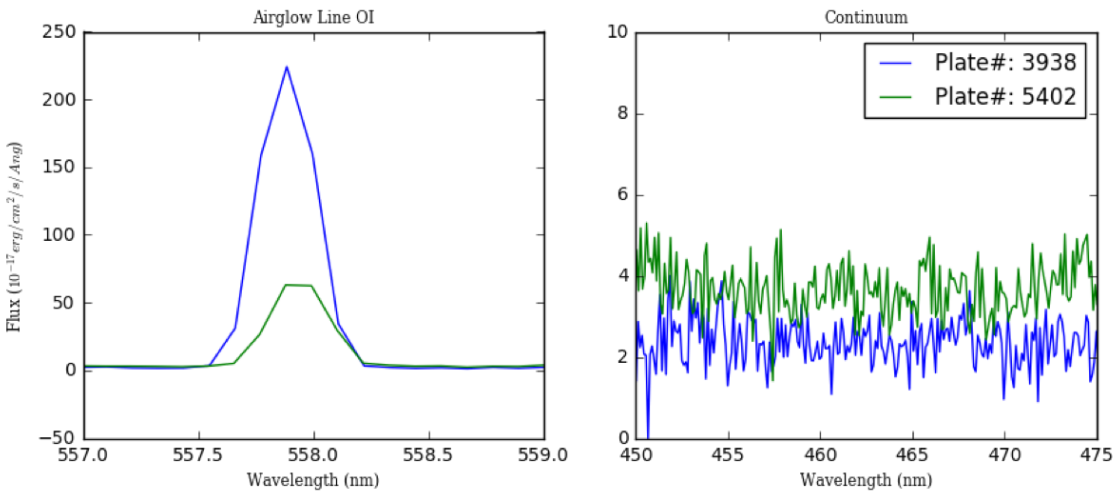

Figure 4.51: Comparing level of continuum to OI flux for two unique observations. The strength of the airglow emission lines does not necessarily scale with the continuum level.

The relationship of the airglow line flux to airmass is mostly linear, with a quick increase from zenith to an airmass of 1.05 (fig. 4.52). There is also a strong linear correlation between the airglow line flux and solar activity (fig. 4.53). The highest correlation is with NI and OI (5577$\mathring{A}$), but all lines show some amount of correlation with different delay times (fig. 4.54). This is consistent with the observations by Patat (2008) and Yee *et al.* (1981). All these lines seem to show some correlation with the seasons (fig. 4.55). The NaD and O2 lines seem to have the same seasonal changes as the continuum, however the NaD also has a peak in Apr/May as observed by Patat (2008) and Takahashi *et al.* (1984). The NI line seems to peak in April and September, as do the red OI lines. The behavior of the blue OI line is different from all, peaking in the summer and winter. The behavior of the blue OI line is also different for the observation time (time since sunset), which seems to increase for the first part of the night instead of decrease (fig. 4.56). These results differ from observations by Patat (2008) and Takahashi *et al.* (1984) and warrant additional study.

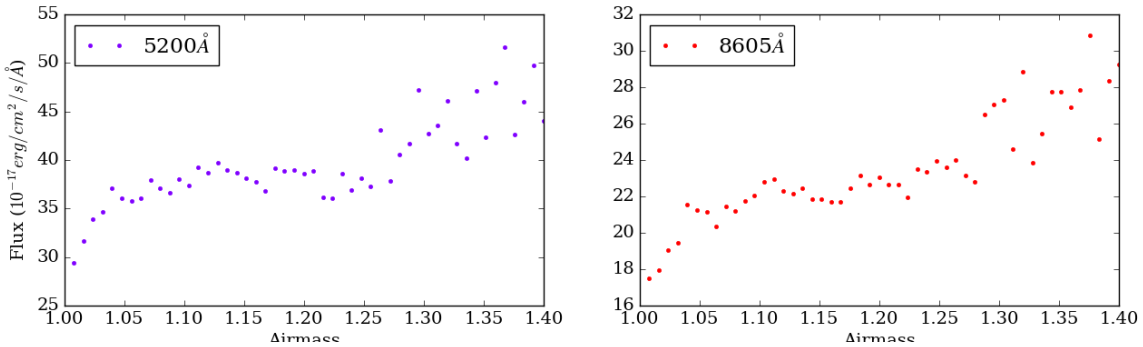

Figure 4.52: Relationship of airglow line flux and airmass for two lines: NI (5200$\mathring{A}$) and O2 (8605$\mathring{A}$). They show a rapid increase to and airmass of 1.05 and then a steady increase.

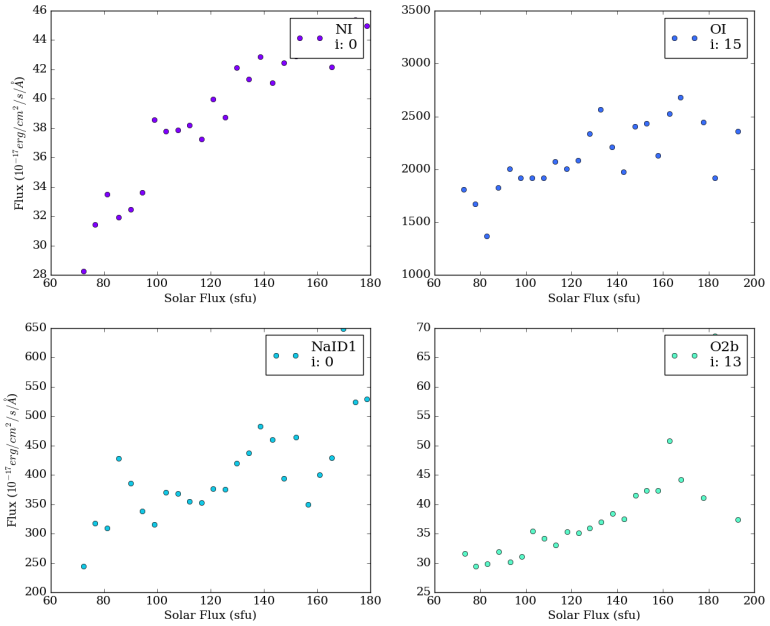

Figure 4.53: Correlation between solar flux and airglow line flux. Each panel shows a different airglow line, where NI is 5200$\mathring{A}$, OI is 5577$\mathring{A}$, NaID1 is at 5890$\mathring{A}$, and O2b is at 8695$\mathring{A}$. Also indicated is the time delay from the observation date (i) used to calculate the solar flux density.

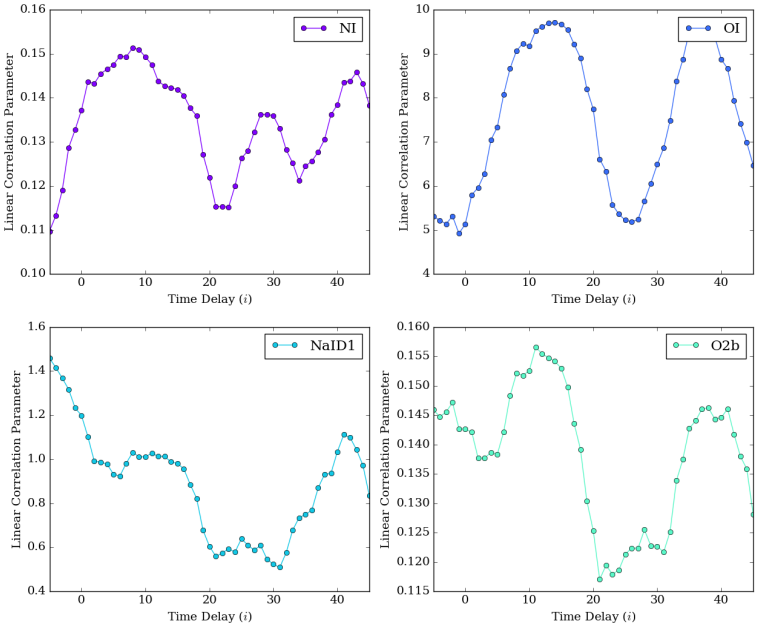

Figure 4.54: Linear correlation between airglow line flux and time delay for solar flux. Higher values indicate stronger correlation. Each panel show the time delay for the same lines as in figure 4.53.

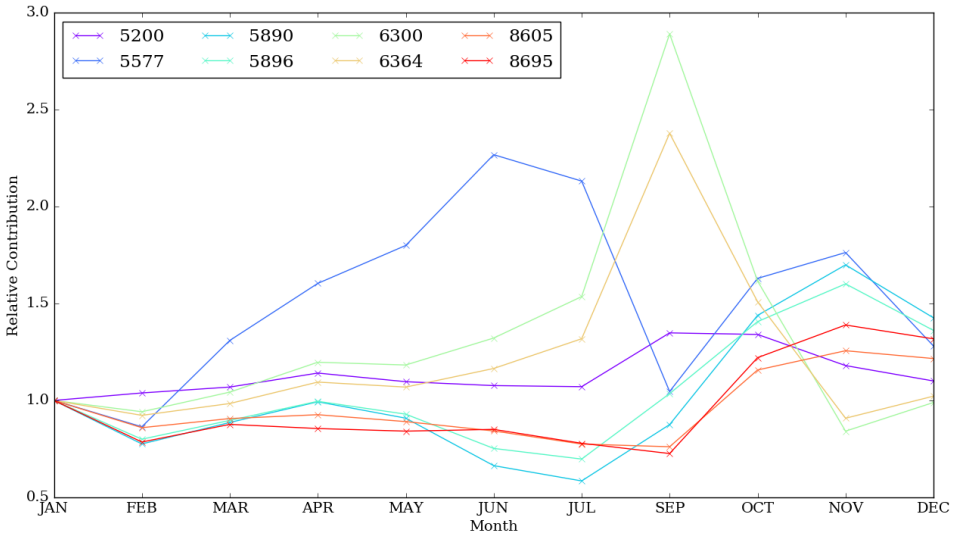

Figure 4.55: Relationship between airglow line flux and time of year. Each line represents the binned airglow emission in a month for a given airglow emission line, as indicated in the key in $\mathring{A}$.

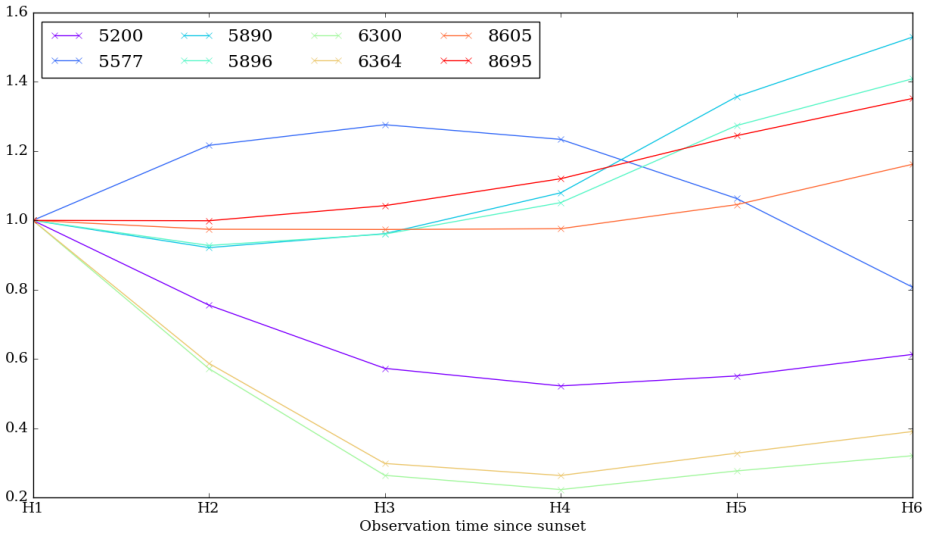

Figure 4.56: Relationship between airglow line flux and time of night. The night is split into six sections from sunset to sunrise (H1-H6). Each line represents the binned airglow emission for observations taken during that fraction of the night, identified by their wavelength (in $\mathring{A}$) in the key.

We have only looked at general trends in the data here. This data set provides an opportunity for an in depth study of these airglow lines and others. As we did with the continuum flux, it would be useful to develop a predictive model for behavior of all airglow emission lines, including the OH Meinel bands.

4.4.3 Terrestrial Light

Apache Point Observatory, which is located in Sunspot, NM, isn't particularly close to any large population centers. The closest town is Alomogordo, NM, which is less than 20 miles away as the crow flies. This small town has a population of $\sim 30,000$ and is the closest town to White Sands Air Force Base. Larger cities are more than 100 miles away, with Las Cruces $\sim$ 100 miles SW, El Paso $\sim$ 120 miles SSW, and Albuquerque $\sim$ 230 miles North (fig. 4.57). To determine if there is a detectable increase of terrestrial light impacting our sky spectra, we look at the observations as a function of azimuth at high airmass. While there are observations at all azimuth values, there are few observations at especially high airmass in the BOSS data set, which makes this difficult in our case. Looking at a few bright lamp lines and the continuum flux at 600 nm, we don't see any significant correlation between the azimuth of an observation and the measured flux at airmass greater than 1.3 (fig 4.58). For the HgI and NaI line at 568 nm, it could be argued that there is an increase at an azimuth

of ∼230 and 260 deg. It is possible that this could be correlated with White Sands Air Force Base and Las Cruces.

Figure 4.57: Map near Apache Point Observatory. Locations of populations centers in the vicinity are identified.

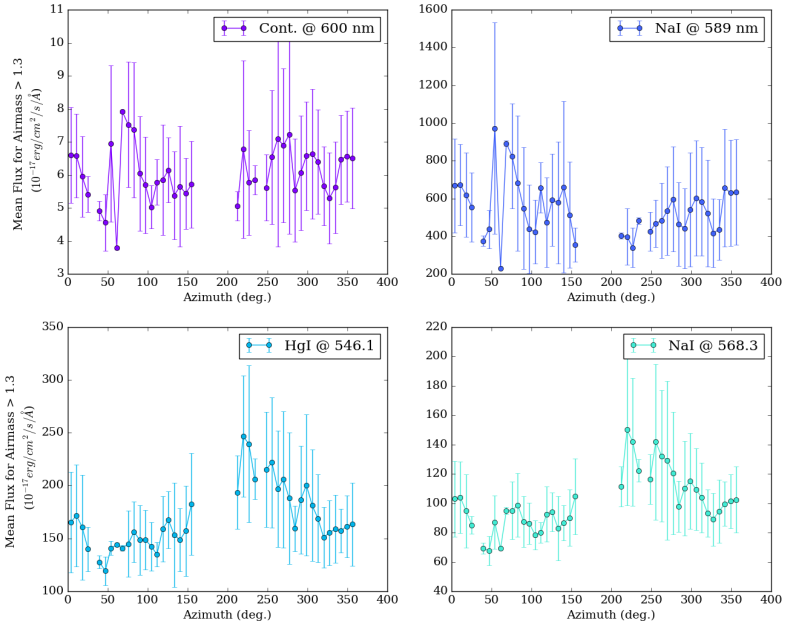

Figure 4.58: Airglow lines flux vs. azimuth for one continuum band and 3 artificial lamp lines, as indicated in the key.

Even though we don't have strong evidence for increased brightness from a city, we certainly see the impact of artificial light in our spectra. Figure 4.59 shows two sky spectra taken at different airmass. While the overall flux is certainly higher at a higher airmass, the strength of the artificial lines (identified) don't scale. In fact, some of these lines decrease in strength at higher airmass. It is not clear what causes this, and constitutes an interesting problem on its own. The artificial light pollution certainly does impact all BOSS observations at all airmass values. Since DESI will be closer to large population centers, this should be investigated at Kitt Peak during DESI commissioning and science validation to determine the overall impact to redshift completion.

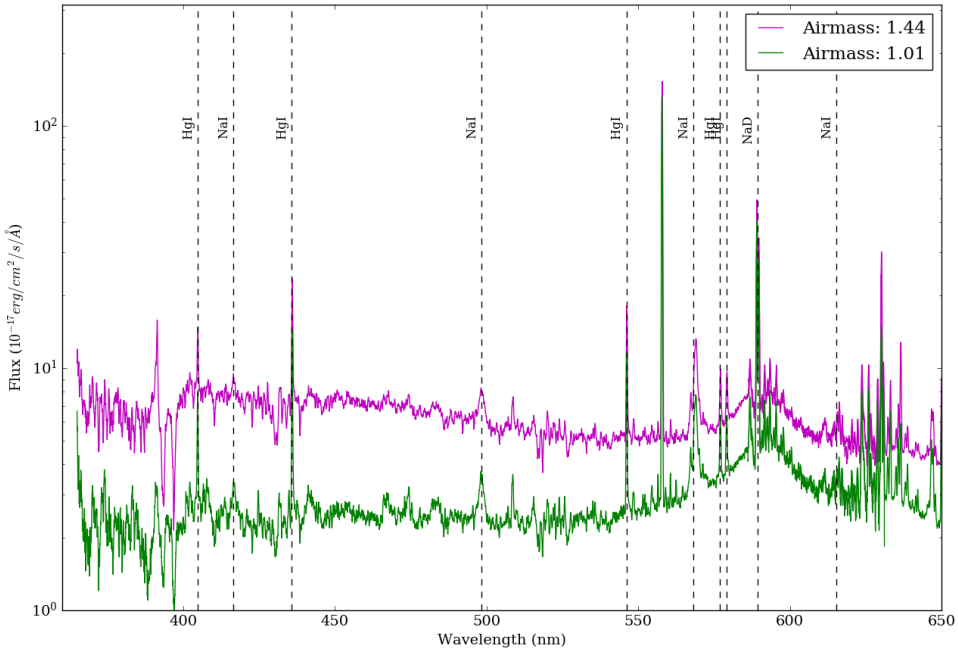

Figure 4.59: Sky spectra at different airmass values. Artificial lamp lines, identified by vertical black lines, are just as significant at low airmass as at higher airmass.

4.4.4 Evaluation of Continuum Model

During dark time, we measured a mean value of $2.55 \times 10^{-17} erg/cm^2/s/\AA$ (0.81×10^{-17} $erg/cm^2/s/\AA/arcsec^2$), mostly constant across the wavelength range except around 590 nm. The variance during dark time is $\sim 0.55 \times 10^{-17} erg/cm^2/s/\AA$ (0.175×10^{-17} $erg/cm^2/s/\AA/arcsec^2$) . The mean continuum value reduces to $2.11 \times 10^{-17} erg/cm^2/s/\AA$ at zenith (airmass < 1.01) when far from the ecliptic and galactic plane (ecliptic and galactic latitudes $> 30°$). The dark continuum and zenith dark continuum mean measurements are plotted in figure 4.60. The dark sky continuum is dependent on the zodiacal contribution, as a function of ecliptic latitude, and solar activity. While the continuum is fairly constant across the $360 - 1040$ nm range, we look at the relationship between a few regions of the dark time continuum (450 - 500 nm, 700 - 750 nm, and 950 - 1000 nm) and ecliptic latitude and solar activity levels in table 4.6. The values in this table were calculated using the continuum model presented in this work, using a reference observation taken in February, 6 hours after sunset at an airmass of 1, galactic latitude of 35°, galactic longitude of 145°, sun and moon altitude of -25°, sun separation of 130°, moon illumination fraction of 0.17, and a moon separation angle of 130°. The above atmosphere values represent the expected contribution from only zodiacal light according to our model. The table shows that the continuum gets brighter with increased

solar flux density, measured in sfu at 2800 MHz, and decreases with ecliptic latitude.

Our continuum model, as defined in eqn. 4.23, can account for up to 50% of the variance, defined as σ^2 in the BOSS sky spectra. Figure 4.61 shows the fraction of unexplained variance, defined as: Var(data - model)/Var(data). For the dark and moon models, the plot shows the fraction of unexplained variance for both the photometric data only and after adding the cloudy data, showing that on average, the non-photometric conditions (clouds) add $\sim 5\%$ unexplained variance to the data. For the twilight model, which uses all data with the sun altitude above $-20°$, there was not enough photometric data to fit the model.

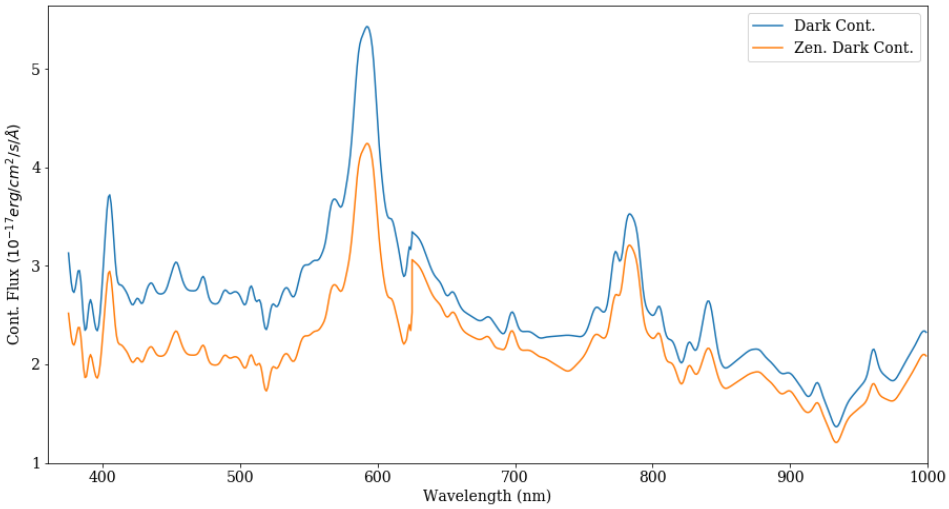

Figure 4.60: Measured Dark Continuum Flux in $10^{-17} erg/cm^2/s/\mathring{A}$. This is shown for mean dark conditions, with airmass < 1.4, moon below the horizon, sun with an altitude less than $-18°$ and galactic latitude greater than $10°$. The dark zenith value further constrains this to observations with airmass less than 1.01 and ecliptic and galactic latitudes greater than $30°$.

Location	λ range (nm)	sfu	$\|\beta\| = 0°$	$\|\beta\| = 30°$	$\|\beta\| = 60°$	$\|\beta\| = 90°$
			Cont. Flux $10^{-17} erg/cm^2/s/\AA$			
APO	450 - 500	70	2.78	2.06	1.67	1.50
APO	450 - 500	110	3.24	2.52	2.13	1.96
APO	450 - 500	200	4.28	3.56	3.18	3.01
Above atm.	450 - 500	-	1.72	1.00	0.62	0.45
APO	700 - 750	70	1.95	1.45	1.18	1.06
APO	700 - 750	110	2.24	1.74	1.48	1.36
APO	700 - 750	200	2.89	2.39	2.13	2.01
Above atm.	700 - 750	-	1.20	0.70	0.43	0.31
APO	950 - 1000	70	1.56	1.17	0.96	0.86
APO	950 - 1000	110	1.82	1.42	1.21	1.12
APO	950 - 1000	200	2.38	2.00	1.79	1.69
Above atm.	950 - 1000	-	0.94	0.55	0.34	0.25

Table 4.6: Dark time continuum sky levels expected from space (above atmosphere) and from ground-based measurements at Apache Point Observatory at times of low solar flux (sfu = 70), typical solar flux (sfu = 110), and high solar flux (sfu = 200), encountered from 2009-2014 as a function of ecliptic latitude ($|\beta|$). The values listed are calculated with our new model, using a reference observation taken in February, 6 hours after sunset at an airmass of 1, galactic latitude of 35°, galactic longitude of 145°, sun and moon altitude of -25°, sun separation of 130°, moon illumination fraction of 0.17, and a moon separation angle f 130°. The above atmosphere values are just the contribution from zodiacal light.

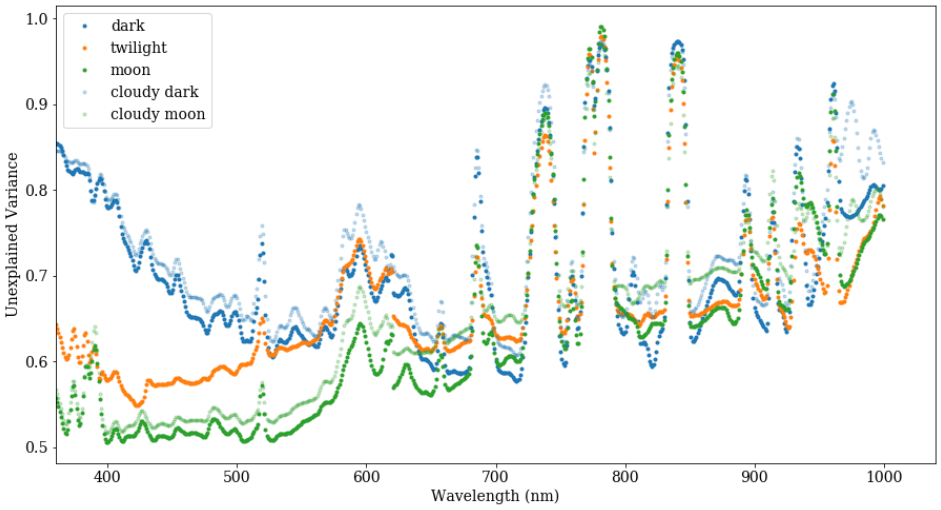

Figure 4.61: Fraction of unexplained variance for the continuum model. The dark and moon models were run with both photometric and non-photometric data sets.

Figure 4.62 shows the distribution of the residuals. For wavelength bins with a relatively low fraction of unexplained variance, like at 510 and 860 nm, the residuals are predominantly normally distributed. The residuals for the wavelength bins with a higher fraction of unexplained variance, like 600 and 740 nm, are more widely distributed than at 510 and 860 nm. The small number of outliers centered at $\sim 7 \times 10^{-17} erg/cm^2/s/\mathring{A}$ in the 740 nm wavelength bin can likely be attributed to the flux from airglow emission lines that weren't perfectly removed. The outliers at $\sim 8\sigma$ have absolute residuals greater than $4{\times}10^{-17} erg/cm^2/s/\mathring{A}$ in the blue and $2{\times}10^{-17} erg/cm^2/s/\mathring{A}$ in the red. We measured the correlation between the continuum flux in these outliers and any measured observational parameters, but found no significant observational similarities. Below we discuss possible improvements to our model to decrease the level of unexplained variance. Before any additional improvements are made to our model, however, it is still a significant improvement to the model currently used on DESI.

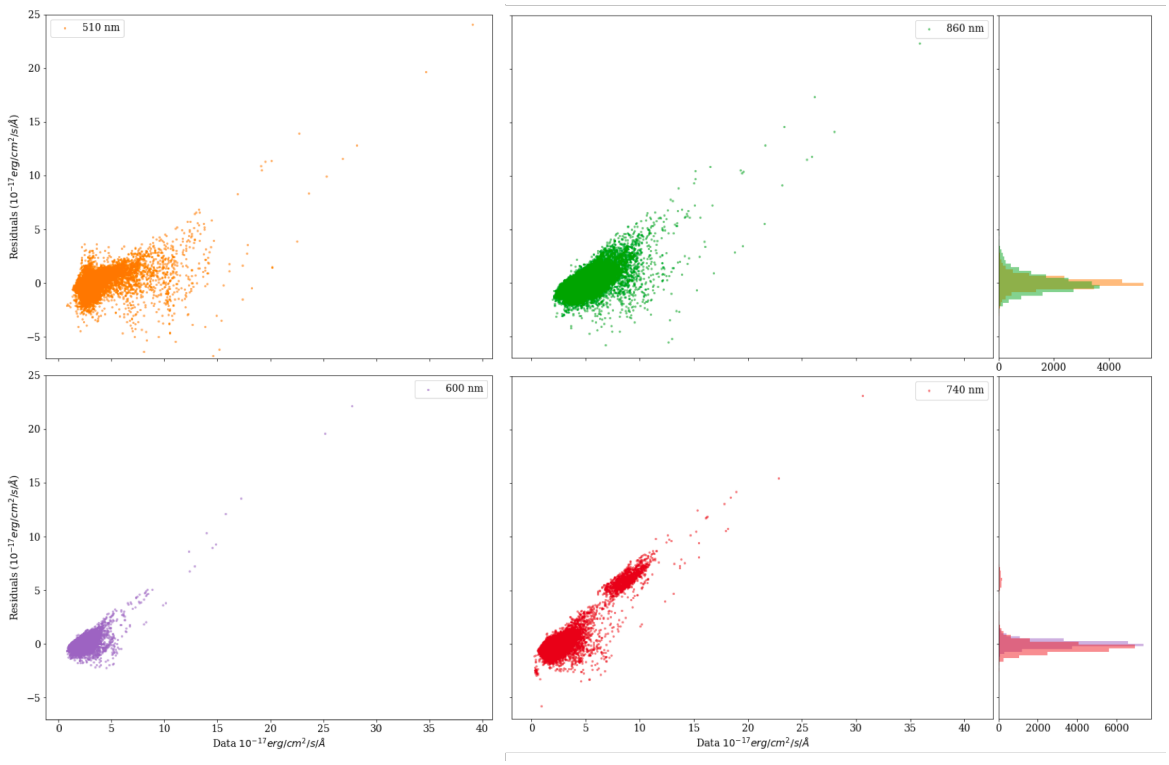

Figure 4.62: Data vs. residuals (data-model) in units of $10^{-17} erg/cm^2/s/\mathring{A}$ for a wavelength bins in the blue (510, 600 nm) and red (740, 860 nm) as indicated in the key. The wavelength bins 600 and 740 nm have higher unexplained variance.

Possible Improvements to Model

There are several places where the unexplained variance is considerably higher using our continuum model. These are around 589, 740, 780, 830, and 900 to 1030 nm. This is likely due to the fact that it was more difficult to get an accurate measurement on the continuum at those points as there are several overlapping airglow lines. Around 589 nm, the NaD is likely mostly terrestrial light since there is considerable broadband emission from both low and high pressure sodium lamps at this wavelength (Sánchez *et al.* 2007). Additionally, the internal calibration errors between the BOSS wavelength channels occurs between 570 and 630 nm, which contributes some additional uncertainty. We believe that improving methods to extract the continuum in these strong airglow emission areas will enable us to reduce the variance considerably in the redder wavelengths.

In addition to the model parameters in eqn. 4.23, we also explored the inclusion of other dependent variables for which we had data, including: air temperature, dew point, wind speed and direction, humidity, pressure, and dust levels in the atmosphere. The addition of these to our model did not improve the goodness-of-fit in any meaningful way. We believe that a more comprehensive study of the mechanisms for the impact of solar flux (i.e. time delay and easement) will lead to a more complex functional model that will improve the overall sky model. Additionally, a model for how broadband artificial light might impact observations at hight airmass would be useful as there is clear evidence of artificial lamp line emission even at zenith.

It would be useful to test the model on other spectra taken at APO, including eBOSS (SDSS-IV), APOGEE, and MaNGA. This will enable us to identify any systematic issues in our model and significantly extend our dataset.

Improvements to DESI Sky Model

The current DESI sky background model for survey planning includes a static dark sky spectrum from Hanuschik (2003) (see fig. 4.2) with no variance and a scattered moonlight model from Krisciunas & Schaefer (1991). Our model is a significant advance over this, as it accounts for the variance in the dark night sky continuum and twilight. Our work indicates that in addition to a dark sky spectrum it is important to account for changes in zodiacal light and other factors that impact the brightness of the airglow continuum (i.e. solar flux and airmass). While few measurements are planned at sun altitudes greater than $-18°$ during the dark campaign, twilight could impact the gray and bright programs.

Using observational parameters from BOSS observations, we can compare the measured values to the model values from both the current DESI model and the new continuum model presented in this work. Figure 4.63 shows the results for dark time observations, and figure 4.64 shows the results for when the moon is above the horizon, both showing that the new model is an improvement over that currently used on DESI. The use of our new model in survey simulations will increase our confidence in our results.

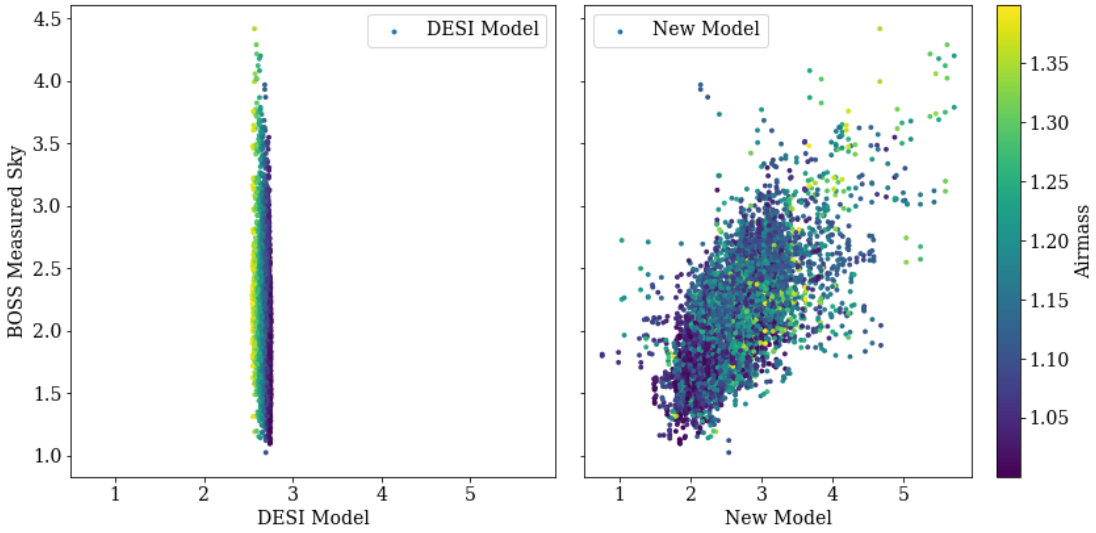

Figure 4.63: **Left:** DESI sky model vs. BOSS measurements for data during dark time. The BOSS measurements are taken at 480 nm and compared to the value calculated by the DESI model at that wavelength. The distribution of the DESI model during dark time shows very little variance because it does not include several important parameters, like ecliptic latitude and solar activity. **Right:** New sky model during dark time better predicts the BOSS measurements by the inclusion of zodiacal light and solar activity in the model.

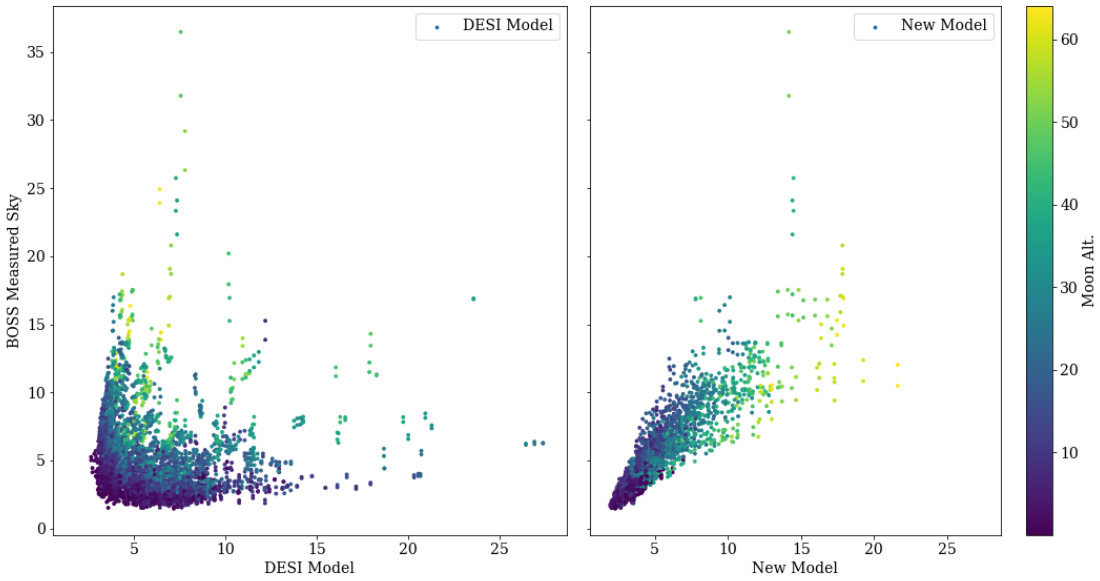

Figure 4.64: **Left:** DESI sky model vs. BOSS measurements for data with the moon above the horizon. The BOSS measurements are taken at 480 nm and compared to the value calculated by the DESI model at that wavelength. **Right:** New sky model during bright better predicts the BOSS measurements by more accurately modeling the lunar parameters.

The DESI dark program, the key project for the DESI survey, currently uses an average UVES sky spectrum for all simulations. This has an average continuum value of $\sim 1 \times 10^{-17} erg/cm^2/\ s/\mathring{A}/arcsec^2$ across all wavelengths. We have measured a value of $\sim 0.81 \times 10^{-17} erg/cm^2/s/\mathring{A}/arcsec^2$. If we also include the impact of zodiacal light and solar activity, we find an additional $\sim$ 18% margin on the current DESI survey plan. This means that, under the assumption that solar cycle 25 is very similar to solar cycle 24, the total dark survey could take up to 18% less time than currently assumed. The DESI survey also has gray and bright programs. Since we are using spectroscopic data, rather than broadband photometry, to fit the scattered moonlight, we are able to better fit the lunar parameters. I find that the lunar model from Krisciunas & Schaefer (1991) (see sec. 4.1), underestimates the brightness of the sky. Based on our new model, we expect that exposure times when the moon is above the horizon will be longer than currently assumed. Overall, we expect that the dark time program is achievable within the 5 year survey allocation time and there is up to 18% additional margin.

As mentioned previously, the current sky model for DESI does not include zodiacal light or effects of solar activity. These were also not considered in the initial footprint selection and survey planning. Our work indicates that future survey designs should consider the contribution of zodiacal light, accounting for the footprint ecliptic latitude relative to the ecliptic plane. Additionally, future survey planning, should consider the impact of solar activity. We will have access to predictions of solar activity and active measurements from

current space observatories, like the Parker Solar Probe (no connection to the author), and since the impact on sky brightness has a delay of $\sim$ 5 days, these measurements can be used in observation planning. Furthermore, the change in solar activity across the DESI survey time introduces additional observational variance, independent of terrestrial weather patterns. We expect up to 30% variance in the sky background from year to year based on the solar activity.

To use our new continuum model for planning on DESI, it will be important to increase the flux due to proximity to Tucson based on the work of Neugent & Massey (2010). Additionally, the altitude of APO is higher than that of Kitt Peak by $\sim$ 700 m which will have an impact on some of the scattering effects. These will need to be calibrated while taking DESI observations during commissioning. To use our model predictively, we have written a simple program, **boss_sky.py**, which will produce continuum spectra based on the input of the following parameters: airmass, ecliptic latitude, date and time of observation, galactic latitude and longitude, sun altitude, sun separation angle, moon illumination or phase, moon separation and moon altitude. Below are two examples of the output spectrum from this program compared to the measured spectrum, one for dark time and one for bright time (fig. 4.65). In the future, we will update this program to include airglow and artificial line emissions, which can then be incorporated into an exposure time calculator to be used for DESI observations.

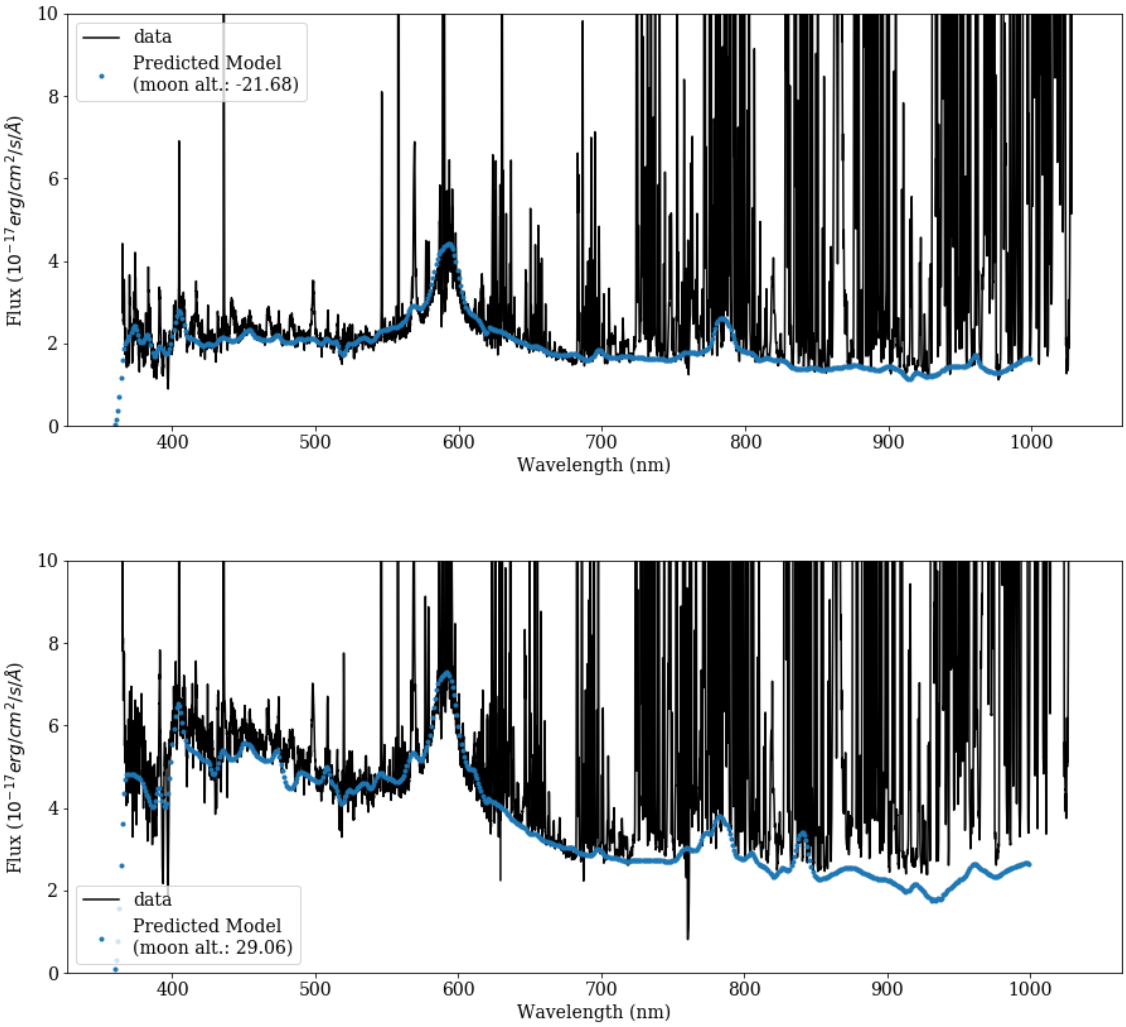

Figure 4.65: Continuum model prediction vs. data, one during dark time and another when the continuum is significantly higher when the moon is above the horizon.

4.4.5 Comparison to Other Results

The night sky above APO appears to be slightly brighter than at Kitt Peak. Comparing the dark time zenith spectrum at Kitt Peak as measured by Neugent & Massey (2010) to our measurements (fig. 4.66), we see that the BOSS spectrum, plotted here as synthetic Vega magnitudes per arcsec^2, is overall slightly brighter. We calculated the synthetic broadband magnitudes for the bessel bands (UBVRI) to compare to past measurements as discussed in section 4.2. Table 4.7 lists the minimum, maximum, and mean levels for the synthetic

broadband measurements, calculated with the airglow and artificial lines included. The mean percentage of the flux in these bands from airglow lines, as opposed to continuum flux, is listed. Also listed are the results from some of the observations listed in table 4.2, including Pilachowski *et al.* (1989), Pedani (2009), and Patat (2008). Figure 4.67 shows the distribution of these magnitudes of dark zenith observations, defined as those with airmass less than 1.01, moon and sun altitude below the horizon, and galactic latitude great than 10°. These observation are further split by solar flux, with high solar flux observations having 100 sfu or larger. The synthetic broadband measurements from BOSS indicate that the dark zenith sky above APO has a higher mean brightness than other observatories. However, our calculated range of values encompass the values from these other sites except for at Kitt Peak.

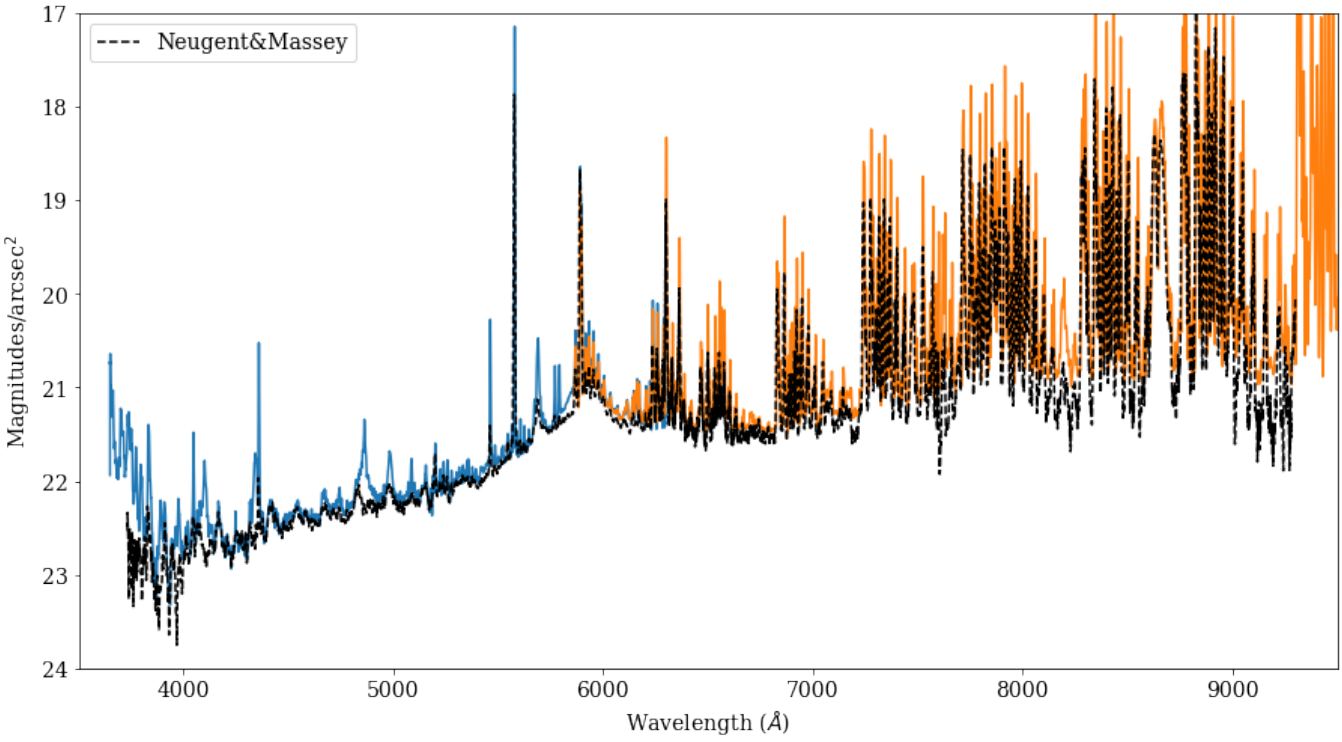

Figure 4.66: Dark zenith spectrum compared to Neugent & Massey (2010) in mag/arcsec^2. The Kitt Peak spectrum is slightly darker than the BOSS spectrum and some of the artificial lamp lines are more pronounced in the BOSS spectrum. Note: lower Vega magnitudes correspond to brighter sky flux.

Band	mean	min	max	% lines	Kitt Peak[a]	Mt. Graham[b]	Cerro Paranal[c]
	mag/arcsec^2						
U	21.55	21.82	21.44	0		21.2	22.4
B	22.27	22.76	21.95	$\sim 5\%$	22.9	22.8	22.7
V	21.33	21.80	20.90	$\sim 20\%$	21.9	21.8	21.7
R	20.73	21.35	20.11	$\sim 20\%$		20.8	20.9
I	19.48	20.18	18.71	$\sim 55\%$		19.8	19.6

Table 4.7: Dark zenith synthetic broadband magnitudes. The column "% lines" is an estimate of the percentage of the flux in that band that comes from airglow and artificial lines. Also listed are the broadband values from three other sites: (a) Pilachowski *et al.* (1989), (b) Pedani (2009), (c) Patat (2008). Measurements from other sites can be found in table 4.2.

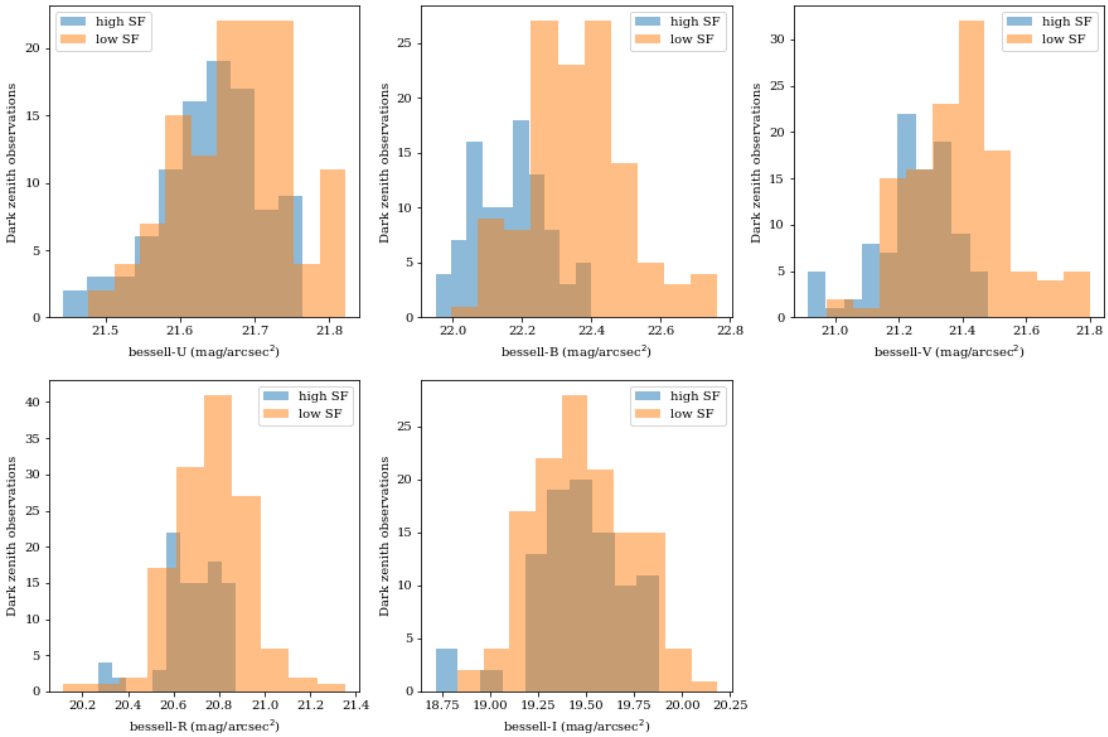

Figure 4.67: Distribution of synthetic broadband (UBVRI) magnitudes for dark zenith observations. They are split into two groups depending on the solar flux (sf) measured for that observation. The low sf observations have values of sfu $\leq$100 and high sf observations have sfu $>$ 100.

While our dark zenith spectrum indicates that the continuum sky level at APO is slightly brighter than that at Kitt Peak, our continuum measurements are somewhat lower than measurements made elsewhere in the optical wavelength range, with a mean value of 0.6×10^{-17} $erg/cm^2/s/\mathring{A}/arcsec^2$ at 860 nm, including zodiacal emission. At first glance, it would seem that our measurements are comparable to $0.682 \pm 0.2 \times 10^{-17}$ $erg/cm^2/s/\mathring{A}/arcsec^2$ measured by Sternberg & Ingham (1972) and $0.65\pm0.169\times10^{-17} erg/cm^2/s/\mathring{A}/arcsec^2$ measured by Noll *et al.* (2012) at the same wavelength. However, those measurements claim explicit removal of the zodiacal light, which can make up to 50% of this flux. It seems then, than our measurement is lower than these previous measurements by $\sim$ 30% accounting for the zodiacal contribution. Noxon (1978) published continuum flux values ranging from 0.213 to 0.682 $\times10^{-17} erg/cm^2/s/\mathring{A}/arcsec^2$ at 857 nm, with a mean value almost half of our measurement. It is possible that his measurements were taken far from the ecliptic plane, but it is not discussed.

Our measurements of the continuum at redder wavelengths are lower than other published values. Sullivan & Simcoe (2012) found that the inter-airglow continuum in the Y band was 20.05 AB mag/arcsec$^2\pm0.04$, corresponding to $\sim 3.13\times10^{-17} erg/cm^2/s/\mathring{A}$. While the full Y band extends beyond the BOSS wavelength coverage, we assume that there is little variation in the continuum flux at 1040 nm and 1080 nm where the Y band ends. We calculated the Y_{AB} magnitudes for our dark time continuum to have a mean of $\sim$ 20.8 mag/arcsec^2, shown in figure 4.68 for two different Y band definitions. This is considerably darker than the Sullivan & Simcoe (2012) findings ($\Delta Y_{AB} = 0.75$ mag/arcsec^2). While the behavior of the OH Meinel lines is complex, the continuum in the red is quite low and not particularly impacted by twilight, and moonlight.

Throughout section 4.4.1 we discussed how certain effects measured in the continuum sky compared to past measurements. We highlight important findings here. First, we find that the change in the sky background from an airmass of 1 to 1.4 ranges from 0.3 - 1.5 $\times10^{-17} erg/cm^2/s/\mathring{A}$, which is consistent with measurements of 0.1 - 0.3 mag increase measured by Leinert *et al.* (1995), Krisciunas (1990), and Pedani (2009). The zodiacal light contribution to the total continuum ranges from 15% to 50%, similar to findings by Mattila *et al.* (1996) and Plauchu-Frayn *et al.* (2017). This partially explains the correlation between continuum flux and the solar flux, as the majority of the continuum is generated by continuum airglow processes. While dependence on both the continuum and airglow emission line flux on solar flux density is clear, the time delay between observation time and the time of correlated solar flux measurements is complicated and dependent on wavelength. Overall, however, our results indicate a time delay of $\sim$ 5 days followed by another χ^2 minimum in the model fit for a time delay $\sim$ 25 days following the first (see fig. 4.37). This result is consistent with findings from both Krisciunas *et al.* (2007), who measured a time delay of 5 days, and Patat (2008) who measured a time delay of $\sim$ 30 days.

The seasonal variations we see in the BOSS data set are similar to those in Patat (2008), however we see that the increase in Oct./Nov. greatly exceeds any possible increase in Mar./Apr. We do see that the sky becomes darker after twilight and then gets brighter about half way through the night (a.k.a. the *Walker Effect*). This effect seems more signifi-

cant in the redder wavelengths, however, which may be why other programs didn't observe it. While there are few published studies of twilight, the behavior of the continuum as a function of sun latitude agrees with the study by Patat (2003). We believe that inclusion of factors for sun separation and a relative throughput factor strengthen our model. For our moon model, we used many components from the Jones *et al.* (2013) model. Therefore, we expect general agreement with that model, but we have not yet measured the accuracy of our model relative to others.

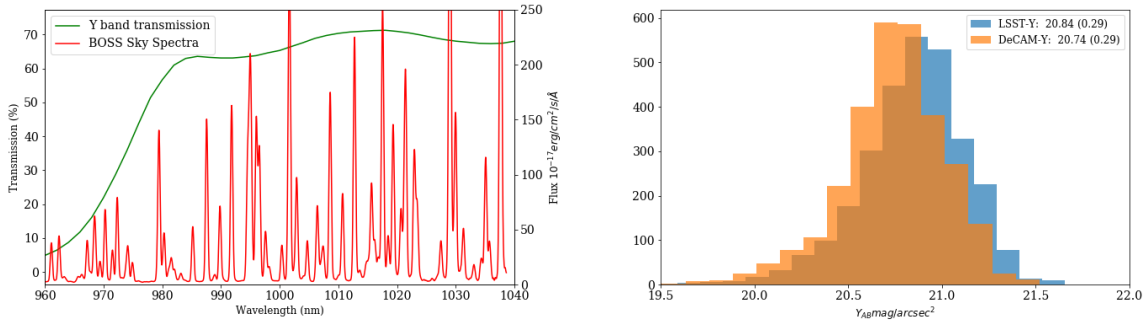

Figure 4.68: **Left:** Y band transmission curve with the BOSS sky flux. The continuum magnitude is calculate only using the inter airglow continuum values up to 1030 nm. **Right:**Y_{AB} mag/arcsec^2 for dark continuum observations

4.4.6 Future Impact of Solar Activity

The variance in the sky background continuum during dark time is dominated by the impact of solar activity on airglow emissions. This implies that any ground based observational program will be impacted by large changes in the sun's activity. We are just now entering solar cycle 25. It is expected that the solar maximum of this solar cycle will be similar to that of that last, which is considered one of the lowest activity cycles recorded since the 1800s. This is generally good news for DESI and other observational programs planned for the next decade, however, this does not make them immune to unique space weather occurrences. Large coronal mass ejections (CMEs), like that seen during the Carrington Event of 1859, would likely shut down our electrical grid. Since that event, others of a similar magnitude have been measured, but were not directed at Earth. Like CMEs, solar radio bursts (SRBs) are directional phenomena, and have a recorded peak flux value of $1.5{\times}10^6$ sfu (1 sfu = $10^{-22}W/m^2/Hz$) at 2800 MHz. This is in contrast to the mean value used in our study of 100 sfu. If the relationship between solar flux density at 2800 MHz and continuum sky brightness remained linear at very high values, the sky brightness would increase by a factor of more than 10,000 if the SRB were to collide with the atmosphere above Arizona. While space weather events like CMEs and SRBs have short timescales (less

than a day), we don't fully understand the mechanism for interaction between solar flux and airglow, so an event might impact astronomical observations for several nights.

4.4.7 Implications for Future Ground and Space Programs

We have measured the inter-airglow continuum around 1μm during low solar activity to be $0.27 \times 10^{-17} erg/cm^2/s/\mathring{A}/arcsec^2$ with an above atmosphere value of 0.08 $\times 10^{-17} erg/cm^2/s/\mathring{A}/arcsec^2$, which indicates there is just a factor of 3.4 improvement when observing from space in these conditions. The cosmology community has a strong need to measure the redshift of galaxies in the near-infrared (NIR), gaining deep observations of highly-redshifted objects. Due to the dense OH emission lines in the NIR, it is often argued that there is a need for a space based platform to measure these distant objects. Ellis & Bland-Hawthorn (2008) argue that if an instrument has sufficient resolution, it could measure between OH lines with the only sky noise coming from a relatively low inter-airglow line continuum. If this were possible, ground-based observations of high redshift objects would be possible. Our measurements give some credence to this assertion. First, we measure that the inter-airglow line continuum at wavelengths between 900 and 1040 nm during dark time is ∼165 $photons/m^2/s/\mu m/arcsec^2$, a lower value than measured by Sullivan & Simcoe (2012) (see sec. 4.4.5) and Ellis *et al.* (2012), who measured a value of 860 $photons/m^2/s/\mu m/arcsec^2$ at 1.65 μm. While we don't have measurements in the J and H bands, we believe the inter-airglow continuum flux is mostly constant.

Furthermore, we measure that 15 - 50% of the light in the continuum, even at redder wavelengths, comes from the zodiacal. In table 4.6, we see that between 950 and 1000 nm, at an ecliptic latitude of 90° during low solar activity, the continuum brightness is $0.27 \times 10^{-17} erg/cm^2/s/\mathring{A}/arcsec^2$ on the ground and $0.08 \times 10^{-17} erg/cm^2/s/\mathring{A}/arcsec^2$ above the atmosphere, just a factor of 3.4. This increases by an additional factor of ~ 2 during high solar activity. It should be noted that our measurements are made with a moderate resolution spectrograph with VPH gratings which have low scattering, allowing us to make observations down to the inter-airglow continuum level. Table 4.8 lists the effective speeds for point source spectroscopy relative to SDSS for both space and ground platforms. These values assume a spectrograph capable of measuring the continuum level between airglow lines. It also assumes the use of adaptive optics (AO) with ground telescopes, expecting that diffraction limited seeing will be achievable with TMT. Given these assumptions, ground observations will be potentially much more capable than space platforms, especially during low solar activity. Even if future AO systems are not able to deliver exactly diffraction limited seeing, we expect great performance. Since the majority of the continuum flux is dependent on the solar activity, which changes on day time scales, they can be predicted and planned around using existing solar observatories.

	Observatory	Aperture (m^2)	Seeing (FWHM arcsec)	NEA[a]	Sky Cont.[b] per arcsec^2	Speed/SDSS[c]
Ground	SDSS	3.68	2”	3.14	0.27	1
	Keck AO	76	0.040”	0.0036	0.27	17,896
	TMT AO	655	0.0125”	0.00035	0.27	1,579,411
Space	HST/WFIRST	4.525	0.050”	0.005	0.08	2,302
	JWST	25	0.038”	0.036	0.08	19,869

Table 4.8: Effective speed for point source spectroscopy for ground and space platforms at $\sim 1\mu$m. (a) NEA is the noise equivalent area which is the unity weighted aperture that would contribute the same variance to the measurement (King 1983). (b) The sky continuum values are taken from table 4.6 for low solar flux (70 sfu) at an ecliptic latitude of 90°. They are listed here with units of $10^{-17} erg/cm^2/s/\mathring{A}/arcsec^2$. (c) The speed is calculated as the inverse exposure time which, in the limit of dim objects, is $(S/N)^2$.

4.5 Conclusions

In the final chapter of this thesis we present the analysis of the largest data set of sky spectra yet published. We created a model of the inter-airglow line continuum sky background using the BOSS sky spectra. The dark time continuum sky is measured to be $\sim 2.55 \times 10^{-17} erg/cm^2/s/\mathring{A}$ across the full wavelength range, with a variance of $\sim 0.55 \times 10^{-17} erg/cm^2/s/\mathring{A}$. The model accounts for up to 50% of the variance in these sky spectra, providing us with a much improved predictive sky model to be used for the planning and operation of DESI. We find that the dark sky continuum is composed of $\sim 30\%$ light from the zodiacal and the remainder attributed to “airglow continuum”, which is strongly impacted by the activity of the sun. Our measurements of the inter-airglow line continuum in the near-infrared is lower than previous measurements, suggesting the possibility that deep observations of high-redshift objects could be achievable from the ground. We also find that the sky continuum is brighter in Oct./Nov. and gets darker after twilight until halfway through the night. Our measurements indicate that Apache Point Observatory is among the darkest astronomical sites, only somewhat brighter than Kitt Peak. The continuum model developed using the BOSS data will be used to more effectively plan the survey for DESI and any future spectroscopic surveys. Our observations indicate that additional margin, up to 18%, can be assumed for the DESI dark program. Using a set of 13 observational parameters, the model will enable us to estimate exposure times for DESI during operations.

Bibliography

References for Chapter 1

2. Abbott, B. P. *et al.* GW170817: Observation of Gravitational Waves from a Binary Neutron Star Inspiral. *Phys. Rev. Lett.* **119,** 161101 (16 Oct. 2017).
3. Alam, S. *et al.* The clustering of galaxies in the completed SDSS-III Baryon Oscillation Spectroscopic Survey: cosmological analysis of the DR12 galaxy sample. *Monthly Notices of the Royal Astronomical Society* **470,** 2617 (Sept. 2017).
5. Albrecht, A. *et al.* Report of the Dark Energy Task Force. *ArXiv Astrophysics e-prints.* eprint: astro-ph/0609591 (Sept. 2006).
9. Anderson, L. *et al.* The clustering of galaxies in the SDSS-III Baryon Oscillation Spectroscopic Survey: Baryon Acoustic Oscillations in the Data Release 9 Spectroscopic Galaxy Sample. *Monthly Notices of the Royal Astronomical Society* **427,** 3435–3467 (2012).
10. Anderson, L. *et al.* The clustering of galaxies in the SDSS-III Baryon Oscillation Spectroscopic Survey: baryon acoustic oscillations in the Data Releases 10 and 11 Galaxy samples. *Monthly Notices of the Royal Astronomical Society* **441,** 24–62 (June 2014).
12. Balbi, A. *et al.* Constraints on Cosmological Parameters from MAXIMA-1. *Astrophysical Journal, Letters* **545,** L1–L4 (Dec. 2000).
13. Baldry, I. K. *et al.* Galaxy And Mass Assembly (GAMA): the input catalogue and star-galaxy separation. *Monthly Notices of the Royal Astronomical Society* **404,** 86–100 (May 2010).
15. Baum, W. A. *Photoelectric Magnitudes and Red-Shifts* in *Problems of Extra-Galactic Research* (ed McVittie, G. C.) **15** (1962), 390.
16. Bautista, J. *et al.* Measurement of BAO correlations at $z = 2.3$ with SDSS DR12 Lyman-α-Forests. *Astronomy and Astrophysics* **603,** A12 (2017).
17. Bautista, J. *et al.* The SDSS-IV extended Baryon Oscillation Spectroscopic Survey: Baryon Acoustic Oscillations at redshift of 0.72 with the DR14 Luminous Red Galaxy Sample. *ArXiv e-prints.* arXiv: 1712.08064 (Dec. 2017).

20. Bennett, C. L. *et al.* Nine-year Wilkinson Microwave Anisotropy Probe (WMAP) Observations: Final Maps and Results. *Astrophysical Journal, Supplement* **208,** 20 (Oct. 2013).

22. Betoule, M. *et al.* Improved Photometric Calibration of the SNLS and the SDSS Supernova Surveys. *Astronomy and Astrophysics* **552,** A124 (2012).

23. Beutler, F. *et al.* The 6dF Galaxy Survey: Baryon Acoustic Oscillations and the Local Hubble Constant. *Monthly Notices of the Royal Astronomical Society* **416,** 3017 (Oct. 2011).

24. Beutler, F. *et al.* The 6dF Galaxy Survey: z≈0 measurements of the growth rate and σ_8. *Monthly Notices of the Royal Astronomical Society* **423,** 3430–3444 (July 2012).

25. Blake, C. & Bridle, S. Cosmology with photometric redshift surveys. *Monthly Notices of the Royal Astronomical Society* **363,** 1329–1348 (Nov. 2005).

26. Blake, C., Collister, A., Bridle, S. & Lahav, O. Cosmological baryonic and matter densities from 600,000 SDSS Luminous Red Galaxies with photometric redshifts. *Monthly Notices of the Royal Astronomical Society* **374,** 1527–1548 (2006).

27. Blake, C. *et al.* The WiggleZ Dark Energy Survey: mapping the distance-redshift relation with baryon acoustic oscillations. *Monthly Notices of the Royal Astronomical Society* **418,** 1707 (Dec. 2011).

28. Blake, C. *et al.* Universal fitting formulae for baryon oscillation surveys. *Monthly Notices of the Royal Astronomical Society* **365,** 255 (2005).

29. Blake, C. *et al.* Galaxy And Mass Assembly (GAMA): improved cosmic growth measurements using multiple tracers of large-scale structure. *Monthly Notices of the Royal Astronomical Society* **436,** 3089–3105 (Dec. 2013).

30. Blake, C. *et al.* The WiggleZ Dark Energy Survey: the growth rate of cosmic structure since redshift z=0.9. *Monthly Notices of the Royal Astronomical Society* **415,** 2876–2891 (Aug. 2011).

31. Bolton, A. S. *et al.* Spectral Classification and Redshift Measurement for the SDSS-III Baryon Oscillation Spectroscopic Survey. *Astronomical Journal* **144,** 144 (Nov. 2012).

32. Busca, N. G. *et al.* Baryon Acoustic Oscillations in the Ly-α forest of BOSS quasars. *Astronomy and Astrophysics* **552,** A96 (2012).

34. Cervantes-Cota, J. L. & Smoot, G. *Cosmology today–A brief review* in *American Institute of Physics Conference Series* (eds Ureña-López, L. A., Aurelio Morales-Técotl, H., Linares-Romero, R., Santos-Rodríguez, E. & Estrada-Jiménez, S.) **1396** (Oct. 2011), 28–52.

35. Cole, S. *et al.* The 2dF Galaxy Redshift Survey: Power-spectrum analysis of the final dataset and cosmological implications. *Monthly Notices of the Royal Astronomical Society* **362,** 505–534 (2005).

36. Colless, M. *et al.* The 2dF Galaxy Redshift Survey: spectra and redshifts. *Monthly Notices of the Royal Astronomical Society* **328,** 1039–1063 (Dec. 2001).

37. Connolly, A. J. *et al.* Slicing Through Multicolor Space: Galaxy Redshifts from Broadband Photometry. *Astronomical Journal* **110,** 2655 (Dec. 1995).

39. Csabai, I. *et al.* The Application of Photometric Redshifts to the SDSS Early Data Release. *Astronomical Journal* **125,** 580–592 (Feb. 2003).

41. da Costa, L. *Galaxy redshift surveys: 20 years later (invited review)* in *Evolution of Large Scale Structure : From Recombination to Garching* (eds Banday, A. J., Sheth, R. K. & da Costa, L. N.) (Jan. 1999), 87.

42. da Costa, L. *et al.* The Southern Sky Redshift Survey. *The Astrophysical Journal* **327,** 544–560 (Apr. 1988).

43. Davis, M., Huchra, J., Latham, D. W. & Tonry, J. A survey of galaxy redshifts. II - The large scale space distribution. *The Astrophysical Journal* **253,** 423–445 (Feb. 1982).

44. Dawson, K. S. *et al.* The Baryon Oscillation Spectroscopic Survey of SDSS-III. *The Astronomical Journal* **145,** 10 (Jan. 2013).

45. Dawson, K. S. *et al.* The SDSS-IV Extended Baryon Oscillation Spectroscopic Survey: Overview and Early Data. *The Astronomical Journal* **151,** 44 (Feb. 2016).

46. de Bernardis, P. *et al.* Multiple Peaks in the Angular Power Spectrum of the Cosmic Microwave Background: Significance and Consequences for Cosmology. *Astrophysical Journal* **564,** 559–566 (Jan. 2002).

47. de Jong, R. S. *et al.* 4MOST: the 4-metre Multi-Object Spectroscopic Telescope project at preliminary design review. *Proc. SPIE* **9908** (Aug. 2016).

49. Delubac, T. *et al.* Baryon Acoustic Oscillations in the Lyα forest of BOSS DR11 quasars. *Astronomy and Astrophysics* **574,** A59 (2014).

50. DESI Collaboration *et al.* The DESI Experiment Part I: Science,Targeting, and Survey Design. *ArXiv e-prints.* arXiv: 1611.00036 [astro-ph.IM] (Oct. 2016).

51. DESI Collaboration *et al.* The DESI Experiment Part II: Instrument Design. eprint: arXiv:1611.00037v2 (Nov. 2016).

52. Dey, A. *et al.* Mosaic3: a red-sensitive upgrade for the prime focus camera at the Mayall 4m telescope. *Proc. SPIE* **9908** (2016).

53. Dey, A. *et al.* Overview of the DESI Legacy Imaging Surveys. *ArXiv e-prints.* arXiv: 1804.08657 [astro-ph.IM] (Apr. 2018).

54. Dodelson, S. *Modern cosmology* (2003).

56. Drinkwater, M. J. *et al.* The WiggleZ Dark Energy Survey: survey design and first data release. *Monthly Notices of the Royal Astronomical Society* **401,** 1429–1452 (Jan. 2010).

57. Du Mas des Bourboux, H. *et al.* Baryon acoustic oscillations from the complete SDSS-III Lyα-quasar cross-correlation function at $z = 2.4$. *Astronomy and Astrophysics* **608,** A130 (2017).

60. Eisenstein, D. J., Seo, H.-J., Sirko, E. & Spergel, D. N. Improving Cosmological Distance Measurements by Reconstruction of the Baryon Acoustic Peak. *The Astrophysical Journal* **664,** 675–679 (Aug. 2007).

61. Eisenstein, D. J. *et al.* Detection of the Baryon Acoustic Peak in the Large-Scale Correlation Function of SDSS Luminous Red Galaxies. *The Astrophysical Journal* **633,** 560–574 (2005).

65. Fagrelius, P., Poppett, C. & Edelstein, J. Fusion splicing: a novel approach to fiber connections for the Dark Energy Spectroscopic Instrument. *Proc. SPIE* **9908** (Aug. 2016).

67. Fagrelius, P. *et al.* ProtoDESI: First On-Sky Technology Demonstration for the Dark Energy Spectroscopic Instrument. *Publications of the Astronomical Society of the Pacific* **130,** 025005 (Feb. 2018).

68. Feldman, H. A., Kaiser, N. & Peacock, J. A. Power-spectrum analysis of three-dimensional redshift surveys. *Astrophysical Journal* **426,** 23–37 (May 1994).

69. Fernández-Soto, A., Lanzetta, K. M. & Yahil, A. A New Catalog of Photometric Redshifts in the Hubble Deep Field. *Astrophysical Journal* **513,** 34–50 (Mar. 1999).

70. Fisher, K. *et al.* The IRAS 1.2 Jy Survey: Redshift Data. *The Astrophysical Journal Supplement Series* **100,** 69 (Sept. 1995).

71. Flaugher, B. *et al.* The Dark Energy Camera. *The Astronomical Journal* **150,** 150 (2015).

72. Font-Ribera, A. *et al.* Quasar-Lyman$-\alpha$ Forest Cross-Correlation from BOSS DR11 : Baryon Acoustic Oscillations. *Journal of Cosmology and Astro-Particle Physics* **2014,** 027 (May 2014).

75. Geller, M. J. & Huchra, J. P. Mapping the universe. *Science* **246,** 897–903 (Nov. 1989).

76. Glazebrook, K. & Blake, C. Measuring the cosmic evolution of dark energy with baryonic oscillations in the galaxy power spectrum. *The Astrophysical Journal* **631,** 1–20 (2005).

77. Guzzo, L. *et al.* A test of the nature of cosmic acceleration using galaxy redshift distortions. *Nature* **451,** 541–544 (Jan. 2008).

78. Gwyn, S. D. J. & Hartwick, F. D. A. The Redshift Distribution and Luminosity Functions of Galaxies in the Hubble Deep Field. *Astrophysical Journal, Letters* **468,** L77 (Sept. 1996).

79. Halverson, N. W. *et al.* Degree Angular Scale Interferometer First Results: A Measurement of the Cosmic Microwave Background Angular Power Spectrum. *Astrophysical Journal* **568,** 38–45 (Mar. 2002).

84. Hogg, D. W. Distance measures in cosmology. *ArXiv Astrophysics e-prints.* eprint: astro-ph/9905116 (May 1999).

86. Honscheid, K. *et al.* The DECam data acquisition and control system. *Proc. SPIE* **7740** (2010).

88. Hu, W. & White, M. Acoustic Signatures in the Cosmic Microwave Background. *Astrophysical Journal* **471,** 30 (Nov. 1996).

91. Jones, D. H. *et al.* The 6dF Galaxy Survey: final redshift release (DR3) and southern large-scale structures. *Monthly Notices of the Royal Astronomical Society* **399,** 683–698 (Oct. 2009).

93. Kaiser, N. Clustering in real space and in redshift space. *Monthly Notices of the Royal Astronomical Society* **227,** 1–21 (July 1987).

94. Kaiser, N. *et al.* The large-scale distribution of IRAS galaxies and the predicted peculiar velocity field. *Monthly Notices of the Royal Astronomical Society* **252,** 1–12 (Sept. 1991).

96. Kazin, E. A. *et al.* The WiggleZ Dark Energy Survey: Improved Distance Measurements to z = 1 with Reconstruction of the Baryonic Acoustic Feature. *Monthly Notices of the Royal Astronomical Society* **441,** 3524–3542 (2014).

100. Kim, A. G. *et al.* Standardizing Type Ia Supernova Absolute Magnitudes Using Gaussian Process Data Regression. *The Astrophysical Journal* **766,** 84 (2013).

102. Kirshner, R. P. & Kwan, J. Distances to extragalactic supernovae. *Astrophysical Journal* **193,** 27–36 (Oct. 1974).

104. Komatsu, E. The Pursuit of Non-Gaussian Fluctuations in the Cosmic Microwave Background. *ArXiv Astrophysics e-prints.* eprint: astro-ph/0206039 (June 2002).

105. Koo, D. C. Optical multicolors - A poor person's Z machine for galaxies. *Astronomical Journal* **90,** 418–440 (Mar. 1985).

111. Lauberts, A. *ESO/Uppsala survey of the ESO(B) atlas* (1982).

115. Lesgourgues, J. & Pastor, S. Neutrino mass from Cosmology. *ArXiv e-prints.* arXiv: 1212.6154 [hep-ph] (Dec. 2012).

117. Linder, E. V. Cosmic growth history and expansion history. *Physical Review D* **72,** 043529 (Aug. 2005).

118. Loh, E. D. & Spillar, E. J. Photometric redshifts of galaxies. *Astrophysical Journal* **303,** 154–161 (Apr. 1986).

119. Maddox, S. J., Sutherland, W. J., Efstathiou, G. & Loveday, J. The APM galaxy survey. I - APM measurements and star-galaxy separation. *Monthly Notices of the Royal Astronomical Society* **243,** 692–712 (Apr. 1990).

121. Mainzer, A. *et al.* Initial Performance of the NEOWISE Reactivation Mission. *Astrophysical Journal* **792,** 30 (Sept. 2014).

128. Neugebauer, G. *et al.* The Infrared Astronomical Satellite (IRAS) mission. *The Astrophysical Journall* **278,** L1–L6 (Mar. 1984).

135. Padmanabhan, N. *et al.* A 2% Distance to z=0.35 by Reconstructing Baryon Acoustic Oscillations - I : Methods and Application to the Sloan Digital Sky Survey. *Monthly Notices of the Royal Astronomical Society* **427,** 2132–2145 (2012).

136. Padmanabhan, N. *et al.* The Clustering of Luminous Red Galaxies in the Sloan Digital Sky Survey Imaging Data. *Monthly Notices of the Royal Astronomical Society* **378,** 852–872 (2006).

137. Palanque-Delabrouille, N. *et al.* Neutrino masses and cosmology with Lyman-alpha forest power spectrum. *Journal of Cosmology and Astroparticle Physics* **11,** 011 (Nov. 2015).

143. Peebles, P. J. E. & Yu, J. T. Primeval Adiabatic Perturbation in an Expanding Universe. *The Astrophysical Journal* **162,** 815 (Dec. 1970).

144. Percival, W. J. *et al.* The 2dF Galaxy Redshift Survey: spherical harmonics analysis of fluctuations in the final catalogue. *Monthly Notices of the Royal Astronomical Society* **353,** 1201–1218 (Oct. 2004).

145. Percival, W. J. *et al.* Baryon Acoustic Oscillations in the Sloan Digital Sky Survey Data Release 7 Galaxy Sample. *Monthly Notices of the Royal Astronomical Society* **401,** 2148 (2009).

146. Percival, W. J. *et al.* The 2dF Galaxy Redshift Survey: The power spectrum and the matter content of the universe. *Monthly Notices of the Royal Astronomical Society* **327,** 1297–1306 (2001).

147. Perlmutter, S. *et al.* Measurements of Ω and Λ from 42 High-Redshift Supernovae. *The Astrophysical Journal* **517,** 565–586 (June 1999).

148. Pezzotta, A. *et al.* The VIMOS Public Extragalactic Redshift Survey (VIPERS). The growth of structure at $0.5 < z < 1.2$ from redshift-space distortions in the clustering of the PDR-2 final sample. *Astronomy and Astrophysics* **604,** A33 (July 2017).

149. Phillips, M. M. The absolute magnitudes of Type IA supernovae. *Astrophysical Journal, Letters* **413,** L105–L108 (Aug. 1993).

151. Planck Collaboration, Ade, P. A. R., Aghanim, N. & Arnaud, M. Planck 2015 results - XIII. Cosmological parameters. *Astronomy and Astrophysics* **594,** A13 (2016).

152. Planck Collaboration *et al.* Planck 2015 results. XVII. Constraints on primordial non-Gaussianity. *Astronomy and Astrophysics* **594,** A17 (Sept. 2016).

153. Planck Collaboration *et al.* Planck 2015 results. XX. Constraints on inflation. *Astronomy and Astrophysics* **594,** A20 (Sept. 2016).

154. Planck Collaboration *et al.* Planck 2018 results. VI. Cosmological parameters. *ArXiv e-prints.* arXiv: 1807.06209 (July 2018).

158. Racca, G. D. *et al.* The Euclid mission design. *Proc. SPIE* **9904** (July 2016).

162. Reid, B. A. *et al.* Cosmological constraints from the clustering of the Sloan Digital Sky Survey DR7 luminous red galaxies. *Monthly Notices of the Royal Astronomical Society* **404,** 60–85 (May 2010).

163. Riemer-Sørensen, S. *et al.* WiggleZ Dark Energy Survey: Cosmological neutrino mass constraint from blue high-redshift galaxies. *Physical Review D* **85,** 081101 (Apr. 2012).

164. Riess, A. G. *et al.* A 2.4% Determination of the Local Value of the Hubble Constant. *Astrophysical Journal* **826,** 56 (July 2016).

165. Riess, A. G. *et al.* Observational Evidence from Supernovae for an Accelerating Universe and a Cosmological Constant. *The Astrophysical Journal* **116,** 1009–1038 (Sept. 1998).

167. Ross, A. J. *et al.* The Clustering of the SDSS DR7 Main Galaxy Sample I: A 4 per cent Distance Measure at z=0.15. *Monthly Notices of the Royal Astronomical Society* **449,** 835–847 (2014).

169. Ryden, B. *Introduction to cosmology* (2003).

170. Samushia, L., Percival, W. J. & Raccanelli, A. Interpreting large-scale redshift-space distortion measurements. *Monthly Notices of the Royal Astronomical Society* **420,** 2102–2119 (Mar. 2012).

171. Samushia, L. *et al.* The clustering of galaxies in the SDSS-III Baryon Oscillation Spectroscopic Survey: measuring growth rate and geometry with anisotropic clustering. *Monthly Notices of the Royal Astronomical Society* **439,** 3504–3519 (Apr. 2014).

173. Saunders, W. *et al.* The PSCz catalogue. *Monthly Notices of the Royal Astronomical Society* **317,** 55–63 (Sept. 2000).

174. Schmidt, B. P., Kirshner, R. P. & Eastman, R. G. Expanding photospheres of type II supernovae and the extragalactic distance scale. *Astrophysical Journal* **395,** 366–386 (Aug. 1992).

175. Schubnell, M. *et al.* The DESI fiber positioner system. *Proc. SPIE* **9908** (2016).

176. Scodeggio, M. *et al.* The VIMOS Public Extragalactic Redshift Survey (VIPERS). Full spectroscopic data and auxiliary information release (PDR-2). *Astronomy and Astrophysics* **609,** A84 (Jan. 2018).

178. Seo, H. J. & Eisenstein, D. J. Improved Forecasts for the Baryon Acoustic Oscillations and Cosmological Distance Scale. *The Astrophysical Journal* **665,** 14–24 (Aug. 2007).

179. Slosar, A., Hirata, C., Seljak, U., Ho, S. & Padmanabhan, N. Constraints on local primordial non-Gaussianity from large scale structure. *Journal of Cosmology and Astroparticle Physics* **8,** 031 (Aug. 2008).

180. Slosar, A. *et al.* Measurement of Baryon Acoustic Oscillations in the Lyman-alpha Forest Fluctuations in BOSS Data Release 9. *Journal of Cosmology and Astro-Particle Physics* **2013,** 026 (2013).

181. Smee, S. A. *et al.* The Multi-object, Fiber-fed Spectrographs for the Sloan Digital Sky Survey and the Baryon Oscillation Spectroscopic Survey. *Astronomical Journal* **146,** 32 (Aug. 2013).

182. Smoot, G. F. *et al.* Preliminary results from the COBE differential microwave radiometers - Large angular scale isotropy of the cosmic microwave background. *Astrophysical Journal, Letters* **371,** L1–L5 (Apr. 1991).

183. Spergel, D. *et al.* Wide-Field InfrarRed Survey Telescope-Astrophysics Focused Telescope Assets WFIRST-AFTA 2015 Report. *ArXiv e-prints.* arXiv: 1503.03757 [astro-ph.IM] (Mar. 2015).

190. Tamura, N. *et al.* Prime Focus Spectrograph (PFS) for the Subaru telescope: overview, recent progress, and future perspectives. *Proc. SPIE* **9908** (Aug. 2016).

191. Tojeiro, R. *et al.* The clustering of galaxies in the SDSS-III Baryon Oscillation Spectroscopic Survey: galaxy clustering measurements in the low redshift sample of Data Release 11. *Monthly Notices of the Royal Astronomical Society* **440,** 2222 (May 2014).

193. Tripp, R. A two-parameter luminosity correction for Type IA supernovae. *Astronomy and Astrophysics* **331,** 815–820 (Mar. 1998).

194. Tully, R. B. & Fisher, J. R. A new method of determining distances to galaxies. *Astronomy and Astrophysics* **54,** 661–673 (Feb. 1977).

201. Wright E. L.and Eisenhardt, P. R. M. *et al.* The Wide-field Infrared Survey Explorer (WISE): Mission Description and Initial On-orbit Performance. *Astronomical Journal* **140,** 1868–1881 (Dec. 2010).

203. York, D. G. *et al.* The Sloan Digital Sky Survey: Technical Summary. *The Astrophysical Journal* **120,** 1579–1587 (Sept. 2000).

204. Zwicky, F., Herzog, E., Wild, P., Karpowicz, M. & Kowal, C. T. *Catalogue of galaxies and of clusters of galaxies, Vol. I* (1961).

References for Chapter 2

8. Allington-Smith, J., Dunlop, C., Lemke, U. & Murray, G. End effects in optical fibres. *Monthly Notices of the Royal Astronomical Society* **436,** 3492–3499 (Dec. 2013).

33. Carrasco, E. & Parry, I. R. A method for determining the focal ratio degradation of optical fibres for astronomy. *Monthly Notices of the Royal Astronomical Society* **271** (Nov. 1994).

48. de Oliveira, A. C. *et al.* Multi-fibers connectors systems for FOCCoS-PFS-Subaru. *Proc.SPIE* **9151** (July 2014).

55. dos Santos, J. B. *et al.* Studying focal ratio degradation of optical fibers for Subaru's Prime Focus Spectrograph. *Proc. SPIE* **9151** (July 2014).

58. Edelstein, J. *et al.* Optical fiber systems for the BigBOSS instrument. *Proc.SPIE* **8450,** 845036 (Sept. 2012).

81. Haynes, D. M., Haynes, R., Rambold, W., Goodwin, M. & Penny, E. J. Multi-way optical fibre connectors for astronomy. *Proc. SPIE* **7739** (July 2010).

82. Haynes, D. M., Withford, M. J., Dawes, J. M., Lawrence, J. S. & Haynes, R. Relative contributions of scattering, diffraction and modal diffusion to focal ratio degradation in optical fibres. *Monthly Notices of the Royal Astronomical Society* **414,** 253–263 (June 2011).

83. Hill, J. M., Angel, J. R. P., Scott, J. S., Lindley, D. & Hintzen, P. Multiple object spectroscopy - The Medusa spectrograph. *The Astrophysical Journal Letters* **242,** L69–L72 (Dec. 1980).

138. Parry, I. R. *The Astronomical Uses of Optical Fibers* in *Fiber Optics in Astronomy III* (eds Arribas, S., Mediavilla, E. & Watson, F.) **152** (1998), 3.

156. Poppett, C. & Allington-Smith, J. The dependence of the properties of optical fibres on length. *Monthly Notices of the Royal Astronomical Society* **404,** 1349–1354 (May 2010).

157. Poppett, C., Edelstein, J., Besuner, R. & Silber, J. H. Focal ratio degradation performance of fiber positioning technology used in the Dark Energy Spectroscopic Instrument (DESI). *Proc. SPIE* **9147,** 914763 (Aug. 2014).

159. Ramsey, L. W. *Focal ratio degradation in optical fibers of astronomical interest* in *Fiber Optics in Astronomy* (ed Barden, S. C.) **3** (1988), 26–39.

References for Chapter 3

1. Abareshi, B. *et al.* A new telescope control software for the Mayall 4-meter telescope. *Proc. SPIE* **9913** (2016).

11. Bahcall, J. N. Star Counts and Galactic Structure. *Annual Review of Astronomy and Astrophysics* **24,** 577–611 (1986).

52. Dey, A. *et al.* Mosaic3: a red-sensitive upgrade for the prime focus camera at the Mayall 4m telescope. *Proc. SPIE* **9908** (2016).

73. Gaia Collaboration *et al.* Gaia Data Release 1. Summary of the astrometric, photometric, and survey properties. *Astronomy and Astrophysics* **595,** A2 (Nov. 2016).

86. Honscheid, K. *et al.* The DECam data acquisition and control system. *Proc. SPIE* **7740** (2010).

87. Honscheid, K. *et al.* The DESI instrument control system. *Proc. SPIE* **9913** (2016).

97. Kent, S. M. Non-axisymmetric Aberration Patterns from Wide-field Telescopes Using Spin-weighted Zernike Polynomials. *Publications of the Astronomical Society of the Pacific* **130,** 044501 (Apr. 2018).

98. Kent, S. *et al.* Impact of optical distortions on fiber positioning in the dark energy spectroscopic instrument. *Proc. SPIE* **9908** (2016).

103. Kleinmann, S. G., Lysaght, M. G., Pughe, W. L., Schneider, S. E. & Skrutskie, M. F. The Two Micron All Sky Survey: Survey rationale and initial testing. *NASA STI/Recon Technical Report N* **95** (1994).

110. Kuehn, K. *et al.* PreCam: A Precursor Observational Campaign for Calibration of the Dark Energy Survey. *Publications of the Astronomical Society of the Pacific* **125,** 409 (Apr. 2013).

175. Schubnell, M. *et al.* The DESI fiber positioner system. *Proc. SPIE* **9908** (2016).

177. Sebag, J. *et al. LSST telescope integration and tests* in *Ground-based and Airborne Telescopes V* **9145** (July 2014), 91454A.

184. Sprayberry, D. *et al.* Modernization of the Mayall Telescope control system: design, implementation, and performance. *Proc. SPIE* **9906** (2016).

195. Tuttle, S. E. *et al.* VIRUS early installation and commissioning. *Proc. SPIE* **9908** (Aug. 2016).

References for Chapter 4

4. Alam, S. *et al.* The Eleventh and Twelfth Data Releases of the Sloan Digital Sky Survey: Final Data from SDSS-III. *Astrophysical Journal, Supplement* **219,** 12 (July 2015).

6. Aldering, G. SNAP Sky Background at the North Ecliptic Pole. *SNAP Technical Memorandum* (2001).

7. Allen, C. W. *Astrophysical quantities* (1973).

14. Barbier, D. La lumière du ciel nocturne. *L'Astronomie* **70,** 449 (Dec. 1956).

18. Benn, C. R. & Ellison, S. L. Brightness of the night sky over La Palma. *La Palma Technical Note 115 (Isaac Newton Group, La Palma)* (1998).

19. Benn, C. R. & Ellison, S. L. Brightness of the night sky over La Palma. *New Astronomy Reviews* **42,** 503–507 (Nov. 1998).

21. Bernstein, R. A., Freedman, W. L. & Madore, B. F. The First Detections of the Extragalactic Background Light at 3000, 5500, and 8000 Å. II. Measurement of Foreground Zodiacal Light. *Astrophysical Journal* **571,** 85–106 (May 2002).

38. Cosby, P. C., Sharpee, B. D., Slanger, T. G., Huestis, D. L. & Hanuschik, R. W. High-resolution terrestrial nightglow emission line atlas from UVES/VLT: Positions, intensities, and identifications for 2808 lines at 314-1043 nm. *Journal of Geophysical Research (Space Physics)* **111,** A12307 (Dec. 2006).

40. Cuby, J. G., Lidman, C. & Moutou, C. ISAAC: 18 Months of Paranal Science Operations. *The Messenger* **101,** 2–8 (Sept. 2000).

51. DESI Collaboration *et al.* The DESI Experiment Part II: Instrument Design. eprint: arXiv:1611.00037v2 (Nov. 2016).

59. Edlén, B. The Refractive Index of Air. *Metrologia* **2,** 71–80 (Apr. 1966).

62. Ellis, S. C. & Bland-Hawthorn, J. The case for OH suppression at near-infrared wavelengths. *Monthly Notices of the Royal Astronomical Society* **386,** 47–64 (May 2008).

63. Ellis, S. C. *et al.* Suppression of the near-infrared OH night-sky lines with fibre Bragg gratings - first results. *Monthly Notices of the Royal Astronomical Society* **425,** 1682–1695 (Sept. 2012).

64. Evans, W. F. J., Gattinger, R. L., Broadfoot, A. L. & Llewellyn, E. J. The observation of chemiluminescent NiO* emissions in the laboratory and in the night airglow. *Atmospheric Chemistry & Physics* **11,** 9595–9603 (Sept. 2011).

66. Fagrelius, P. & Schlegel, D. A predictive optical sky background model for DESI. *Proc. SPIE* **10702** (2018).

74. Garstang, R. H. Night-sky brightness at observatories and sites. *Publications of the Astronomical Society of the Pacific* **101,** 306–329 (Mar. 1989).

80. Hanuschik, R. W. A flux-calibrated, high-resolution atlas of optical sky emission from UVES. *Astronomy and Astrophysics* **407,** 1157–1164 (Sept. 2003).

85. Hogg, D. W., Finkbeiner, D. P., Schlegel, D. J. & Gunn, J. E. A Photometricity and Extinction Monitor at the Apache Point Observatory. *The Astronomical Journal* **122,** 2129–2138 (Oct. 2001).

89. Hull, C. L., Limmongkol, S. & Siegmund, W. A. Sloan Digital Sky Survey cloud scanner. *Proc. SPIE* **2199** (ed Stepp, L. M.) 852–857 (June 1994).

90. Ingham, M. F. The Spectrum of the Airglow. *Scientific American* **226,** 78–85 (Jan. 1972).

92. Jones, Noll, S., Kausch, W., Szyszka, C. & Kimeswenger, S. An advanced scattered moonlight model for Cerro Paranal. *Astronomy and Astrophysics* **560,** A91 (Dec. 2013).

95. Kalinowski, J. K., Roosen, R. G. & Brandt, J. C. The night sky brightness at McDonald Observatory. *Publications of the Astronomical Society of the Pacific* **87,** 869–876 (Dec. 1975).

99. Kieffer, H. H. & Stone, T. C. The Spectral Irradiance of the Moon. *Astronomical Journal* **129,** 2887–2901 (June 2005).

101. King, I. R. Accuracy of measurement of star images on a pixel array. *Publications of the Astronomical Society of the Pacific* **95,** 163–168 (Feb. 1983).

106. Krisciunas, K. Further measurements of extinction and sky brightness on the island of Hawaii. *Publications of the Astronomical Society of the Pacific* **102,** 1052–1063 (Aug. 1990).

107. Krisciunas, K. Optical Night-Sky Brightness at Mauna Kea over the Course of a Complete Sunspot Cycle. *Publications of the Astronomical Society of the Pacific* **109,** 1181–1188 (Oct. 1997).

108. Krisciunas, K. & Schaefer, B. E. A model of the brightness of moonlight. *Publications of the Astronomical Society of the Pacific* **103,** 1033–1039 (Sept. 1991).

109. Krisciunas, K. *et al.* Optical Sky Brightness at Cerro Tololo Inter-American Observatory from 1992 to 2006. *Publications of the Astronomical Society of the Pacific* **119,** 687–696 (June 2007).

112. Leinert, C. & Mattila, K. *Natural Optical Sky Background* in *Preserving The Astronomical Windows* (eds Isobe, S. & Hirayama, T.) **139** (1998), 17.

113. Leinert, C., Vaisanen, P., Mattila, K. & Lehtinen, K. Measurements of sky brightness at the Calar Alto Observatory. *Astronomy and Astrophysics, Supplement* **112,** 99 (July 1995).

114. Leinert, C. *et al.* The 1997 reference of diffuse night sky brightness. *Astronomy and Astrophysics, Supplement* **127,** 1–99 (Jan. 1998).

116. Levasseur-Regourd, A. C. & Dumont, R. Absolute photometry of zodiacal light. *Astronomy & Astrophysics* **84,** 277–279 (Apr. 1980).

120. Maihara, T. *et al.* Observations of the OH airglow emission. *Publications of the Astronomical Society of the Pacific* **105,** 940–944 (Sept. 1993).

122. Massey, P. & Foltz, C. B. The Spectrum of the Night Sky over Mount Hopkins and Kitt Peak: Changes after a Decade. *Publications of the Astronomical Society of the Pacific* **112,** 566–573 (Apr. 2000).

123. Massey, P., Gronwall, C. & Pilachowski, C. A. The spectrum of the Kitt Peak night sky. *Publications of the Astronomical Society of the Pacific* **102,** 1046–1051 (Aug. 1990).

124. Mattila, K. Synthetic spectrum of the integrated starlight between 3,000 and 10,000 A. I - Method of calculation and results. *Astronomy and Astrophysics, Supplement* **39,** 53–65 (Jan. 1980).

125. Mattila, K., Vaeisaenen, P. & Appen-Schnur, G. F. O. V. Sky brightness at the ESO La Silla Observatory 1978 to 1988. *Astronomy and Astrophysics, Supplement* **119,** 153–170 (Oct. 1996).

126. Meinel, I. A. B. OH Emission Bands in the Spectrum of the Night Sky. *Astrophysical Journal* **111,** 555 (May 1950).

127. Melchior, A.-L., Combes, F. & Gould, A. The surface brightness of the Galaxy at the solar neighbourhood. *Astronomy and Astrophysics* **462,** 965–976 (Feb. 2007).

129. Neugent, K. F. & Massey, P. The Spectrum of the Night Sky Over Kitt Peak: Changes Over Two Decades. *Publications of the Astronomical Society of the Pacific* **122,** 1246 (Oct. 2010).

130. Noll, S. *et al.* An atmospheric radiation model for Cerro Paranal. I. The optical spectral range. *Astronomy and Astrophysics* **543,** A92 (July 2012).

131. Noxon, J. F. The near infrared nightglow continuum. *Planetary and Space Science* **26,** 191 (Feb. 1978).

132. Oliva, E. *et al.* Lines and continuum sky emission in the near infrared: observational constraints from deep high spectral resolution spectra with GIANO-TNG. *Astronomy and Astrophysics* **581,** A47 (Sept. 2015).

133. Osterbrock, D. E., Walker, M. F. & Koski, A. T. The spectrum of light pollution at Mount Hamilton. *Publications of the Astronomical Society of the Pacific* **88,** 349–352 (June 1976).

134. Osterbrock, D. E. *et al.* Night-Sky High-Resolution Spectral Atlas of OH and O2 Emission Lines for Echelle Spectrograph Wavelength Calibration. *Publications of the Astronomical Society of the Pacific* **108,** 277 (Mar. 1996).

139. Patat, F. The dancing sky: 6 years of night-sky observations at Cerro Paranal. *Astronomy and Astrophysics* **481,** 575–591 (Apr. 2008).

140. Patat, F. UBVRI night sky brightness during sunspot maximum at ESO-Paranal. *Astronomy and Astrophysics* **400,** 1183–1198 (Mar. 2003).

141. Patat, F., Ugolnikov, O. S. & Postylyakov, O. V. UBVRI twilight sky brightness at ESO-Paranal. *Astronomy and Astrophysics* **455,** 385–393 (Aug. 2006).

142. Pedani, M. Sky Surface Brightness at Mount Graham: UBVRI Science Observations with the Large Binocular Telescope. *Publications of the Astronomical Society of the Pacific* **121,** 778 (July 2009).

150. Pilachowski, C. A., Africano, J. L., Goodrich, B. D. & Binkert, W. S. Sky brightness at the Kitt Peak National Observatory. *Publications of the Astronomical Society of the Pacific* **101,** 707–712 (Aug. 1989).

155. Plauchu-Frayn, I. *et al.* Night Sky Brightness at San Pedro Martir Observatory. *Publications of the Astronomical Society of the Pacific* **129,** 035003 (Mar. 2017).

160. Rayleigh, L. The Light of the Night Sky: Its Intensity Variations when Analysed by Colour Filter. III. *Proceedings of the Royal Society of London Series A* **119,** 11–33 (May 1928).

161. Rayleigh, L. & Jones. The Light of the Night-Sky: Analysis of the Intensity Variations at Three Stations. *Proceedings of the Royal Society of London Series A* **151,** 22–55 (Aug. 1935).

166. Roach, F. E. & Gordon, J. L. *The Light of the Night Sky* (1973).

168. Rousselot, P., Lidman, C., Cuby, J.-G., Moreels, G. & Monnet, G. Night-sky spectral atlas of OH emission lines in the near-infrared. *Astronomy and Astrophysics* **354,** 1134–1150 (Feb. 2000).

172. Sánchez, S. F., Aceituno, J., Thiele, U., Pérez-Ramírez, D. & Alves, J. The Night Sky at the Calar Alto Observatory. *Publications of the Astronomical Society of the Pacific* **119,** 1186–1200 (Oct. 2007).

181. Smee, S. A. *et al.* The Multi-object, Fiber-fed Spectrographs for the Sloan Digital Sky Survey and the Baryon Oscillation Spectroscopic Survey. *Astronomical Journal* **146,** 32 (Aug. 2013).

185. Staude, H. J. Scattering in the Earth's Atmosphere: Calculations for Milky Way and Zodiacal Light as Extended Sources. *Astronomy and Astrophysics* **39,** 325 (Mar. 1975).

186. Sternberg, J. R. Photochemistry of the airglow continuum. *Monthly Notices of the Royal Astronomical Society* **159,** 21 (1972).

187. Sternberg, J. R. & Ingham, M. F. Observations of the airglow continuum. *Monthly Notices of the Royal Astronomical Society* **159,** 1 (1972).

188. Sullivan, P. W. & Simcoe, R. A. A Calibrated Measurement of the Near-IR Continuum Sky Brightness Using Magellan/FIRE. *Publications of the Astronomical Society of the Pacific* **124,** 1336 (Dec. 2012).

189. Takahashi, H., Sahai, Y. & Batista, P. P. Tidal and solar cycle effects of the O I 5577-A, NaD and OH(8,3) airglow emissions observed at 23 deg S. *Planetary and Space Science* **32,** 897–902 (July 1984).

192. Toller, G. N. *A study of galactic light, extragalactic light, and galactic structure using Pioneer 10 observations of background starlight* PhD thesis (State University of New York, Stony Brook., 1981).

196. van Rhijn, P. J. On the brightness of the sky at night and the total amount of starlight. *Publications of the Kapteyn Astronomical Laboratory Groningen* **31,** 1–83 (1921).

197. Walker. *NOAO Newsletter* **10,** 12 (1987).

198. Walker. The effect of solar activity on the V and B band sky brightness. *Publications of the Astronomical Society of the Pacific* **100,** 496–505 (Apr. 1988).

199. Wolstencroft, R. D. & van Breda, I. G. The Determination of Isophotes of Extended Sources in the Night Sky: Scattering in the Earth's Atmosphere. *Astrophysical Journal* **147,** 255 (Jan. 1967).

200. Woods, T. N., Wrigley III, R. T., Rottman, G. J. & Haring, R. E. Scattered-light properties of diffraction gratings. *Applied Optics* **33,** 4273–4285 (July 1994).

202. Yee, J. H., Abreu, V. J. & Hays, P. B. The O II /7320-7330 A/ airglow - A morphological study. *Journal of Geophysics Research* **86,** 1564–1568 (Mar. 1981).